ABSTRACT

| | |
|---|---|
| Title of Dissertation: | EXPERIMENTAL CHARACTERIZATION OF ATMOSPHERIC TURBULENCE SUPPORTED BY ADVANCED PHASE SCREEN SIMULATIONS |
| | Daniel A. Paulson, Doctor of Philosophy, 2020 |
| Dissertation directed by: | Professor Christopher C. Davis<br>Department of Electrical and Computer Engineering |

Characterization of optical propagation through the low turbulent atmosphere has been a topic of scientific investigation for decades, and has important engineering applications in the fields of free space optical communications, remote sensing, and directed energy. Traditional theories, starting with early radio science, have flowed down from the assumption of three dimensional statistical symmetry of so-called fully developed, isotropic turbulence. More recent experimental results have demonstrated that anisotropy and irregular frequency domain characteristics are regularly observed near boundaries of the atmosphere, and similar findings have been reported in computational fluid dynamics literature. We have used a multi-aperture transmissometer in field testing to characterize atmospheric transparency, refractive index structure functions, and turbulence anisotropy near atmospheric boundaries. Additionally, we have fielded arrays of resistive temperature detector probes

alongside optical propagation paths to provide direct measurements of temperature and refractive index statistics supporting optical turbulence observations. We are backing up these experimental observations with a modified algorithm for modeling optical propagation through atmospheric turbulence. Our new phase screen approach utilizes a randomized spectral sampling algorithm to emulate the turbulence energy spectrum and improve modeling of low frequency fluctuations and improve convergence with theory. We have used the new algorithm to investigate open theoretical topics, such as the behavior of beam statistics in the strong fluctuation regime as functions of anisotropy parameters, and energy spectrum power law behavior. These results have to be leveraged in order to develop new approaches for characterization of atmospheric optical turbulence.

# EXPERIMENTAL CHARACTERIZATION OF ATMOSPHERIC TURBULENCE SUPPORTED BY ADVANCED PHASE SCREEN SIMULATIONS

by

Daniel A. Paulson

Dissertation submitted to the Faculty of the Graduate School of the
University of Maryland, College Park, in partial fulfillment
of the requirements for the degree of
Doctor of Philosophy
2020

Advisory Committee:
Professor Christopher C. Davis, Chair
Professor Thomas M. Antonsen, Jr.
Professor Douglas G. Currie
Professor Julius Goldhar
Professor Phillip A. Sprangle

# Acknowledgements

The work contained within this dissertation is the result of collaborative work among many people. First, I thank my adviser Professor Christopher C. Davis for his support during this process, kind words of encouragement, and for providing the academic freedom to investigate areas which I found particularly interesting and seek creative solutions to problems. Secondly, I would like to thank all the current and former members of the Maryland Optics Group I had the pleasure of working with during my graduate research: Dr. Quirino Balzano, Nathaniel Ferlic, Dr. Jonathan Ko, Dr. William Nelson, Dr. John Rzasa, Dr. Igor I. Smolyaninov, Dr. Miranda van Iersel, and Dr. Chensheng Wu. Dr. Rzasa and Dr. Wu were particularly instrumental in conceptualizing the experimental optical equipment used in this dissertation, and Dr. van Iersel dedicated many hours of assistance in field testing. I also thank the staff of Townes Institute Science and Technology Experimentation Facility who were key collaborators during this effort.

Additionally, I would like to thank the committee members: Professor Phillip Sprangle, Professor Thomas Antonsen, Professor Julius Goldhar, and Professor Douglas Currie for taking the time to review my dissertation and defense. During my graduate education I also had the pleasure of attending classes instructed by Professor Antonsen and Professor Sprangle which helped to spur my interest in electrophysics research. I'd also like to thank Sarwat Chappell of the Office of

Naval Research for supporting the bulk of these efforts. Finally, my parents deserve a great deal of gratitude for encouraging my pursuit of higher education.

This work was supported by the Office of Naval Research (ONR) under contract number N000141812008.

# Table of Contents

Acknowledgements ..... ii
Table of Contents ..... iv
List of Figures ..... vi
Definitions and abbreviations ..... xix

Chapter 1 : Overview and Theoretical Considerations ..... 1
1.1: Introduction ..... 1
1.2: Theoretical Background Regarding the Nature of Optical Turbulence ..... 2
1.3: Mathematical Background Regarding the Simulation of Optical Propagation ..... 12
1.4: Theoretical Considerations for Propagation through Anisotropic, Non-Kolmogorov Turbulence ..... 20
1.5: A Note Regarding Alternatives to the Paraxial Approximations ..... 33

Chapter 2 : A Revised Method for Simulation of Atmospheric Turbulence ..... 39
2.1: Background ..... 39
2.2: Overview of the Split Step Algorithm for Simulation of Optical Propagation through Atmospheric Turbulence ..... 40
2.3: Motivation for a New Method ..... 48
2.4: Randomized FFT-based Spectral Sampling, Core Algorithm ..... 51
2.5: Core Algorithm Results for Anisotropic, non-Kolmogorov Spectral Models ..... 56
2.6: Core Algorithm Results for Bounded Spectral Models ..... 68
2.7: Hybrid Algorithm Including Subharmonics ..... 77
2.8: Addition of White Noise to Phase Screens to Support Subresolution Inner Scales ..... 81
2.9: Hybrid Algorithm Results for Unbounded Spectral Models ..... 88
2.10: Hybrid Algorithm Results for Bounded Spectral Models ..... 93

Chapter 3 : Numerical Verification of the Statistical Theories of Propagation of Optical Beams through Anisotropic, Non-Kolmogorov Turbulence ..... 98
3.1: Background ..... 98
3.2: Spot Size Predictions in the Presence of Non-Kolmogorov Turbulence ..... 98
3.3: Focused Beams in Non-Kolmogorov Turbulence ..... 103
3.4: Weak Turbulence Regime Predictions of Spot Size ..... 106
3.5: Scintillation Index and Aperture Averaging of Scintillation in the Presence of Optical Turbulence and Refractivity Distortions ..... 109

Chapter 4 : Experimental Investigations Atmospheric Distortions Using a Multi-Aperture Transmissometer....134
4.1: Introduction....134
4.2: MOG MAT Fundamentals....135
4.2: Synchronization of Transmitter and Receiver for Elimination of Background Light....139
4.3: Estimates of Extinction Coefficient....144
4.4: An Iterative Beam Fitting Approach to Capture Refractivity and Turbulence Effects....149
4.5: Turbulence Profiling Results in the Weak Fluctuation Regime....165
4.6: Simultaneous Extinction Rate and Turbulence Profiling in the Deep Fluctuation Regime....190

Chapter 5 : Summary and Future Work....204
5.1: Summary....204
5.2: Future Work....208

Appendices....212
Appendix A: Tables of RMS Error Statistics over Region of Interest....213
Appendix B: Charts of RMS Error Statistics over Entire Domain....227
Appendix C: Tables of Non-Kolmogorov RMS Error Statistics over Entire Domain....235

Bibliography....242

# List of Figures

Figure 1-1: Illustrations of the inertial subrange concept of classical turbulence theory, from [9]. ....3

Figure 2-1: Illustration of a generic phase screen simulation using five screens. The beam is propagated a distance of $\Delta z/2$ or $\Delta z$ using the FFT-based angular spectrum propagation algorithm. After all but the final propagation step, a random phase screen is applied as a phase modulation of the propagating wave. 41

Figure 2-2: Visual aid demonstrating fractal nature of the subharmonic expansion, taken from [52]. ....47

Figure 2-3: Demonstration of the traditional FFT phase screen method's observed structure function's agreement with theory degrading as the three dimensional spectral power law, $\alpha$, increases. ....50

Figure 2-4: Example $\kappa$-space grid partitioning and sampling showing traditional spectral sampling approach versus randomized spectral sampling approach. Black dots represent traditional sampling points, red dots represent one realization of the randomized sampling approach, and the blue grid lines demarcate the sampling boundaries for the randomized method....53

Figure 2-5: a) Phase screen produced using traditional FFT-based algorithm on a 1024×1024 grid; b) same phase screen as previous, repeated four times and placed adjacent to itself in order to illustrate the periodicity associated with traditional FFT-based screens; c) phase screen produced using modified FFT-based algorithm on a 1024×1024 grid; d) same phase screen as directly previous, repeated four times and placed adjacent to itself in order to illustrate the lack of periodicity associated the modified randomized FFT-based algorithm. The colors shown denote the phase shift of the screen in radians on the simulated propagating wave, as per the colorbar. ....55

Figure 2-6: RMS error as a percent relative to theory over 50,000 phase screen trials for the simulated domain region of interest as parameterized by the three dimensional spectral power law, $\alpha$. 512 × 512, 1024 × 1024, 2048 × 2048 grid results are shown for randomized method. For the traditional method, the 2048 × 2048 grid is shown. Other grid sizes are not shown for the traditional method because the results appear to completely overlap at this scale. ....58

Figure 2-7: Phase screen structure function produced by the randomized and traditional methods compared to theory over $x$- and $y$-directions over 25,000 phase screen for several values of the three dimensional spectral power law, $\alpha$, 1024 × 1024 grid results. The coherence length used to produce the screens was $\rho_{0,x} = \rho_{0,y} = 0.05$ cm for all $\alpha$'s. .....62

Figure 2-8: Histogram plots of probability density for: a) natural logarithm of the magnitude of phase at phase screen center using the randomized method for various values of the three dimension spectral power law, $\alpha$; b) relative phase difference across the region of interest using the randomized method for various values of the three dimension spectral power law, $\alpha$. For each subplot, the probability densities were collected over 5,000 phase screens using a 2048 × 2048 grid created using the randomized method. .....63

Figure 2-9: a) AoA variance averaged over a 40 cm diameter aperture of a plane wave propagating through Kolmogorov turbulence plotted as a function of Rytov variance for wave optics simulations using the randomized method and the traditional method compared to theory for Rytov variance 0.1; b) aperture averaged AoA variance of a plane wave propagating through turbulence plotted as a function of aperture diameter for wave optics simulations using the randomized method and the traditional method compared to theory Kolmogorov spectrum and Rytov variance 0.1; c) aperture averaged AoA variance of a plane wave propagating through turbulence plotted as a function of the three dimensional spectral power law for wave optics simulations using the randomized method and the traditional method compared to theory for Rytov variance 0.1 and aperture size 40 cm. All simulations were performed using a 1024 × 1024 grid and 20 equally spaced phase screens over a 2 km propagation distance. .....67

Figure 2-10: Comparison of phase screen structure function versus theory using 2048 × 2048 grid, inner scale 1 cm, outer scale 100 km, and effective coherence length of $\rho_0 = 5$ cm. .....72

Figure 2-11: RMS error as a percent relative to theory over 50,000 phase screen trials for the simulated domain region of interest as parameterized by the three dimensional spectral power law, $\alpha$. 512 × 512, 1024 × 1024, 2048 × 2048 grid results are shown for randomized method. The outer scale has been normalized by the domain width, $M\Delta x$ (m), to make the results applicable for any domain size. For the traditional method only the 2048 × 2048 grid is shown due to significant overlap of the RMS error metric. .....73

Figure 2-12: Histogram plots of probability density for: a) absolute phase using outer scale $L0 = 1 \cdot M\Delta x$; b) relative phase over region of interest using outer scale $L0 = 1 \cdot M\Delta x$; c) natural logarithm of the magnitude of absolute phase using outer scale $L0 = 102 \cdot M\Delta x$; d) relative phase over region of interest using outer scale $L0 = 102 \cdot M\Delta x$; e) natural logarithm of the magnitude of absolute phase using outer scale $L0 = 104 \cdot M\Delta x$; f ) relative phase over region of interest using outer scale $L0 = 104 \cdot M\Delta x$. For each subplot, the probability densities collected over 5000 phase screens using a 2048 × 2048 grid created using the randomized algorithm and modified spectrum. .....75

Figure 2-13: a) AoA variance averaged over a 40 cm diameter aperture of a plane wave propagating through turbulence plotted as a function of Rytov variance for wave optics simulations using the randomized method and the traditional method compared to theory; b) aperture averaged AoA variance of a plane wave propagating through turbulence plotted as a function of aperture diameter for wave optics simulations using the randomized method and the traditional method compared to theory. All simulations were performed using a 1024 × 1024 grid and 13 equally spaced phase screens over a 2 km propagation distance. .....76

Figure 2-14: Example $\kappa$-space grid partitioning and sampling showing traditional subharmonic sampling approach versus hybrid randomized spectral sampling approach for $N_p = 1$. Black dots represent traditional sampling points (including subharmonic expansion), red dots represent one realization of the randomized sampling approach, and the blue grid lines demarcate the sampling boundaries for the randomized method. .....80

Figure 2-15: *X*-axis structure function of phase screens made with the randomized, hybrid subharmonic algorithm and white noise added, as well as screens using the traditional subharmonic method. Parameters for the screens are 1024 × 1024 grid, $N_p = 1$, and effective coherence length $\rho_{0,x} = 5$ cm. .....86

Figure 2-16: *X*-axis structure function normalized by theory of phase screens produced with the randomized, hybrid subharmonic algorithm both with and without white noise added, as well as screens using the traditional subharmonic method. The parameters used to create this figure are identical to those in Figure 2-15. .....87

Figure 2-17: RMS error over region of interest computed along x and y directions of 50,000 phase screens for 512 × 512 grid using various spectral power laws ($\alpha$'s) and number of subharmonic constellations, $N_p$. $\mu_x = \mu_y = 1$ for all data points. The randomized hybrid method (green), Frehlich subharmonic method

(black), and Lane subharmonic method (magenta) are shown. Full results for all grid sizes and spectra under test are given in Appendix A.. .....90

Figure 2-18: RMS error over region of interest computed along x and y directions of 50,000 phase screens for 1024 × 1024 grid using various spectral power laws ($\alpha$'s) and number of subharmonic constellations, $N_p$. $\mu_x = 1$, $\mu_y = 2$ for all data points. The randomized hybrid method (blue) and Frehlich subharmonic method (black) are shown. .....91

Figure 2-19: RMS error over region of interest computed along x and y directions of 5,000 phase screens for 2048 × 2048 grid using various spectral power laws ($\alpha$'s) and number of subharmonic constellations, $N_p$. $\mu_x = 1$, $\mu_y = 2$ for all data points. The randomized hybrid method (red) and Frehlich subharmonic method (black) are shown. .....92

Figure 2-20: RMS error over region of interest computed along *x*- and *y*-directions for 5000 phase screens using modified spectrum, with $l0 = M\Delta x/100$ and $M = 512$ (i.e. grid size 512 × 512). Complete tables of results for all grid sizes and spectra under test can be found in Appendix A.....94

Figure 2-21: RMS error over region of interest computed along *x*- and *y*-directions for 5000 phase screens using modified spectrum, with $l0 = M\Delta x/100$ and $M = 1024$ (i.e. grid size 1024 × 1024). .....95

Figure 2-22: RMS error over region of interest computed along *x*- and *y*-directions for 5000 phase screens using modified spectrum, with $l0 = M\Delta x/100$ and $M = 2048$ (i.e. grid size 2048 × 2048). .....96

Figure 3-1: Beam diameter theoretical predictions vs simulation result across various α's, with the Rytov variance held at 10 and i.e. grid size 2048 × 2048. Trials were performed with 10 evenly spaced phase screens each, and 5 km propagation distance using a collimated, 50 cm diameter, 1060 nm beam. Phase screens were 2048 × 2048 with 0.5 mm grid spacing for α's below 3.8, however a 4096 × 4096 grid with .25 mm spacing was used for α's of 3.8 and 3.9 to avoid aliasing effects during propagation. .....102

Figure 3-2: Measured beam diameter results for an initially 50 cm diameter, 632.8 nm focused beam propagating through 5 km of of $Cn2 = 10^{-14}$ $m^{3-\alpha}$ anisotropic turbulence with $\mu_x = 1$ and $\mu_y = 3$. Phase screens were 2048 × 2048 with 0.5 mm grid spacing.....104

Figure 3-3: Simulation results vs theory for on-axis scintillation index, $\sigma I2(0,0)$, of focused 1060 nm beam propagating through 5 km of anisotropic turbulence. Simulation results do not trend well with theoretical predictions.....106

Figure 3-4: Simulation results for long term beam diameters in anisotropic turbulence versus theory as $\mu_x$ is held at one, and $\mu_y$ is swept from one to ten, for an initially 10 cm diameter beam propagating across a 2 km path in $Cn2 = 10^{-14}$ $m^{-7/10}$ of turbulence, with $\alpha = 3.7$. The $x$-direction spot size does not trend well with theory, though the simulation does show that the $x$- and $y$-direction spot sizes are not independent of the anisotropy parameter in the orthogonal direction. ....108

Figure 3-5: Output plane scintillation index in decibels for $\mu x = \mu y = 1$, $W0 =$ 1.4 cm, $Wx = 15$ cm, $Wy = 7.5$ cm, $L$ = 530 m, spherical wave Rytov variance of .1 case. .....112

Figure 3-6: Comparison of observed and theoretically predicted scintillation indices in for $\mu x = \mu y = 1$, $W0 = 1.4$ cm, $Wx = 15$ cm, $Wy = 7.5$ cm, $L$ = 530 m, spherical wave Rytov variance of .1 case. .....113

Figure 3-7: Output plane aperture averaged scintillation index in decibels for $\mu x = \mu y = 1$, $W0 = 1.4$ cm, $Wx = 15$ cm, $Wy = 7.5$ cm, $L$ = 530 m, spherical wave Rytov variance of .1 case. Beam intensity was averaged over a 2.5 cm diameter aperture for this trial.....114

Figure 3-8: Comparison of observed and theoretically predicted scintillation indices in for $\mu x = \mu y = 1$, $W0 = 1.4$ cm, $W = 15$ cm, $L$ = 530 m, spherical wave Rytov variance of .1 case.....116

Figure 3-9: Comparison of observed and theoretically predicted scintillation indices in for $\mu x = \mu y = 1$, $W0 = 1.4$ cm, $W = 7.5$ cm, $L$ = 530 m, spherical wave Rytov variance of .1 case.....117

Figure 3-10: Comparison of observed and theoretically predicted scintillation indices plotted as functions of the spherical wave Rytov variance for an asymmetric beam in isotropic turbulence for a range of $\mu y$'s with $\mu x = 1$, $W0 =$ 1.4 cm, $Wx = 15$ cm, $Wy = 11.25$ cm, $L$ = 530 m. .....119

Figure 3-11: Comparison of observed and theoretically predicted scintillation indices for an asymmetric beam in anisotropic turbulence for $\mu y = 1/3$, $W0 =$ 1.4 cm, $W = 15$ cm, $L$ = 530 m, spherical wave Rytov variance of .01 case. ...122

Figure 3-12: Comparison of observed and theoretically predicted scintillation indices for an asymmetric beam in isotropic turbulence for $\mu x = \mu y = 1$, $W0 =$ 1.4 cm, $Wx = 15$ cm, $Wy = 7.5$ cm, $L$ = 530 m, spherical wave Rytov variance of .01 case. .....123

Figure 3-13: Theoretically predicted scintillation index as a function of inner scale, $l0$, for a variety of beams in isotropic turbulence: 1) Blue curves represent prediction for a beam with $W0 = 50$ cm; 2) Green curves represent prediction for an initially collimated beam with $W0 = 1.4$ cm and $F0 = 120$ m; 3) Red curves represent prediction for a beam with $W0 = 50$ μm and $F0 = 530$ m, which was the propagation distance for all curves. All results are for a wavelength of 632.8 μm and a plane wave Rytov variance of .05. .....125

Figure 3-14: Theoretically predicted 2.5 cm diameter aperture averaged scintillation index as a function of inner scale, $l0$, for a variety of beams in isotropic turbulence: 1) Blue curves represent prediction for a beam with $W0 =$ 50 cm; 2) Green curves represent prediction for an initially collimated beam with $W0 = 1.4$ cm and $F0 = 120$ m; 3) Red curves represent prediction for a beam with $W0 = 50$ μm and $F0 = 530$ m, which was the propagation distance for all curves. All results are for a wavelength of 632.8 μm and a plane wave Rytov variance of .05.....127

Figure 3-15: Aperture averaging factors along *x*- and *y*-axes for $\mu x = \mu y = 1$, $W0 = 1.4$ cm, $Wx = 15$ cm, $Wy = 11.25$ cm, $L$ = 530 m, spherical wave Rytov variance of .1 case. .....129

Figure 3-16: Comparison of point vs 2.5 diameter aperture averaged scintillation indices for a variety of spherical wave Rytov variances and an asymmetric beam in isotropic turbulence using $\mu x = \mu y = 1$, $W0 = 1.4$ cm, $Wx = 15$ cm, $Wy =$ 7.5 cm, $L$ = 530 m. .....130

Figure 3-17: Comparison of 2.5 diameter aperture averaging factors for a variety of spherical wave Rytov variances for an asymmetric beam in isotropic turbulence using $\mu x = \mu y = 1$, $W0 = 1.4$ cm, $Wx = 15$ cm, $Wy = 7.5$ cm, $L$ = 530 m. The results were further averaged using the following methods .....131

Figure 3-18: Aperture averaging factor for various values of $\mu y$ plotted as a function of the spherical wave Rytov variances using an asymmetric beam in isotropic turbulence using $W0 = 1.4$ cm, $Wx = 15$ cm, $Wy = 7.5$ cm, $L$ = 530 m. .....132

Figure 4-1: Juxtaposition of: a) Traditional single aperture transmissometer used for making a short range extinction estimate in an airfield; b) Maryland Optics Group multi-aperture transmissometer designed for estimating extinction coefficients over path lengths of the order of magnitude of a kilometer. .....136

Figure 4-2: Pictures of the multi-aperture hexagonal transmissometer displacing: a) The thirteen detectors and corner cube reflectors; b) the local user interface. 136

Figure 4-3: Example phase frequency correlation matrix generated by summing the final three dimensional data structure described in the text along the *z*-direction. Note, one cycle equals $2\pi$ radians. .....142

Figure 4-4: Example juxtaposition of the 13 signals from each aperture of a test (dashed lines) and the replica chopping wheel clock (red square wave) and the sampling clock (blue dotted line), which both appear at or below 1 on the *y*-axis of the plot. Sample clock values of 1 indicate that *on*-samples are taken and sample clock values of -1 indicate that *off*-samples are taken. .....143

Figure 4-5: Example output of elliptic Gaussian fitting as displayed in MATLAB.....145

Figure 4-6: Comparison of visibility meter and MAT metrics over 2 days: a) Extinction coefficient estimates from the MAT (red) vs the visibility meter (black), b) Precipitation rate estimates from the visibility meter (blue), c) another rendition of the top figure, with the axis zoomed in to demonstrate that overall trends, and small features, of both devices' estimates of extinction correspond. 147

Figure 4-7: Equipment locations over TISTEF range: a) Layout picture on the receiver end; b) overall view of the TISTEF range from the transmitter end.....148

Figure 4-8: Simulation results illustrating differing scintillation index profiles despite comparable intensity profiles: a) Scintillation index profile for an initially collimated beam propagating 530 m through Kolmogorov, anisotropic turbulence with $\mu_x = 1$, $\mu_y = 1/3$, and spherical wave Rytov variance of 1; b) Mean intensity profile for an initially collimated beam propagating 530 m through Kolmogorov, anisotropic turbulence with $\mu_x = 1$, $\mu_y = 1/3$, and spherical wave Rytov variance of 1; c) Scintillation index profile approximating non-turbulent optical refractivity distortion using a beam which is initially collimated across the *x*-axis but with a radius of curvature of -4,142 m in the y-direction propagating through 530 m of Kolmogorov, isotropic turbulence with spherical wave Rytov variance of 1; d) Mean intensity profile approximating non-turbulent optical refractivity distortion

using a beam which is initially collimated across the *x*-axis but with a radius of curvature of -4,142 m in the y-direction propagating through 530 m of Kolmogorov, isotropic turbulence with spherical wave Rytov variance of 1. A 2.5 cm diameter aperturing filter was used to collect all results for comparison with the collected transmissometer data. .....150

Figure 4-9: Example observed main intensity at the MAT receiver and from an outdoor field experiment. The observation that the intensity spot ellipse and the scintillation index are pointing in approximately the same directions indicate that refractivity effects are dominating optical propagation distortions. The subplots are: a) Interpolated mean optical intensity profile; b) Detector-by-detector mean optical intensity; c) Interpolated scintillation index profile; d) Detector-by-detector scintillation index. .....152

Figure 4-10: High level visual summary of the iterative fitting approach. .....156

Figure 4-11: Behavior of turbulence and beam parameter estimates during iterative fitting. The subplots shown are as follows: a) The estimated refractive index structure constant, $C_n^2$; The turbulent and refractivity angles, $\theta_R$ and $\theta_T$, respectively; c) Fresnel parameters, $\Lambda_1$ and $\Lambda_2$, respectively; d) the anisotropy parameter, $\mu_y$. .....158

Figure 4-12: Output data from MAT experiment using the iterative fitting method: a) Refractive and turbulent angle estimates, $\theta_R$ and $\theta_T$, relative the an objective horizontal angle; b) Non-turbulence spot size estimate produced from best fits for $\Lambda_1$ and $\Lambda_2$; c) Estimates of the anisotropy parameter, $\mu_y$, given as both as an instantaneous estimate and the five minute median; d) Estimates of the refractive index structure constants, $C_{n,x}^2$ and $C_{n,y}^2$, with the *x*-axis being along the turbulent angle. .....164

Figure 4-13: Approximate location of the Southern Maryland optical propagation path shown in within the St. Mary's County Airport complex light orange within the St. Mary's County Regional Airport complex. The MAT transmitter was in place on the east side, and the MAT receiver to the west. .....165

Figure 4-14: Images of the MAT transmitter breadboard: a) Without markup labeling; b) With markup labeling. In Image b) the labeled components are as follows: 1) Helium neon laser transmitter; 2) First redirection mirror; 3) Second redirection mirror; 4) Fixed magnification beam expander with adjustable sliding lens; 5) Steering mirror for downfield pointing. Additionally, although obscured by the beam expander, an optical chopping wheel is in place between the two

redirection mirrors on the breadboard. A scope is placed on the breadboard adjacent to the steering mirror for alignment, however it is not a permanent component of the optical breadboard.....166

Figure 4-15: Alternative view of the MAT transmitter optical breadboard with the illuminated retroreflectors of the MAT receiver shown in the background. Note that the placement of the optical chopping wheel is shown more clearly in this figure.....167

Figure 4-16: Overall view of the MAT transmitter rack. Note that vibrational stabilization is applied using both sandbags and cinderblocks at the base. A weather station is attached at the top of the rack.....168

Figure 4-17: MAT receiver placed upon gimbal mount within structural framing rack and the operator shown during alignment. Note that the operator is standing upon a weatherized pelican case housing the logging computer for the MAT receiver.....169

Figure 4-18: View of two RTD arrays mounted using tripods: 1) Horizontally oriented eight probe RTD array mounted to a tripod; 2) Vertically oriented eight probe RTD array mounted to the base of a heavy-duty tripod.....171

Figure 4-19: Power law estimates from the RTD array systems: a) Power law histogram in the spatial domain using a three minute variance scan time; b) Power law estimate in the time-frequency domain compared to the -5/3$^{rds}$ Law predicted by theory.....173

Figure 4-20: Output data from MAT experiment using the iterative fitting method, as well as a comparison with the RTD array averaged $C_n^2$ estimate with both sets of systems configured for 150 cm average elevation: a) Refractive and turbulent angle estimates, $\theta_R$ and $\theta_T$, relative the an objective horizontal angle; b) Non-turbulence spot size estimate produced from best fits for $\Lambda_1$ and $\Lambda_2$; c) Estimates of the anisotropy parameter, $\mu_y$, given as both as an instantaneous estimate and the five minute median; d) Estimates of the refractive index structure constants, $C_{n,x}^2$ and $C_{n,y}^2$, with the $x$-axis being along the turbulent angle, as well as the $C_n^2$ estimate from the RTD arrays averaged across all three systems.....176

Figure 4-21: Anisotropy parameters using the MAT iterative fitting method compared with the estimate using the RTD array systems. The MAT system's instantaneous samples are computed using the normalized variance over one minute duration, with 10 seconds resolution. In addition to the instantaneous

samples, a 5 minute median value is also shown. The RTD array systems' anisotropy parameter estimates are computed using temperature variances over three minutes duration, with 10 second resolution. Please note that the RTD array system's anisotropy estimate has be produced along the approximate turbulent angle estimated for this test, i.e. the *x*-direction is vertical and the *y*-direction is horizontal in this figure. ..... 177

Figure 4-22: Output data from MAT experiment using the iterative fitting method, as well as a comparison with the RTD array averaged $C_n^2$ estimate with both sets of systems configured for 100 cm average elevation: a) Refractive and turbulent angle estimates, $\theta_R$ and $\theta_T$, relative the an objective horizontal angle; b) Non-turbulence spot size estimate produced from best fits for $\Lambda_1$ and $\Lambda_2$; c) Estimates of the anisotropy parameter, $\mu_y$, given as both as an instantaneous estimate and the five minute median; d) Estimates of the refractive index structure constants, $C_{n,x}^2$ and $C_{n,y}^2$, with the *x*-axis being along the turbulent angle. ..... 181

Figure 4-23: Example observed main intensity at the MAT receiver and from an outdoor field experiment on October 1st, 2018 at 100 cm elevation. The subplots are: a) Interpolated mean optical intensity profile; b) Detector-by-detector mean optical intensity; c) Interpolated scintillation index profile; d) Detector-by-detector scintillation index. ..... 183

Figure 4-24: Output data from MAT experiment using the iterative fitting method, as well as a comparison with the RTD array averaged $C_n^2$ estimate with both sets of systems configured for 50 cm average elevation on September 27th, 2018: a) Refractive and turbulent angle estimates, $\theta_R$ and $\theta_T$, relative the an objective horizontal angle; b) Non-turbulence spot size estimate produced from best fits for $\Lambda_1$ and $\Lambda_2$; c) Estimates of the anisotropy parameter, $\mu_y$, given as both as an instantaneous estimate and the five minute median; d) Estimates of the refractive index structure constants, $C_{n,x}^2$ and $C_{n,y}^2$, with the *x*-axis being along the turbulent angle. ..... 186

Figure 4-25: Output data from MAT experiment using the iterative fitting method, as well as a comparison with the RTD array averaged $C_n^2$ estimate with both sets of systems configured for 50 cm average elevation on October 3rd, 2018: a) Refractive and turbulent angle estimates, $\theta_R$ and $\theta_T$, relative the an objective horizontal angle; b) Non-turbulence spot size estimate produced from best fits for $\Lambda_1$ and $\Lambda_2$; c) Estimates of the anisotropy parameter, $\mu_y$, given as both as an instantaneous estimate and the five minute median; d) Estimates of the refractive index structure constants, $C_{n,x}^2$ and $C_{n,y}^2$, with the *x*-axis being along the turbulent angle. ..... 187

Figure 4-26: Example observed main intensity at the MAT receiver and from an outdoor field experiment on September 27th, 2018 at 50 cm elevation. The subplots are: a) Interpolated mean optical intensity profile; b) Detector-by-detector mean optical intensity; c) Interpolated scintillation index profile; d) Detector-by-detector scintillation index. .....188

Figure 4-27: Example observed main intensity at the MAT receiver and from an outdoor field experiment on October 3rd, 2018 at 50 cm elevation. The subplots are: a) Interpolated mean optical intensity profile; b) Detector-by-detector mean optical intensity; c) Interpolated scintillation index profile; d) Detector-by-detector scintillation index. .....189

Figure 4-28: (a) Aerial view of the SLF site; (b) MAT receiver with a GPS receiver resting on the sun-shield. .....191

Figure 4-29: a) MAT receiver initial setup; (b) MAT receiver in operation partially under a canopy adjacent to a USC trailer with a scintillometer transmitter on the roof. .....192

Figure 4-30: Images of the shearing interferometer hologram during collimation procedure, with the beam propagating from left to right: a) Shearing interferometer readout for weakly divergent beam; b) Shearing interferometer readout for a collimated beam.....193

Figure 4-31: $C_n^2$ estimates from the MAT system as well as two RTD array systems from May, 2018 testing. .....194

Figure 4-32: a) Extinction rate estimate from the MAT system on May 2nd, 2018; b) Extinction rate estimate from UCF's commercial visibility meter on May 2nd, 2018.....195

Figure 4-33: $C_n^2$ estimates from the MAT system as well as two RTD array systems from May 2nd, 2018 testing. Please note that the *x*-direction for the MAT estimate is given by the beam angle in the next figure. .....196

Figure 4-34: a) Anisotropy parameter estimate from the MAT system from May 2nd, 2018 testing; b) Beam angle estimate from the MAT system from May 2nd, 2018 testing, i.e. the major axis of turbulence under our assumptions. .....197

Figure 4-35: a) Extinction rate estimate from the MAT system on May 3rd, 2018; b) Extinction rate estimate from UCF's commercial visibility meter on May 3rd, 2018.....198

Figure 4-36: $C_n^2$ estimates from the MAT system as well as two RTD array systems from May 3rd, 2018 testing. Please note that the *x*-direction for the MAT estimate is given by the beam angle in the next figure. .....199

Figure 4-37: a) Anisotropy parameter estimate from the MAT system from May 3rd, 2018 testing; b) Beam angle estimate from the MAT system from May 3rd, 2018 testing, i.e. the major axis of turbulence under our assumptions. .....200

Figure 4-38: MAT long term spot size estimates on: a) May 2nd, 2018; b) May 3rd, 2018. .....203

Figure 5-1: View of test laser transmitter and LCF in October 2019 experiment.....210

Figure 5-2: Recovered WSF's from the LFC October 2019 experiment: a) Along the minor axis of turbulence; b) Along the major axis of turbulence. .....210

Figure B-1: RMS error as a percent relative to theory over 50,000 phase screen trials over the entire simulated domain as parameterized by the three dimensional spectral power law, $\boldsymbol{\alpha}$. 512 × 512, 1024 × 1024, 2048 × 2048 grid results are shown for randomized method. For the traditional method, the 2048 × 2048 grid is shown. Other grid sizes are not shown for the traditional method because the results appear to completely overlap at this scale. No subharmonics were used in the phase screens used to generate statistics in this chart. .....227

Figure B-2: RMS error as a percent relative to theory for the modified spectrum over 50,000 phase screen trials for the entire domain region of interest as parameterized by the three dimensional spectral power law, $\alpha$. 512 × 512, 1024 × 1024, 2048 × 2048 grid results are shown for randomized method. The outer scale has been normalized by the domain width, $\boldsymbol{M\Delta x}$ (m), to make the results applicable for any domain size. For the traditional method only the 2048 × 2048 grid is shown due to significant overlap of the RMS error metric.....228

Figure B-3: RMS error over entire domain computed along *x*- and *y*-directions of 50,000 phase screens for 512 × 512 grid using various spectral power laws ($\alpha$'s) and number of subharmonic constellations, $N_p$. $\mu_x = \mu_y = 1$ for all data points.

The randomized hybrid method (green), Frehlich subharmonic method (black), and Lane subharmonic method (magenta) are shown.....229

Figure B-4: RMS error over entire domain computed along *x*- and *y*-directions of 50,000 phase screens for 1024 × 1024 grid using various spectral power laws ($\alpha$'s) and number of subharmonic constellations, $N_p$. $\mu_x = 1$, $\mu_y = 2$ for all data points. The randomized hybrid method (blue) and Frehlich subharmonic method (black) are shown. .....230

Figure B-5: RMS error over entire domain computed along *x*- and *y*-directions of 5,000 phase screens for 2048 × 2048 grid using various spectral power laws ($\alpha$'s) and number of subharmonic constellations, $N_p$. $\mu_x = 1$, $\mu_y = 2$ for all data points. The randomized hybrid method (red) and Frehlich subharmonic method (black) are shown. .....231

Figure B-6: RMS error over entire domain for the modified spectrum computed along *x*- and *y*-directions for 5,000 phase screens using modified spectrum, with $l_0 = M\Delta x/100$ and $M = 512$ (i.e. grid size 512 × 512). .....232

Figure B-7: RMS error over entire domain computed along *x*- and *y*-directions for 5000 phase screens using modified spectrum, with $l_0 = M\Delta x/100$ and $M = 1024$ (i.e. grid size 1024 × 1024). .....233

Figure B-8: RMS error over entire domain computed along *x*- and *y*-directions for 5000 phase screens using modified spectrum, with $l_0 = M\Delta x/100$ and $M = 2048$ (i.e. grid size 2048 × 2048). .....234

# Definitions and abbreviations

| | |
|---|---|
| AoA | Angle of Arrival |
| AWI | All Weather Incorporated |
| C | Celsius |
| CFI | Covariance Function of Intensity |
| DE | Directed Energy |
| DFT | Discrete Fourier Transform |
| FFT | Fast Fourier Transform |
| FSO | Free Space Optical |
| GPS | Global Positioning System |
| IFFT | Inverse Fast Fourier Transform |
| K | Kelvin |
| KSC | Kennedy Space Center |
| LFC | Light Field Camera |
| MAT | Multi-Aperture Transmissometer |
| mb | Millibar |
| MCF | Mutual Coherence Function |
| MOG | Maryland Optics Group |
| ND | Neutral Density |
| RMS | Root Mean Squared |
| RS | Remote Sensing |
| RTD | Resistance Temperature Detector |
| Scint Index | Scintillation Index |
| SLF | Shuttle Landing Facility |
| TISTEF | Townes Institute Science and Technology Experimentation Facility |
| UAS | Unmanned Aircraft Systems |
| UMD | University of Maryland |
| WSF | Wave Structure Function |

# Chapter 1 : Overview and Theoretical Considerations

## 1.1: Introduction

Spurred by the fluid dynamics theories of Taylor [1], Kolmogorov [2, 3], and Obukhov [4], the study of wave propagation through turbulent media is at the intersection of fluid dynamics and electromagnetics. There is a rich tradition of knowledge [5, 6, 7, 8, 9] in the theoretical study of optical propagation of electromagnetic waves through isotropic turbulence. However, experimental data from telescope interferometric systems [10], focal plane images [11, 12], Shack-Hartman wave front sensors [12, 13], Differential Image Motion Monitor (DIMM) systems [14], thin wire anemometers [15], and temporal statistics from various instruments [12] indicate that anisotropy and non-Kolmogorov behavior can commonly occur under certain conditions. There are also studies of anisotropic turbulence in the computational fluid dynamics literature [16, 17, 18], supporting the claims of experimentalists.

The issues outlined above have, in recent years, led to an increasing interest in studies of anisotropic, non-Kolmogorov turbulence [11, 19, 20, 21, 22, 23, 24, 25]. However, open questions remain regarding the behavior of beam propagation in the presence of anisotropic, non-Kolmogorov turbulence within traditional assumptions and approximations [25], and also practical methods to link anisotropy and irregular turbulence spectra in a reliable way to other observable phenomena

have not been well developed. In this author's dissertation work we use a combination of simulation and field experiments in order further reliable methods for estimating variations of anisotropy and deviations from the 2/3$^{rds}$ law of Kolmogorov (i.e. non-Kolmogorov turbulence) in an experimental environment. That said, this work covers three key areas:

1. Improvements to the Split Step Propagation Phase Screen Method Using Randomized Sampling of the Turbulence Spectrum
2. Computational Analysis to Verify Theoretical Claims Using Split Step Propagation Phase Screen Methods
3. Experimental Investigations of Anisotropic and Non-Kolmogorov Turbulence

## 1.2: Theoretical Background Regarding the Nature of Optical Turbulence

The study of optical propagation through isotropic random media has been extended well beyond the benchmark theories of Taylor [1], Kolmogorov [2, 3], and Obukhov [4] to include finite scale sizes [8, 9] and the rise in spectral energy (spectral *bump*) in the viscous-convective range investigated by Hill [26]. More general theories of anisotropic, non-Kolmogorov turbulence have not yet tackled all of these idiosyncrasies, and as such we start not with traditional models of isotropic turbulence and extend in the direction of anisotropy and *non-Kolmogorov-*

*ness*, but start by generalizing the initial assumptions of the earlier theories, and moving forward.

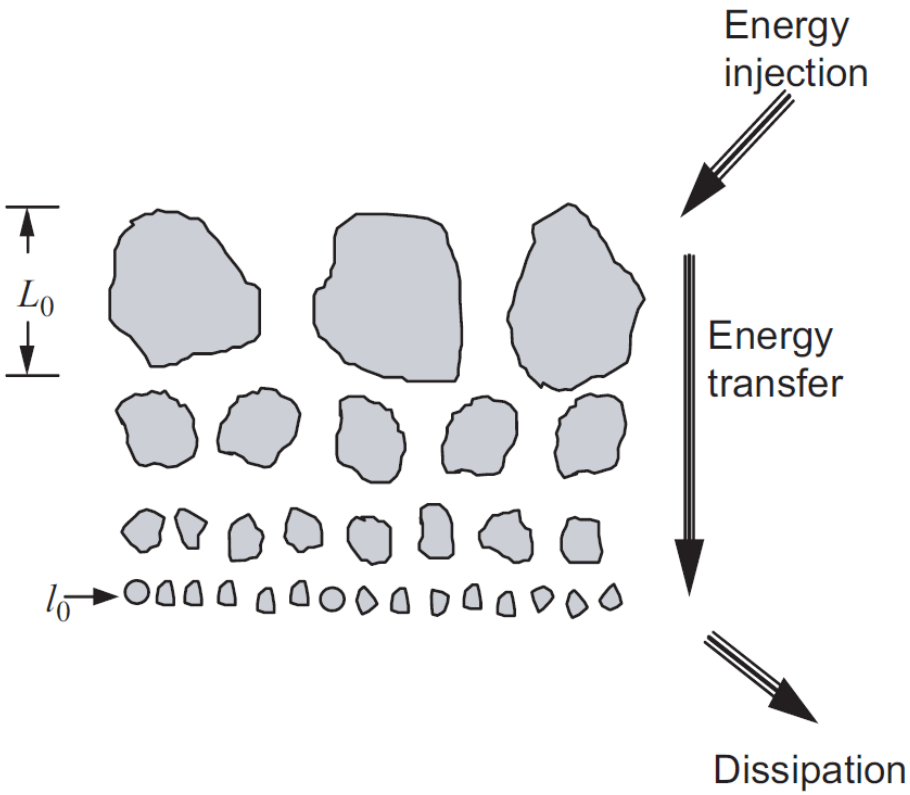


**Figure 1-1:** Illustrations of the inertial subrange concept of classical turbulence theory, from [9].

In his first 1941 paper on turbulence [2], Andrey Kolmogorov used assumptions of isotropy and scale invariance to argue for a universal power law governing the second statistical moment of fluid velocity as a function of spatial separation, which we will define more formally later using the concept of a structure function. His second 1941 paper on turbulence [3] makes a more straightforward dimensional analysis claim, which we will attempt to concisely paraphrase. The claim is that far away from the largest scale sizes (the outer scale)

and the limitations of fluid viscosity (the inner scale), the spatial frequency energy spectrum of turbulence should depend only on the kinematic energy dissipation rate of the system, $\epsilon$, with units of $\frac{\left(\frac{m}{s}\right)^2}{s} = m^2 s^{-3}$, and the spatial wavenumber, $\kappa$, which has units of $m^{-1}$. The one dimensional energy spectrum, $E(\kappa)$, is a frequency domain representation of the kinematic energy, $k_E$, with units $\left(\frac{m}{s}\right)^2 = m^2 s^{-2}$. Given $E(\kappa)$ is the kinematic energy density per unit wavenumber, its units are $m^3 s^{-2}$. Due to the units of $\epsilon$ and $\kappa$ the only function, $E(\kappa)$, that satisfies the dimensional criteria is $\sim \epsilon^{2/3} \kappa^{-5/3}$, i.e.:

$$E(\kappa) = C\epsilon^{2/3} |\kappa|^{-5/3} \tag{1-1}$$

where $C$ is a unitless constant.

For obvious reasons, we wish to relate the energy spectrum to spatial domain intuition regarding the nature of turbulence. The Weiner-Khinchin theorem [27] relates the autocorrelation, $B_f(r) = \langle f(r - r_0) f(r_0) \rangle$, of a function or field to its energy spectrum by a Fourier transform relation:

$$B_{u_i}(r) = \int_{-\infty}^{\infty} E(\kappa)\, e^{j\kappa r}\, d\kappa = 2C\epsilon^{2/3} \int_0^{\infty} \kappa^{-5/3} \cos(\kappa r)\, d\kappa \tag{1-2}$$

where the $u_i$ subscript of $B_{u_i}$ indicates that this is the $i^{th}$ component of the velocity vector, $\vec{u}$ $\left(\text{e.g. } u_1 = \frac{dx}{dt}\right)$, and $j = \sqrt{-1}$. Because we have assumed an infinite inertial range, this integral diverges, however we shall demonstrate that other useful statistical metrics do converge.

We now define the structure function, $D_f$, of a function, $f$, as [6]:

$$D_f(x) = \langle (f(x + x_0) - f(x_0))^2 \rangle \tag{1-3}$$

where $\langle x \rangle$ denotes the expectation value of $x$, and we note the following relation for stationary fields (i.e. $\langle f(x_0)^2 \rangle = \langle f(0)^2 \rangle$ and $\langle f(x + x_0) f(x_0) \rangle = \langle f(x) f(0) \rangle$):

$$\begin{aligned} D_f(x) &= \langle f(x + x_0)^2 \rangle + \langle f(x_0)^2 \rangle - 2\langle f(x + x_0) f(x_0) \rangle \\ &= 2\langle f(x_0)^2 \rangle - 2\langle f(x + x_0) f(x_0) \rangle \\ &= 2\langle f(0)^2 \rangle - 2\langle f(x) f(0) \rangle \\ &= 2\big(B_f(0) - B_f(x)\big) \end{aligned} \tag{1-4}$$

Applying Wiener-Khinchin again:

$$D_f(x) = 2 \int_{-\infty}^{\infty} E_f(\kappa) \big(1 - e^{j\kappa x}\big)\, d\kappa \tag{1-5}$$

For our quantity of interest, the velocity structure function is given by:

$$\begin{aligned} D_{u_i}(r) &= 4C\epsilon^{2/3} \int_0^{\infty} \kappa^{-5/3}\, (1 - \cos(\kappa r))\, d\kappa \\ &= 4r^{2/3} C\epsilon^{2/3} \int_0^{\infty} \kappa'^{-5/3}\, (1 - \cos(\kappa'))\, d\kappa' \end{aligned} \tag{1-6}$$

Where we have made the change of variables, $\kappa' = r\kappa$. In Equation (1-6), we have demonstrated the $r^{2/3}$ dependence of the famous Kolmogorov's $2/3^{rds}$ law [2, 3], as we note that $\int_0^{\infty} \kappa'^{-5/3}\, (1 - \cos(\kappa'))\, d\kappa'$ is both a definite integral and is not a function of $r$. Clearly, from the form of (1-6) we can see a $r^p$ dependence in the spatial domain maps to a $\kappa^{-(p+1)}$ dependence in the frequency domain, with $p$ an

arbitrary constant between 0 and 2, exclusive. It can be shown [6] for integrals of the form of (1-6):

$$\int_0^\infty x^{-(p+1)}\,(1-\cos(x))\,dx = \frac{2\pi}{\sin\left(\frac{\pi p}{2}\right)\Gamma(1+p)},\quad 0<p<2 \qquad (1\text{-}7)$$

where $x$ and $p$ are arbitrary, and $\Gamma(x)$ is the gamma function of $x$.

As applied to optical propagation, we will generally be more interested in the three dimensional energy spectrum, $\Phi(\vec{\kappa})$, of the wave vector, $\vec{\kappa} = \kappa_x\hat{e}_1 + \kappa_y\hat{e}_2 + \kappa_z\hat{e}_3$, where the $\hat{e}$'s are orthogonal unit vectors in three dimensional frequency space. $\Phi(\vec{\kappa})$ can be expressed as a function of the vector autocorrelation function, $B_{u_i}(\vec{r}) = B_{u_i}(|\vec{r}|)$, as [6]:

$$\begin{aligned}\Phi(\vec{\kappa}) &= \frac{1}{(2\pi)^3}\iiint_{-\infty}^{\infty}\cos(\vec{\kappa}\cdot\vec{r})\,B_{u_i}(\vec{r})\,d\vec{r}\\ &= \frac{1}{(2\pi)^2}\int_0^\infty\int_0^\pi\cos(\kappa r\cdot\cos\theta)\,B_{u_i}(r)\,r^2\sin\theta\,d\theta\,dr \qquad (1\text{-}8)\\ &= \frac{1}{2\pi^2\kappa}\int_0^\infty r\sin(\kappa r)\,B_{u_i}(r)\,dr\end{aligned}$$

where in the second step $\theta$ is the angle between $\vec{\kappa}$ and $\vec{r}$. By noting that $2B_{u_i}(r)$ and $E(\kappa)$ are Fourier transform pairs, this implies:

$$E(\kappa) = \pi^{-1}\int_0^\infty B_{u_i}(r)\cos(\kappa r)\,d\kappa \qquad (1\text{-}9)$$

$$\frac{dE(\kappa)}{d\kappa} = -\pi^{-1}\int_0^{\infty} r\, B_{u_i}(r)\sin(\kappa r)\, d\kappa \tag{1-10}$$

Investigating Equations (1-8) and (1-10), we establish a useful relation between the one dimensional and three dimensional energy spectra:

$$\Phi(\vec{\kappa}) = -\frac{1}{2\pi\kappa}\frac{dE(\kappa)}{d\kappa} \tag{1-11}$$

In the earth's atmosphere wind is primarily a product of natural convection due to the sun's heating of the ground and the ground's cooling of the air at night [9]. There is also a natural relationship between the refractive, *n*, index of air and temperature given by [28]:

$$\begin{aligned} n(\vec{r}) &= 1 + 77.6\cdot 10^{-6}\cdot\left(1 + \frac{7.52\cdot 10^{-15}}{\lambda^2}\right)\frac{P(\vec{r})}{T(\vec{r})} \\ &\cong 1 + 79\cdot 10^{-6}\frac{P(\vec{r})}{T(\vec{r})} \end{aligned} \tag{1-12}$$

where the approximation given is valid for optical wavelengths, $\lambda$, in the visible and infrared range, *P* is pressure in millibar (mb), and *T* is temperature in Kelvin (K). Consistency of the experimental observations of temperature flows with velocity flows have led to the assumption that the convective transfer of temperature is driven primarily by advection [9, 26, 29], the transfer due to bulk flow, as opposed to diffusion (transfer due to Brownian motion). It flows naturally from this assumption that we have a structure function for temperature of the form:

$$D_T(r) = \langle (T(r + r_0) - T(r_0))^2 \rangle \tag{1-13}$$

$$= C_T^2 r^p$$

where $C_T^2$ is the temperature structure constant with units $K \cdot m^{-p}$. With a natural link between turbulent atmospheric mixing and refractive index already established, we now consider index of refraction index structure functions, $D_n$, of the form:

$$\begin{aligned} D_n(r) &= \langle \big(n(r + r_0) - n(r_0)\big)^2 \rangle = C_n^2 r^p \\ &\cong \left(79 \cdot 10^{-6} \frac{P}{T^2}\right)^2 C_T^2 r^p \end{aligned} \tag{1-14}$$

where $C_n^2$ is the index of refraction structure constant. Because the index of refraction, $n$, is unitless $C_n^2$ has units $m^{-p}$. For Kolmogorov turbulence, the units of $C_n^2$ are $m^{-2/3}$, as $p = 2/3$. The structure given in Equation (1-14), along with the definite integral relation given in Equation (1-7), corresponds to a one dimensional energy spectrum given by:

$$\begin{aligned} E_n(\kappa) &= C_n^2 \frac{\sin\left(\frac{\pi p}{2}\right) \Gamma(1+p)}{2\pi} \, |\kappa|^{-(p+1)} \\ &= C_n^2 \frac{\cos\left(\frac{\pi \alpha}{2}\right) \Gamma(\alpha - 2)}{2\pi} \, |\kappa|^{2-\alpha} \end{aligned} \tag{1-15}$$

where we have introduced a new variable, $\alpha = p + 3$, which is the three dimension spectral power law. Applying equation (1-11), we have the three dimensional spectrum:

$$\phi_n(\vec{\kappa}) = \frac{\cos\left(\frac{\pi\alpha}{2}\right)\Gamma(\alpha-2)}{4\pi^2}\,(\alpha-2)|\kappa|^{-\alpha} = \frac{C_n^2 A(\alpha)}{\left({\kappa_x}^2+{\kappa_y}^2+{\kappa_z}^2\right)^{\alpha/2}} \tag{1-16}$$

Where we use the relation $\Gamma(x+1) = x\Gamma(x)$ to define the $A$ function, given by:

$$A(\alpha) = \frac{\cos\left(\frac{\pi\alpha}{2}\right)\Gamma(\alpha-1)}{4\pi^2} \tag{1-17}$$

For Kolmogorov turbulence $\alpha = 11/3$ and $A(\alpha) = A(11/3) \cong 0.0330$.

We have been careful to derive the refractive index spectral model, initially justified by dimensional arguments, in a more flexible manner that allows for varying dependence of the energy spectrum on wave number, and structure on radial distance. It is also notable, that although the traditional units of $C_n^2$ are $m^{-2/3}$, in the generalized model the units of $\tilde{C}_n^2$ are $m^{3-\alpha}$. We now have a framework to discuss non-Kolmogorov turbulence without consideration of inner and outer scale sizes, which is applicable to propagation of beams with diameters well between that of the inner and outer scales.

To include statistical anisotropy, or directional dependence, we can modify the three dimensional energy spectrum, again, to be of the form [19, 23]:

$$\Phi_n(\vec{\kappa}) = \frac{\tilde{C}_n^2 A(\alpha)\,\mu_x\,\mu_y}{\left(\mu_x^2\kappa_x^2+\mu_y^2\kappa_y^2+\kappa_z^2\right)^{\alpha/2}} \tag{1-18}$$

where we have introduced $\mu_x$ and $\mu_y$ as the unitless anisotropy parameters in the *x*- and *y*-directions, respectively, and we have added the tilde notation above $\tilde{C}_n^2$ to indicate it is no longer the structure function in any direction, but only in the *z*-direction. Note that for the ranges of $\alpha$'s that allow the structure function implied by Equation (1-19), given below, to converge (i.e. $3 < \alpha < 5$), independently increasing $\mu$ in either direction decreases the energy in the spectrum. Additionally, direct investigation of the structure function predicted by Equation (1-18) after change of variables $\kappa' = \mu\kappa$ indicates increasing $\mu$ effectively lowers the structure function in the *x*-, *y*- directions:

$$\begin{aligned} D_n(\vec{r}) &= \tilde{C}_n{}^2 A(\alpha) \iiint_{-\infty}^{\infty} \frac{1-\cos\left(\frac{x\kappa_x{}'}{\mu_x}+\frac{y\kappa_y{}'}{\mu_x}+z\kappa_z\right)}{(\kappa_x{}'^2+\kappa_x{}'^2+\kappa_z{}^2)^{\alpha/2}}\, d\vec{\kappa}' \\ &= \tilde{C}_n^2\left(\sqrt{\frac{x^2}{\mu_x^2}+\frac{y^2}{\mu_y^2}+z^2}\right)^{\alpha-3} \end{aligned} \tag{1-19}$$

However, as it is a convention that propagation is in the *z*-direction [9], and in keeping with the paraxial approximation [9] of light which assumes propagation is by-in-large in a single direction, the refractive index fluctuations in the direction of propagation are not considered [9], and so we simplify Equation (1-18), also expressible as $\Phi_n(\vec{\kappa}) = \Phi_n(\vec{\kappa}_\rho, \kappa_z) = \Phi_n(\kappa_x, \kappa_y, \kappa_z)$ as [24]:

$$\Phi_n(\vec{\kappa}_\rho, 0) = \frac{\tilde{C}_n^2 A(\alpha)\, \mu_x\, \mu_y}{\left(\mu_x^2 \kappa_x^2 + \mu_y^2 \kappa_y^2\right)^{\alpha/2}} \tag{1-20}$$

Given we will assume the direction of mean propagation as $z$, $\rho = x\hat{e}_1 + y\hat{e}_2$ and $\vec{\kappa}_\rho = \kappa_x \hat{e}_1 + \kappa_y \hat{e}_2$. Equation (1-20) gives the form of the refractive index three dimensional spectrum we will use for the majority of this work.

Finally, we note that in later sections the statistics of an ideal atmospheric turbulence phase screen an understanding of the covariance function of refractive index will be necessary. The classical theory for propagation through random media derives all statistics in light of the Markov Approximation, which is the assumption that atmospheric turbulence is approximately *delta-correlated* in the direction of propagation. Formally:

$$\begin{aligned} B_n(\vec{\rho}, z) &= \iiint_{-\infty}^{\infty} \Phi_n(\vec{\kappa}_\rho, \kappa_z) \exp\left[j\left(\vec{\kappa}_\rho \cdot \vec{\rho} + \kappa_z z\right)\right] d\vec{\kappa}_\rho d\kappa_z \\ &\cong \int_{-\infty}^{\infty} \exp(j\kappa_z z)\, d\kappa_z \iint_{-\infty}^{\infty} \Phi_n(\vec{\kappa}_\rho, 0) \exp\left(j\vec{\kappa}_\rho \cdot \vec{\rho}\right) d\vec{\kappa}_\rho \\ &= 2\pi\delta(z) A_n(\vec{\rho}) \end{aligned} \tag{1-21}$$

In Equation (1-21) we have implicitly defined the two dimensional autocorrelation, $A_n(\vec{\rho})$, and made use of the identity [9]:

$$\int_{-\infty}^{\infty} \exp(j\kappa z)\, d\kappa = 2\pi\delta(z) \tag{1-22}$$

With regards to Equation (1-22), we note also that:

$$\delta(x) \equiv \lim_{a\to\infty} \int_{-\frac{a}{2}}^{\frac{a}{2}} \exp(2\pi jxf)\, df = \lim_{a\to\infty} \left[\frac{\exp(2\pi jxf)}{2\pi jx}\right]_{-\frac{a}{2}}^{\frac{a}{2}} \tag{1-23}$$

$$= \lim_{a\to\infty} \frac{\sin(\pi xa)}{\pi x}$$

Equation (1-22) is an extension of Equation (1-23) under a change of variables within the integral.

## 1.3: Mathematical Background Regarding the Simulation of Optical Propagation

In this section we shall discuss the paraxial approximation of the Green's function for optical propagation, the use of this function to define a transfer function for propagation, how this is approximated in discretized simulations, and a modification to the traditional propagation technique which allows for shrinking and expanding grid spacing with each propagation step. The Green's function for optical propagation in vacuum is given by [30]:

$$G(\vec{r}) = \frac{\exp(jk_0|\vec{r}|)}{4\pi|\vec{r}|} \tag{1-24}$$

where $k_0 = \frac{2\pi}{\lambda}$ is the vacuum optical number with $\lambda$ the wavelength, and $\vec{r} = x\hat{e}_x + y\hat{e}_y + z\hat{e}_z$ is the position vector. For the study of coherent light relevant to this thesis, i.e. beam waves, Equation (1-24) is approximated by the paraxial approximation:

$$G(\vec{\rho},z)=\frac{\exp\left(jk_0\sqrt{\rho^2+z^2}\right)}{4\pi\sqrt{\rho^2+z^2}}=\frac{\exp\left(jk_0z\sqrt{1+\frac{\rho^2}{z^2}}\right)}{4\pi z\sqrt{1+\frac{\rho^2}{z^2}}} \tag{1-25}$$

$$\cong\frac{\exp(jk_0z)\exp\left(jk_0\frac{\rho^2}{2z}\right)}{4\pi z}$$

where $\vec{\rho}=x\hat{e}_x+y\hat{e}_y$ and $\rho=|\vec{\rho}|$. The Huygen-Fresnel Integral yields the diffracted field at any point due to an input complex field, $U(\vec{\rho}',0)$, as per:

$$U(\vec{\rho},z)\cong-2jk_0\iint_{-\infty}^{\infty}G(\vec{\rho}-\vec{\rho}',z)\,U(\vec{\rho}',0)d\vec{\rho}' \tag{1-26}$$

Equation (1-26) implies that paraxial optical propagation a distance, $z$, can be approximated as a convolution with a kernel given by the Fresnel impulse response [31]:

$$H(\vec{\rho},z)=\frac{\exp(jk_0z)\exp\left(jk_0\frac{\rho^2}{2z}\right)}{jz\lambda} \tag{1-27}$$

Acknowledging that the constant phase rotation term, $\exp(jk_0z)$, associated with $z$-direction propagation is of little interest, we note that simulations of optical propagation usually take advantage of the Fourier Convolution Theorem [32] (also known as the Convolution Theorem or convolution property of the Fourier transform). The Fourier Convolution Theorem states that the convolution operator is equivalent to the inverse transform of the product of Fourier transforms of the

impulse response and input field. As we shall later demonstrate, neglecting the phase rotation term, the Fourier transform of Equation (1-27) is given by:

$$\widetilde{H}(\vec{q},z) = e^{-\pi j z \lambda |\vec{q}|^2} \tag{1-28}$$

where $\vec{q} = q_x \hat{e}_x + q_y \hat{e}_y$ is the spatial frequency vector. In most manifestations of phase screen simulation of optical turbulence, the discretized complex field matrix, $\mathbf{U_{out}}_{,nm}$, is computed from the input field matrix, $\mathbf{U_{in}}_{,nm}$, and the Fresnel impulse response matrix, $\mathbf{Q}_{mn}$, with use of the two dimensional Fast Fourier Transform (FFT) and Inverse FFT (IFFT):

$$\mathbf{q}_{mn}^2 \equiv (m\Delta q_x)^2 + \left(n\Delta q_y\right)^2 \tag{1-29}$$

$$\mathbf{Q}_{mn} \equiv \text{fftshift}\{\exp[-j\pi\Delta z\lambda \mathbf{q}_{mn}^2]\} \tag{1-30}$$

$$\mathbf{U_{out}}_{,nm} = \text{IFFT}_2\left\{\mathbf{Q}_{mn} \cdot \text{FFT}_2\{\mathbf{U_{in}}_{,nm}\}\right\} \tag{1-31}$$

Equations (1-29) - (1-31) define the relevant matrices and summarize the propagation algorithm, with $\Delta q_x = \frac{1}{M\Delta x}$, $\Delta q_y = \frac{1}{N\Delta y}$ are the frequency domain grid spacings in terms of the spatial grid spacings, $\Delta x$, $\Delta y$, with $M$, $N$ the number of grid points in the *x*- and *y*-directions (respectively), fftshift{ } represents the process of FFT-shifting [33] a two dimensional matrix, and $\text{FFT}_2\{\,\}$, $\text{IFFT}_2\{\,\}$ represent the FFT and IFFT operators (respectively).

Equation (1-31) has a notable limitation, which is that it does not allow for a change in spatial resolution (and by extension spatial domain size) between the

source and receive planes. The angular spectrum propagation algorithm [33] enacts a change in spatial resolution between the source and receive planes by noting that:

$$\begin{aligned} U(\vec{\rho}_2, z) &= \iint_{-\infty}^{\infty} G(\vec{\rho}_2 - \vec{\rho}_1, z)\, U(\vec{\rho}_1, 0) d\vec{\rho}_1 \\ &\cong \iint_{-\infty}^{\infty} \frac{\exp\left(jk_0 \frac{|\vec{\rho}_2 - \vec{\rho}_1|^2}{2z}\right)}{j\lambda z} U(\vec{\rho}_1, 0) d\vec{\rho}_1 \end{aligned} \tag{1-32}$$

We can write, using $\rho_1 = |\vec{\rho}_1|$, $\rho_2 = |\vec{\rho}_2|$, and introducing a scaling factor, $m$:

$$\begin{aligned} |\vec{\rho}_2 - \vec{\rho}_1|^2 &= {\rho_2}^2 - 2\vec{\rho}_2 \cdot \vec{\rho}_1 + {\rho_1}^2 \\ &= \left({\rho_2}^2 + \frac{{\rho_2}^2}{m} - \frac{{\rho_2}^2}{m}\right) - 2\vec{\rho}_2 \cdot \vec{\rho}_1 + ({\rho_1}^2 + m{\rho_1}^2 - m{\rho_1}^2) \\ &= \frac{{\rho_2}^2}{m} + \left(1 - \frac{1}{m}\right){\rho_2}^2 - 2\vec{\rho}_2 \cdot \vec{\rho}_1 + [m{\rho_1}^2 + (1-m){\rho_1}^2] \\ &= m\left[\left(\frac{\rho_2}{m}\right)^2 - 2\left(\frac{\vec{\rho}_2}{m}\right) \cdot \vec{\rho}_1 + {\rho_1}^2\right] + \left(1 - \frac{1}{m}\right){\rho_2}^2 + (1-m){\rho_1}^2 \\ &= m\left|\frac{\vec{\rho}_2}{m} - \vec{\rho}_1\right|^2 - \left(\frac{1-m}{m}\right){\rho_2}^2 + (1-m){p_1}^2 \end{aligned} \tag{1-33}$$

Insertion of (1-33) into (1-32) yields:

$$\begin{aligned} U(\vec{\rho}_2, z) &\cong \iint_{-\infty}^{\infty} \frac{e^{\frac{jk_0}{2z}\left[m\left|\frac{\vec{\rho}_2}{m} - \vec{\rho}_1\right|^2 - \left(\frac{1-m}{m}\right){\rho_2}^2 + (1-m){p_1}^2\right]}}{j\lambda z} U(\vec{\rho}', 0) d\vec{\rho}' \\ &= \frac{e^{\frac{-jk_0}{2z}\left(\frac{1-m}{m}\right){\rho_2}^2}}{j\lambda z} \iint_{-\infty}^{\infty} e^{\frac{jk_0}{2z}(1-m){\rho_1}^2} e^{\frac{jk_0 m}{2z}\left|\frac{\vec{\rho}_2}{m} - \vec{\rho}_1\right|^2} U(\vec{\rho}_1, 0) d\vec{\rho}_1 \end{aligned} \tag{1-34}$$

In order to use the Fourier Convolution Theorem, we wish to rewrite (1-34) in terms of a convolutional integral. First, we define:

$$U'(\vec{\rho}_1, 0) \equiv \frac{1}{m} U(\vec{\rho}_1, 0) e^{\frac{jk_0}{2z}(1-m)\vec{\rho}_1{}^2} \tag{1-35}$$

The above allows us to write (1-34) as:

$$U(\vec{\rho}_2, z) \cong \frac{e^{\frac{-jk_0}{2z}\left(\frac{1-m}{m}\right)\rho_2{}^2}}{j\lambda z} \iint_{-\infty}^{\infty} mU'(\vec{\rho}_1, 0) e^{\frac{jk_0 m}{2z}\left|\frac{\vec{\rho}_2}{m} - \vec{\rho}_1\right|^2} d\vec{\rho}_1 \tag{1-36}$$

We now introduce the scaled coordinates:

$$\vec{\rho}_2{}' = \frac{\vec{\rho}_2}{m}, \qquad \rho_2{}' = \frac{\rho_2}{m} \tag{1-37}$$

$$z' = \frac{z}{m} \tag{1-38}$$

Use of (1-37) and (1-38) yields in (1-36):

$$U(m\vec{\rho}_2{}', z) \cong \frac{e^{\frac{-jk_0}{2z'}(1-m)\rho_2{}'^2}}{j\lambda z'} \iint_{-\infty}^{\infty} U'(\vec{\rho}_1, 0) e^{\frac{jk_0}{2z'}\left|\vec{\rho}_2{}' - \vec{\rho}_1\right|^2} d\vec{\rho}_1 \tag{1-39}$$

(1-39) is now in the form of a convolutional integral, with kernel $H(\vec{\rho}_2{}' - \vec{\rho}_1, z')$:

$$H\left(\vec{\rho}_2{}' - \vec{\rho}_1, z'\right) \equiv \frac{e^{\frac{jk_0}{2z'}\left|\vec{\rho}_2{}' - \vec{\rho}_1\right|^2}}{j\lambda z'} \tag{1-40}$$

$$U(m\vec{\rho}_2{}', z) \cong e^{\frac{-jk_0}{2z'}(1-m)\rho_2{}'^2} \iint_{-\infty}^{\infty} U'(\vec{\rho}_1, 0) H(\vec{\rho}_2{}' - \vec{\rho}_1, z')\, d\vec{\rho}_1 \tag{1-41}$$

The Fourier transform of the kernel, $\widetilde{H}(\vec{q}_1, z')$, which using $\vec{\rho} = x\hat{e}_1 + y\hat{e}_2$ as a dummy variable of integration, is given by:

$$\widetilde{H}(\vec{q}_1, z') = \iint_{-\infty}^{\infty} H(\vec{\rho}, z') \exp(-2\pi j \vec{\rho} \cdot \vec{q}_1)\, d\vec{\rho}$$
$$= \iint_{-\infty}^{\infty} \frac{\exp\left[\pi j \left(\frac{\rho^2}{z'\lambda} - 2\vec{\rho} \cdot \vec{q}_1\right)\right]}{j\lambda z'} d\vec{\rho} \tag{1-42}$$

We have written (1-42) in terms of a spatial frequency vector, $\vec{q}_1 = q_{1,x}\hat{e}_1 + q_{1,y}\hat{e}_2$, as opposed to a spatial angular frequency (e.g. a $\vec{\kappa}_1$), because ultimately we are deriving these expressions for use with the FFT, which is not implemented using angular frequencies. We continue:

$$\widetilde{H}(\vec{q}_1, z') = e^{-\pi j z' \lambda {q_1}^2} \iint_{-\infty}^{\infty} \frac{e^{\pi j\left(\frac{\rho^2}{z'\lambda} - 2\vec{\rho}\cdot\vec{q}_1 + z'\lambda {q_1}^2\right)}}{j\lambda z'} d\vec{\rho}$$

$$= \frac{e^{-\pi j z' \lambda {q_1}^2}}{j\lambda z'} \int_{-\infty}^{\infty} e^{\pi j\left(\frac{x^2}{z'\lambda} - 2x q_{1,x} + z'\lambda {q_{1,x}}^2\right)} dx \int_{-\infty}^{\infty} e^{\pi j\left(\frac{y^2}{z'\lambda} - 2y q_{1,y} + z'\lambda {q_{1,y}}^2\right)} dy \tag{1-43}$$

$$= \frac{e^{-\pi j z' \lambda {q_1}^2}}{j\lambda z'} \int_{-\infty}^{\infty} e^{\pi j\left(\frac{x}{\sqrt{\lambda z'}} - q_{1,x}\sqrt{\lambda z'}\right)^2} dx \int_{-\infty}^{\infty} e^{\pi j\left(\frac{y}{\sqrt{\lambda z'}} - q_{1,y}\sqrt{\lambda z'}\right)^2} dy$$

We now examine the first integral in the final form of (1-43). We note that through a change of variables to $x' = x - q_{1,x}\lambda z'$ we can write:

$$\int_{-\infty}^{\infty} e^{\pi j\left(\frac{x}{\sqrt{\lambda z'}} - q_{1,x}\sqrt{\lambda z'}\right)^2} dx = \int_{-\infty + q_{1,x}\lambda z'}^{\infty + q_{1,x}\lambda z'} e^{\frac{-\pi {x'}^2}{j\lambda z'}} dx' = \int_{-\infty}^{\infty} e^{\frac{-\pi {x'}^2}{j\lambda z'}} dx' \tag{1-44}$$

The Gaussian integral identity given by (1-44) is readily generalizable as (1-45), given below using $r' = \frac{r^2}{2}$, $dr' = r dr$, $x' = \sqrt{a}x$, and $dx' = \sqrt{a}dx$:

$$\int_{-\infty}^{\infty} e^{\frac{-x^2}{2}}\,dx = \sqrt{\int_{-\infty}^{\infty} e^{\frac{-x^2}{2}}\,dx \int_{-\infty}^{\infty} e^{\frac{-y^2}{2}}\,dy} = \sqrt{2\pi \int_{0}^{\infty} r e^{\frac{-r^2}{2}}\,dr} \tag{1-45}$$

$$= \sqrt{2\pi \int_{0}^{\infty} e^{-r'}\,dr'} = \sqrt{2\pi}$$

$$\int_{-\infty}^{\infty} e^{\frac{-ax^2}{2}}\,dx = \frac{1}{\sqrt{a}} \int_{-\infty}^{\infty} e^{\frac{-x'^2}{2}}\,dx' = \sqrt{\frac{2\pi}{a}} \tag{1-46}$$

Substituting $\frac{2\pi}{j\lambda z'}$ for $a$ in (1-46) allows us to write (1-44) as:

$$\int_{-\infty}^{\infty} e^{\pi j\left(\frac{x}{\sqrt{\lambda z'}} - q_{1,x}\sqrt{\lambda z'}\right)^2}\,dx = \int_{-\infty}^{\infty} e^{\frac{-\pi x'^2}{j\lambda z'}}\,dx' = \sqrt{j\lambda z'} \tag{1-47}$$

Noting that, in reality, both integrals in the final form of Equation (1-43) are equivalent yields our optical transfer function:

$$\widetilde{H}(\vec{q}_1, z') = \frac{e^{-\pi j z' \lambda {q_1}^2}}{j\lambda z'} \left( \int_{-\infty}^{\infty} e^{\pi j\left(\frac{x}{\sqrt{\lambda z'}} - q_{1,x}\sqrt{\lambda z'}\right)^2}\,dx \right)^2 \tag{1-48}$$

$$= e^{-\pi j z' \lambda {q_1}^2}$$

Using the Fourier Convolution Theorem, we can now write (1-39) as:

$$U(m\vec{\rho}_2', z) \cong \frac{e^{\frac{-jk_0}{2z'}(1-m){\rho_2}'^2}}{j\lambda z'} \tag{1-49}$$

$$\times \iint_{-\infty}^{\infty} \widetilde{H}(\vec{q}_1, z') \left( \iint_{-\infty}^{\infty} U'(\vec{\rho}_1, 0)\, e^{2\pi j \vec{\rho}_1 \cdot \vec{q}_1} d\vec{\rho}_1 \right) e^{2\pi j \vec{\rho}_2{}' \cdot \vec{q}_1} d\vec{q}_1$$

For discretized simulations, this can be implemented using FFTs by defining the following matrices:

$$\mathbf{r}_{\mathbf{1},lk}^2 = (l\Delta x_1)^2 + (k\Delta y_1)^2 \tag{1-50}$$

$$\mathbf{r}_{\mathbf{2},lk}^2 = (l\Delta x_2)^2 + (k\Delta y_2)^2 \tag{1-51}$$

$$\mathbf{q}_{\mathbf{1},lk}^2 = \left(l\Delta q_{1,x}\right)^2 + \left(k\Delta q_{1,y}\right)^2 \tag{1-52}$$

$$\mathbf{Q}_{\mathbf{1},lk} = \exp\left[\frac{jk_0(1-m)}{2\Delta z}\mathbf{r}_{1,lk}^2\right] \tag{1-53}$$

$$\mathbf{Q}_{\mathbf{2},lk} = \text{fftshift}\left\{\exp\left[\frac{-2j\pi^2\Delta z}{mk_0}\mathbf{q}_{1,lk}^2\right]\right\} \tag{1-54}$$

$$\mathbf{Q}_{\mathbf{3},lk} = \exp\left[\frac{jk_0(m-1)}{2m\Delta z}\mathbf{r}_{2,lk}^2\right] \tag{1-55}$$

$$\mathbf{U}_{\mathbf{out},lk} = \mathbf{Q}_{\mathbf{3},lk} \cdot \text{IFFT}_2\left\{\mathbf{Q}_{\mathbf{2},lk} \cdot \text{FFT}_2\left\{\mathbf{Q}_{\mathbf{1},lk} \cdot \frac{\mathbf{U}_{\mathbf{in},lk}}{m}\right\}\right\} \tag{1-56}$$

where $\Delta x_1, \Delta y_1$ are the simulated spatial domain spacing in the input plane, $\Delta q_{1,x} = \frac{1}{M\Delta x_1}$, $\Delta q_{1,y} = \frac{1}{N\Delta y_1}$ are the frequency domain grid spacings with $M, N$ the number of grid points in the *x*- and *y*-directions (respectively), $\Delta q_{1,y}$ are the , $\Delta x_2, \Delta y_2$ are the simulated spatial domain spacing in the output plane. Note that for $m = 1$, $\mathbf{Q}_{\mathbf{1},lk}$ and $\mathbf{Q}_{\mathbf{3},lk}$ are always one at all points in the matrix, and $\mathbf{Q}_{\mathbf{2},lk}$ simplifies to the traditional Fresnel transfer function given by other sources [31]. (1-56) is the method of propagation used for all computational work in this thesis.

1.4: Theoretical Considerations for Propagation through Anisotropic, Non-Kolmogorov Turbulence

The theory derived in Section 1.2 has interesting repercussions when applied to the theory of optical propagation. In this section, we largely follow the approach give in [9] which is most applicable to this proposal. An important quantity in the study of propagation through isotropic turbulence is the Rytov variance [9], $\sigma_R^2 = 1.23{C_n}^2{k_0}^{7/6}L^{11/6}$, where $k_0 = \frac{2\pi}{\lambda}$ is the optical wavenumber, and $L$ is the propagation distance. The Rytov variance physically represents the normalized irradiance fluctuations, or scintillation index, $\sigma_I^2$, of an unbounded plain wave traveling through isotropic, Kolmogorov turbulence. Theorists have developed a generalized form of the Rytov variance applicable to anisotropic, non-Kolmogorov turbulence as [23]:

$$\tilde{\sigma}_R^2(L,\alpha,\mu_x,\mu_y) = \frac{-\Gamma(\alpha-1)}{\alpha\pi}\Gamma\left(1-\frac{\alpha}{2}\right)\sin\left(\frac{\pi\alpha}{4}\right)\cos\left(\frac{\pi\alpha}{2}\right){\tilde{C}_n}^2{k_0}^{3-\frac{\alpha}{2}}L^{\frac{\alpha}{2}}\int_0^{2\pi}\left(\frac{\cos^2\varphi}{{\mu_x}^2}+\frac{\sin^2\varphi}{{\mu_y}^2}\right)^{\frac{\alpha}{2}-1}d\varphi \quad (1\text{-}57)$$

where the combined factors $\frac{1}{2\pi}\int_0^{2\pi}\left(\frac{\cos^2\varphi}{{\mu_y}^2}+\frac{\sin^2\varphi}{{\mu_y}^2}\right)^{\frac{\alpha}{2}-1}d\varphi$ are sometimes [24] referred to as the multiplicative anisotropy factor. Equation (1-57) gives the scintillation index of an unbounded plane wave propagating through anisotropic, non-Kolmogorov turbulence, with scintillation index defined by:

$$\sigma_I^2 \equiv \frac{\langle (I - \langle I \rangle)^2 \rangle}{\langle I \rangle^2} = \frac{\langle I^2 \rangle - \langle I \rangle^2}{\langle I \rangle^2} \tag{1-58}$$

where because $\sigma_I^2$ is normalized, and therefore unitless, and $I$ can be either the irradiance with units $W \cdot m^{-2}$ or the electric field intensity ($E^2$) with units $V^2 \cdot m^{-2}$. Both choices of units are related by a constant, the impedance of the medium, $Z=Z_0/n$, where $Z_0$ is the vacuum impedance of the medium, and $n$ is the refractive index. Also of interest is the scintillation index of a spherical wave propagating though anisotropic, non-Kolmogorov in the weak fluctuation regime, i.e. the generalized Rytov variance for a spherical wave, which is given by the below expression [24]:

$$\begin{aligned}
&\tilde{\sigma}_{R,S}^2(L, \alpha, \mu_x, \mu_y) \\
&= \frac{-\Gamma(\alpha-1)\Gamma\left(1-\frac{\alpha}{2}\right)\Gamma^2\left(\frac{\alpha}{2}\right)}{2\pi\Gamma(\alpha)} \cos\left(\frac{\pi\alpha}{2}\right) \cos\left[\frac{\pi(\alpha-2)}{4}\right] \tilde{C}_n{}^2 k_0{}^{3-\frac{\alpha}{2}} L^{\frac{\alpha}{2}} \\
&\qquad \times \int_0^{2\pi} \left(\frac{\cos^2\varphi}{\mu_x{}^2} + \frac{\sin^2\varphi}{\mu_y{}^2}\right)^{\frac{\alpha}{2}-1} d\varphi \\
&= \frac{\alpha \cdot \tilde{\sigma}_R^2(L, \alpha, \mu_x, \mu_y) \cdot \Gamma^2\left(\frac{\alpha}{2}\right)}{2 \cdot \sin\left(\frac{\pi\alpha}{4}\right) \cdot \Gamma(\alpha)} \cos\left[\frac{\pi(\alpha-2)}{4}\right]
\end{aligned} \tag{1-59}$$

The most widely accepted method of analyzing the statistical nature of the propagation of light through optical turbulence, at least for Rytov variances less than or equal to unity, is the Rytov Method, which assumes that the long term statistics of turbulence can be modeled as a modulating function affecting the mean field of the otherwise vacuum diffracted light, $U_0(\vec{\rho}, L)$, with $U_0(\vec{\rho}, 0)$ being the

undiffracted complex field. A rigorous examination of the two point mutual coherence function (MCF) at a given propagation distance [9]:

$$\Gamma_2(\vec{\rho}_1, \vec{\rho}_2, L) = \langle U(\vec{\rho}_1, L) U^*(\vec{\rho}_2, L) \rangle \tag{1-60}$$

where the *2* subscript of $\Gamma_2$ denotes that this is the 2nd order moment of the field, *U* is the true field propagating through turbulence, and * denotes complex conjugation. This method predicts the long term mean irradiance via:

$$\langle |U(\vec{\rho}_1, L)|^2 \rangle = \Gamma_2(\vec{\rho}_1, \vec{\rho}_1, L) \tag{1-61}$$

Although there is more than one manner to express the behavior of a Gaussian beam diffracting in vacuum [34], we use a convention associated with the derivation of diffractive behavior in the paraxial approximation, defining behavior in terms of non-dimensional beam parameters. That is, the input plane curvature parameter and Fresnel ratio, $\Theta_0$ and $\Lambda_0$, respectively, and the output plane curvature parameter and Fresnel ratio, $\Theta$ and $\Lambda$, as [9]:

$$\Theta_0 = 1 - \frac{z}{F_0}, \qquad \Lambda_0 = \frac{2z}{k_0 {W_0}^2}, \qquad \overline{\Theta}_0 = \frac{z}{F_0} \tag{1-62}$$

$$\Theta = \frac{\Theta_0}{{\Theta_0}^2 + {\Lambda_0}^2}, \qquad \Lambda = \frac{\Lambda_0}{{\Theta_0}^2 + {\Lambda_0}^2}, \qquad \overline{\Theta} = 1 - \Theta \tag{1-63}$$

$$U_0(\rho, z) = \sqrt{\Theta^2 + \Lambda^2} \exp\left(-\frac{k_0 \Lambda r^2}{2z}\right) \exp\left(j\left(k_0 z - \tan^{-1}\left(\frac{\Lambda_0}{\Theta_0}\right) + \frac{k_0 \overline{\Theta} r^2}{2z}\right)\right) \tag{1-64}$$

where $W_0$ is the initial spot size (radius of $e^{-1}$ field magnitude relative to the maximum) and $F_0$ is the initial beam radius of curvature. The diffracted spot size, *W*, and radius of curvature, *F*, are given by [9]:

$$W = \sqrt{\frac{2z}{k_0\Lambda}}, \qquad F = -\frac{\overline{\Theta}}{z} \tag{1-65}$$

Equation (27) is consistent with a Green's function for propagation given by [30]:

$$\begin{aligned} G(\vec{r},\vec{r}') &= \frac{\exp(jk_0|\vec{r}-\vec{r}'|)}{4\pi|\vec{r}-\vec{r}'|} \\ &\cong \frac{1}{4\pi(z-z')}\exp\left[jk_0\left(z-z'+\frac{|\vec{\rho}-\vec{\rho}'|^2}{2(z-z')}\right)\right] \end{aligned} \tag{1-66}$$

The approximation in the last step of (1-66) is the paraxial approximation as applied to the Green's function.

Next, we consider the Born Approximation [9]:

$$\begin{aligned} n^2(\vec{\rho},z) &= \left(n_0(\vec{\rho},z)+n_1(\vec{\rho},z)\right)^2 \\ &\cong n_0(\vec{\rho},z)+2n_1(\vec{\rho},z) \end{aligned} \tag{1-67}$$

$$U(\vec{\rho},L) \cong U_0(|\vec{\rho}|,L)+\sum_{m=1}^{\infty} U_m(\vec{\rho},L) \tag{1-68}$$

Where we have already defined $U_0$, and the $U_m$'s are given by:

$$U_m(\vec{\rho},L) = \frac{k_0}{2\pi}\int_0^L dz' \iint_{-\infty}^{\infty} d\vec{\rho}' \exp\left(jk_0\left(L-z'+\frac{|\vec{\rho}-\vec{\rho}'|^2}{2(L-z')}\right)\right) U_{m-1}(\vec{\rho}',z)\frac{n_1(\vec{\rho},z')}{L-z'} \tag{1-69}$$

As previously referred to, the Rytov Method assumes that turbulence acts as a modulating function on the beam, via the Rytov Approximation:

$$U(\vec{\rho},L) \cong U_0(|\vec{\rho}|,L)\exp\left(\psi(\vec{\rho},L)\right) \tag{1-70}$$

$$= U_0(|\vec{\rho}|, L) \exp\left(\sum_{m=1}^{\infty} \psi_m(\vec{\rho}, L)\right)$$

It is noteworthy what the Born and Rytov approximations can be shown to be by introducing the normalized Born perturbations, $\Phi_m$:

$$\Phi_m(\vec{\rho}, L) = \frac{U_m(\vec{\rho}, L)}{U_0(\vec{\rho}, L)} \tag{1-71}$$

$$\sum_{m=1}^{\infty} \psi_m(\vec{\rho}, L) = \ln\left(1 + \sum_{m=1}^{\infty} \Phi_m(\vec{\rho}, L)\right) \tag{1-72}$$

In looking for the 1st and 2nd order terms in the Rytov approximation, taking the Maclaurin series around the right side of Equation (1-73) and keeping the 1st and 2nd order terms yields the relation:

$$\psi_1(\vec{\rho}, L) + \psi_2(\vec{\rho}, L) \cong \Phi_1(\vec{\rho}, L) + \left[\Phi_2(\vec{\rho}, L) + \frac{1}{2}{\Phi_1}^2(\vec{\rho}, L)\right] \tag{1-73}$$

Where we will equate the bracketed terms with $\psi_2(\vec{\rho}, L)$. As it has been shown [9] that the mean field, $\langle U(\vec{\rho}, L)\rangle$, goes rapidly to zero propagating any distance beyond a few meters in even weak turbulence, and because we are typically interested in the field intensity and fluctuations thereof, we ignore the 1st order moment, and begin in looking at the second previously given in (1-60):

$$\begin{aligned} \Gamma_2(\vec{\rho}_1, \vec{\rho}_2, L) &= U_0(|\vec{\rho}_1|, L) {U_0}^*(|\vec{\rho}_2|, L) \langle \exp\big(\psi(\vec{\rho}_1, L) + \psi^*(\vec{\rho}_2, L)\big)\rangle \\ &= \Gamma_2^0(\vec{\rho}_1, \vec{\rho}_2, L) \langle \exp\big(\psi(\vec{\rho}_1, L) + \psi^*(\vec{\rho}_2, L)\big)\rangle \end{aligned} \tag{1-74}$$

Where $\Gamma_2^0(\vec{\rho}_1, \vec{\rho}_2, L)$ is the mutual coherence function of the unperturbed field.

Evaluation of the exponent requires us to borrow from the method of cumulants [9, 35]:

$$\langle \exp(\psi) \rangle = \exp\left( \sum_{m=1}^{\infty} \frac{K_m}{m!} \right) \tag{1-75}$$

$$K_1 = \langle \psi \rangle, \qquad K_m = \langle (\psi - \langle \psi \rangle)^m \rangle \tag{1-76}$$

Therefore, to second order:

$$\begin{aligned} &\langle \exp\big(\psi(\vec{\rho}_1, L) + \psi^*(\vec{\rho}_2, L)\big) \rangle \\ &\cong \exp\left[ \begin{array}{c} \langle \psi(\vec{\rho}_1, L) + \psi^*(\vec{\rho}_2, L) \rangle \\ + \frac{1}{2}\Big( \langle \big(\psi(\vec{\rho}_1, L) + \psi^*(\vec{\rho}_2, L)\big)^2 \rangle - \langle \psi(\vec{\rho}_1, L) + \psi^*(\vec{\rho}_2, L) \rangle^2 \Big) \end{array} \right] \end{aligned} \tag{1-77}$$

Applying (1-73), along with the assumption $\langle \Phi_1(\vec{\rho}, L) \rangle = 0$ due to the mean field approaching zero, and then dropping all terms smaller than $\langle {\psi_1}^2 \rangle$, $\langle \psi_1 {\psi_1}^* \rangle$, $\langle \psi_2 \rangle$ yields [9]:

$$\begin{aligned} &\langle \exp\big(\psi(\vec{\rho}_1, L) + \psi^*(\vec{\rho}_2, L)\big) \rangle \\ &\quad \cong \exp(2\langle \psi_2(0, L) \rangle + \langle \psi_1(0, L)^2 \rangle + \langle \psi_1(\vec{\rho}_1, L) \psi_1(\vec{\rho}_2, L)^* \rangle) \end{aligned} \tag{1-78}$$

where 0's now appear in some of the function arguments by virtue of an assumption of homogeneity of turbulence (not isotropy, necessarily).

Equation (1-78) applied to (1-74) allows an approximation to the mean field having propagated through turbulence:

$$\begin{aligned}\langle I\rangle &= \langle U(|\vec{\rho}|,L)U(|\vec{\rho}|,L)^*\rangle = \Gamma_2(\vec{\rho},\vec{\rho},L)\\ &= |U_0(|\vec{\rho}|,L)|^2\exp(2\langle\psi_2(0,L)\rangle + \langle\psi_1(0,L)^2\rangle\\ &\qquad + \langle\psi_1(\vec{\rho}_1,L)\psi_1(\vec{\rho}_2,L)^*\rangle)\\ &= \frac{W_0^2}{W^2}\exp(\frac{-2|\vec{\rho}|^2}{W^2})\exp(2\langle\psi_2(0,L)\rangle + \langle\psi_1(0,L)^2\rangle\\ &\qquad + \langle\psi_1(\vec{\rho}_1,L)\psi_1(\vec{\rho}_2,L)^*\rangle)\end{aligned} \tag{1-79}$$

For Kolmogorov turbulence, examination of the above leads to [9]:

$$\begin{aligned}\langle I(\rho,L)\rangle &= \frac{W_0^2}{W^2}\exp\left(\frac{-2\rho^2}{W^2} + 1.32\sigma_R^2\Lambda^{\frac{5}{6}}\left(1 - {}_1F_1\left(-\frac{5}{6};1;\frac{2\rho^2}{W^2}\right)\right) - 1.33\sigma_R^2\Lambda^{\frac{5}{6}}\right)\\ &\cong \frac{W_0^2}{W^2}\exp\left(\frac{-2\rho^2}{W^2}\right)\exp\left(2.22\sigma_R^2\Lambda^{\frac{5}{6}}\frac{\rho^2}{W^2} - 1.33\sigma_R^2\Lambda^{\frac{5}{6}}\right)\end{aligned} \tag{1-80}$$

where ${}_1F_1$ represents the confluent hypergeometric function [36]. To simplify, we define $T$ as per (1-81) and make the approximations given in (1-82), (1-83), and (1-84) yields the final weak fluctuation theory mean irradiance approximation, (1-85):

$$T = 1.33\sigma_R^2\Lambda^{\frac{5}{6}} \tag{1-81}$$

$$2.22\sigma_R^2\Lambda^{\frac{5}{6}}\frac{\rho^2}{W^2} = 1.67\cdot T\frac{\rho^2}{W^2} \cong 2\cdot T\frac{\rho^2}{W^2} \tag{1-82}$$

$$e^{-T} = \frac{1}{1+T} \tag{1-83}$$

$$\frac{-2\rho^2}{W^2} + 2\cdot T\frac{\rho^2}{W^2} = \frac{-2\rho^2}{W^2}(1-T) \cong \frac{-2\rho^2}{W^2(1+T)} \tag{1-84}$$

$$\langle I(\rho, L)\rangle \cong \frac{{W_0}^2}{W^2(1+T)} \exp\left(\frac{-2\rho^2}{W^2(1+T)}\right) \tag{1-85}$$

Clearly, the perturbation theory based derivation for Kolmogorov turbulence predicts the long term spot size, $W_{LT}$, can be approximated by:

$$W_{LT} \cong W\sqrt{1 + 1.33\sigma_R^2 \Lambda^{\frac{5}{6}}} = W\sqrt{1+T} \tag{1-86}$$

In the course of this derivation, we started with the Born approximation and made further approximations based upon keeping only leading order non-zero-mean terms in the exponential functions. These approximations as applied to the Born and Rytov approximations constitute the Weak Fluctuation Regime, which is assumed valid for $\sigma_R^2 \ll 1$. Given the number of approximations that have been made in the process of deriving (47), it is not surprising that pragmatic adjustments have been made to the theoretical prediction [23]:

$$W_{LT} \cong W\left(1 + 1.33\sigma_R^2 \Lambda^{\frac{5}{6}}\right)^{3/5} = W(1+T)^{3/5} \tag{1-87}$$

This has been extended to anisotropic, non-Kolmogorov turbulence as [23, 24]:

$$W_{LT,x} \cong W\left(1 + T_x(\alpha, \mu_x, \mu_y)\right)^{\frac{3}{5}}, \qquad W_{LT,y} \cong W\left(1 + T_y(\alpha, \mu_x, \mu_y)\right)^{\frac{3}{5}} \tag{1-88}$$

$$\begin{aligned} T_x(\alpha, \mu_x, \mu_y) = 2\pi \frac{\Gamma\left(2 - \frac{\alpha}{2}\right)}{(\alpha-1){\mu_x}^2} \mathrm{A}(\alpha)\, {\tilde{C}_n}^2 {k_0}^{3-\frac{\alpha}{2}} L^{\frac{\alpha}{2}} \Lambda^{\frac{\alpha}{2}-1} \\ \cdot \int_0^{2\pi} \cos^2\varphi \left(\frac{\cos^2\varphi}{{\mu_y}^2} + \frac{\sin^2\varphi}{{\mu_y}^2}\right)^{\frac{\alpha}{2}-2} d\varphi \end{aligned} \tag{1-89}$$

$$T_y(\alpha,\mu_x,\mu_y) = 2\pi\frac{\Gamma\left(2-\frac{\alpha}{2}\right)}{(\alpha-1){\mu_y}^2}\mathrm{A}(\alpha)\,{\tilde{C}_n}^2 {k_0}^{3-\frac{\alpha}{2}} L^{\frac{\alpha}{2}}\Lambda^{\frac{\alpha}{2}-1} \cdot \int_0^{2\pi}\sin^2\varphi\left(\frac{\cos^2\varphi}{{\mu_y}^2}+\frac{\sin^2\varphi}{{\mu_y}^2}\right)^{\frac{\alpha}{2}-2} d\varphi \tag{1-90}$$

Note that the $\tilde{C}_n$, $k_0$, and $L$ dependences of  are identical to the generalized Rytov variance of (1-89) and (1-90), and the $\Lambda$ dependence is the same as the *T* in (1-81). Because of the connection with Equation (1-87), later in this proposal we will refer to the use of Equation (1-88) a Rytov variance based approach.  In order to estimate the fluctuations of the intensity of light, theorists analyzed the 4th moment of the field, given by:

$$\begin{aligned}\Gamma_2(\vec{\rho}_1,\vec{\rho}_2,\vec{\rho}_3,\vec{\rho}_4,L) &= \langle U(|\vec{\rho}_1|,L)U^*(|\vec{\rho}_2|,L)U(|\vec{\rho}_3|,L)U^*(|\vec{\rho}_4|,L)\rangle \\ &= U_0(|\vec{\rho}_1|,L){U_0}^*(|\vec{\rho}_2|,L)U_0(|\vec{\rho}_3|,L){U_0}^*(|\vec{\rho}_4|,L) \\ &\quad\cdot\langle\exp\left(\psi(\vec{\rho}_1,L)+\psi^*(\vec{\rho}_2,L)+\psi(\vec{\rho}_3,L)+\psi^*(\vec{\rho}_4,L)\right)\rangle\end{aligned} \tag{1-91}$$

Investigation using (1-91) yields an on-axis scintillation index of [9]:

$$\sigma_I^2(0,\alpha,\mu_x,\mu_y) = \frac{\tilde{\sigma}_R^2(\alpha,\mu_x,\mu_y)}{\sin\left({}^{\alpha\pi}/_4\right)} Re\left(j^{\frac{\alpha}{2}-1}\,{}_2F_1\left(1-\frac{\alpha}{2},\frac{\alpha}{2};1+\frac{\alpha}{2};\overline{\Theta}+j\Lambda\right)-\frac{\alpha\Lambda^{\frac{\alpha}{2}-1}}{2(\alpha-1)}\right) \tag{1-92}$$

where ${}_2F_1$ is the Gaussian hypergeometric function [36].

For $\sigma_R^2 \gg 1$, theorists have applied similar methods to the *parabolic equation method*.  Chernov [5] gives the stochastic wave equation as:

$$\nabla^2\vec{E}(\vec{r}) + {k_0}^2 n_1(\vec{r})\vec{E}(\vec{r}) + 2\nabla\left(\vec{E}(\vec{r})\cdot\nabla\log\left(n(\vec{r})\right)\right) = 0 \tag{1-93}$$

Where $\vec{E}$ is the electric vector field. The last term on the right hand side results in and is related to changes in the polarization state of the light, and is typically ignored [5, 9]. For a plane wave, the substitution of any transverse component of the field as $U(\vec{r}) = V(\vec{r})e^{jk_0 z}$ yields the parabolic equation:

$$2jk_0\frac{\partial V(\vec{r})}{\partial z} + \nabla_T^2 V(\vec{r}) + 2{k_0}^2 n_1(\vec{r})V(\vec{r}) = 0 \tag{1-94}$$

$$2jk_0\left\langle\frac{\partial V(\vec{r})}{\partial z}\right\rangle + \nabla_T^2\langle V(\vec{r})\rangle + 2{k_0}^2\langle n_1(\vec{r})V(\vec{r})\rangle = 0 \tag{1-95}$$

with $\nabla_T^2 = \frac{\partial^2}{\partial x^2} + \frac{\partial^2}{\partial y^2}$. Tatarskii suggested the approximation [37]:

$$\langle n_1(\vec{r})V(\vec{r})\rangle = \frac{jk_0}{2}A_n(0)\langle V(\vec{\rho},z)\rangle \tag{1-96}$$

$$\begin{aligned} A_n(\vec{\rho}) &= 2\pi\iint_{-\infty}^{\infty}\Phi_n\left(\left|\vec{\kappa}_\rho\right|\right)\exp\left(j\vec{\kappa}_\rho\cdot\vec{\rho}\right)d\vec{\kappa}_\rho \\ &= 4\pi^2\int_0^{\infty}\kappa_\rho\Phi_n\left(\kappa_\rho\right)J_0\left(\kappa_\rho|\vec{\rho}|\right)d\kappa_\rho \end{aligned} \tag{1-97}$$

Equation (1-95) then becomes:

$$\left[2jk_0\frac{\partial}{\partial z} + \nabla_T^2 + jk_0{}^3 A_n(0)\right]\langle V(\vec{\rho},z)\rangle = 0 \tag{1-98}$$

Following an approach similar to that done in the weak fluctuation regime eventually leads to, for plane waves of initial field magnitude of 1:

$$\Gamma_2(\vec{\rho}_1,\vec{\rho}_2,L) = \exp\left(-{k_0}^2 z[A_n(0) - A_n(\vec{\rho}_1 - \vec{\rho}_2)]\right) \tag{1-99}$$

$$= \exp\left(-4\pi^2 {k_0}^2 z \int_0^\infty \kappa_\rho \Phi_n(\kappa_\rho)\left(1 - J_0\left(\kappa_\rho|\vec{\rho}_1 - \vec{\rho}_2|\right)\right) d\kappa_\rho\right)$$

For Gaussian beam waves, in the strong fluctuation regime, we look for solutions of the form:

$$U(\vec{\rho}, L) = \frac{-jk_0}{2\pi L} \iint_{-\infty}^{\infty} d\vec{\rho}'\, U_0(\vec{\rho}', 0) \exp\left(\frac{jk_0|\vec{\rho} - \vec{\rho}'|^2}{2L} + \psi(\vec{\rho}, \vec{\rho}')\right) \qquad (1\text{-}100)$$

Then, again following similar methods as in earlier in this section [9]:

$$\langle I(\vec{\rho}, L)\rangle = \Gamma_2(\vec{\rho}, \vec{\rho}, L)$$

$$= \left(\frac{k_0}{2\pi L}\right)^2 \iint_{-\infty}^{\infty} d\vec{\rho}_1{}' \iint_{-\infty}^{\infty} d\vec{\rho}_2{}' \exp\left(-\frac{2\left|\vec{\rho}_1{}'\right|^2}{{W_0}^2} - \frac{\left|\vec{\rho}_2{}'\right|^2}{{W_0}^2}\right)$$

$$\cdot \exp\left(\frac{jk_0}{L}\left(\left(1 - \frac{L}{F_0}\right)\vec{\rho}_1{}' \cdot \vec{\rho}_2{}' - \vec{\rho} \cdot \vec{\rho}_1{}'\right)\right) \qquad (1\text{-}101)$$

$$\cdot \exp\left(-4\pi^2 {k_0}^2 L \int_0^1 \int_0^\infty \kappa_\rho \Phi_n(\kappa_\rho)(1 - J_0(\kappa_\rho|\vec{\rho}_2|\xi))d\kappa_\rho\, d\xi\right)$$

Further approximations lead to:

$$W_{LT} \cong W\sqrt{1 + 1.63\sigma_R^{\frac{12}{5}}\Lambda} \qquad (1\text{-}102)$$

Equation (1-102) can be modified and extended to anisotropic, non-Kolmogorov turbulence, however for examples of interest (1-102) yields similar results to the method described below.

An alternative expression for the long term spot size which, as we will examine later sections, seems appropriate in deep turbulence, $\sigma_R^2 \gg 1$, is derived from the *spatial coherence radius*. The wave structure function (WSF) for a spherical wave is given by [23]:

$$D(\vec{\rho}_1, \vec{\rho}_2, L)$$

$$= 8\pi^2 A(\alpha) \tilde{C}_n{}^2 k_0{}^2 L \int_0^1 \int_0^\infty \frac{1 - J_0\left(\kappa_\rho \xi \sqrt{\left(\frac{x_1 - x_2}{\mu_x}\right)^2 - \left(\frac{y_1 - y_2}{\mu_y}\right)^2}\right)}{\kappa_\rho{}^{\alpha-1}} d\kappa_\rho d\xi \qquad (1\text{-}103)$$

$$= \tilde{C}_n{}^2 k_0{}^2 L \frac{\alpha\, \Gamma(\alpha-1)\Gamma\left(-\frac{\alpha}{2}\right)}{(\alpha-1)\, 2^{\alpha-1}\, \Gamma\left(\frac{\alpha}{2}\right)} \cos\left(\frac{\alpha\pi}{2}\right) \left(\left(\frac{x_1 - x_2}{\mu_x}\right)^2 - \left(\frac{y_1 - y_2}{\mu_y}\right)^2\right)^{\frac{\alpha-2}{2}}$$

Note the emergence of the $\xi$ symbol is due to the change of variables, $\xi = 1 - \frac{z}{L}$, to an integral originally over $z$. The spatial coherence radius, $\tilde{\rho}_s$, in the $x$- and $y$-directions is given by solving $D(\vec{\rho}_0, \vec{\rho}_0, L) = \frac{D(0,0,L)}{2}$, and setting $\tilde{\rho}_s = |\vec{\rho}_0|$. For isotropic turbulence, we have:

$$\tilde{\rho}_s = \left( \tilde{C}_n{}^2 k_0{}^2 L \frac{\alpha\, \Gamma(\alpha-1)\Gamma\left(-\frac{\alpha}{2}\right)}{(\alpha-1)\, 2^{\alpha}\, \Gamma\left(\frac{\alpha}{2}\right)} \cos\left(\frac{\alpha\pi}{2}\right) \right)^{\frac{1}{2-\alpha}} \qquad (1\text{-}104)$$

Solving Equation (1-103) with $\tilde{\rho}_s = \sqrt{\frac{x^2}{\mu_x{}^2} - \frac{y^2}{\mu_y{}^2}}$ for $x = 0$ and $y = 0$ then predicts the $x$-, $y$-coherence lengths $\rho_{s,x} = \mu_x \tilde{\rho}_s$, $\rho_{s,y} = \mu_y \tilde{\rho}_s$ giving the spatial coherence ratios in the $x$- and $y$-directions:

$$\rho_{s,x} = \mu_x \left( \tilde{C}_n{}^2 k_0{}^2 L \frac{\alpha\, \Gamma(\alpha-1)\Gamma\left(-\frac{\alpha}{2}\right)}{(\alpha-1)\, 2^\alpha\, \Gamma\left(\frac{\alpha}{2}\right)} \cos\left(\frac{\alpha\pi}{2}\right) \right)^{\frac{1}{2-\alpha}} \tag{1-105}$$

$$\rho_{s,y} = \mu_y \left( \tilde{C}_n{}^2 k_0{}^2 L \frac{\alpha\, \Gamma(\alpha-1)\Gamma\left(-\frac{\alpha}{2}\right)}{(\alpha-1)\, 2^\alpha\, \Gamma\left(\frac{\alpha}{2}\right)} \cos\left(\frac{\alpha\pi}{2}\right) \right)^{\frac{1}{2-\alpha}} \tag{1-106}$$

Xiao and Voelz [38] give an estimate for the long term *x*- and *y*-spot size as:

$$\begin{aligned} W_{LT,x}(z) &\cong W_0 \sqrt{\left(1-\frac{z}{F}\right)^2 + \left(1+\frac{2W_0{}^2}{\rho_{s,x}{}^2}\right)\left(\frac{2z}{k_0 W_0{}^2}\right)^2} \\ &= W_0 \sqrt{\Theta_0{}^2 + \left(1+\frac{2W_0{}^2}{\rho_{s,x}{}^2}\right)\Lambda_0{}^2} \end{aligned} \tag{1-107}$$

$$\begin{aligned} W_{LT,y}(z) &\cong W_0 \sqrt{\left(1-\frac{z}{F}\right)^2 + \left(1+\frac{2W_0{}^2}{\rho_{s,y}{}^2}\right)\left(\frac{2z}{k_0 W_0{}^2}\right)^2} \\ &= W_0 \sqrt{\Theta_0{}^2 + \left(1+\frac{2W_0{}^2}{\rho_{s,y}{}^2}\right)\Lambda_0{}^2} \end{aligned} \tag{1-108}$$

Note that for $\tilde{C}_n{}^2 = 0$, $\rho_{s,x} = \rho_{s,y} = \infty$:

$$\begin{aligned} W_{LT}(z) = W(z) &= W_0 \sqrt{\left(1-\frac{z}{F}\right)^2 + \left(\frac{2z}{k_0 W_0{}^2}\right)^2} \\ &= \sqrt{\frac{2z}{k_0\Lambda_0}\left(\Theta_0{}^2 + \Lambda_0{}^2\right)} = \sqrt{\frac{2z}{k_0\Lambda}} \end{aligned} \tag{1-109}$$

which is consistent with earlier equations for free space beam propagation. This completes the background knowledge necessary to understand the proposed areas of study detailed in the rest of this proposal.

1.5: A Note Regarding Alternatives to the Paraxial Approximations

We now examine the Green's function for optical propagation given by [30]:

$$G(r) = \frac{\exp(jk_0 r)}{4\pi r} \tag{1-110}$$

Taking the Fourier transform:

$$\begin{aligned}
\tilde{G}(\kappa) &= \iiint_{-\infty}^{\infty} \frac{\exp(jk_0 r)}{4\pi r} \exp(-j\kappa r \cos\theta) r^2 \sin\theta \, d\varphi d\theta dr \\
&= \int_0^{\infty} \frac{\exp(jk_0 r)\sin(\kappa r)}{\kappa} dr \\
&= \frac{j}{2\kappa} \int_0^{\infty} \exp(j(k_0 - \kappa)r) - \exp(j(k_0 + \kappa)r)\, dr \\
&= \frac{j}{2\kappa}\left( \frac{-\exp(j(k_0 - \kappa)r)}{j(\kappa - k_0)} \Big|_0^{\infty} - \frac{\exp(j(k_0 + \kappa)r)}{j(\kappa + k_0)} \Big|_0^{\infty} \right)
\end{aligned} \tag{1-111}$$

If we assume either that $k_0$ has a small imaginary part (there is some small attenuation in propagation) or that $\exp(j(k_0 - \kappa)r)$, $\exp(j(k_0 + \kappa)r)$ equal their average value (of 0) at $r = \infty$, we have:

$$\tilde{G}(\kappa) = \frac{j}{2\kappa}\left(\frac{1}{j(\kappa - k_0)} + \frac{1}{j(\kappa + k_0)}\right) = \frac{\kappa + k_0 + \kappa - k_0}{2\kappa\left(\kappa^2 - {k_0}^2\right)} = \frac{1}{\kappa^2 - {k_0}^2} \quad (1\text{-}112)$$

In order for this to be useful to us, as we will see shortly, we need to inverse transform this in $\kappa_z$:

$$\tilde{G}(\kappa_\rho, z) = \frac{1}{2\pi}\int_{-\infty}^{\infty} \frac{\exp(j\kappa_z z)}{{\kappa_\rho}^2 + {\kappa_z}^2 - {k_0}^2} d\kappa_z \quad (1\text{-}113)$$

The integrand is analytic on the real line, and has first order poles at $\kappa_z = \pm\sqrt{{k_0}^2 - {\kappa_\rho}^2}$. Assuming $Re(k_0) > \kappa_\rho$, (which will be a good approximation for the grids used in our simulations of optical phenomena), and that $k_0$ has a small and positive imaginary part, $k_{0,i}$, such that $k_0 = k_{0,r} + j \cdot k_{0,i}$ closing the contour of (1-113) upwards leads to:

$$\tilde{G}(\kappa_\rho, z) = \frac{1}{2\pi}\oint \frac{\exp(j\kappa_z z)}{{\kappa_\rho}^2 + {\kappa_z}^2 - {k_0}^2} d\kappa_z = \frac{j\exp\left(jz\sqrt{{k_0}^2 - {\kappa_\rho}^2}\right)}{2\sqrt{{k_0}^2 - {\kappa_\rho}^2}} \quad (1\text{-}114)$$

Taking the limit as $k_{0,i} \to 0$, $k_0 \to k_{0,r}$ demonstrates that this equation is valid for vacuum propagation.

It is interesting to note that although typically the paraxial approximation is used for studies of laser propagation, by noting $\sqrt{{k_0}^2 - {\kappa_\rho}^2} = k_0\sqrt{1 - \frac{{\kappa_\rho}^2}{{k_0}^2}}$ and taking advantage of the Taylor series for $\sqrt{1 + x}$ we achieve:

$$\sqrt{{k_0}^2 - {\kappa_\rho}^2} = k_0\left(1 + \sum_{n=1}^{\infty} \frac{(-1)^n (2n)!}{4^n (n!)^2 (2n-1)} \left(\frac{\kappa_\rho}{k_0}\right)^{2n}\right), \qquad \left|\frac{\kappa_\rho}{k_0}\right| < 1 \quad (1\text{-}115)$$

one this allows us to write $\tilde{G}(\kappa_\rho, z)$ as:

$$\tilde{G}(\kappa_\rho, z) = \frac{j\exp(jzk_0)}{2\sqrt{{k_0}^2 - {\kappa_\rho}^2}} \exp\left(jzk_0 \sum_{n=1}^{\infty} \frac{(-1)^n (2n)!}{4^n (n!)^2 (2n-1)} \left(\frac{\kappa_\rho}{k_0}\right)^{2n}\right) \quad (1\text{-}116)$$

The above expression is valid for $\left|\frac{\kappa_\rho}{k_0}\right| < 1$. We have written $\tilde{G}(\kappa_\rho, z)$ in this form, with two exponentials function, for reasons related to computing $\tilde{G}(\kappa_\rho, z)$ for use in simulation. Because the $jzk_0$ term in the 1st exponential is expected to be very large compared to the non-constant phase terms given by the rest of the series, we have noted when this form of $\tilde{G}(\kappa_\rho, z)$ is used to compute the effective Green's function (or point spread function) for the simulation of optical propagation quantization errors can become significant leading to error in the relative phase between points in $\vec{\kappa}_\rho$-space. For simulations of complex optical fields bandlimited by $|\kappa_\rho| < k_0$, Equation (1-116) provides a method of performing non-paraxial propagations. By noting that the $\exp(jzk_0)$ contributes only to the constant phase term of the propagated wave, and noting that the infinite summation in Equation (1-116) cannot be computed, we note that an approximation for non-paraxial propagation is given by:

$$\tilde{G}(\kappa_\rho, z) \cong \frac{j}{2\sqrt{{k_0}^2 - {\kappa_\rho}^2}} \exp\left( jzk_0 \sum_{n=1}^{N} \frac{(-1)^n (2n)!}{4^n (n!)^2 (2n-1)} \left(\frac{\kappa_\rho}{k_0}\right)^{2n} \right) \quad (1\text{-}117)$$

where $N$, the number of terms, should be larger than 1 for non-paraxial simulations. For paraxial simulations, $N = 1$ as we will demonstrate. We note, however, that in paraxial simulations, there is no harm in using more than just the 1st series term aside from increases in computation time.

The Huygen-Fresnel integral [9, 39] gives the propagated, $U(\vec{\rho}, z)$, field at distance $z$, in terms of the Green's function for propagation, $G(\vec{\rho}, z)$, and the initial field in the $z = 0$ plane, $U(\vec{\rho}, 0)$, as per:

$$U(\vec{\rho}, z) = -2jk_0 \iint_{-\infty}^{\infty} G(\vec{\rho} - \vec{\rho}', z)\, U(\vec{\rho}', 0) d\vec{\rho}' \quad (1\text{-}118)$$

As (1-118) contains a convolutional integral, we can use the Fourier Convolution Theorem which equates convolution in the spatial domain as equivalent to multiplication in the frequency domain. This allows us to write:

$$\tilde{U}(\vec{\kappa}_\rho, z) = -2jk_0 \tilde{G}(\vec{\kappa}_\rho, z) \tilde{U}(\vec{\kappa}_\rho, 0) \quad (1\text{-}119)$$

$$\begin{aligned} U(\vec{\rho}, z) &= \frac{-j}{\pi\lambda} \iint_{-\infty}^{\infty} \tilde{G}(\vec{\kappa}_\rho, z)\, \tilde{U}(\vec{\kappa}_\rho, 0) \exp(j\vec{\rho} \cdot \vec{\kappa}_\rho)\, d\vec{\kappa}_\rho \\ &= (2\pi)^{-2} \iint_{-\infty}^{\infty} \tilde{G}'(\vec{\kappa}_\rho, z)\, \tilde{U}(\vec{\kappa}_\rho, 0) \exp(j\vec{\rho} \cdot \vec{\kappa}_\rho)\, d\vec{\kappa}_\rho \end{aligned} \quad (1\text{-}120)$$

where we dub $\tilde{G}'(\vec{\kappa}_\rho, z)$ in (1-120) as the Fourier transform of the *effective Green's function* for propagation. For paraxial propagation, $\tilde{G}'(\vec{\kappa}_\rho, z)$ is determined from the $\tilde{G}(\kappa_\rho, z)$ of (1-117) as per:

$$\begin{aligned}\tilde{G}'(\vec{\kappa}_\rho, z) &\cong -2jk_0\tilde{G}(\kappa_\rho, z) \\ &= \frac{k_0}{\sqrt{{k_0}^2 - {\kappa_\rho}^2}} \exp\left(jzk_0 \sum_{n=1}^{N} \frac{(-1)^n (2n)!}{4^n (n!)^2 (2n-1)} \left(\frac{\kappa_\rho}{k_0}\right)^{2n}\right)\end{aligned} \tag{1-121}$$

By approximating (1-121) and as per [33, 40] we confirm that we recover a paraxial approximation form of the Green's function:

$$\tilde{G}'(n\Delta\kappa_x, m\Delta\kappa_y, \Delta z) \cong \exp\left(-j\Delta z \frac{n^2{\Delta\kappa_x}^2 + m^2{\Delta\kappa_y}^2}{2k_0}\right) \tag{1-122}$$

where $N$, $M$ are the number of grid points in the x-, y-directions, $\Delta z$ is the propagation distance, $\Delta x$, $\Delta y$ are the $x$-, $y$- grid resolutions, and $\Delta\kappa_x$, $\Delta\kappa_y$ are the spatial angular frequency resolutions. The act of propagating takes advantage of the convolution / multiplication equivalence in the space and spatial frequency domains, respectively, and we may propagate distorted beams via inverse FFT (IFFT) as per:

$$\begin{aligned}&U(n\Delta x, m\Delta y, z) = \\ &\quad IFFT\left(\tilde{U}(n\Delta\kappa_x, m\Delta\kappa_y, z - \Delta z) \cdot \tilde{G}'(n\Delta\kappa_x, m\Delta\kappa_y, \Delta z) N\Delta\kappa_x M\Delta\kappa_y\right)\end{aligned} \tag{1-123}$$

where $\widetilde{U}$ is the Fast Fourier Transform (FFT) of the electric field, $U$, and the $N\Delta\kappa_x M\Delta\kappa_y$ factor implements a change of variables to normalize the spatial frequencies in the discrete approximation to the Fourier integral. We also note that as per computational conventions involving FFTs, there is also a circular shift necessary of the spatial frequency domain Green's function which is not include in the above equation for clarity and consistency with continuous space integrals.

# Chapter 2 : A Revised Method for Simulation of Atmospheric Turbulence

## 2.1: Background

The split-step propagation method for modeling optical propagation through atmospheric turbulence has been widely used in statistical analysis of beam propagation since its introduction by Fleck et al. [40, 41]. This method remains popular in simulations of long-range, linear optical propagation due to computation time advantages associated with using the fast FFT algorithm to compute the DFT, which are used in both the optical propagation and atmospheric distortion algorithms of the cited method. In simulations of nonlinear optical propagation, phase screens are also widely used [42, 43, 44, 45], including when supporting studies centering on filamentation [46, 47, 48, 49, 50, 51]. However, due to periodicity and aliasing effects associated with the DFT, significant effort has gone into the development of computational methods that add subharmonic, low-spatial-frequency components to the atmospheric screens [52, 53]. Additionally, Zernike-polynomial-based methods [54] and other creative methods [55] have been pioneered partly to address this issue, including methods using randomized sampling of the turbulence energy spectrum introduced by Charnotskii [56]. However, due to the computational efficiency of leveraging the FFT algorithm, DFT-based methods for phase screen generation remain popular [33, 38, 57, 58, 59, 60].

In this section, we present a modified method that exploits the Fourier transform shift theorem [39], which also extends to the DFT [61], in order to include low-frequency components in an FFT-centric method in a straightforward manner. For many applications, this method may provide sufficient phase screen accuracy relative to theory without additional computational penalty associated with subharmonics and other methods. Additionally the method can be combined with the subharmonic method of Lane et al. [52] in order to give very accurate results across a range of spectral models of practical and theoretical importance.

## 2.2: Overview of the Split Step Algorithm for Simulation of Optical Propagation through Atmospheric Turbulence

The split step algorithm for simulations of optical propagation through turbulence was first pioneered by Fleck, et. al, in order to study the time-dependent propagation of lasers through the atmosphere [40, 41]. Since that time, significant effort has been devoted by the computational optics community to increasing the fidelity of phase screen statistics [52, 53, 54, 55, 56, 62, 63], as well as providing modifications to the vacuum propagation algorithm [33]. In most implementations of the split step algorithm, FFT's are utilized for the purposes of both propagating the beam and for creating the simulated atmospheric distortion. We note, however, in certain implementations [54, 56, 62] phase screens may be produced without use of the FFT. Propagation is typically performed using an optical transfer function [31] derived from a point spread function derived from the paraxial approximation

to the Green's function for propagation, given by (1-122). In order to simulate optical atmospheric turbulence distortions a refractive index energy spectrum, similar to (1-20), defines a noise filter which is used to create a random phase screen with the correct spectral energy statistics. Both the propagation and distortion steps both provide approximate solutions via inverse FFT, and as such are pseudo-spectral methods [64]. The typical implementation of algorithm alternates the propagation and distortion steps as per Figure 2-1, although we note that partial propagations may be used between atmospheric distortion steps [33].

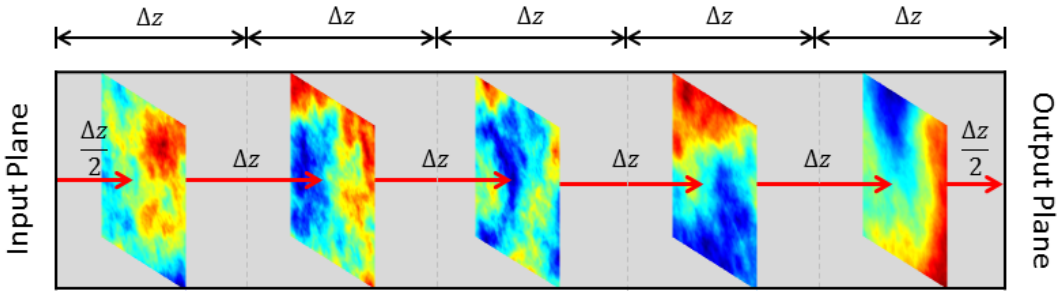


**Figure 2-1:** Illustration of a generic phase screen simulation using five screens. The beam is propagated a distance of Δz/2 or Δz using the FFT-based angular spectrum propagation algorithm. After all but the final propagation step, a random phase screen is applied as a phase modulation of the propagating wave.

Optical propagation may be performed simply, without changes in grid spacings between steps, by using the method outlined in Equation (1-56). The atmospheric optical turbulence phase screens used to modulate the propagating wave have traditionally been created by defining a noise filter using the three dimensional energy spectrum of turbulence (see Section 2), and using that filter to

shape complex noise in the frequency domain. The output of this noise filtering process is given by:

$$\theta(m,n) = k_0 \sqrt{\Delta\kappa_x \Delta\kappa_y} \sum_{k=-\frac{M}{2}}^{\frac{M}{2}-1} \sum_{l=-\frac{N}{2}}^{\frac{N}{2}-1} \tilde{c}\left(m\Delta\kappa_x, n\Delta\kappa_y\right) e^{j\left(m\Delta x k\Delta\kappa_x + n\Delta y l\Delta\kappa_y\right)}$$
$$= k_0 \sqrt{\Delta\kappa_x \Delta\kappa_y} \sum_{k=-\frac{M}{2}}^{\frac{M}{2}-1} \sum_{l=-\frac{N}{2}}^{\frac{N}{2}-1} \tilde{c}\left(m\Delta\kappa_x, m\Delta\kappa_y\right) \exp\left[2\pi j\left(\frac{mk}{M} + \frac{nl}{M}\right)\right] \tag{2-1}$$

where $N$, $M$ are the number of grid points in the $x$, $y$ directions, $\Delta\kappa_x = \frac{2\pi}{M\Delta x} = \frac{2\pi}{L_x}$, $\Delta\kappa_y = \frac{2\pi}{N\Delta y} = \frac{2\pi}{L_y}$, with $L_x$, $L_y$ being the $x$-, $y$-direction screen lengths, $\Delta x = \frac{L_x}{N}$, $\Delta y = \frac{L_y}{M}$, and $\tilde{c}$ is a random variable given by:

$$\tilde{c}\left(k\Delta\kappa_x, l\Delta\kappa_y\right) = (a + jb) \cdot \sqrt{2\pi\Delta z \Phi_n\left(k\Delta\kappa_x, l\Delta\kappa_y\right)}, \qquad (k,l) \neq (0,0) \tag{2-2}$$

where $a$, $b$ are Gaussian random variables with variance 1. $\tilde{c}(0,0)$ is typically set to 0 as it represents a constant phase factor, and only relative phase differences in $x$, $y$ should affect propagation. The $2\pi$ factor appears under the square root in the expression representing our noise filter due to the approximation of the refractive index correlation function given by (1-21).

Equation (2-1) produces a finite grid of random complex variables, and each real and imaginary part of $\theta(m,n)$ may be taken as an independent phase screen. The author has been careful to give two forms of equation (2-1) as, while the first form is somewhat

intuitive relative to the previous calculus expressions given in regards to atmospheric turbulence statistics, the second form demonstrates clearly that the phase screen algorithm is readily implementable via the inverse FFT. By allowing the random function $\tilde{c}\left(k\Delta\kappa_x, l\Delta\kappa_y\right)$ to define a random matrix, $\tilde{\mathbf{c}}_{kl}$, as per:

$$\boldsymbol{\theta}_{mn} = k_0 \sqrt{\Delta\kappa_x \Delta\kappa_y}\, IFFT_2\{\tilde{\mathbf{c}}_{kl}\} \tag{2-3}$$

In order to assess the accuracy of this phase screen method, as well as those not yet discussed, it is helpful to derive the theoretical structure function, denoted as $D_\theta$, of three dimensional turbulence collapsed into two dimensions. $D_\theta$ is given by [53]:

$$D_\theta(\vec{\rho}, \Delta z) = 4\pi k^2 \Delta z \int_{-\infty}^{\infty} \left(1 - \cos\left(\vec{\rho} \cdot \vec{\kappa}_\rho\right)\right) \Phi_n\left(\vec{\kappa}_\rho\right) d\vec{\kappa}_\rho \tag{2-4}$$

Writing $\vec{\rho} = \rho \cos\phi\, \hat{e}_x + \rho \sin\phi\, \hat{e}_y$, and $\vec{\kappa}_\rho = \kappa_\rho \cos\phi_\kappa\, \hat{e}_\mathrm{x} + \kappa_\rho \sin\phi_\kappa\, \hat{e}_\mathrm{y}$, for isotropic turbulence we can re-write as:

$$\begin{aligned} D_\theta(\vec{\rho}, \Delta z) &= 4\pi k^2 \Delta z \int_0^{\infty} \int_0^{2\pi} \left[1 - \cos\left(\rho\kappa_\rho \cos(\varphi)\right)\right] \Phi_n\left(\kappa_\rho\right) \kappa_\rho \, d\varphi \, d\kappa_\rho \\ &= 8\pi^2 k^2 \Delta z \int_0^{\infty} \left(1 - J_0\left(\rho\kappa_\rho\right)\right) \Phi_n\left(\kappa_\rho\right) \kappa_\rho \, d\kappa_\rho \end{aligned} \tag{2-5}$$

where $\rho = |\vec{\rho} - \rho_0|$, $\varphi$ is the angle between $\vec{\rho}$ and $\vec{\kappa}_\rho$, and $J_0$ is the 0th order Bessel function of the first kind. In later sections, we shall use (2-5) directly for numerical calculations of the theoretic structure function associated with spectral models including inner and outer scales.

For the general models of isotropic turbulence discussed in Section 1.4, in the absence of scale sizes, we have a structure function:

$$D_\theta(\vec{\rho},\Delta z) = 8\pi^2 \cdot \mathrm{A}(\alpha) \cdot k_0^2 \Delta z \tilde{C}_n^2 \int_0^\infty \frac{1 - J_0(\rho\kappa_\rho)}{{\kappa_\rho}^{\alpha-1}} d\kappa_\rho \tag{2-6}$$

After using the identity given in [65], $\int_0^\infty \frac{1-J_0(t)}{\mathrm{t}^\mu} d\mathrm{t} = -\frac{\pi \sec\left(\frac{\mu\pi}{2}\right)}{2^\mu \Gamma^2\left(\frac{\mu+1}{2}\right)}, 1 < \mu < 3$, and change of variables from $\rho\kappa_\rho \to {\kappa_\rho}'$, we arrive at:

$$\begin{aligned} D_\theta(\rho,\Delta z) &= \frac{8\pi^3 \cdot \mathrm{A}(\alpha) \cdot k_0^2 \Delta z \tilde{C}_n^2}{2^{\alpha-1}\cos\frac{(\alpha-3)\pi}{2}\Gamma^2\left(\frac{\alpha}{2}\right)} \rho^{\alpha-2} \\ &= \frac{\pi^2\,\Gamma(\alpha-1)\cdot\cos\frac{\alpha\pi}{2}\cdot k_0^2 \Delta z \tilde{C}_n^2}{2^{\alpha-2}\cos\frac{(\alpha-3)\pi}{2}\Gamma^2\left(\frac{\alpha}{2}\right)} \rho^{\alpha-2} \end{aligned} \tag{2-7}$$

For anisotropic turbulence:

$$\begin{aligned} D_\theta(x,y,\Delta z) &= 4\pi^2 \mathrm{A}(\alpha) k_0^2 \Delta z \tilde{C}_n^2\, \mu_x \mu_y \int_{-\infty}^{\infty} \frac{1-\cos\left(x\kappa_x + y\kappa_y\right)}{\left({\mu_x}^2{\kappa_x}^2 + {\mu_y}^2{\kappa_y}^2\right)^{\alpha/2}} d\vec{\kappa} \\ &= 4\pi^2 \mathrm{A}(\alpha) k_0^2 \Delta z \tilde{C}_n^2 \int_{-\infty}^{\infty} \frac{1-\cos\left(\frac{x}{\mu_x}{\kappa_x}' + \frac{y}{\mu_y}{\kappa_y}'\right)}{\left({\kappa_x}'^2 + {\kappa_y}'^2\right)^{\frac{\alpha}{2}}} d\vec{\kappa}' \\ &= 4\pi^2 \mathrm{A}(\alpha) k_0^2 \Delta z \tilde{C}_n^2 \int_0^\infty \int_0^{2\pi} \frac{1-\cos\left(\rho\sqrt{\frac{\cos^2\theta}{{\mu_x}^2} + \frac{\sin^2\theta}{{\mu_y}^2}}\,\kappa_\rho' \cos\phi_\kappa\right)}{{\kappa_\rho'}^{\alpha-1}} d\varphi_\kappa\, d{\kappa_\rho}' \end{aligned} \tag{2-8}$$

$$= 4\pi^2 \mathrm{A}(\alpha) k_0^2 \Delta z \tilde{C}_n^2 \left( \rho \sqrt{\frac{\cos^2\theta}{{\mu_x}^2} + \frac{\sin^2\theta}{{\mu_y}^2}} \right)^{\alpha-2} \int_0^\infty \frac{1 - J_0(\kappa_\rho')}{{\kappa_\rho'}^{\alpha-1}} \, d{\kappa_\rho}'$$

$$= \frac{\pi^2 \Gamma(\alpha-1) \cdot \cos\frac{\alpha\pi}{2} \cdot k_0^2 \Delta z \tilde{C}_n^2}{2^{\alpha-2} \cos\frac{(\alpha-3)\pi}{2} \Gamma^2\left(\frac{\alpha}{2}\right)} \left( \sqrt{\frac{x^2}{{\mu_x}^2} + \frac{y^2}{{\mu_y}^2}} \right)^{\alpha-2}$$

The above expressions give the theoretical structure functions in continuous space for phase screen distortions applied to optical paraxial waves, where we have made the substitutions:

- $\vec{\kappa}' = \mu_x \kappa_x \hat{e}_x + \mu_y \kappa_y \hat{e}_y = {\kappa_x}' \hat{e}_x + {\kappa_y}' \hat{e}_y$
- ${\kappa_x}' = {\kappa_\rho}' \cos\varphi_\kappa \; , \; {\kappa_y}' = {\kappa_\rho}' \sin\varphi_\kappa$
- $\rho = \sqrt{x^2 + y^2}$
- $\theta = \angle(x + jy)$
- $\phi_\kappa = \varphi_\kappa - \theta$

We note that the distance power law in expressions (2-7) and (2-8) is lower by 1 from the three dimension structure function predicted by (1-19) of $\alpha - 3$. This is consistent, however, because when a three dimensional volume is summed, or integrated across, assuming the *z*-dependence is expressible via Fourier series, only the 0-frequency (constant) term survives, which is why $\kappa_z$ can be set to 0 in (1-20). Another way to look at this is that the statistic of sums of line segments with the same *z*-bounds and directions should not be expected to have the same statistics as the statistics between points. As we can only perform discretized simulations with

computer technology, we seek to approximate these expressions in creating our phase screens for distorting propagating beams and will later use these expressions to generate root mean square (RMS) error statistics.

Returning to the pragmatic discussion of phase screen creation, We note the expression given in Equation (2-1) is typically achieved via FFT, however because a large amount of the distortion energy spectrum is represented around the $(\kappa_x, \kappa_y) = (0,0)$ grid point, Lane, Glindemann, and Dainty [52] suggested that convergence with theory could be improved by partitioning the (0,0) section of the grid up into subsections, and adding so-called *subharmonic* frequency components to the traditional phase screen, as per:

$$\theta_{SH}(m,n) = \sum_{p=1}^{N_p} \frac{\sqrt{\Delta\kappa_x \Delta\kappa_y}}{3^p} \sum_{k=-1}^{1} \sum_{l=-1}^{1} \tilde{c}\left(k\frac{\Delta\kappa_x}{3^p}, l\frac{\Delta\kappa_y}{3^p}\right) \cdot e^{j\left(\frac{(k\Delta\kappa_x m\Delta x}{3^p M} + \frac{l\Delta\kappa_y n\Delta y}{3^p N}\right)} \quad (2\text{-}9)$$

The subharmonic method summarized by Equation (2-9) is referred to throughout the remainder of this work as the *Lane subharmonic method*. Figure 2-2, taken from [52], illustrates the manner in which the method partitions the frequency domain in a fractal manor around the $(\kappa_x, \kappa_y) = (0,0)$ point.

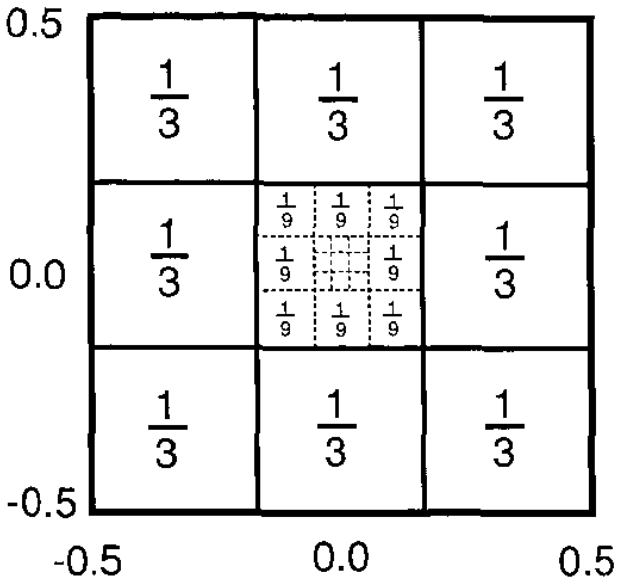


**Figure 2-2:** Visual aid demonstrating fractal nature of the subharmonic expansion, taken from [52].

Frehlich created an algorithm designed to improve convergence in scenarios of interest via [53]:

$$\theta_{SH,f}(m,n) = \sum_{p=1}^{N_p} \sum_{k=-1}^{1} \sum_{l=-1}^{1} \tilde{c}'\left(k, l, \frac{\Delta\kappa_x}{3^p}, \frac{\Delta\kappa_y}{3^p}\right) \cdot e^{j\left(\frac{(k\Delta\kappa_x m\Delta x}{3^p M} + \frac{l\Delta\kappa_y n\Delta y}{3^p N}\right)} \quad (2\text{-}10)$$

$$\tilde{c}'\left(k, l, \frac{\Delta\kappa_x}{3^p}, \frac{\Delta\kappa_y}{3^p}\right) = (a+jb)k\sqrt{2\pi\Delta z \cdot I_f\left(k, l, \frac{\Delta\kappa_x}{3^p}, \frac{\Delta\kappa_y}{3^p}\right)}, (k,l) \neq (0,0) \quad (2\text{-}11)$$

$$I_f\left(k, l, \frac{\Delta\kappa_x}{3^p}, \frac{\Delta\kappa_y}{3^p}\right) = \int_{\left(k-\frac{1}{2}\right)\frac{\Delta\kappa_x}{3^p}}^{\left(k+\frac{1}{2}\right)\frac{\Delta\kappa_x}{3^p}} \int_{\left(l-\frac{1}{2}\right)\frac{\Delta\kappa_y}{3^p}}^{\left(l+\frac{1}{2}\right)\frac{\Delta\kappa_y}{3^p}} \Phi_n(\kappa_x, \kappa_y)\, d\kappa_x d\kappa_y \quad (2\text{-}12)$$

The subharmonic method summarized by Equations (2-10) - (2-12) is referred to throughout the remainder of this work as the *Frehlich subharmonic method*. These

equations summarize what we will generally refer to as *traditional subharmonic methods* in the later sections of this thesis.

## 2.3: Motivation for a New Method

The randomized spectral sampling algorithm was originally motivated by investigation of the three dimensional structure function integrand vs the ideal structure function of a phase screen (which is analogous and equal to the wave structure function of a plane wave [9]). For anisotropic optical turbulence, analyzing the first equality of (1-19) under a change of variables, we are able to write the three dimensional structure function of the refractive index in terms of a sinc transform [6] relation as:

$$D_n(x,y,z) = 8\pi A(\alpha)\tilde{C}_n^2 \left( \sqrt{\frac{x^2}{{\mu_x}^2} + \frac{y^2}{{\mu_y}^2} + z^2} \right)^{\alpha-3} \int_0^\infty [1 - \sin(\kappa')]{\kappa'}^{2-\alpha} d\kappa' \quad (2\text{-}13)$$

We note the following features of the integral of Equation (2-13):

1. For small $\kappa'$, the integrand behaves like ${\kappa'}^{4-\alpha}$
2. The integrand is finite over all $\kappa'$ for $\alpha \leq 4$
3. The integrand approaches zero as $\kappa'$ approaches zero, for $\alpha < 4$
4. The integral converges to $[8\pi \cdot A(\alpha)]^{-1}$ for $3 < \alpha < 5$

On the other hand, the desired structure function for a phase screen is given by an integral of the form:

$$D_\theta(x,y) = 8\pi^2 A(\alpha) k_0^2 \Delta z \tilde{C}_n^2 \left( \sqrt{\frac{x^2}{{\mu_x}^2} + \frac{y^2}{{\mu_y}^2}} \right)^{\alpha-2} \int_0^\infty \left[1 - J_0(\kappa'_\rho)\right] {\kappa'_\rho}^{1-\alpha} d\kappa'_\rho \quad (2\text{-}14)$$

An important aspect of Equation (2-14) relative to Equation (2-13) is that the spatial power law has increased from $\alpha - 3$ to $\alpha - 2$, which is related to the discussion of the Fourier series in Section 2. We note the following features of the integral of equation (2-14):

1. For small $\kappa'_\rho$, the integrand behaves like ${\kappa'_\rho}^{3-\alpha}$
2. The integrand diverges at $\kappa'_\rho = 0$ for $\alpha > 3$
3. The integral converges for $2 < \alpha < 4$ to [65]:

$$\int_0^\infty \left[1 - J_0(\kappa'_\rho)\right] {\kappa'_\rho}^{1-\alpha} d\kappa'_\rho = \frac{\pi \sec\left[\frac{(\alpha-3)\pi}{2}\right]}{2^{\alpha-1}\Gamma^2\left(\frac{\alpha}{2}\right)} \quad (2\text{-}15)$$

Additionally, due to our formation of the $A$ function in (1-17), equation (2-14) gives a positive and finite two dimensional structure for alphas between $3 < \alpha < 4$, and other power laws produce integrals that are either divergent or unphysical (e.g. structure functions with negative power law).

With regards to using phase screens to perform optical propagation simulations, it is very important to note that, unlike the three dimension $\kappa$-space integrand in (2-13), the contributions of the integrand in equation (2-15) grow without bound as the normalized wavenumber approaches zero. Additionally, as the spectral power law, α, approaches 4, more and more of the integrand's total

contribution to structure is attributable to low wavenumber spectral components. This implies that for non-Kolmogorov turbulence, higher α's will require more care in modeling low frequency components, and lower α's may be modeled with relaxed simulation constraints relative to Kolmogorov turbulence.

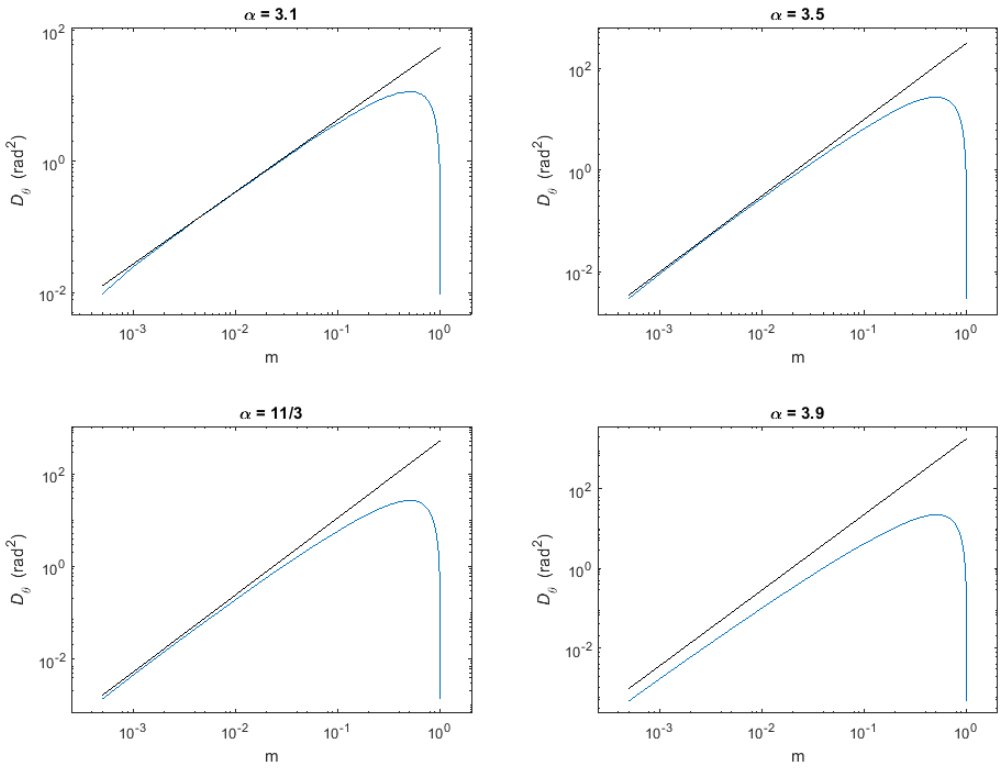


**Figure 2-3:** Demonstration of the traditional FFT phase screen method's observed structure function's agreement with theory degrading as the three dimensional spectral power law, $\boldsymbol{\alpha}$, increases.

The above point is best demonstrated by investigating the accuracy of the simulated structure function over many trials vs the desired theory for the phase screen structure function. Using the traditional FFT-based method of Fleck, Figure 2-3 demonstrates how the phase screen structure function diverges from theory as

more and more of the total spectral energy becomes concentrated at low spatial frequencies with increasing $\alpha$. Sections to follow will expand upon the relationship between low frequency optical turbulence spectral energy and convergence with theory in phase screen modeling.

## 2.4: Randomized FFT-based Spectral Sampling, Core Algorithm

Traditional phase screen simulations using square grids [33, 40, 41, 52, 53] approximate the continuous energy spectrum as discrete, and generate complex screens as per (2-1). Equation (2-1) represents a Fourier series using elements that are all harmonic across the spatial domain, creating screens that are periodic [52]. Investigating the effect the $\tilde{c}(0,0)$ term has on the summation in (2-1), we note that it results in only the addition of a constant phase, piston term across all of $\theta(m,n)$. This piston term does not contribute tip, tilt, focus, or defocus effects at any scale, or otherwise contribute to the behavior of the propagating field. Should $\tilde{c}(0,0)$ have a large enough value, a quantization error [61] will result. $\tilde{c}(0,0)$ is commonly set to zero in practice [33, 53], which avoids these issues.

In defining a new type of complex phase screen, $\theta_R$, we propose a more meaningful use of the point closest to the -space origin by virtue of:

$$\theta_R(m,n) = \sum_{k=-\frac{M}{2}}^{\frac{M}{2}-1} \sum_{l=-\frac{M}{2}}^{\frac{M}{2}-1} \tilde{c}\left(k\Delta\kappa_x + \delta\kappa_x, l\Delta\kappa_y + \delta\kappa_y\right) \cdot \exp\left[j\left(m\Delta x(k\Delta\kappa_x + \delta\kappa_x) + n\Delta y\left(l\Delta\kappa_y + \delta\kappa_y\right)\right)\right] \tag{2-16}$$

where $\delta\kappa_x$ and $\delta\kappa_y$ are random variables described by a uniform distribution bound by $\delta\kappa_x = \Delta\kappa_x/2$ and $\delta\kappa_y = \Delta\kappa_y/2$, respectively. This offsets the lowest wavenumber grid point away from the origin, along with also translating the rest of the sampling grid in the frequency domain. By allowing $\tilde{c}\left(k\Delta\kappa_x + \delta\kappa_x, l\Delta\kappa_y + \delta\kappa_y\right)$ to define the elements of a matrix, $\tilde{\mathbf{c}}_{kl,R}$, we find that Equation (2-16) is implementable via inverse FFT as per:

$$\mathbf{c}_{mn,R} = M^2 \cdot IFFT_2\left[\tilde{\mathbf{c}}_{jk,R}\right] \tag{2-17}$$

$$\theta_R(m,n) = \exp\left[j\left(m\Delta x\delta\kappa_x + m\Delta y\delta\kappa_y\right)\right] \cdot \mathbf{c}_{mn,R} \tag{2-18}$$

We note that the FFT can be used in place of the IFFT in Equation (2-17) by appropriate conditioning of the $\tilde{\mathbf{c}}_{kl,R}$ matrix.

Figure 2-4 juxtaposes the sampling methods discussed, where the convention of setting $\tilde{c}(0,0)$ to zero is reflected by the lack of a traditional spectral sampling grid point at the origin. $\theta_R(m,n)$ represents a single complex-number-valued phase screen, with the real and imaginary parts therein defining a pair of real-number-valued phase screens. Simulated atmospheric turbulence distortion is applied via multiplication of our complex propagating beam or wave by

$\exp[j \cdot Re(\theta_R(m,n))]$ or $\exp[j \cdot Im(\theta_R(m,n))]$, where the $Re$ and $Im$ functions represent taking the real and imaginary parts of an array, respectively.

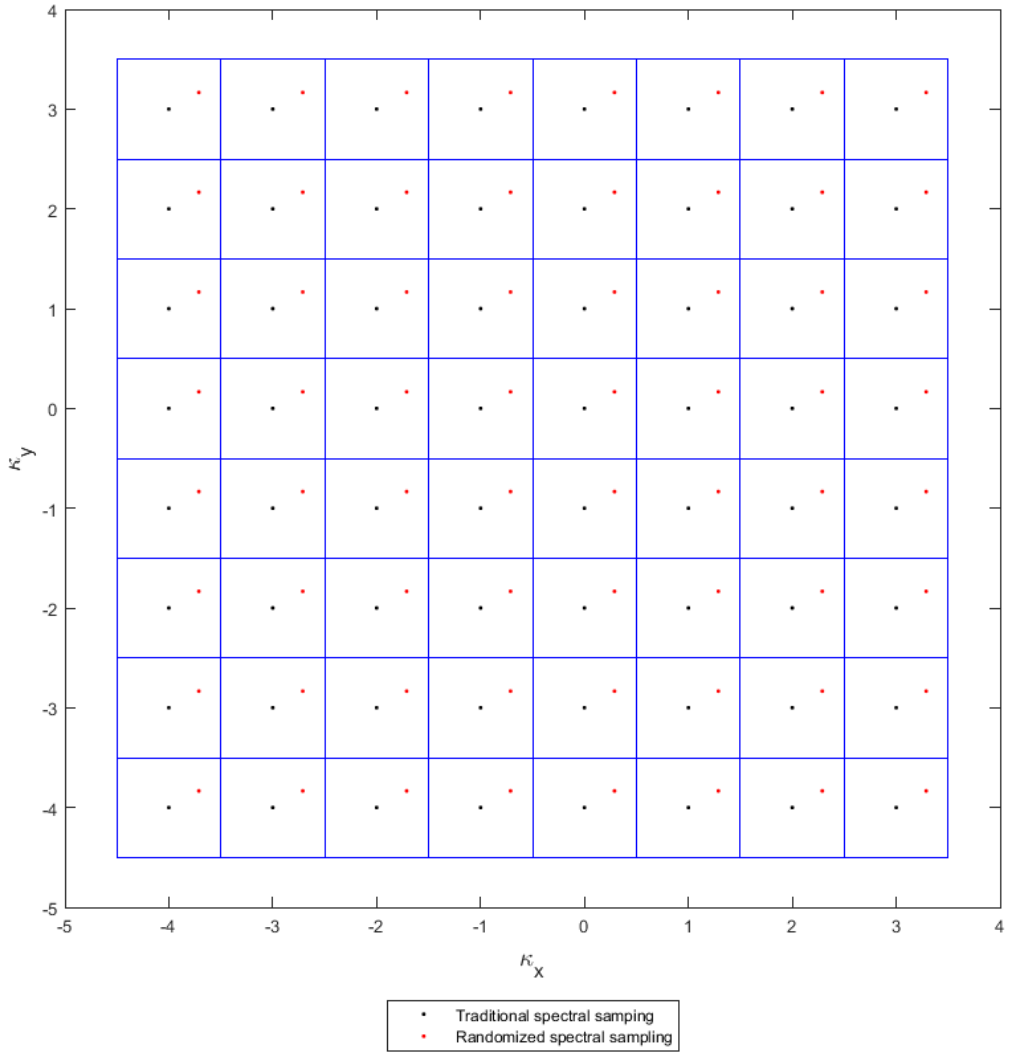


**Figure 2-4:** Example $\boldsymbol{\kappa}$-space grid partitioning and sampling showing traditional spectral sampling approach versus randomized spectral sampling approach. Black dots represent traditional sampling points, red dots represent one realization of the randomized sampling approach, and the blue grid lines demarcate the sampling boundaries for the randomized method.

$\theta_R(m,n)$ and the real-valued phase screens it produces no longer exhibit periodicity, and will have domain-wide low spatial-frequency distortions.

Additionally, we find the increase in computational delays associated with the use of the algorithm given in Equation (2-16) relative to Equation (2-1), in the context of split-step wave optics simulations, to be only 25.4% – 28.5% for grid sizes between $512 \times 512$ and $2048 \times 2048$. The phase screens shown in Figure 2-5 were generated using the Kolmogorov spectrum ($\alpha = 11/3$). Note that tip and tilt components can be seen across the *x*- and *y*-axes, respectively, in the screen shown in Figure 2-5c. Additionally, Figure 2-5a displays periodicity [52], in that should one circularly shift [61] the phase screen in either or both directions, no sharp discontinuities would be apparent within the boundaries of the screen. To help visualize this, we have added Figure 2-5b and Figure 2-5d to illustrate the presence and lack of periodicity resulting from the relevant algorithms, respectively.

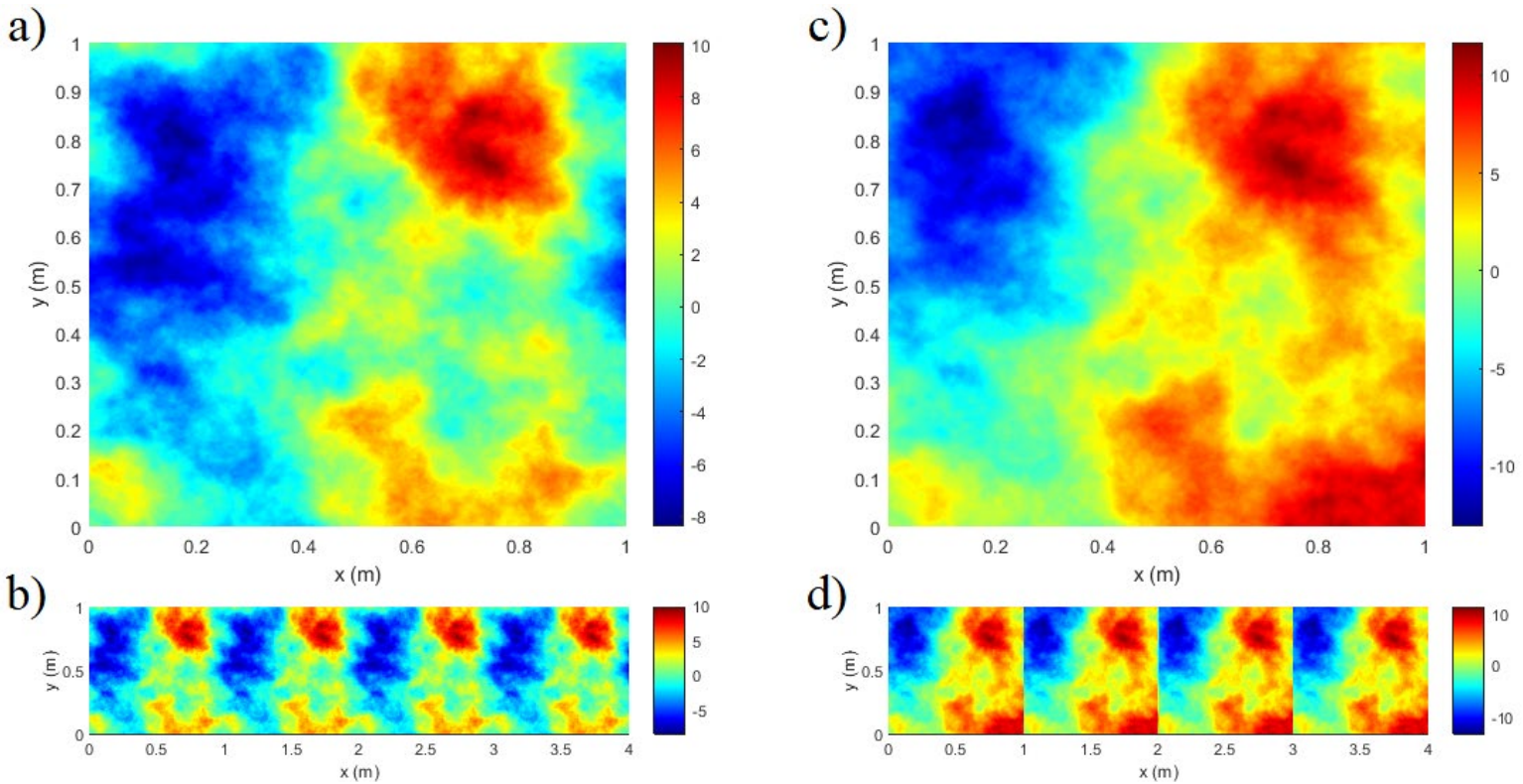


**Figure 2-5:** a) Phase screen produced using traditional FFT-based algorithm on a 1024×1024 grid; b) same phase screen as previous, repeated four times and placed adjacent to itself in order to illustrate the periodicity associated with traditional FFT-based screens; c) phase screen produced using modified FFT-based algorithm on a 1024×1024 grid; d) same phase screen as directly previous, repeated four times and placed adjacent to itself in order to illustrate the lack of periodicity associated the modified randomized FFT-based algorithm. The colors shown denote the phase shift of the screen in radians on the simulated propagating wave, as per the colorbar.

2.5: Core Algorithm Results for Anisotropic, non-Kolmogorov Spectral Models

To assess the accuracy of the revised method, we must designate our metrics of interest. We had previously defined the refractive index three-dimensional structure function, $D_n(\vec{r})$, via the spectral model of interest in Equation (1-3). The structure function we are interested in, however, is that of an atmospheric phase screen that approximates the cumulative effects of optical propagation through a finite propagation distance, $\Delta z$. By substituting Equation (2-15) into Equation (2-14), we are able to produce an equation for the ideal theoretical phase screen structure function as per [66]:

$$D_\theta(x,y) =$$

$$\Delta z A(\alpha) C_n^2 2^{4-\alpha} \pi^3 k_0^2 \sec\left[\frac{(\alpha-3)\pi}{2}\right]\left[\Gamma\left(\frac{\alpha}{2}\right)\right]^{-2}\left(\sqrt{\frac{x^2}{{\mu_x}^2}+\frac{y^2}{{\mu_y}^2}}\right)^{\alpha-2} \quad (2\text{-}19)$$

It is well documented that aliasing effects associated with the FFT-based propagation step of the split-step algorithm make parts of the simulation domain unusable [33, 40, 67, 68]. For this reason, a region of interest must be defined, which drives properties of the simulation. Number of grid points, simulated resolution, as well as the propagation distance between screens must be chosen carefully [33]. This requires consideration of many factors, including wavelength, coherence lengths, aperture sizes, etc. As a practical matter, many studies explicitly dedicate half of the *x*- and *y*-domains of simulation as guard bands to protect against

edge effect aliasing [69, 70]. Additionally, the requirement of grid sizes greater than or equal to twice the size of the limiting apertures (or regions of interest) is explicit in some analyses of simulated propagation using changes of scale between the source and observation planes [67, 68]. In our own simulations of Gaussian beam propagation [57, 63, 71], we typically constrain the beam diameter to half the domain of simulation in each *x*- and *y*-direction in order to avoid edge aliasing effects. In order to present our results in a simple fashion, we assume that most users would have a region of interest defined by approximately this inner portion of the simulation domain.

Defining the measured *x*-direction structure function along the $M/2$th row from the $M/4$th point to the $M/4 + m$th point as $D_x(m\Delta x)$, and *y*-direction structure function along the $M/2$th column for its corresponding points as $D_y(n\Delta y)$, we can define our percent root mean square (RMS) error metric, $\mathcal{E}_{M/2}$, in terms of the $D_\theta$ defined by Equation (2-32) via the equations:

$$\mathcal{E}_{M/2,x} = \sqrt{\frac{2}{M}\sum_{m=1}^{M/2}\left[\frac{D_x(m\Delta x) - D_\theta(m\Delta x)}{D_\theta(m\Delta x)}\right]^2} \tag{2-20}$$

$$\mathcal{E}_{M/2,y} = \sqrt{\frac{2}{M}\sum_{n=1}^{M/2}\left[\frac{D_y(n\Delta y) - D_\theta(n\Delta y)}{D_\theta(n\Delta y)}\right]^2} \tag{2-21}$$

$$\mathcal{E}_{M/2} = 100\% \times \frac{\mathcal{E}_{M/2,x} + \mathcal{E}_{M/2,y}}{2} \tag{2-22}$$

It should also be noted that as part of this study, the diagonal direction structure function was also assessed, with similar results. However, because the grid diagonals are not orthogonal to the *x*- and *y*- directions, those metrics are not included in our overall statistics as they are not independent.

We have found that for the range of outer scale values from one to 1000 times the domain of simulation, the RMS error as a percent assessed over half the simulation domain is constrained to less than 4%. More precisely, errors observed over the range $1 \leq L_0/(M\Delta x) \leq 10^3$ range from 0.34% to 3.79%. For the non-randomized grid, errors range from 2.57% to 61.51% over the same region.

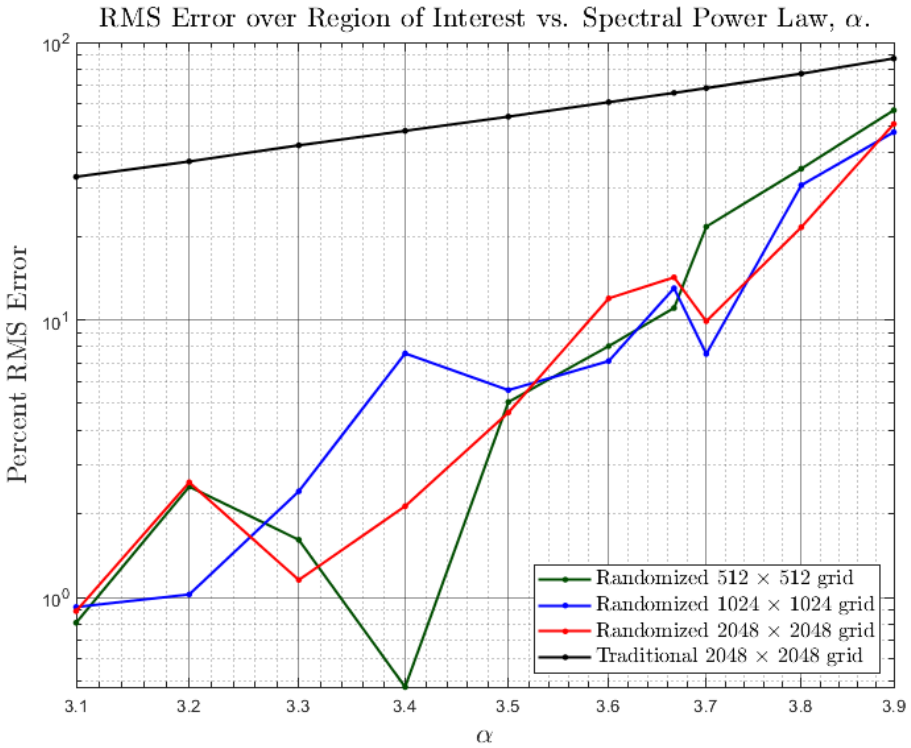


**Figure 2-6:** RMS error as a percent relative to theory over 50,000 phase screen trials for the simulated domain region of interest as parameterized by the three dimensional

spectral power law, $\boldsymbol{\alpha}$. 512 × 512, 1024 × 1024, 2048 × 2048 grid results are shown for randomized method. For the traditional method, the 2048 × 2048 grid is shown. Other grid sizes are not shown for the traditional method because the results appear to completely overlap at this scale.

Figure 2-6 displays the Monte Carlo simulation results over 25,000 complex phase screens. All data in this study were collected using MATLAB. Because each complex screen contains a real and imaginary component, and structure function is computed over orthogonal *x*- and *y*-directions, this simulation set contains 100,000 independent samples per point. Results are not shown for $512 \times 512$ or $1024 \times 1024$ traditional grids due to overlap of the plotted results, i.e., the results are largely indiscernible from the $2048 \times 2048$ traditional grid results. Additionally, in order to impress a sense of proportionality upon the reader, we have included Figure 2-7, which is parameterized by the grid size, outer scale, inner scale, and effective coherence lengths, $\rho_{0,x}$ and $\rho_{0,y}$, given for non-Kolmogorv turbulence as [59]:

$$\rho_{0,x} = \mu_x \left[ A(\alpha) \tilde{C}_n^2 k_0^2 z \frac{-2^{3-\alpha} \pi^2 \Gamma\left(1 - \frac{\alpha}{2}\right)}{(\alpha - 1)\Gamma\left(\frac{\alpha}{2}\right)} \right]^{\frac{1}{2-\alpha}}$$
$$\rho_{0,y} = \mu_y \left[ A(\alpha) \tilde{C}_n^2 k_0^2 z \frac{-2^{3-\alpha} \pi^2 \Gamma\left(1 - \frac{\alpha}{2}\right)}{(\alpha - 1)\Gamma\left(\frac{\alpha}{2}\right)} \right]^{\frac{1}{2-\alpha}} \quad (2\text{-}23)$$

On the logarithmic scale, the randomized method follows the theoretical structure function very closely, relative to the traditional method for $\alpha$'s at or below the Kolmogorov turbulence power law, 11/3.

In general we note that for these $\alpha$'s the RMS error over the region of interest using the randomized method appears to be constrained below 15%, however for the traditional method errors range from 32.73% - 65.76% over this range. In general, lower $\alpha$'s perform closer to theory for either method. In later sections we shall verify that this is because more and more of the spectral energy is concentrated around the origin in frequency space for higher $\alpha$'s, which will require better resolution sampling via use of a non-uniform Fourier series around the origin in $\kappa$-space to complement the uniformly sampled IFFT.

During the peer review process which led to the publication of the new method, it became apparent that reviewers had concerns regarding the probability distribution of absolute phase produced by the screens. For small variations in temperature, the relationship between refractive index and temperature is approximately linear [see Equation (1-12)], and as such it is seen as a desirable property that the phase of the screens be approximately distributed according to a Gaussian distribution. Confirming the reviewers' concerns, we have found that the randomized sampling technique produces approximately log-normally distributed statistics, as displayed in Figure 2-8. Although a log-normal characteristic of absolute phase may seem undesirable, we do not believe this to be a significant issue with the randomized method, as the phase difference histograms maintain approximately zero mean Gaussian distributed characteristics. Results from the trials for several spectral power laws are shown in Figure 2-7. We note that the

relative phase statistics in the x and y directions were combined to create the plots of Figure 2-8. Additionally, we remind the reader that the assumption that only relative phase statistics meaningfully affect the wave statistics of interest, as absolute phase associated with each screen only affect the constant phase rotation of the wave.

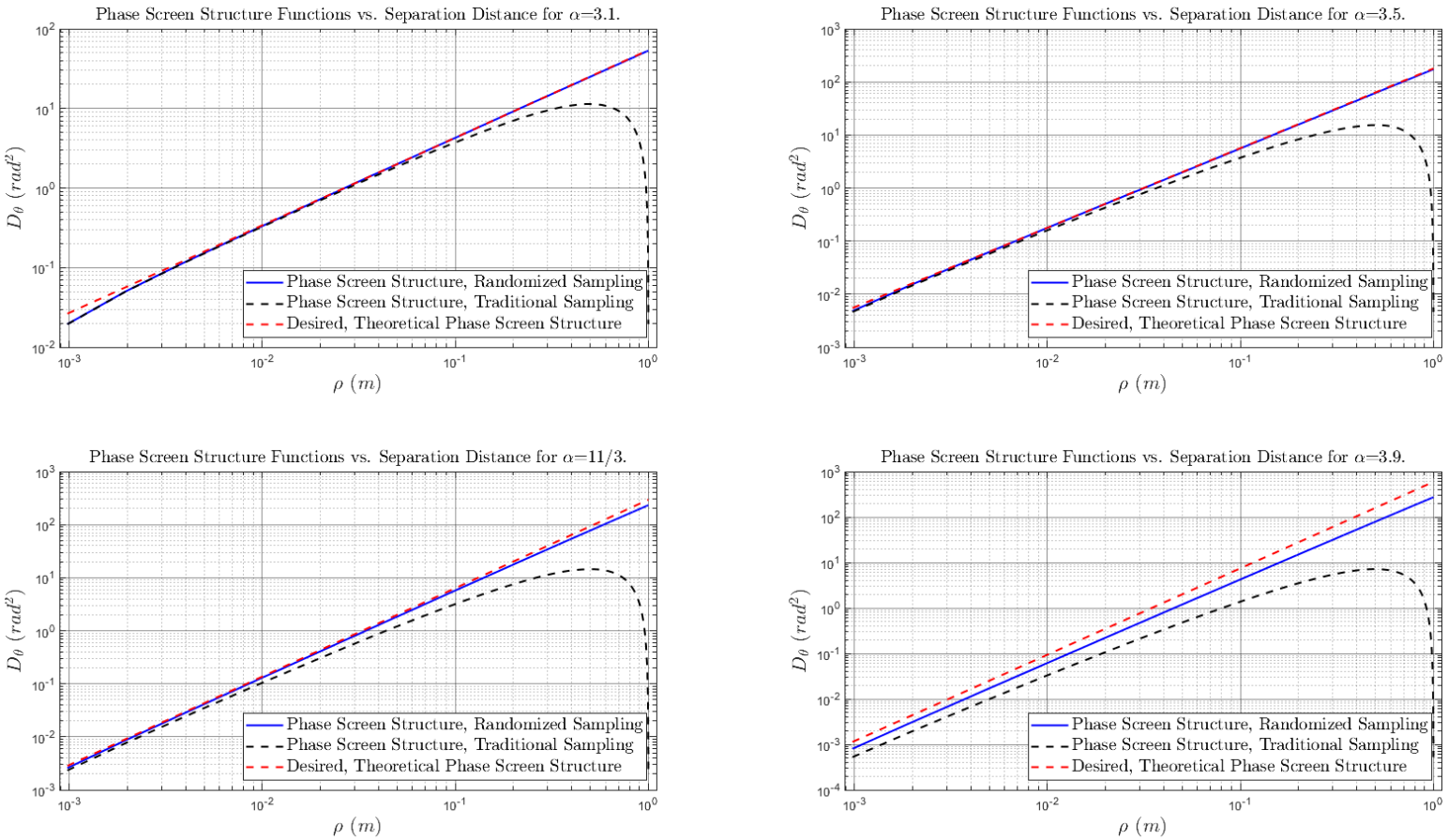


**Figure 2-7:** Phase screen structure function produced by the randomized and traditional methods compared to theory over *x*- and *y*-directions over 25,000 phase screen for several values of the three dimensional spectral power law, $\alpha$, 1024 × 1024 grid results. The coherence length used to produce the screens was $\rho_{0,x} = \rho_{0,y} = 0.05$ cm for all $\alpha$'s.

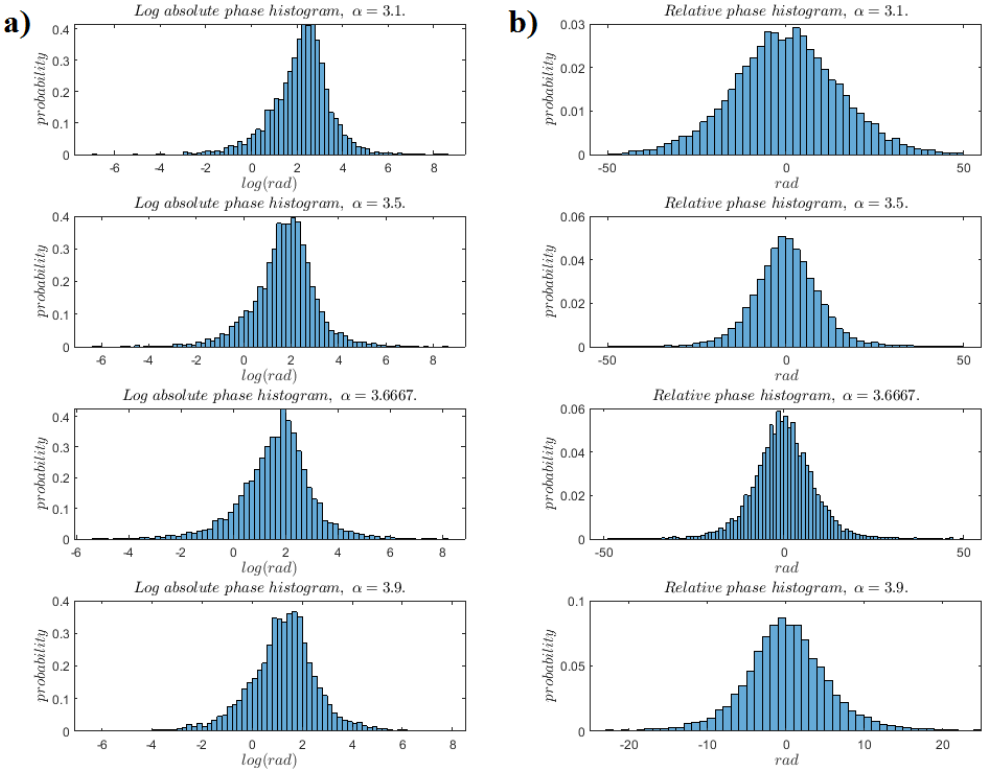


**Figure 2-8:** Histogram plots of probability density for: a) natural logarithm of the magnitude of phase at phase screen center using the randomized method for various values of the three dimension spectral power law, $\alpha$; b) relative phase difference across the region of interest using the randomized method for various values of the three dimension spectral power law, $\alpha$. For each subplot, the probability densities were collected over 5,000 phase screens using a 2048 × 2048 grid created using the randomized method.

In order to demonstrate that the refinement in structure function accuracy using the randomized method reliably improves statistics of propagating light, we have performed wave optics simulations quantifying the angle of arrival (AoA) fluctuations of plane waves propagating through optical turbulence using both our randomized method and the traditional FFT-based method. Closely following the methodology used by Voelz, et al. [60], we have simulated 500 nm plane waves

propagating through multiple phase screens, using a number of Rytov variances, and collected the aperture averaged AoA's for each trial by focusing the light collected over varying aperture sizes and examining the location of the centroid in the focal plane. We have deviated from Voelz's method, however, in that instead of fixing the relationship between the propagating plane wave's spatial domain size and aperture diameter, $D$, such that $D/(M\Delta x) = .4$, we have always chosen a spatial domain of $M\Delta x = 1$ m prior to aperturing. Once the propagating light reaches the aperture plane, a focusing transmittance function [31] is applied, followed by circular aperture functions of several diameters ranging from .5 cm to 50 cm. The resulting waves from each aperture function are separately propagated to the focal plane using the angular spectrum propagation method discussed by Schmidt [33] in order to allow for differing spatial domain sizes between the aperture and focal planes.

In Voelz's method, a constraint on the number of phase screens, $N_s$, as well as propagation distance associated with each screen, i.e. $\Delta z = z/N_s$, is that the associated Rytov variance associated with each phase screen application and propagation remains approximated by weak fluctuation regime statistics. For our application, this boils down to the following constraint:

$$\tilde{\sigma}_R^2\left(\Delta z, \alpha, \mu_x, \mu_y\right) \leq 0.1 \tag{2-24}$$

Analyzing (1-57) with $z = \Delta z N_s$ and $\mu_x = \mu_y = 1$:

$$\Delta z = \frac{z}{N_s} \leq \left[\frac{-20 \cdot \Gamma(\alpha - 1)}{\alpha} \Gamma\left(1 - \frac{\alpha}{2}\right) \sin\left(\frac{\pi\alpha}{4}\right) \cos\left(\frac{\pi\alpha}{2}\right) \tilde{C}_n{}^2 k_0{}^{3-\frac{\alpha}{2}}\right]^{-\frac{2}{\alpha}} \qquad (2\text{-}25)$$

Alternatively, because we have function handles to calculate the generalized Rytov variance, we choose to actually use the equivalent constraint:

$$N_s = \frac{z}{\Delta z} \geq ceil\left(\left[10 \cdot \tilde{\sigma}_R^2(z, \alpha, \mu_x, \mu_y)\right]^{\frac{2}{\alpha}}\right) \qquad (2\text{-}26)$$

where the *ceil* operator reflects rounding up to the nearest integer. If one wishes to verify this is correct, note that insertion of $\Delta z \leq z \cdot \left[10 \cdot \tilde{\sigma}_R^2(z, \alpha, \mu_x, \mu_y)\right]^{-\frac{2}{\alpha}}$ for $L$ in Equation (1-57) ensures that $\tilde{\sigma}_R^2(L = \Delta z, \alpha, \mu_x, \mu_y) \leq 10^{-1}$. For the range $3.1 \leq \alpha \leq 3.9$, $\alpha = 3.9$ requires the most screens to meet this constraint, at 20. Therefore, we have elected to use 20 screens for all simulations in this set. We note that this range of $\alpha$'s was chosen because for any non-zero $\tilde{C}_n^2$ the weak fluctuation theory wave structure function, which has values identical to those given in Equation (1-14), only converges to a non-zero, non-negative values for $\alpha = (0,2)$ and (2n - 1, 2n), with n any integer greater than 1. Given that turbulence has been famously observed displaying a three dimensional structure function with power law $\alpha - 3 \approx 11/3$, which is justified by Kolmogorov's theoretical work [2, 3], for these reasons alpha's below or equal to 3 and above or equal to 4 are ruled out as unphysical.

A theoretical expression for the variance of AoA for apertured plane waves for isotropic turbulence is given by Cheon [72] as:

$$\langle \bar{\theta}^2 \rangle = \pi^2 L \int_0^\infty \kappa^3 \Phi_n(\kappa) \left[ 1 + \frac{2\pi}{(\kappa f)^2} \sin\left( \frac{(\kappa f)^2}{2\pi} \right) \right] A_f\left( \frac{D\kappa}{2} \right) d\kappa \quad (2\text{-}27)$$

where $f = \sqrt{\lambda L}$ is the Fresnel length, and $A_f(x) = \left( \frac{2J_1(x)}{x} \right)^2$ is the Airy function with $J_1$ denoting the first-order Bessel function of the first kind. We note that we believe there may have been a typo in [72], and have added a factor of $\pi$ to Equation (5) in the reference in order to make the equation compatible with later derivations therein. This theoretical metric has been compared to the results of the wave optics simulations in Figure 2-9. In general, we find a marked improvement of results relative to theory when the randomized method is in use for all Rytov variances and aperture sizes.

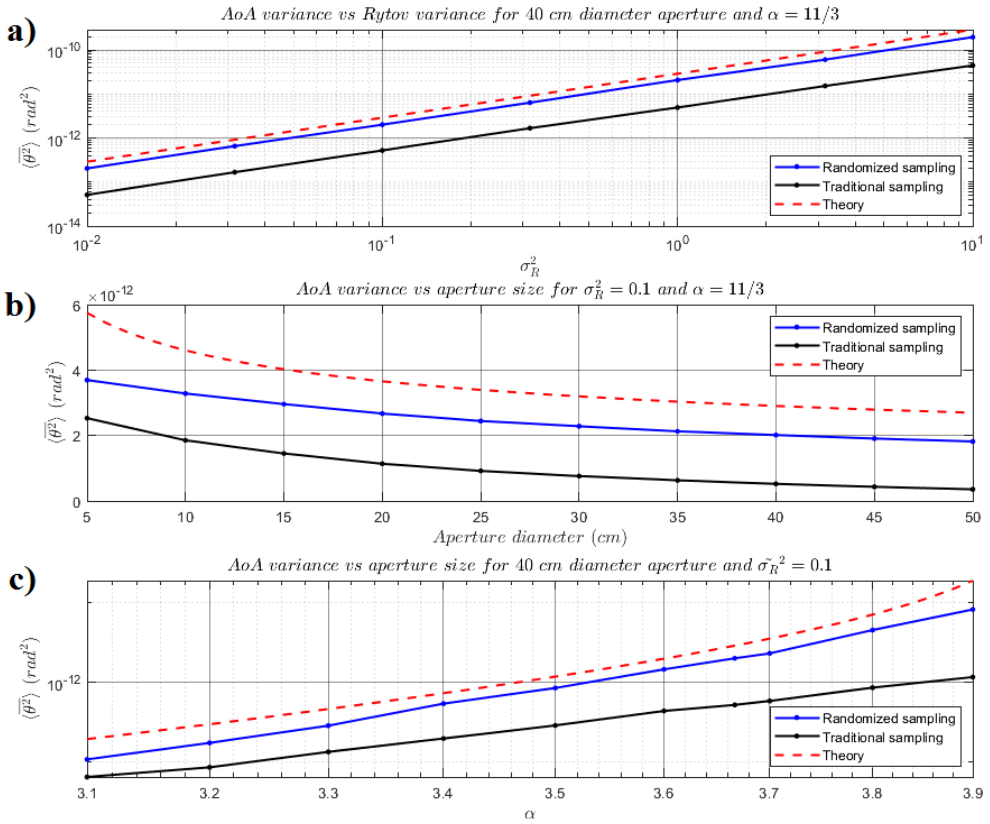


**Figure 2-9:** a) AoA variance averaged over a 40 cm diameter aperture of a plane wave propagating through Kolmogorov turbulence plotted as a function of Rytov variance for wave optics simulations using the randomized method and the traditional method compared to theory for Rytov variance 0.1; b) aperture averaged AoA variance of a plane wave propagating through turbulence plotted as a function of aperture diameter for wave optics simulations using the randomized method and the traditional method compared to theory Kolmogorov spectrum and Rytov variance 0.1; c) aperture averaged AoA variance of a plane wave propagating through turbulence plotted as a function of the three dimensional spectral power law for wave optics simulations using the randomized method and the traditional method compared to theory for Rytov variance 0.1 and aperture size 40 cm. All simulations were performed using a 1024 × 1024 grid and 20 equally spaced phase screens over a 2 km propagation distance.

To summarize the results in this section, we have noted a marked improvement in the results relative to theory for both raw structure function measurements and wave optics metrics. Though, the accuracy of our method still does not always converge closely with theory, especially for higher $\alpha$'s when

viewing the raw statistics. The wave optics simulations still show substantial disagreements across all alphas. Luckily, we are aware of methods to improve the accuracy of the traditional method, which we shall again modify and apply in later sections. Although originally conceived for application of non-Kolmogorov and anisotropic turbulence, our intuition is that when applied to other spectral models of interest, specifically ones which band limit the inertial range of turbulence using finite inner and outer scales, this method may perform better relative to theory and does not have complications associated with having infinite spectral energy. In the next section, we consider additional spectral models and demonstrate that our intuition is correct.

## 2.6: Core Algorithm Results for Bounded Spectral Models

The most widely used three-dimensional spectral model of atmospheric turbulence is derived from A. Kolmogorov's famous 2/3 law as [6, 9]:

$$\Phi_n(\vec{\kappa}) = A\left({}^{11}/_{3}\right) \cdot C_n^2 \cdot |\vec{\kappa}|^{-\frac{11}{3}} = 0.0330 \cdot C_n^2 \cdot |\vec{\kappa}|^{-\frac{11}{3}} \qquad (2\text{-}28)$$

This model is popular due to its simple formulation and approximate accuracy when the beam statistics of interest are within the inertial subrange of turbulence. However, this spectrum diverges at the $\kappa$-space origin leading to unphysical properties such as containing infinite energy, divergent covariances, lack of a viscosity-driven minimum feature size, and lack of a maximum feature size [9]. For these reasons, we refer to this type of spectral model as *unbounded*. As we alluded

to in the previous section and will demonstrate in the next section, additional modifications to the FFT-based algorithm may be required to accurately model unbounded spectral models using phase screens, as is the case for Kolmogorov turbulence.

We turn our attention to a practical atmospheric turbulence spectral model that accounts for inner scale, $l_0$, and outer scale, $L_0$, bounds on the inertial subrange, as well as intricacies of the experimentally observed energy spectra at higher spatial frequencies [26, 29, 73]. The modified atmospheric spectrum is given by Andrews [9, 74]:

$$\Phi_n(\kappa) = 0.0330 \cdot C_n^2 \cdot f_n\left(\frac{\kappa}{\kappa_l}\right) \cdot \frac{\exp(-\kappa^2/{\kappa_l}^2)}{(\kappa^2 + \kappa_0^2)^{11/6}} \tag{2-29}$$

where $\kappa_l = 3.3/l_0$, $\kappa_0 = 2\pi/L_0$, $\kappa = |\vec{\kappa}|$, and we define the function $f_n$ as:

$$f_n(x) = 1 + 1.802x - 0.254x^{7/6} \tag{2-30}$$

The $f_n$ function serves to implement a spectral rise at higher wave numbers observed by Hill [26], and which we note will have a marked effect on the scintillation index of the propagating beam [9]. This spectral model can be thought of as a modification to the von Kármán Spectrum [9], which includes the *Hill Bump*. As this spectral model does not present the same complications as that of Equation (2-28), we refer to this as a *bounded* spectral model.

To assess the accuracy of the revised method, we again must designate our metrics of interest. We, again, assume that the phase screen structure function is of

primary importance and will compare simulation results with the theoretical ideal, $D_\theta(\vec{\rho})$. $D_\theta(\vec{\rho})$ is defined by the two-dimensional integral over all $\vec{\kappa}_\rho = \kappa_x \hat{e}_x + \kappa_y \hat{e}_y$ as per [53]:

$$D_\theta(\vec{\rho}) = 4\pi k_0^2 \Delta z \iint_{-\infty}^{\infty} \Phi_n(\vec{\kappa}_\rho)\left[1 - \cos(\vec{\rho} \cdot \vec{\kappa}_\rho)\right] d^2\vec{\kappa}_\rho \qquad (2\text{-}31)$$

For the modified atmospheric spectrum, though we are aware of closed-form approximations of turbulent structure functions for plane waves applicable to our analysis [75], we have instead developed our theoretical structure function via numerical integration of the equivalent form for isotropic turbulence:

$$D_\theta(\rho) = 8\pi^2 k_0^2 \Delta z \int_{-\infty}^{\infty} \kappa_\rho \Phi_n(\vec{\kappa}_\rho)\left[1 - J_0(\rho\kappa_\rho)\right] d\kappa_\rho \qquad (2\text{-}32)$$

where $\rho = |\vec{\rho}|$, $\kappa_\rho = \left|\vec{\kappa}_\rho\right|$, and $J_0$ denotes the zeroth-order Bessel function of the first kind. We will again be primarily interested in the RMS error of different approaches over the region of interest (the inner quarter by area of the simulation domain) as defined by Equations (1-20) - (1-22). It should also be noted that as part of this study, the diagonal direction structure function was also assessed, with similar results. However, because the grid diagonals are not orthogonal to the x and y directions, those metrics are not included in our overall statistics.

We have found that for the range of outer scale values from one to 1,000 times the domain of simulation, the RMS error as a percent assessed over half the simulation domain is constrained to less than 4%. More precisely, errors observed

over the range $1 \leq L_0/(M\Delta x) \leq 10^3$ range from 0.34% to 3.79%. For the non-randomized grid, errors range from 2.57% to 61.51% over the same region. Figure 2-11 displays the Monte Carlo simulation results over 25,000 complex phase screens. All data in this study were collected using MATLAB. Because each complex screen contains a real and imaginary component, and structure function is computed over orthogonal x and y directions, this simulation set contains 100,000 independent samples per point. Results are not shown for $512 \times 512$ or $1024 \times 1024$ traditional grids due to overlap of the plotted results, i.e., the results are largely indiscernible from the $2048 \times 2048$ traditional grid results. Additionally, in order to impress a sense of proportionality upon the reader, we have included Figure 2-11, which is parameterized by the grid size, outer scale, inner scale, and effective coherence length, $\rho_0$, given for isotropic turbulence and Kolmogorov's 11/3$^{rds}$ spectral power laws as [33]:

$$\rho_0 = (1.46k_0^2 \Delta z C_n^2)^{-3/5} \tag{2-33}$$

On the logarithmic scale, the randomized method follows the theoretical structure function very closely relative to the traditional method as displayed in Figure 2-10.

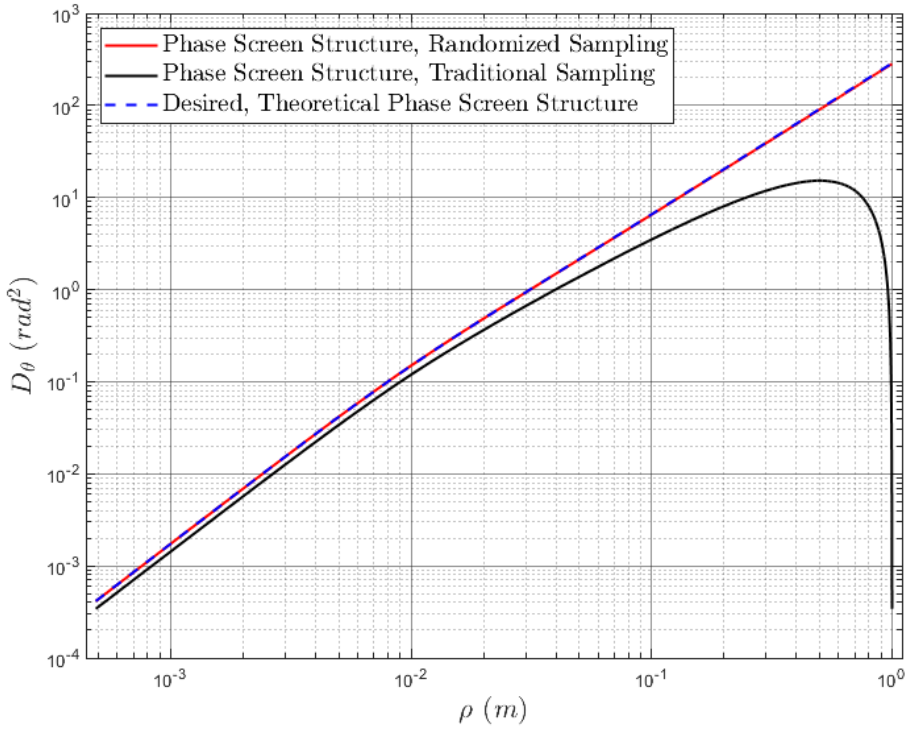


**Figure 2-10:** Comparison of phase screen structure function versus theory using 2048 × 2048 grid, inner scale 1 cm, outer scale 100 km, and effective coherence length of $\rho_0$ = 5 cm.

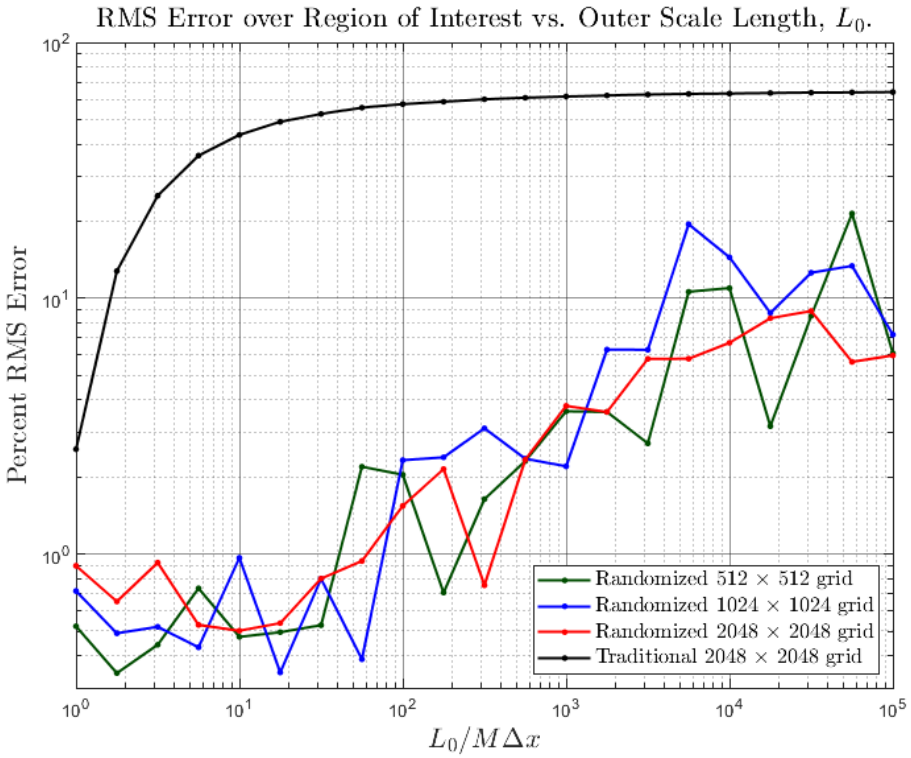


**Figure 2-11:** RMS error as a percent relative to theory over 50,000 phase screen trials for the simulated domain region of interest as parameterized by the three dimensional spectral power law, $\alpha$. 512 × 512, 1024 × 1024, 2048 × 2048 grid results are shown for randomized method. The outer scale has been normalized by the domain width, $M\Delta x$ (m), to make the results applicable for any domain size. For the traditional method only the 2048 × 2048 grid is shown due to significant overlap of the RMS error metric.

Histogram analysis of the phase screen statistics has been performed in a manner similar to the previous section based on peer reviewer comments. The histograms of results showed some interesting characteristics of the collected samples. For small $L_0$'s, the probability density of the absolute phase was clearly Gaussian in nature; however, as $L_0$ was increased, this property quickly faded. Analysis of the natural logarithm of $|\theta_R(M/2, M/2)|$ showed a clear log-normal characteristic as $L_0$ was increased beyond $M\Delta x = 10$ m. As discussed in the

previous section, though a log-normal characteristic of absolute phase may seem undesirable we do not believe this to be a significant issue with the randomized method as the phase difference histograms maintain approximately zero mean Gaussian distributed characteristics. Results for several $L_0$'s are shown in Fig. 6. We note that the relative phase statistics in the *x*- and *y*-directions were combined to create the plots on the right-hand side of Figure 2-12. Repeating this exercise over several different grid sizes, as well as different separations over which the phase differences were measured, yielded qualitatively similar results. Since the statistical fluctuations of interest (e.g., scintillation, beam wander, etc.) of the light undergoing atmospheric turbulence distortion are induced by relative phase, we do not believe that the log-normal characteristic of the absolute phase measured will harm the overall statistical properties of the simulated light, provided the relative phase maintains zero mean Gaussian characteristics.

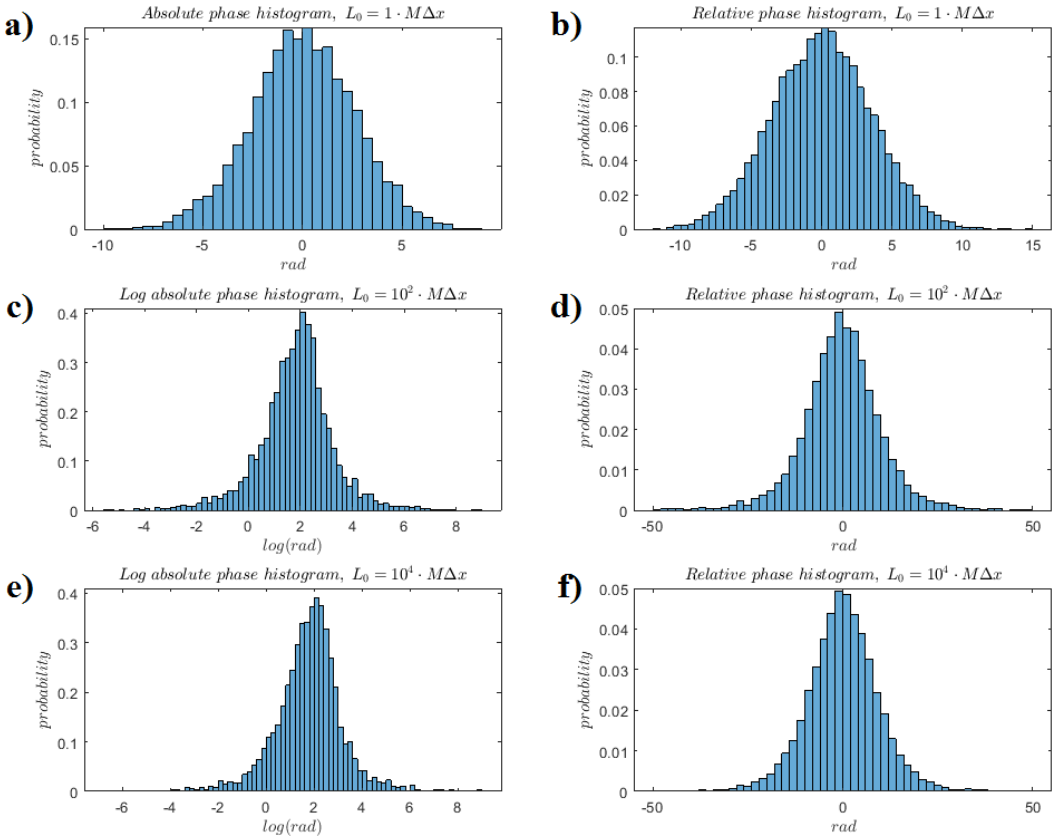


**Figure 2-12:** Histogram plots of probability density for: a) absolute phase using outer scale $\boldsymbol{L_0 = 1 \cdot M\Delta x}$; b) relative phase over region of interest using outer scale $\boldsymbol{L_0 = 1 \cdot M\Delta x}$; c) natural logarithm of the magnitude of absolute phase using outer scale $\boldsymbol{L_0 = 10^2 \cdot M\Delta x}$; d) relative phase over region of interest using outer scale $\boldsymbol{L_0 = 10^2 \cdot M\Delta x}$; e) natural logarithm of the magnitude of absolute phase using outer scale $\boldsymbol{L_0 = 10^4 \cdot M\Delta x}$; f ) relative phase over region of interest using outer scale $\boldsymbol{L_0 = 10^4 \cdot M\Delta x}$. For each subplot, the probability densities collected over 5000 phase screens using a 2048 × 2048 grid created using the randomized algorithm and modified spectrum.

In order to demonstrate efficacy of the revised method in reliably improving statistics of propagating light, we have performed wave optics simulations quantifying the AoA fluctuations of plane waves propagating through optical turbulence using both our randomized method and the traditional FFT-based method in a manor analogous to what was done in the previous section, but

parametrized by outer scale length as opposed to spectral power law, $\alpha$, which is fixed at 11/3 for the results in this section. For all simulation results and theoretical curves shown, the modified spectrum with inner scale $l_0 = 1$ cm and outer scale $L_0$ = 100 m was used. A 2 km propagation distance and Rytov variances between .001 and 10 were used. In order for the Rytov variance associated with each $\Delta z$ propagation and phase screen application to meet weak fluctuation regime criteria, 13 phase screens were used for each simulation run as an outcome of using Equation (2-26) and Rytov variance 10, i.e. $N_s = ceil\left([10 \cdot 10]^{\frac{6}{11}}\right) = 13$.

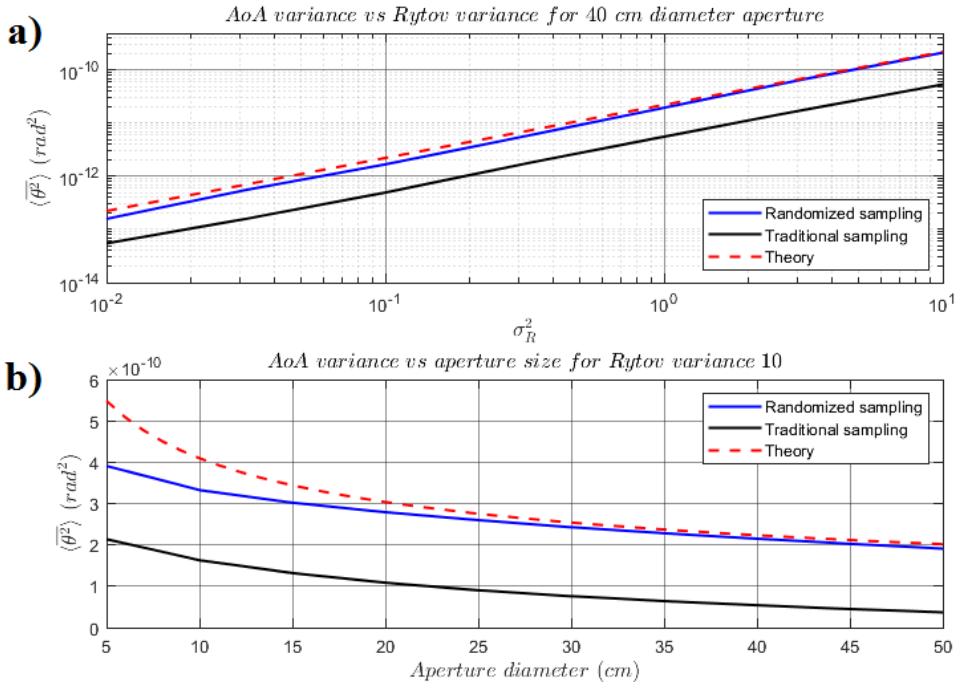


**Figure 2-13:** a) AoA variance averaged over a 40 cm diameter aperture of a plane wave propagating through turbulence plotted as a function of Rytov variance for wave optics simulations using the randomized method and the traditional method compared to theory; b) aperture averaged AoA variance of a plane wave propagating through turbulence plotted as a function of aperture diameter for wave optics simulations using the randomized method and the traditional method compared to theory. All simulations were

performed using a 1024 × 1024 grid and 13 equally spaced phase screens over a 2 km propagation distance.

## 2.7: Hybrid Algorithm Including Subharmonics

The modified algorithm discussed in previous sections was first investigated with regards to unbounded, anisotropic, non- Kolmogorov spectral models [63]. Therein it was discovered that for structure function power laws greater than the 2/3 of Kolmogorov, the randomized algorithm alone was not sufficient to ensure accurate statistics of observed simulated structure functions. For this reason, we have developed an algorithm utilizing both FFT-based frequency sampling randomization and subharmonic frequency sampling randomization. We define the following:

$$\theta_R(m,n) = \sum_{k,l=-\frac{M}{2}}^{\frac{M}{2}-1} (1-\delta[k,l]) \cdot \tilde{c}\left(k\Delta\kappa_x + \delta\kappa_x, l\Delta\kappa_y + \delta\kappa_y\right) \cdot exp\left(j\left[m\Delta x(k\Delta\kappa_x + \delta\kappa_x) + n\Delta y\left(l\Delta\kappa_y + \delta\kappa_y\right)\right]\right) \tag{2-34}$$

$$\theta_{out}(m,n,p) = 3^{-p} \sum_{k,l=-1}^{1} (1-\delta[k,l]) \cdot \tilde{c}\left(\frac{k\Delta\kappa_x + \delta\kappa_x}{3^p}, \frac{l\Delta\kappa_y + \delta\kappa_y}{3^p}\right) \cdot exp\left[j\left(m\Delta x\frac{k\Delta\kappa_x + \delta\kappa_x}{3^p} + n\Delta y\frac{l\Delta\kappa_y + \delta\kappa_y}{3^p}\right)\right] \tag{2-35}$$

$$\theta_{in}(m,n) = 3^{-N_p-1} \cdot \tilde{c}\left(\frac{k\Delta\kappa_x + \delta\kappa_x}{3^{N_p+1}}, \frac{l\Delta\kappa_y + \delta\kappa_y}{3^{N_p+1}}\right) \cdot exp\left[j\left(m\Delta x \frac{k\Delta\kappa_x + \delta\kappa_x}{3^{N_p+1}} + n\Delta y \frac{l\Delta\kappa_y + \delta\kappa_y}{3^{N_p+1}}\right)\right] \tag{2-36}$$

In Equation (2-36), $N_p$ is the number of subharmonic constellations of sampled frequencies (groups of eight subharmonics chosen from common subgrid boundaries), and $\delta[k,l]$ is the two dimensional discrete Dirac delta function ($\delta[k,l] = 1$ for $k = l = 0$, otherwise $\delta[k,l] = 0$), which we use to ignore the DFT frequency domain origin and the central point of each constellation. It is very important to note that in Equations (2-35) and (2-36), we choose a different $\delta\kappa_x$, $\delta\kappa_y$ for each element of the summation (see Figure 2-14). That is, for any index (n, m) change in Equation (18) or (19), we choose a new $\delta\kappa_x$, $\delta\kappa_y$ according to a uniform distribution. This is not done for Equation (2-34), because it is implemented using an FFT.

The final *hybrid* phase screen, $\theta_H$, is given by:

$$\theta_H(m,n) = \theta_R(m,n) + \sum_{p=1}^{N_p} \theta_{out}(m,n,p) + \theta_{in}(m,n) \tag{2-37}$$

In Equation (2-37), the summation over $\theta_{out}$ represents the contributions of each of the $N_p$ subharmonic constellations to the phase screen, and $\theta_{in}$ in provides the final low-frequency contribution to the phase screen from a spectral sample closest to the origin in $\kappa$-space. The sampling approach described by Equation (2-37) is

shown in Figure 2-14 for $N_p = 1$. In Figure 2-14, the red dot closest to the origin represents the $\theta_{in}$ in spectral sample, and the red dots in the surrounding eight grid partitions represent the $\theta_{out}$ spectral samples associated with the subharmonic constellation. We have found by choosing the correct number of subharmonic constellations, $N_p$, Equation (2-37) yields very accurate results for any reasonable spectral model. We shall demonstrate results for both bounded and unbounded spectral models later in this section.

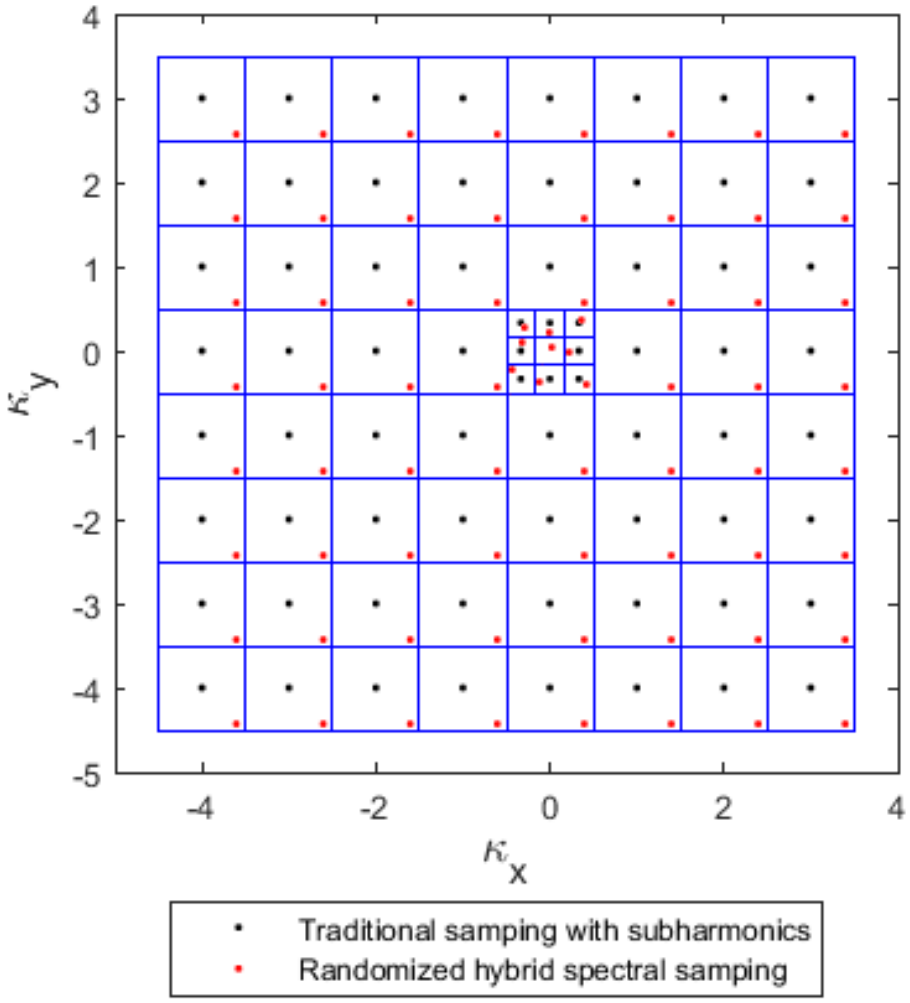


**Figure 2-14:** Example $\kappa$-space grid partitioning and sampling showing traditional subharmonic sampling approach versus hybrid randomized spectral sampling approach for $N_p = 1$. Black dots represent traditional sampling points (including subharmonic expansion), **red** dots represent one realization of the randomized sampling approach, and the **blue** grid lines demarcate the sampling boundaries for the randomized method.

2.8: Addition of White Noise to Phase Screens to Support Subresolution Inner Scales

Since the introduction of generalized spectral models by Kon [19], much theoretical work has gone into the study of wave propagation through anisotropic, non-Kolmogorov turbulence defined by unbounded refractive index spectra [22, 23, 59, 76, 77, 78, 79]. These spectral models are derived from the structure function of refractive index of the form:

$$D_n(x,y,z) = \tilde{C}_n^2 \left( \frac{x^2}{\mu_x^2} + \frac{y^2}{\mu_y^2} + z^2 \right)^{\frac{\alpha-3}{2}} \tag{2-38}$$

where $\mu_x$, $\mu_y$ are the anisotropy parameters in the $x$- and $y$-directions, respectively, is the three-dimensional spectral power law, and $\tilde{C}_n^2$ is the generalized refractive index structure function constant with units $m^{3-\alpha}$. Although occasionally studies state that this structure function model is valid only for $l_0 \ll \sqrt{x^2+y^2+z^2} \ll L_0$ [77], as applied to integrals for calculating second- and fourth-order beam statistics, the inner and outer scales appear as zero and infinity, respectively. In order for the phase structure function integral definitions of Equations (1-19), (2-4), and (2-5) to converge to positive quantities is typically limited to the range $3 < \alpha < 4$. Also note that for $\alpha = 11/3$ and $\mu_x = \mu_y = 1$, Equation (2-38) simplifies to the 2/3 law of Kolmogorov. It can be shown [22] that Equation (2-38) corresponds to a three-dimensional energy spectrum given by:

$$\Phi_n(\kappa_x, \kappa_y, \kappa_z) = \frac{\tilde{C}_n^{\,2} A(\alpha) \mu_x \mu_y}{(\mu_x^{\,2}\kappa_x^{\,2} + \mu_y^{\,2}\kappa_y^{\,2} + \kappa_z^{\,2})^{\alpha/2}} \tag{2-39}$$

These spectral models do not address practical matters of maximum feature sizes (outer scales) or Kolmogorov microscales (inner scales), where the internal subrange ends and dissipation is the primary form of energy transfer [80, 81]. However, these models are useful for studies of non-classical turbulence when the inertial subrange can be approximated as infinite. For these unbounded cases, great attention has so far been devoted to modeling low spatial frequency components. In order to explain why this is necessary, we note that insertion of the energy spectrum $\Phi_n(\kappa_x, \kappa_y, 0)$ given by Equation (2-39) into the structure function identity given in Equation (2-31) results in an integrand that diverges as the magnitude of $\vec{\kappa}_\rho = \kappa_x \hat{e}_x + \kappa_y \hat{e}_y$ approaches zero. For a more thorough explanation of issues involving use of spectral models that diverge at the zero-frequency point, please see [63].

Very little emphasis, however, has been placed on high frequency components outside of the simulated $\kappa$-space. As demonstrated in Figure 2-15 and Figure 2-16, this results in a *sag* of the phase screen structure function relative to theory over small distances. In order to explain why this sag occurs, we note that the DFT formation of the phase screen algorithm given by Equations (2-1), (2-16), and (2-34) includes spectral energy contributions only within its frequency domain sample space, which we later define explicitly as $K_{in}$. Spectral energy outside this

sample space, $K_{out}$, is not typically included in the discretized simulations, although the structure function integral definition given by Equation (2-4) includes spectral energy across all $\kappa$-space. We attempt to resolve this problem via addition of white noise to the screen, in order to simulate spectral energy not included in the $\kappa$-space sampling grid or subharmonic subgrids. Recalling the formation of the structure function in Equation (2-4), we calculate the variance of the white noise to be added to the screen as per the set of area integrals:

$$\sigma_x^2 = 2\pi\Delta z k_0^2 \times \iint_{K_{out}} \Phi_n(\kappa_x, \kappa_y, 0)[1 - \cos(\Delta x \cdot \kappa_x)] d\kappa_x d\kappa_y \tag{2-40}$$

$$\sigma_y^2 = 2\pi\Delta z k_0^2 \times \iint_{K_{out}} \Phi_n(\kappa_x, \kappa_y, 0)[1 - \cos(\Delta y \cdot \kappa_y)] d\kappa_x d\kappa_y \tag{2-41}$$

where $K_{out}$ represents the region spanning all of the $\kappa_z = 0$ plane, which we define unambiguously via:

$$K = \left\{ (\kappa_x, \kappa_y) : \begin{matrix} -\infty < \kappa_x < \infty, \\ -\infty < \kappa_y < \infty \end{matrix} \right\} \tag{2-42}$$

$$K_{in} = \left\{ (\kappa_x, \kappa_y) : \begin{matrix} -\Delta\kappa_x \dfrac{M}{2} < \kappa_x < \Delta\kappa_x \dfrac{M-1}{2}, \\ -\Delta\kappa_y \dfrac{M}{2} < \kappa_y < \Delta\kappa_y \dfrac{M-1}{2} \end{matrix} \right\} \tag{2-43}$$

$$K_{out} = \{ (\kappa_x, \kappa_y) : (\kappa_x, \kappa_y) \in K | (\kappa_x, \kappa_y) \notin K_{in} \} \tag{2-44}$$

In practice, the variances of Equations (2-40) and (2-41) can be evaluated numerically as the sum of several integrals. For the data sets in this paper, four integrals per parameter set were used for spanning from each corner of $K_{in}$ to a

$|\kappa_x| = |\kappa_y| = \infty$ point in an adjacent quadrant of $\kappa$-space. Finally, the variances of two white noise processes are calculated as:

$$\sigma_1^2 = \text{Minimum}\left(\sigma_x^2, \sigma_y^2\right) \tag{2-45}$$

$$\sigma_1^2 = \left|\sigma_x^2 - \sigma_y^2\right| \tag{2-46}$$

In order to whiten our phase screens, a $M \times M$ matrix of white-noise-generated variance $\sigma_1^2$ is added to the screen, and is followed by addition of a random number with variance $\sigma_2^2$ across each column (if $\sigma_x^2 > \sigma_y^2$) or row (if $\sigma_y^2 > \sigma_x^2$) of the grid. For isotropic turbulence $\sigma_x^2 = \sigma_y^2$, $\sigma_2^2 = 0$, and the second step can be negated. This method ensures the small-scale structure function across the x, y, and diagonal directions is improved relative to theory. All random elements pertaining to white noise are generated using a zero-mean Gaussian distribution.

Figure 2-15 and Figure 2-16 show qualitative results of using this method. As lower power law values place a higher portion of their spectral energy at high frequencies, we have chosen to display a power law of $\alpha = 3.1$. In order to reduce the number of independent variables specifying each plot, Figure 2-15 has been given in terms of effective coherence length, $\rho_{0,x} = 5$ cm, which for non-Kolmogorov, anisotropic turbulence is given by Equation (2-23). Additionally, we have included a curve in Figure 2-16 showing the phase screen structure function, normalized by theory, produced using the hybrid method but without the addition of white noise. This is intended to demonstrate the positive effects of our white

noise algorithm on the relative error at small separations (i.e., near 1% of the spatial domain and below). The following sections will characterize the performance associated with this addition combined with the subharmonic method described in the previous section.

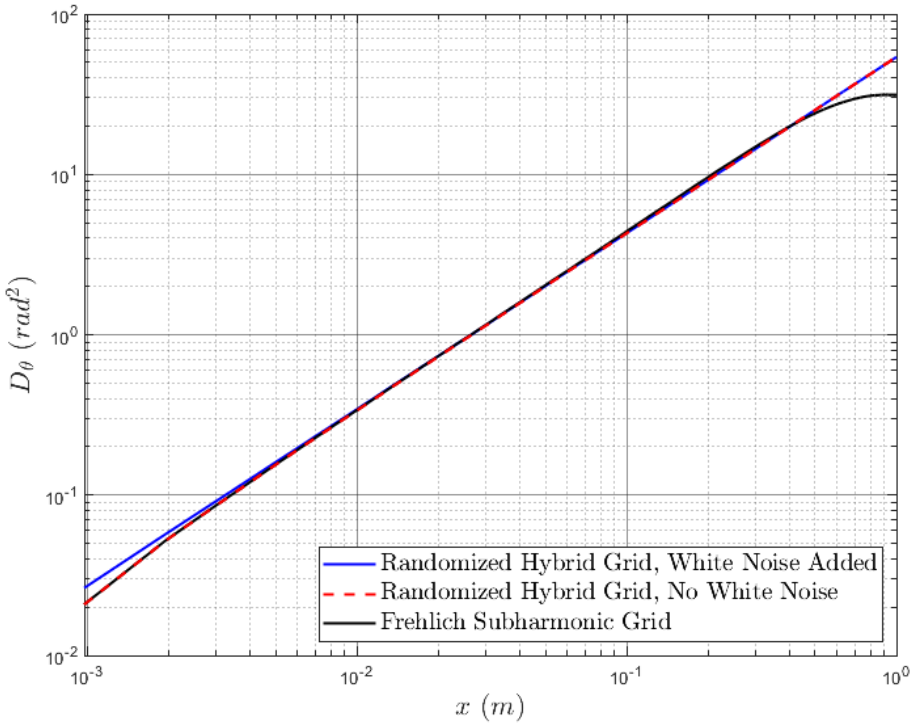


**Figure 2-15**: *X*-axis structure function of phase screens made with the randomized, hybrid subharmonic algorithm and white noise added, as well as screens using the traditional subharmonic method. Parameters for the screens are 1024 × 1024 grid, $N_p = 1$, and effective coherence length $\rho_{0,x} = 5$ cm.

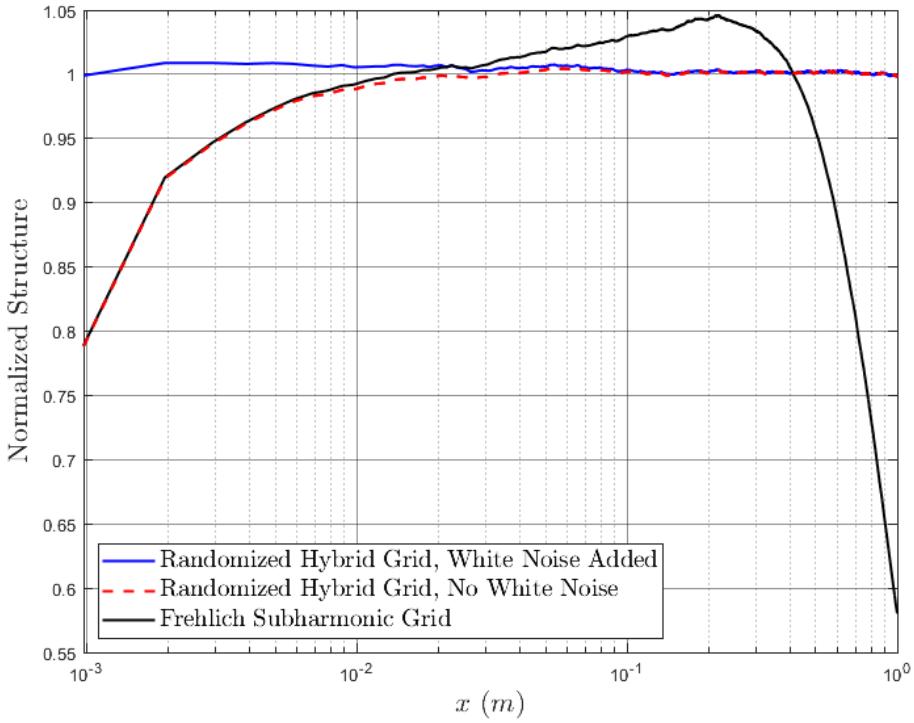


**Figure 2-16:** *X*-axis structure function normalized by theory of phase screens produced with the randomized, hybrid subharmonic algorithm both with and without white noise added, as well as screens using the traditional subharmonic method. The parameters used to create this figure are identical to those in Figure 2-15.

2.9: Hybrid Algorithm Results for Unbounded Spectral Models

We wish to assess the accuracy of our revised algorithm for the cases of generalized anisotropic, non-Kolmogorov turbulence spectra discussed. Due to the combination of our assessment of error as a ratio relative to a theory, as well as the scale invariance [52] of this section's turbulence models, the specific $\tilde{C}_n^2$'s and domain lengths, $M\Delta x$ and $M\Delta y$, do not affect results. The results are, however, sensitive to the number of grid points in use and the number of subharmonic constellations. Figure 12 displays a comparison of the hybrid method, including the addition of white noise, versus the Frehlich subharmonic method for multiple $\alpha$'s over 5,000 independent phase screens using various numbers of subharmonic constellations. The tables of Appendix A summarize the errors observed in testing for both schemes, as well as associated $N_p$. We have observed that our hybrid method outperforms the Frehlich subharmonic method on any grid size for any number of subharmonic constellations, except for $\alpha = 3.7$ and 3.9 with the $512 \times 512$ grid. Comparing the minimum RMS error observed using each method for $\alpha = 3.1$ to 3.9, we note that the average ratio of our Frehlich method's minimum $\mathcal{E}_{M/2}$ to that of the hybrid method is 4.77 for the $512 \times 512$ grid, 11.13 for the $1024 \times 1024$ grid, and 7.00 for the $2048 \times 2048$ grid. For the $512 \times 512$ grid, statistics were also collected for the Lane subharmonic method [52] and the error ratio between the Lane and hybrid method over all $\alpha$'s under test was 16.89. In general, as previously stated in the literature [53] the Frehlich method outperforms

the Lane method with the choice of an optimum $N_p$. The ratio of minimum $\mathcal{E}_{M/2}$ between Lane vs Frelich's method was 5.32.

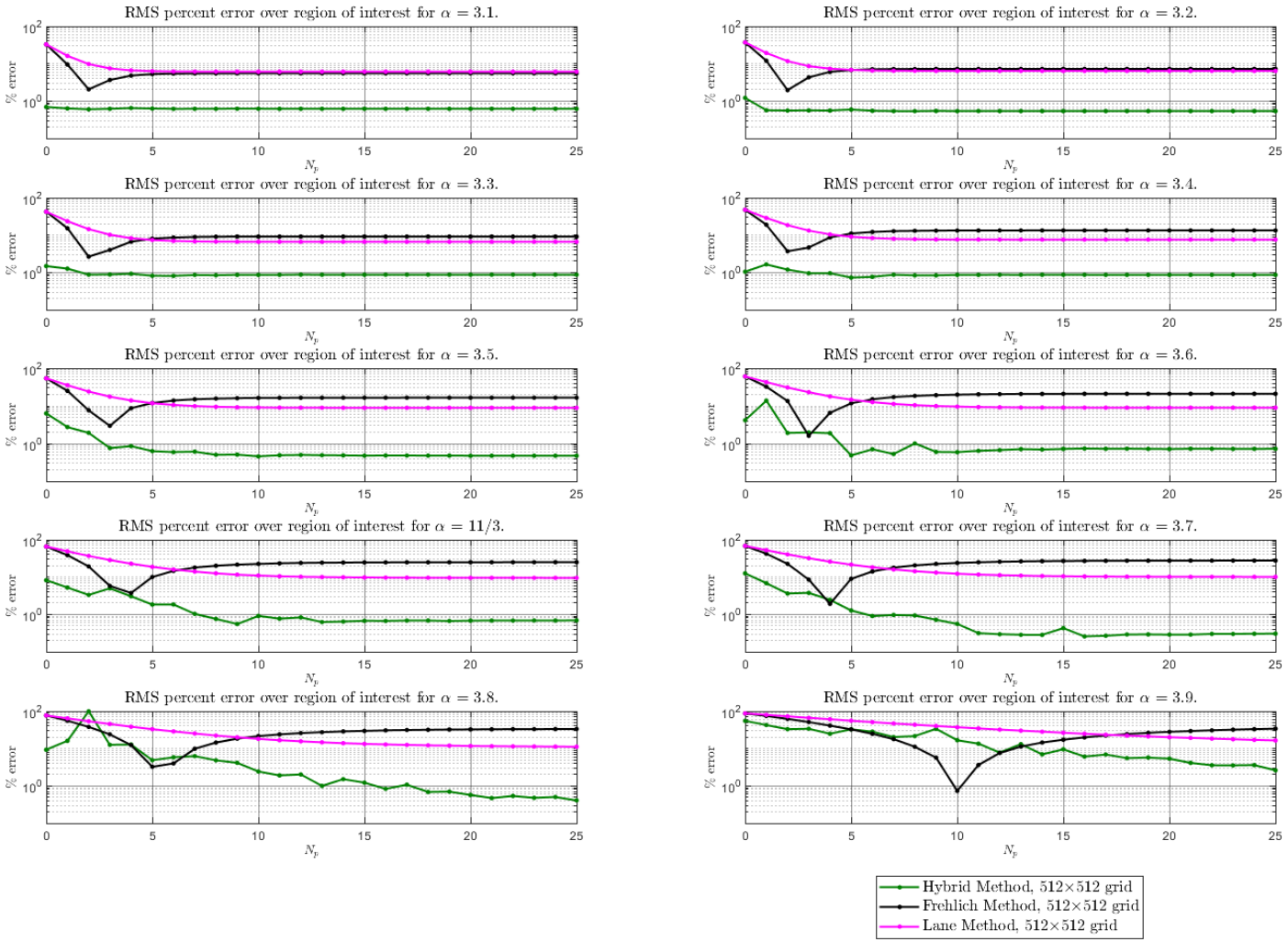


**Figure 2-17:** RMS error over region of interest computed along x and y directions of 50,000 phase screens for 512 × 512 grid using various spectral power laws ($\alpha$'s) and number of subharmonic constellations, $N_p$. $\mu_x = \mu_y = 1$ for all data points. The randomized hybrid method (**green**), Frehlich subharmonic method (**black**), and Lane subharmonic method (**magenta**) are shown. Full results for all grid sizes and spectra under test are given in Appendix A..

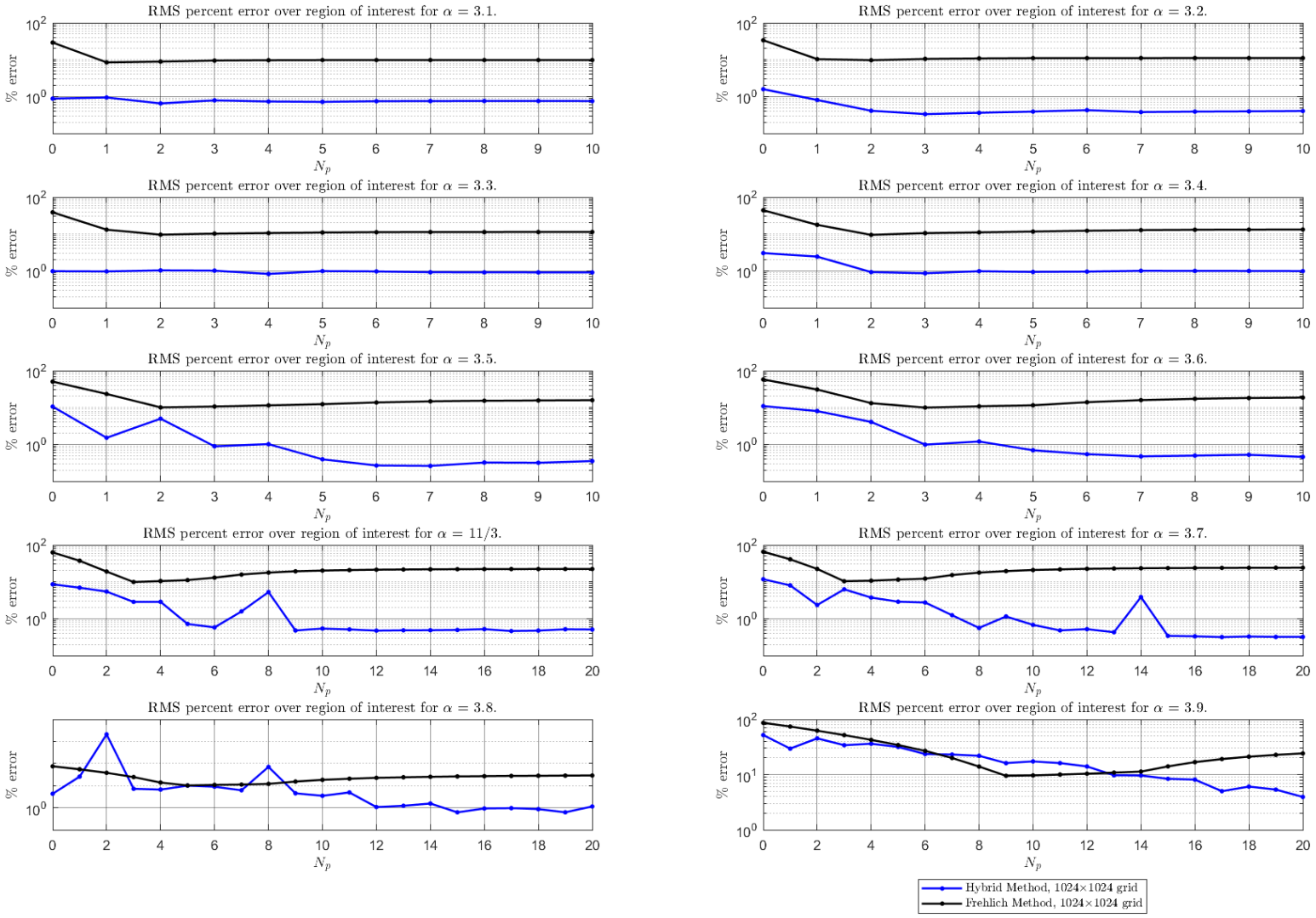


**Figure 2-18:** RMS error over region of interest computed along x and y directions of 50,000 phase screens for 1024 × 1024 grid using various spectral power laws ($\alpha$'s) and number of subharmonic constellations, $N_p$. $\mu_x = 1$, $\mu_y = 2$ for all data points. The randomized hybrid method (**blue**) and Frehlich subharmonic method (**black**) are shown.

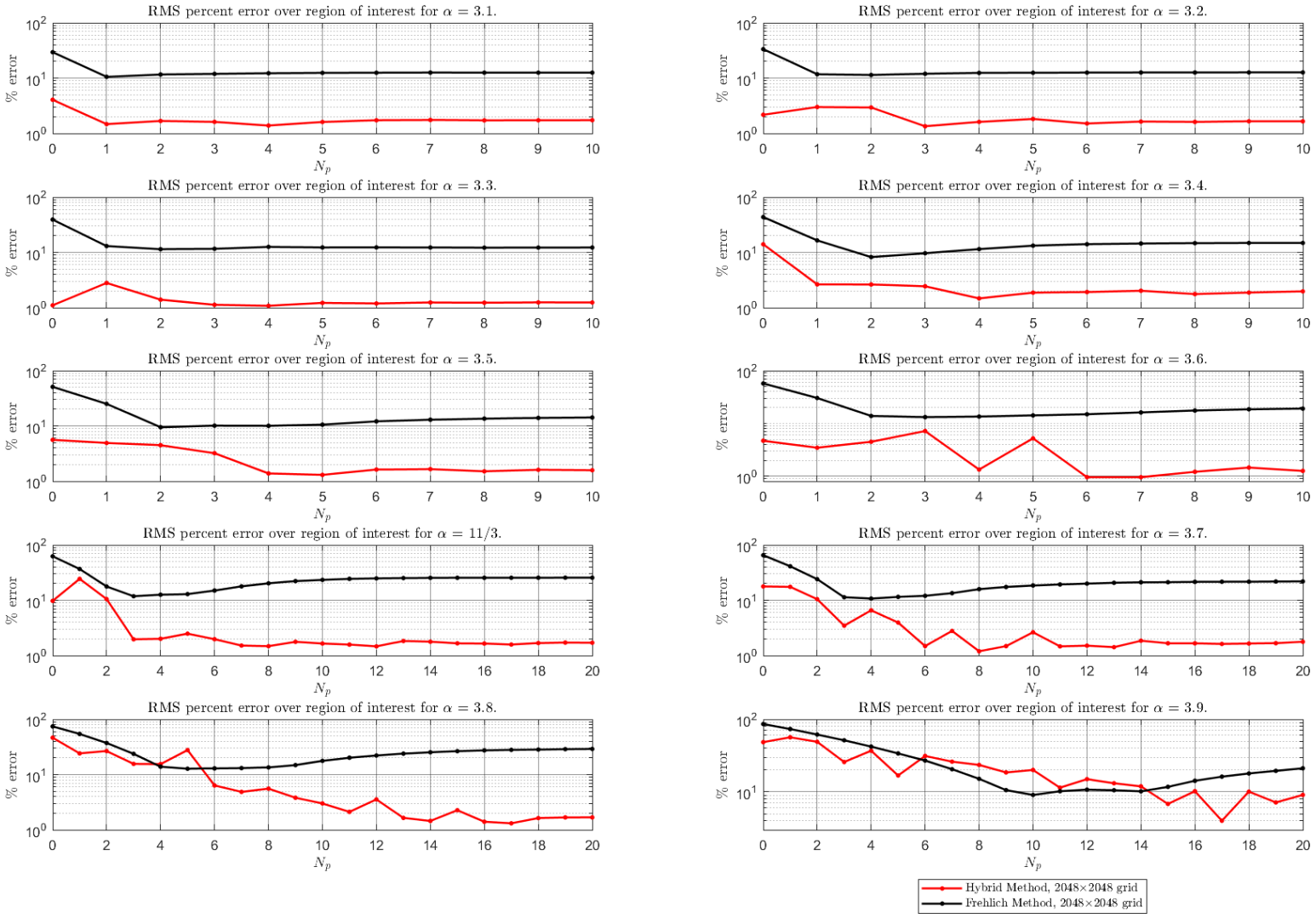


**Figure 2-19:** RMS error over region of interest computed along x and y directions of 5,000 phase screens for 2048 × 2048 grid using various spectral power laws ($\alpha$'s) and number of subharmonic constellations, $N_p$. $\mu_x = 1$, $\mu_y = 2$ for all data points. The randomized hybrid method (**red**) and Frehlich subharmonic method (**black**) are shown.

## 2.10: Hybrid Algorithm Results for Bounded Spectral Models

Returning to the modified atmospheric spectrum discussed in Section 2.6, we observe a marked difference in accuracy of the hybrid method versus the subharmonic method of Frehlich [53], which we refer to interchangeably as the traditional subharmonic method. We have chosen to compare with this specific subharmonic method, as opposed to other candidates [82], due to its improved convergence with theory [53] by virtue of weighting the subharmonic amplitude variances using area integrals of spectral models of interest, as opposed to (nonrandomized) spectral samplings. Results for various values of the outer scale, $L_0$, are shown in Figure 4-20 through Figure 4-22, for grid sizes of 512 × 512 through 2048 × 2048 with full results given in Appendices A and C. For each case, the size of the outer scale has been set as a factor of the total simulated $x$-, $y$-domain, which was always 1 m for this simulation set (i.e., $M\Delta x$ = 1 m for all bounded spectrum data sets). The inner scale for the simulations of this section was fixed at $l_0 = M\Delta x$ = 1 cm. Because the inner scale of interest was many times larger than the resolution of the grid, we elected not to include the white noise algorithm in the results of this section.

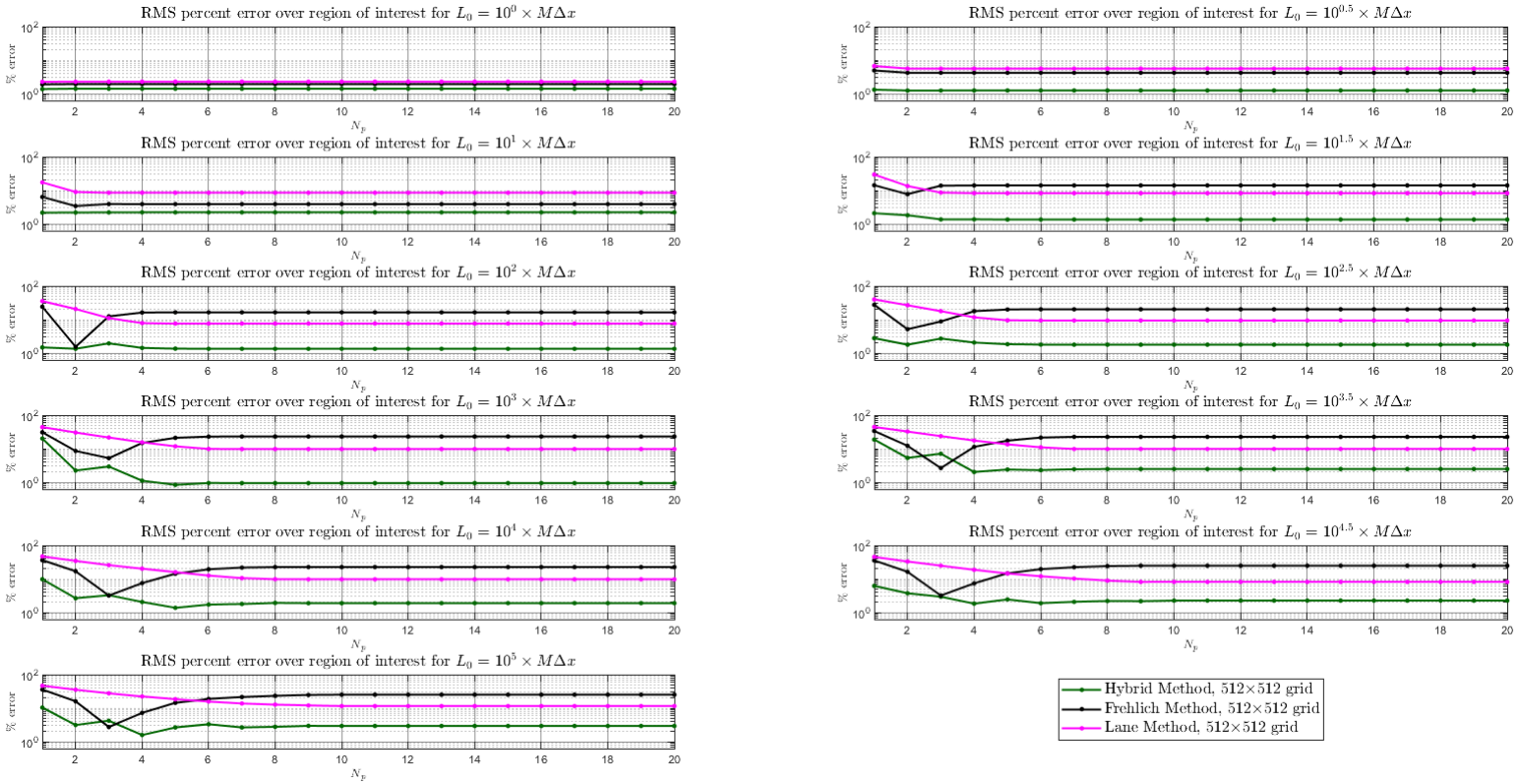


**Figure 2-20:** RMS error over region of interest computed along *x*- and *y*-directions for 5000 phase screens using modified spectrum, with $l_0 = M\Delta x/100$ and $M = 512$ (i.e. grid size 512 × 512). Complete tables of results for all grid sizes and spectra under test can be found in Appendix A.

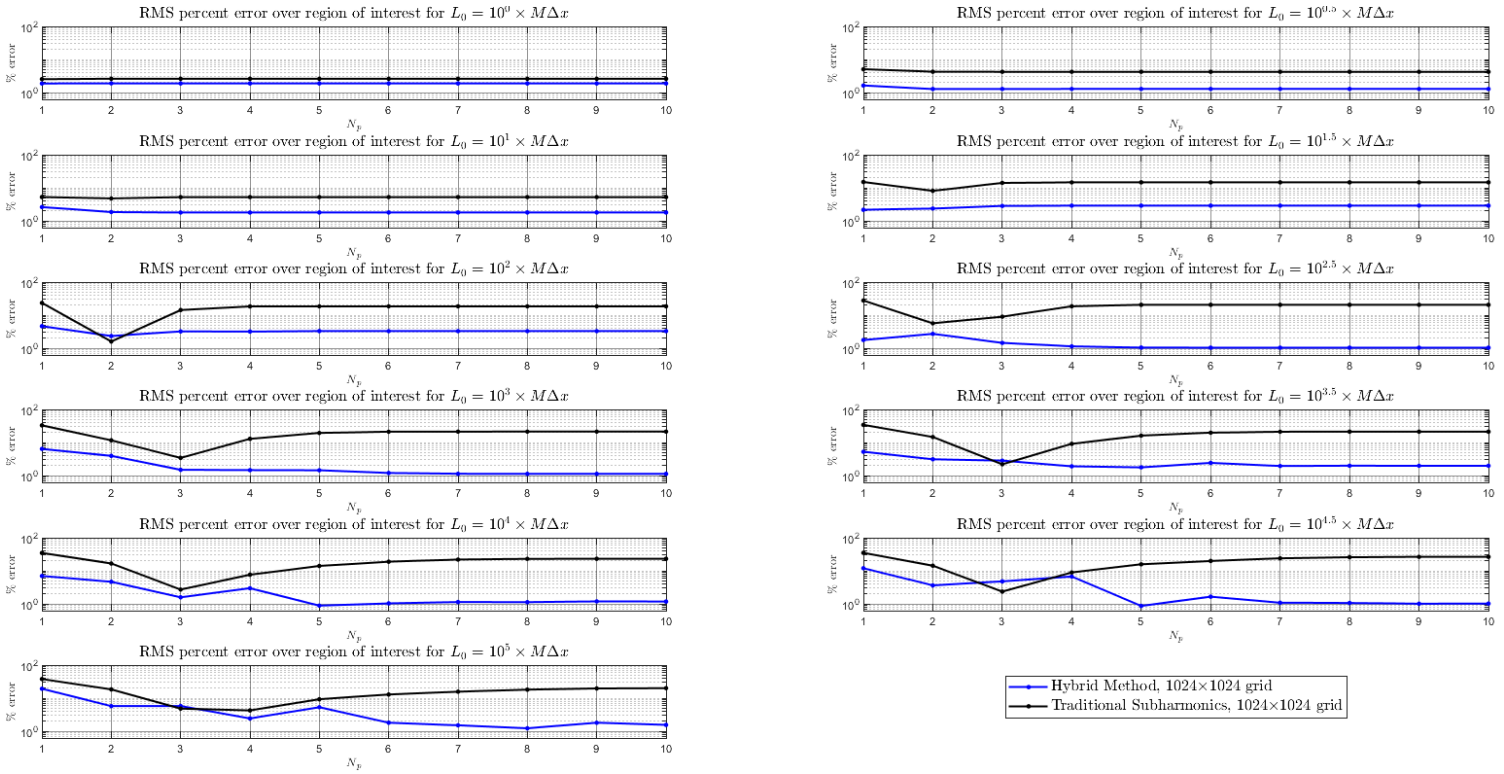


**Figure 2-21:** RMS error over region of interest computed along *x*- and *y*-directions for 5000 phase screens using modified spectrum, with $l_0 = M\Delta x/100$ and $M = 1024$ (i.e. grid size 1024 × 1024).

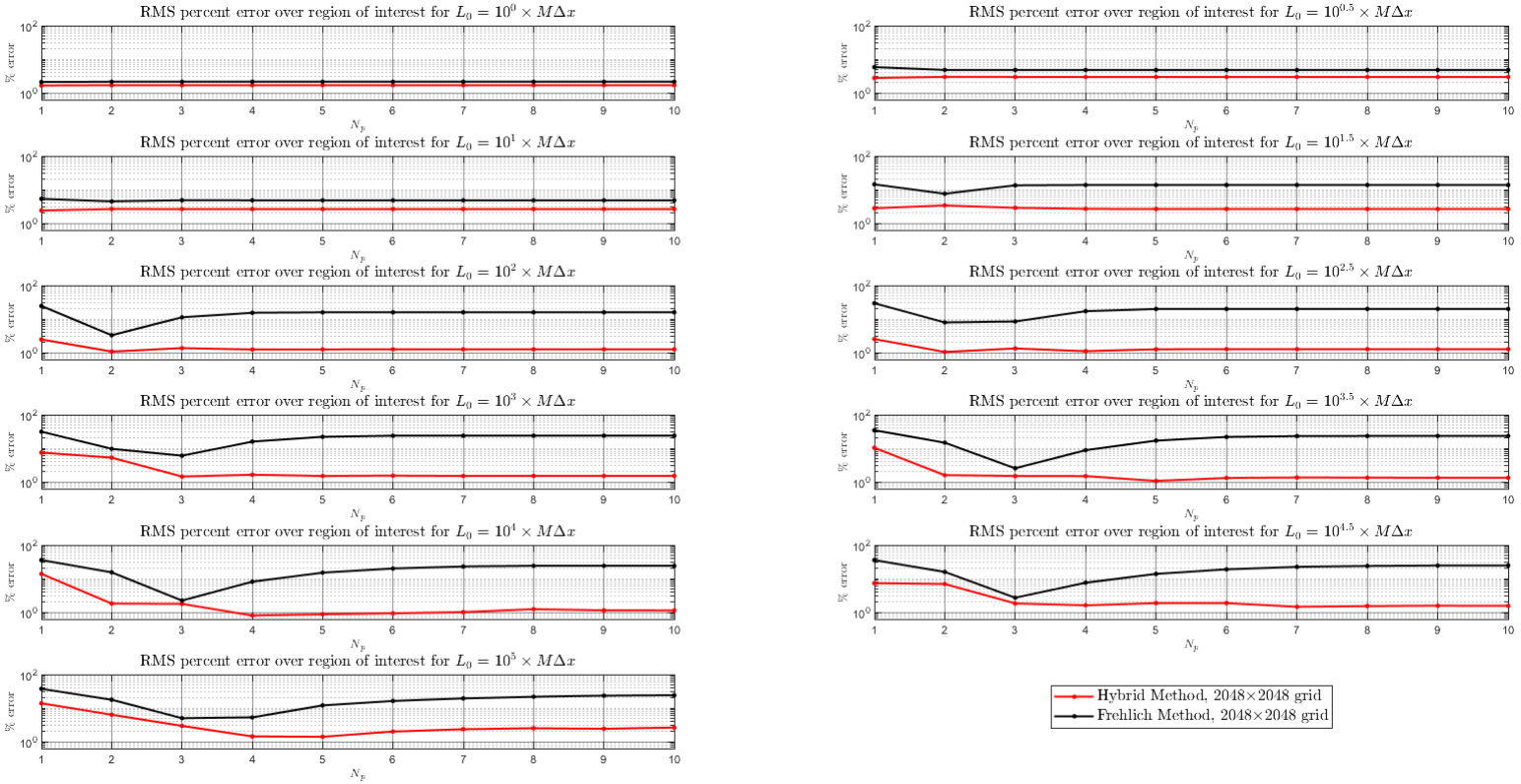


**Figure 2-22:** RMS error over region of interest computed along $x$- and $y$-directions for 5000 phase screens using modified spectrum, with $l_0 = M\Delta x/100$ and $M = 2048$ (i.e. grid size 2048 × 2048).

The data in this section represent statistics taken from a large sampling of phase screens, along the number $M/2 + 1$ ordered row and column of each screen. Because the sampling directions are orthogonal, the sample set sizes are, essentially, 10,000 trials. We find that for each case, the hybrid method outperforms the traditional subharmonic method, which can be verified by close inspection of the tables in the appendices. Comparing the minimum RMS error observed using each method for $L_0 = 1$ to $10^5$, we note that the average ratio of our Frehlich method's minimum $\mathcal{E}_{M/2}$ to that of the hybrid method is 2.54 for the $512 \times 512$ grid, 2.76 for the $1024 \times 1024$ grid, and 3.13 for the $2048 \times 2048$ grid. For the $512 \times 512$ grid, statistics were also collected for the Lane subharmonic method [52] and the error ratio between the Lane and hybrid method over all $L_0$'s under test was 5.63. In general, as previously stated in the literature [53] the Frehlich method outperforms the Lane method with the choice of an optimum $N_p$. The ratio of minimum $\mathcal{E}_{M/2}$ between Lane vs Frehlich's method was 2.21.

# Chapter 3 : Numerical Verification of the Statistical Theories of Propagation of Optical Beams through Anisotropic, Non-Kolmogorov Turbulence

## 3.1: Background

Other the past year, we have performed a large number of simulations of anisotropic and non-Kolmogorov turbulence. During this time, careful review of the theoretical literature [22, 23, 25, 59] showed various expressions for predicted spot sizes and scintillations indices in the presence of anisotropic turbulence. We have compared these theoretical predictions with simulation in order to determine which expressions to use in beam profiling-based turbulence analysis [83]. Although it is not possible to convey all that we have learned, the following sections are intended to convey the most important points of interest. All cases used the split-step method, and the angular spectrum propagation algorithm [33]. With regards to number of subharmonic groups added to phase screens, for each test a calibration was done to determine the minimum RMS percent error over the strong fluctuation theory beam diameter, with the best performing configuration chosen.

## 3.2: Spot Size Predictions in the Presence of Non-Kolmogorov Turbulence

Several expressions exist in the literature for the long-term beam radii (spot sizes) for Gaussian beams propagating in non-Kolmogorov turbulence, within the deep fluctuation regime (Rytov variance much greater than one). Before moving

on, we will introduce the non-dimensional curvature parameter and Fresnel parameter for the input and output planes, respectively, as:

$$\Theta_0 = 1 - \frac{L}{F} \tag{3-1}$$

$$\Lambda_0 = \frac{2L}{k_0 W_0^2} \tag{3-2}$$

$$\Theta = \frac{\Theta_0}{\Theta_0^2 + \Lambda_0^2} \tag{3-3}$$

$$\Lambda = \frac{\Lambda_0}{\Theta_0^2 + \Lambda_0^2} \tag{3-4}$$

$$W = \sqrt{\frac{2L}{k_0 \Lambda}} \tag{3-5}$$

with $k_0$ the optical wavenumber, $F$ the radius of curvature in the transmit plane, $W_0$ the beam spot size in the transmit plane, $L$ the propagation distance, and $W$ the diffraction limited spot size. It has been implied, that the weak fluctuation regime prediction, based upon the Rytov method, can be extended to the strong fluctuation regime with reasonable accuracy [25]. In terms of the diffraction limited spot size, $W$, and the output plane Fresnel parameter, the prediction is given by [25]:

$$W_{LT,x} \cong W(1 + T_x)^{3/5} \tag{3-6}$$

$$W_{LT,y} \cong W\left(1 + T_y\right)^{3/5} \tag{3-7}$$

$$T_x = 2\pi \frac{\Gamma\left(2 - \frac{\alpha}{2}\right)}{(\alpha - 1)\mu_x^2} k_0^2 L^2 A(\alpha) \Lambda^{\frac{\alpha}{2}-1} \tilde{C}_n^2 \times \int_0^{2\pi} \cos^2\varphi \left(\frac{\cos^2\varphi}{\mu_x^2} + \frac{\sin^2\varphi}{\mu_Y^2}\right)^{\frac{\alpha}{2}-2} \mathrm{d}\varphi \tag{3-8}$$

$$T_y = 2\pi \frac{\Gamma\left(2-\frac{\alpha}{2}\right)}{(\alpha-1)\mu_y^2} k_0^2 L^2 A(\alpha) \Lambda^{\frac{\alpha}{2}-1} \tilde{C}_n^2 \times \int_0^{2\pi} \sin^2\varphi \left(\frac{\cos^2\varphi}{\mu_x^2} + \frac{\sin^2\varphi}{\mu_Y^2}\right)^{\frac{\alpha}{2}-2} \mathrm{d}\varphi \tag{3-9}$$

We shall refer to this method as the *Rytov variance based method*, because it is derived using the same technique as the expression for Kolmogorov turbulence, $W_{LT} \cong W\,(1+1.33\sigma_R^2\Lambda^{5/6})^{3/5}$, in which the perturbation term is proportional to the Rytov variance.

Perhaps of greater interest, there are two expressions in the strong fluctuation regime that are derived from the concept of coherence width. We define the *inverse spatial coherence method 1* using the coherence width of a plane wave, $\rho_0$, as [25]:

$$W_{LT,x} \cong \sqrt{W^2 + \frac{8L^2}{3k_0\rho_{0,x}^2}} \tag{3-10}$$

$$W_{LT,y} \cong \sqrt{W^2 + \frac{8L^2}{3k_0\rho_{0,y}^2}} \tag{3-11}$$

$$\rho_{0,x} = \mu_x \left[A(\alpha)\tilde{C}_n^2 k_0^2 L \frac{-\pi^2\Gamma\left(1-\frac{\alpha}{2}\right)}{2^{\alpha-3}\Gamma\left(\frac{\alpha}{2}\right)}\right]^{\frac{1}{2-\alpha}} \tag{3-12}$$

$$\rho_{0,y} = \mu_y \left[A(\alpha)\tilde{C}_n^2 k_0^2 L \frac{-\pi^2\Gamma\left(1-\frac{\alpha}{2}\right)}{2^{\alpha-3}\Gamma\left(\frac{\alpha}{2}\right)}\right]^{\frac{1}{2-\alpha}} \tag{3-13}$$

We define *inverse spatial coherence method 2* using the coherence width of a spherical wave, $\rho_s$, as [59]:

$$W_{LT,x} \cong \sqrt{W^2 + \frac{8L^2}{k_0 \rho_{s,x}^2}} \tag{3-14}$$

$$W_{LT,y} \cong \sqrt{W^2 + \frac{8L^2}{k_0 \rho_{s,y}^2}} \tag{3-15}$$

$$\rho_{s,x} = \mu_x \left[ A(\alpha) \tilde{C}_n^2 k_0^2 L \frac{-\pi^2 \Gamma\left(1 - \frac{\alpha}{2}\right)}{2^{\alpha-3}(\alpha - 1)\Gamma\left(\frac{\alpha}{2}\right)} \right]^{\frac{1}{2-\alpha}} \tag{3-16}$$

$$\rho_{s,y} = \mu_y \left[ A(\alpha) \tilde{C}_n^2 k_0^2 L \frac{-\pi^2 \Gamma\left(1 - \frac{\alpha}{2}\right)}{2^{\alpha-3}(\alpha - 1)\Gamma\left(\frac{\alpha}{2}\right)} \right]^{\frac{1}{2-\alpha}} \tag{3-17}$$

In order to test the validity of the above equations, we ran 1,000 independent propagation simulations using nine $\alpha$'s between 3.1 and 3.9, in steps of .1, as well as a Kolmogorov turbulence case. Trials were performed with 10 evenly spaced phase screens each, and 5 km propagation distance using a collimated, 50 cm diameter, 1060 nm beam. Phase screens were 2048 × 2048 with 0.5 mm grid spacing for $\alpha$'s below 3.8, however a 4096 × 4096 grid with .25 mm spacing was used for $\alpha$'s of 3.8 and 3.9 to avoid aliasing effects during propagation. The generalized Rytov variance [23] was held at 10 for all cases. As in two of the theoretical predictions of interest the anisotropy factor in one direction had no effect on the spot size in the orthogonal direction, we chose to simulate isotropic turbulence ($\mu_x = 1$, $\mu_y = 1$) for this example. As is evident in Figure 3-1, Equations (3-14) and (3-15) which makes use of the spherical wave coherence length produces the best agreement with theory across the span of $\alpha$'s of interest.

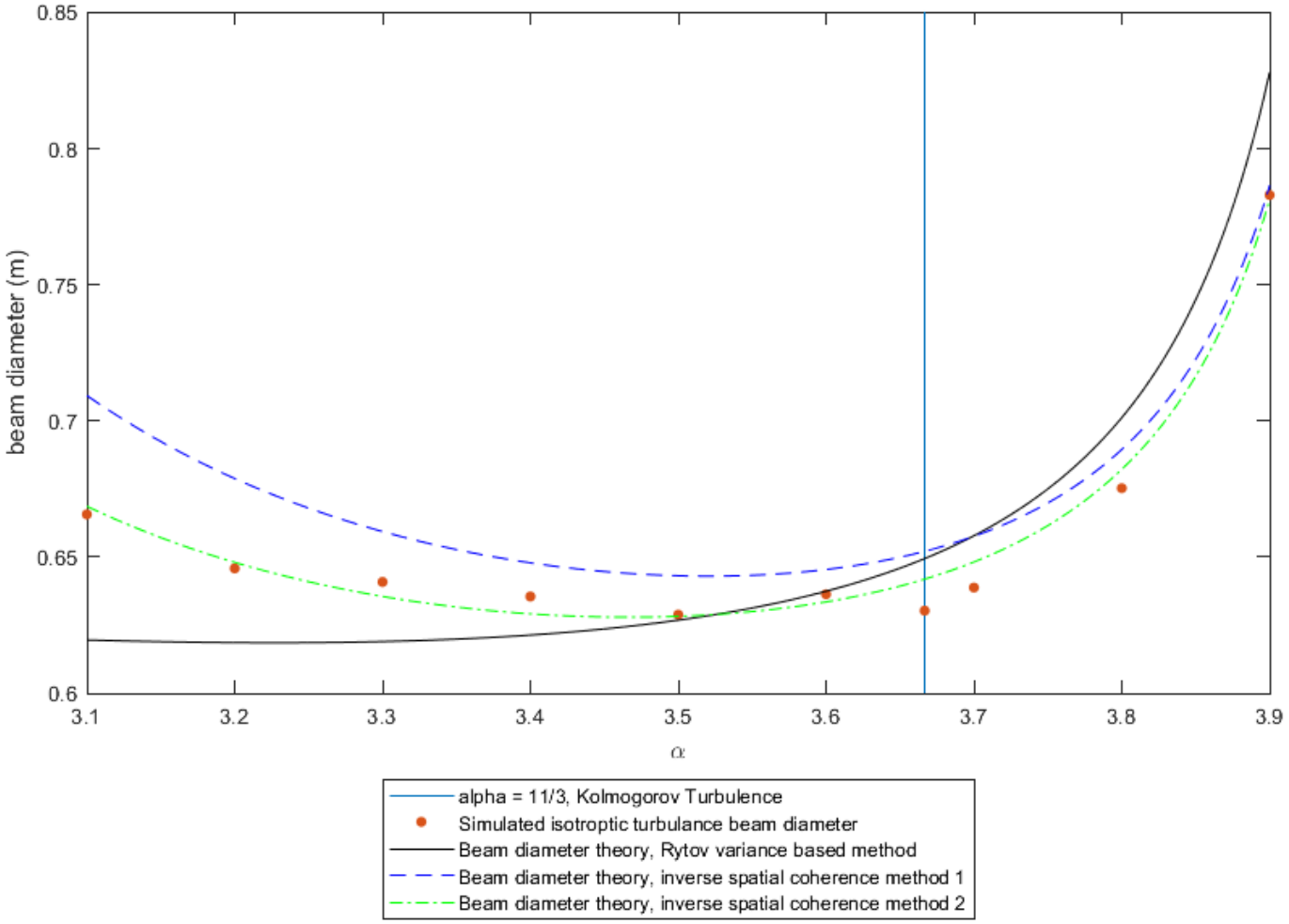


**Figure 3-1:** Beam diameter theoretical predictions vs simulation result across various α's, with the Rytov variance held at 10 and i.e. grid size 2048 × 2048. Trials were performed with 10 evenly spaced phase screens each, and 5 km propagation distance using a collimated, 50 cm diameter, 1060 nm beam. Phase screens were 2048 × 2048 with 0.5 mm grid spacing for α's below 3.8, however a 4096 × 4096 grid with .25 mm spacing was used for α's of 3.8 and 3.9 to avoid aliasing effects during propagation.

3.3: Focused Beams in Non-Kolmogorov Turbulence

After reading comments from Xiao and Voelz [38] regarding the superior accuracy of the inverse spherical wave coherence width based method, shown in Equations (3-14) and (3-15) for focused beams, we investigated for several wavelengths, $\mu_y$ values, and propagation distances. Specifically, Figure 3-2 shows the result for an initially 50 cm diameter, 632.8 nm beam propagating through 5 km of $\tilde{C}_n^2 = 10^{-14}$ m$^{3-\alpha}$ anisotropic turbulence with $\mu_x = 1$ and $\mu_y = 3$. Phase screens were 2048 × 2048 with 0.5 mm grid spacing. Although Equations (3-14) and (3-15) does appear to trend best with simulation results, agreement is not as good as in the collimated beam case of Figure 3-1. Additionally, when running additional simulations with increased wavelength and increased $\mu_y$, in order to lower the generalized Rytov variance, the undershooting of the simulation beam diameters relative to theory was sustained, suggesting it is not an artifact of different turbulence regimes being applicable to differing values of $\alpha$. Perhaps the most interesting feature in Figure 3-2 is the Rytov variance based method's differing shape relative to all the other curves and simulation trends shown. This may be related to the manner in which the perturbation term is applied in Equations (3-6) and (3-7), vs Equations (3-10), (3-11), (3-14), and (3-15).

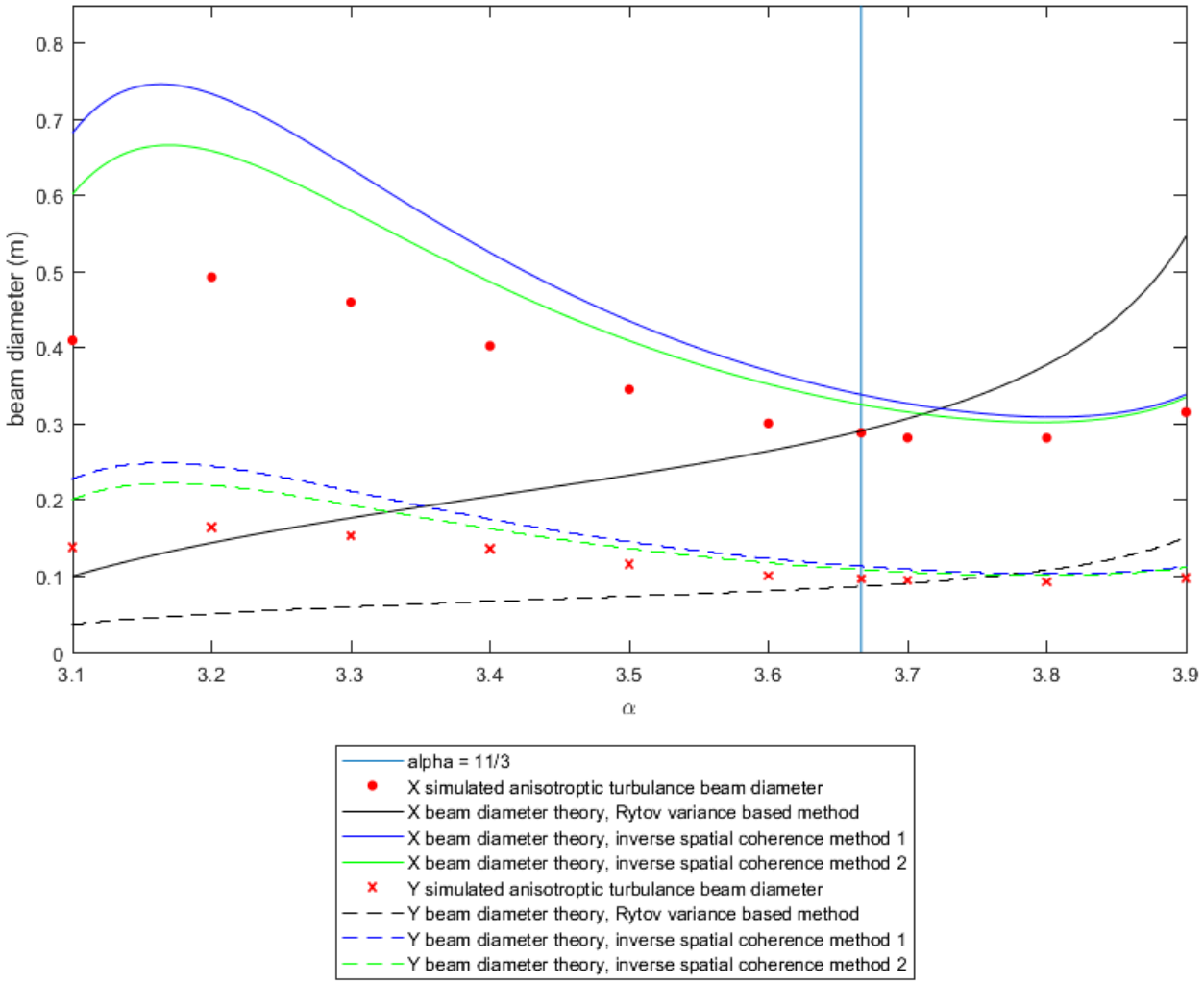


**Figure 3-2:** Measured beam diameter results for an initially 50 cm diameter, 632.8 nm focused beam propagating through 5 km of of $\tilde{C}_n^2 = 10^{-14}$ m$^{3-\alpha}$ anisotropic turbulence with $\mu_x = 1$ and $\mu_y = 3$. Phase screens were 2048 × 2048 with 0.5 mm grid spacing.

The on-axis scintillation indices of focused beams in non-Kolmogorov, anisotropic turbulence were analyzed in various configurations during the course of this study. Although we note very good agreement with theory for collimated beams, even with effective beam parameters considered [84] the results do not trend well, as shown in Figure 3-3 which we feel is representative of many of the simulations run. The configuration used for generation of Figure 3-3 was similar to that of Figure 3-2, however we used a 1060 nm beam in isotropic turbulence ($\mu_x = \mu_y = 1$). We should note that simulations in the weak fluctuation regime were not run, as extreme contracting the grid spacing of simulation during each propagation step would most likely be necessary to get accurate estimates. Although we later altered our propagation algorithm in order to allow for this adjustment [33], a more detailed method of choosing the best configuration for the phase screens would need to be considered, as we assumed a constant basis of simulation in our calibration for optimum number of subharmonics groups to be added for each value of $\alpha$.

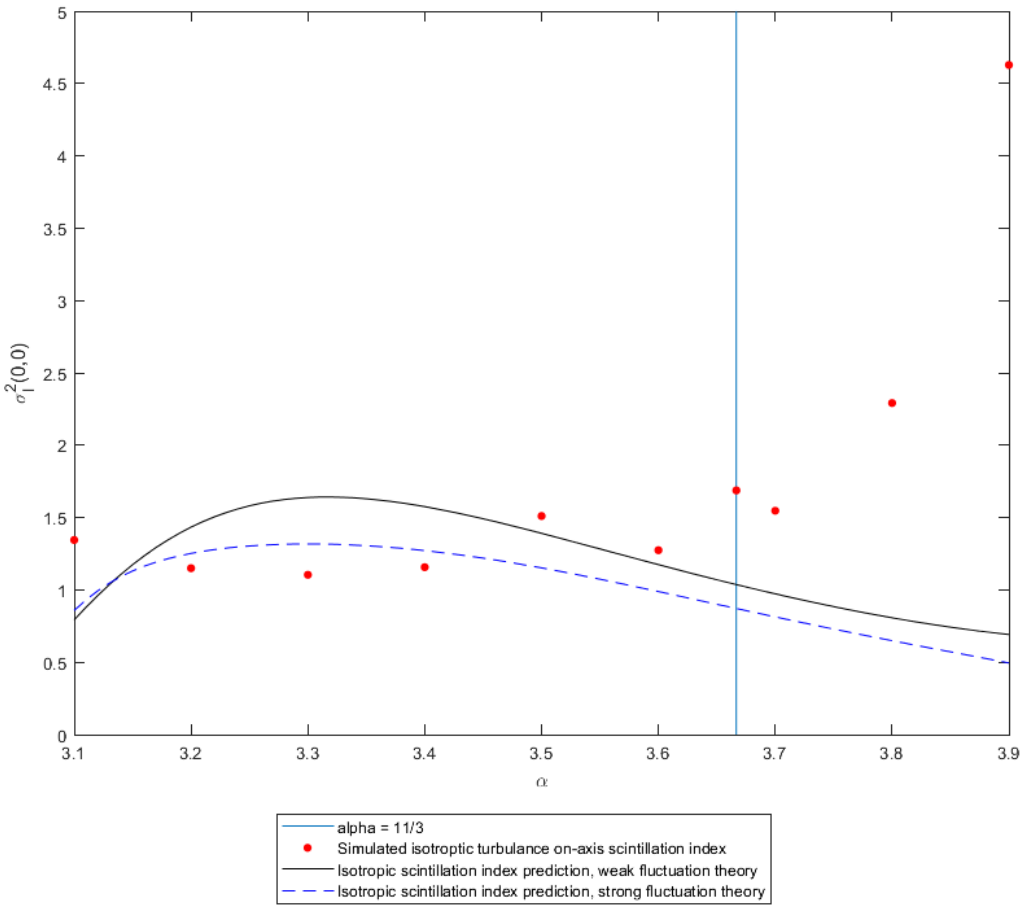


**Figure 3-3:** Simulation results vs theory for on-axis scintillation index, $\sigma_I^2(0,0)$, of focused 1060 nm beam propagating through 5 km of anisotropic turbulence. Simulation results do not trend well with theoretical predictions.

## 3.4: Weak Turbulence Regime Predictions of Spot Size

Equations (3-6) though (3-9) were initially derived using weak fluctuation theory assumptions [23]. An interesting feature of Equations (3-6) though (3-9) is that as $\mu_x$ is held constant, and $\mu_y$ increases, the spot size in the $x$-direction is predicted to slightly increase, and the $y$-direction spot size decrease, for valid values of $\alpha$. We found this surprising, as the generalized Rytov variance is expected to

decrease as $\mu_y$ increases [23], indicating less optical turbulence. Other similarly derived equations [76] predict no change in the *x*-direction spot size, or a radially symmetric beam [23]. In order to test this, a simulation was carried out for an initially 10 cm diameter beam propagating across a 2 km path in $\tilde{C}_n^2 = 10^{-14}$ $m^{-7/10}$ of turbulence, with $\alpha = 3.7$. These values were chosen such that the highest generalized Rytov variance under test was just under one, placing us squarely outside the strong fluctuation regime for collimated beams [9]. As shown in Figure 8, the *x*-direction spot size does not show good agreement with theory. On a positive note, this test does in-fact demonstrate that in the weak turbulence regime the *x*- and *y*-direction spot sizes are not independent of the anisotropy parameter in the orthogonal direction, as predicted by the coherence radius predictions of Equations (3-10), (3-11), (3-14), and (3-15).

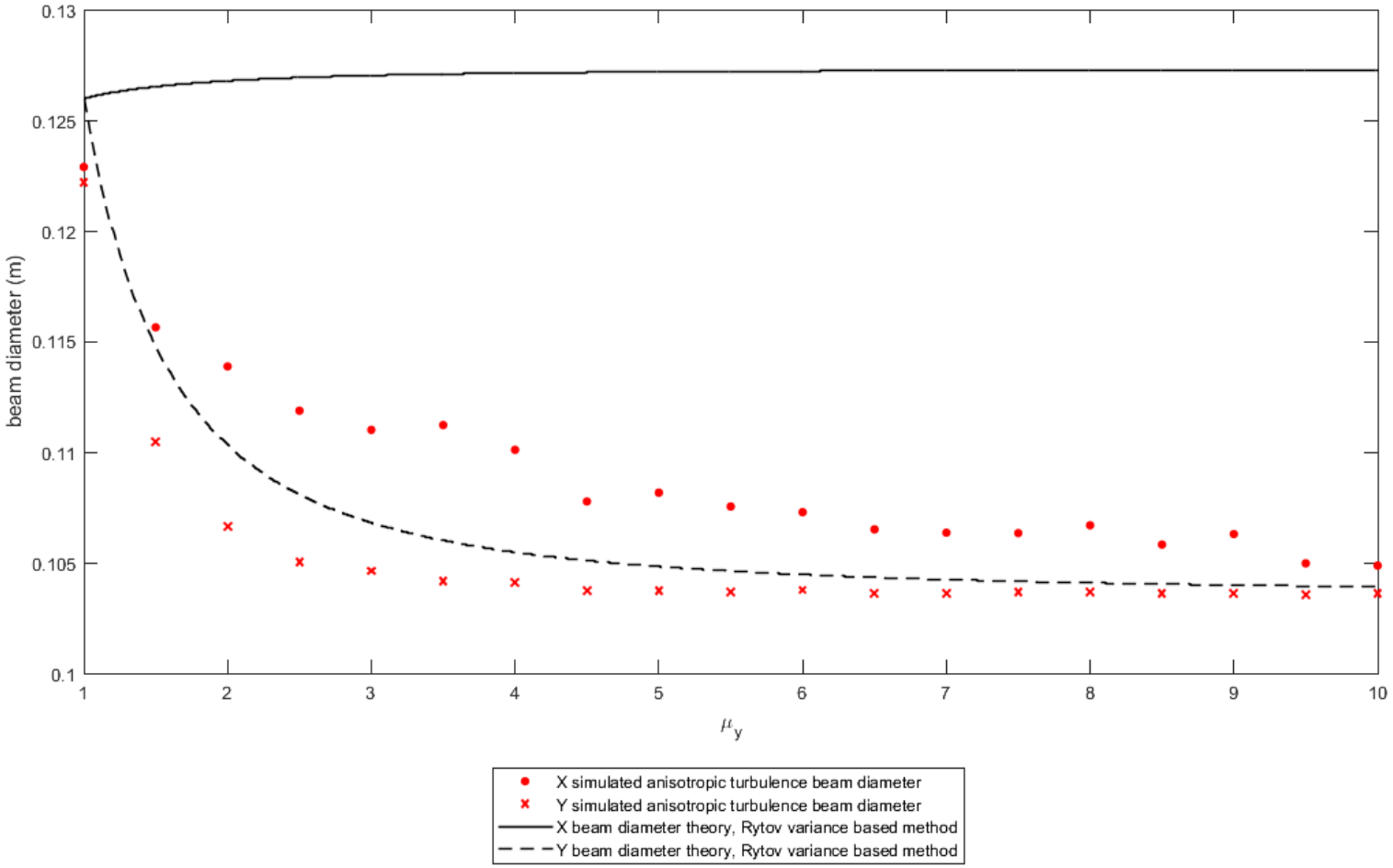


**Figure 3-4:** Simulation results for long term beam diameters in anisotropic turbulence versus theory as $\mu_x$ is held at one, and $\mu_y$ is swept from one to ten, for an initially 10 cm diameter beam propagating across a 2 km path in $\tilde{C}_n^2 = 10^{-14}$ m$^{-7/10}$ of turbulence, with $\alpha = 3.7$. The $x$-direction spot size does not trend well with theory, though the simulation does show that the $x$- and $y$-direction spot sizes are not independent of the anisotropy parameter in the orthogonal direction.

3.5: Scintillation Index and Aperture Averaging of Scintillation in the Presence of Optical Turbulence and Refractivity Distortions

During the course of performing the research relevant to this thesis, concerns began to grow within the atmospheric modelling community that the effects of non-turbulent optical refractivity were non-negligible [85, 86, 87]. In addition to a renewed focus on the models used for the optical refractive index in the atmosphere [85, 86], researchers have also generalized the weak fluctuation regime predictions associated with propagation through non-Kolmogorov, anisotropic turbulence to encompass non-turbulence spot size asymmetries in the receiver plane. To analyze these predictions using the phase screen Monte Carlo methods, we define the following:

$$\Theta_{0,x} = 1 - \frac{z}{F_{0,x}}, \quad \Theta_{0,y} = 1 - \frac{z}{F_{0,y}} \tag{3-18}$$

$$\Lambda_x = \frac{\Lambda_0}{\Lambda_0^2 + \Theta_{0,x}^2}, \quad \Lambda_y = \frac{\Lambda_0}{\Lambda_0^2 + \Theta_{0,y}^2} \tag{3-19}$$

$$\Theta_x = \frac{\Theta_{0,x}}{\Lambda_0^2 + \Theta_{0,x}^2}, \quad \Theta_y = \frac{\Theta_{0,y}}{\Lambda_0^2 + \Theta_{0,y}^2} \tag{3-20}$$

$$\overline{\Theta}_x = 1 - \Theta_x, \quad \overline{\Theta}_y = 1 - \Theta_y \tag{3-21}$$

$$W_x = \sqrt{\frac{2L}{k_0 \Lambda_x}}, \quad W_y = \sqrt{\frac{2L}{k_0 \Lambda_y}} \tag{3-22}$$

where $\Theta_{0,x}$ and $\Theta_{0,y}$ are the transmit plane curvature beam parameters in the *x*- and *y*-directions, $\Lambda_x$ and $\Lambda_y$ transmit plane Fresnel beam parameters in the *x*- and *y*-

directions, $\Theta_x$ and $\Theta_y$ are the receive plane curvature beam parameters in the *x*- and *y*-directions, and $W_x$ and $W_y$ are the receive plane diffraction limited spot sizes *x*- and *y*-directions. In the weak fluctuation regime, the scintillation index at any point can be expressed at the sum of off-axis and axial contributions [9, 24], i.e.:

$$\sigma_I^2(x,y,L) = \sigma_{I,r}^2(x,y,L) + \sigma_{I,l}^2(L) \tag{3-23}$$

The off-axis contribution, $\sigma_{I,r}^2$, axial contributions, $\sigma_{I,l}^2$, and mean intensity, *I*, according to weak fluctuation regime approximations are given by:

$$\sigma_{I,r}^2(x,y,L) = 4\pi k_0^2 L \int_0^1 d\xi \int_{-\infty}^{\infty} d\kappa_x \int_{-\infty}^{\infty} d\kappa_y\, \Phi_n(\kappa_x,\kappa_y) \exp\left[-\frac{L\xi^2}{k_0}\left(\kappa_x^2\Lambda_x + \kappa_y^2\Lambda_y\right)\right] \times \left\{\exp\left[2\xi\left(\kappa_x\Lambda_x x + \kappa_y\Lambda_y y\right)\right] - 1\right\} \tag{3-24}$$

$$\sigma_{I,l}^2(L) = 4\pi k_0^2 L \int_0^1 d\xi \int_{-\infty}^{\infty} d\kappa_x \int_{-\infty}^{\infty} d\kappa_y\, \Phi_n(\kappa_x,\kappa_y) \exp\left[-\frac{L\xi^2}{k_0}\left(\kappa_x^2\Lambda_x + \kappa_y^2\Lambda_y\right)\right] \times \left\{1 - \cos\left(\frac{L\xi}{k_0}\left[\left(1-\overline{\Theta}_x\xi\right)\kappa_x^2 + \left(1-\overline{\Theta}_y\xi\right)\kappa_y^2\right]\right)\right\} \tag{3-25}$$

$$\begin{aligned} I(x,y,L) &\propto \exp\left[-\frac{k_0^2\left(x^2\Lambda_x + y^2\Lambda_y\right)}{2L^2}\right] \times \exp\left[\frac{\sigma_{I,r}^2(x,y,L)}{2}\right] \\ &= \exp\left[-\left(\frac{2x^2}{W_x^2} + \frac{2y^2}{W_y^2}\right) + \frac{\sigma_{I,r}^2(x,y,L)}{2}\right] \end{aligned} \tag{3-26}$$

In order to check the reliability of the above expressions, phase screen simulations were performed using the hybrid method discussed in Chapter 2. Based on observations from experiments which will be discussed in the next chapter, a two to one ratio of the *x*- and *y*-axis diffraction limited spot sizes was chosen as a worst case for examination. Simulations were performed for a range of $\mu_y$ values,

generalized Rytov variances, and input plane beam parameters. $\mu_x$ and the propagation distance were held constant at 1 and 530 m, respectively. For weak fluctuation regime experiments, we have been mainly interested in the study of divergent beams in because we generally needed to defocus the beam expander calibration away from collimated in order to fully illuminate the instrument collecting apertures. All cases shown used 1,000 trials, 10 phase screens and propagations, and 4 subharmonic constellations ($N_p = 4$). In this section, only Kolmogorov ($\alpha = 11/3$) turbulence has been considered. For the below three figures, the elliptical diffraction limited beam was achieved by warping the input plane radius of curvature such that $F_{0,x} = -54.63$ m and $F_{0,y} = -122.42$ m. These values were chosen in order to achieve diffraction limited spot sizes of $W_x =$ 15 cm and $W_y = 7.5$ cm.

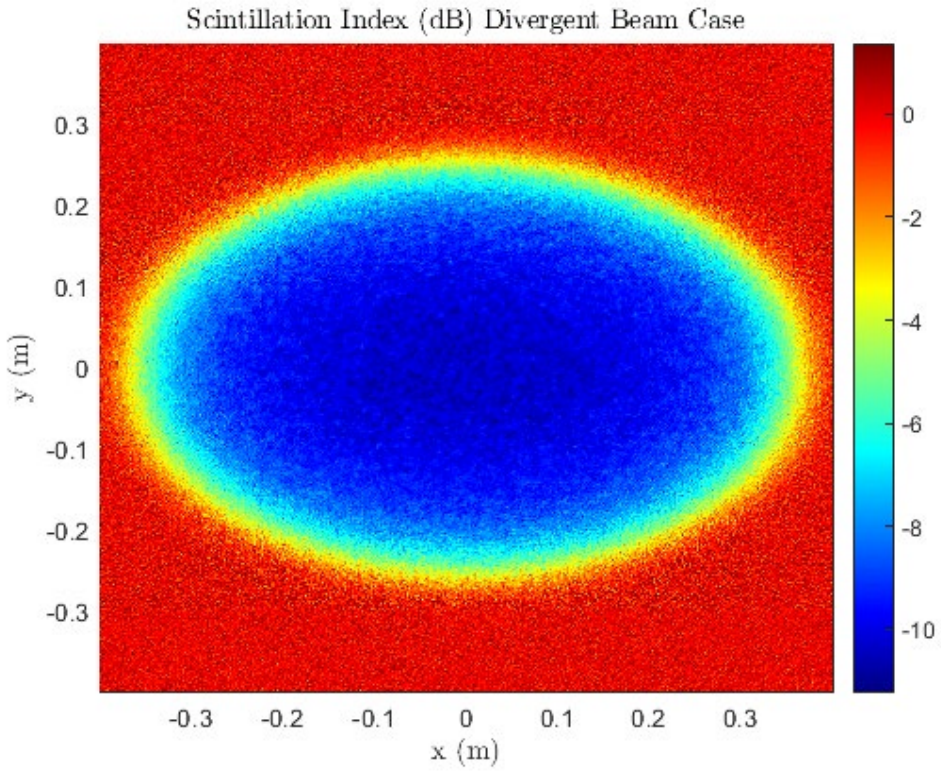


**Figure 3-5:** Output plane scintillation index in decibels for $\mu_x = \mu_y = 1$, $W_0 = 1.4$ cm, $W_x = 15$ cm, $W_y = 7.5$ cm, $L$ = 530 m, spherical wave Rytov variance of .1 case.

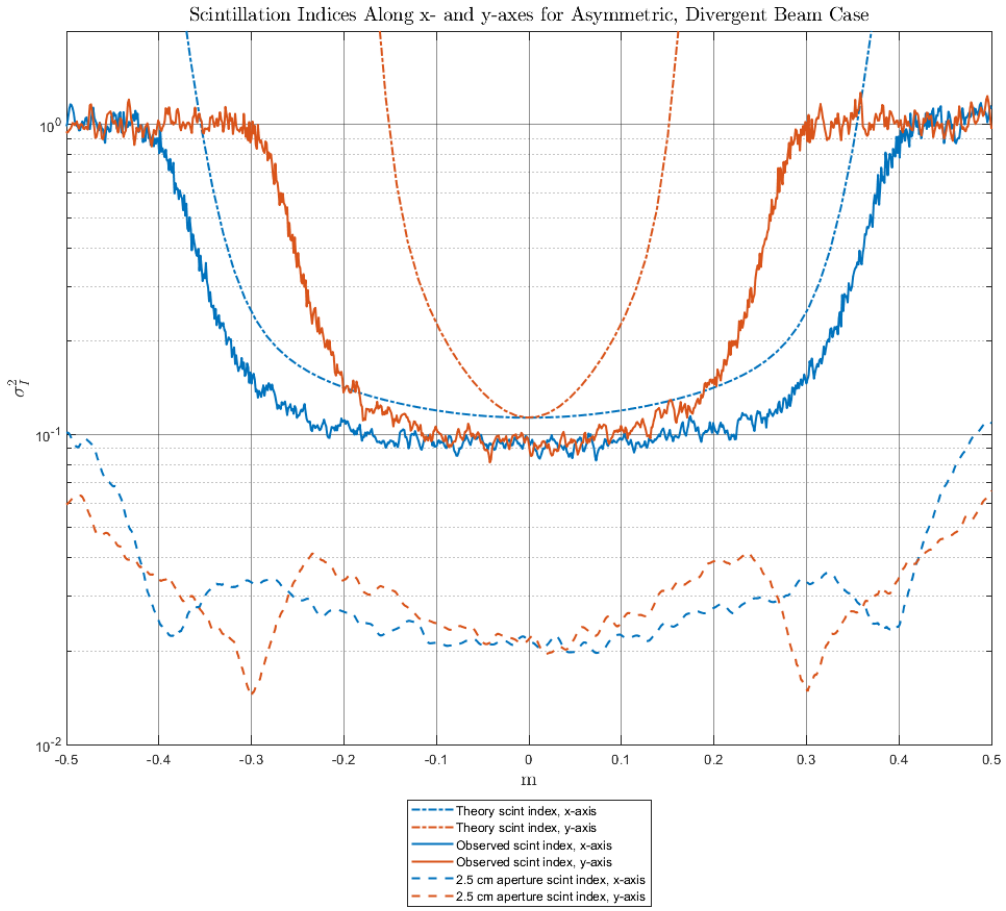


**Figure 3-6:** Comparison of observed and theoretically predicted scintillation indices in for $\mu_x = \mu_y = 1$, $W_0 = 1.4$ cm, $W_x = 15$ cm, $W_y = 7.5$ cm, $L$ = 530 m, spherical wave Rytov variance of .1 case.

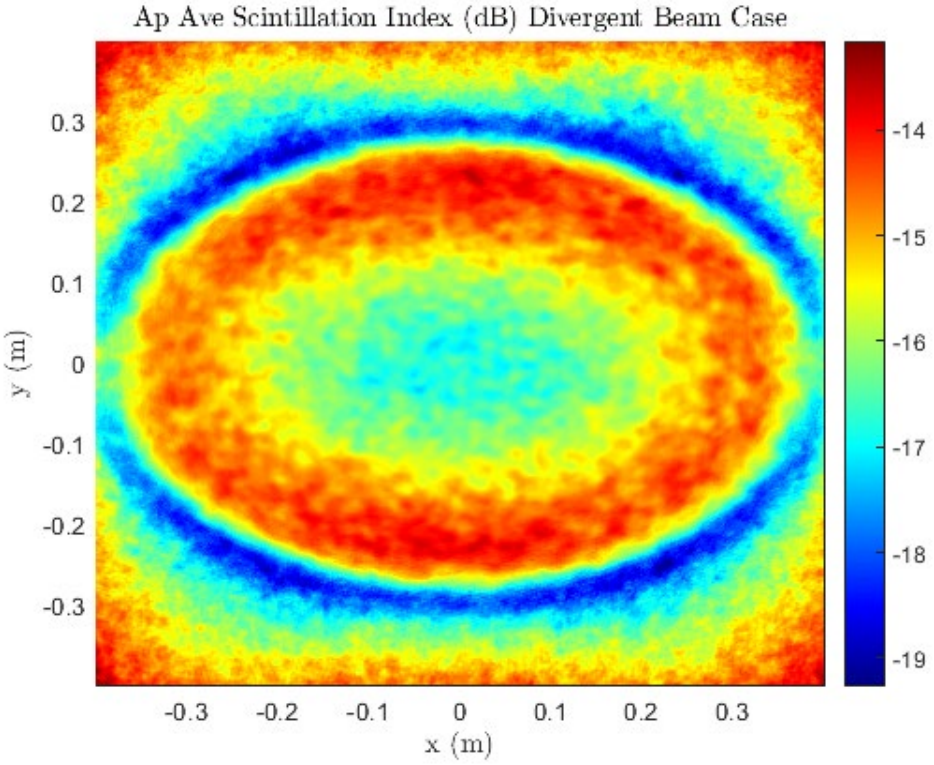


**Figure 3-7:** Output plane aperture averaged scintillation index in decibels for $\mu_x = \mu_y = 1$, $W_0 = 1.4$ cm, $W_x = 15$ cm, $W_y = 7.5$ cm, $L$ = 530 m, spherical wave Rytov variance of .1 case. Beam intensity was averaged over a 2.5 cm diameter aperture for this trial.

Figure 3-6 underscores problems with the theoretical predictions from the weak fluctuation theory. We make the following observations:

1. The on-axis scintillation index is roughly accurate, but overestimates turbulence at the beam's long term center.
2. The scintillation index prediction trends well with theory along the semi-major axis of the spot ellipse.
3. The scintillation index prediction trends very poorly with theory along the semi-minor axis of the spot ellipse.

4. The scintillation index produced from the phase screen simulation observations near the diffraction limited spot radii are approximately equal.
5. Use of a 2.5 cm aperture provides significant attenuation of the observed scintillation index.
6. The on-axis scintillation index is better approximated by the spherical wave Rytov variance (0.1) than the theoretical prediction.

Regarding observations number 2 and 3, in order to sanity check the results we have also included simulation results for a symmetric divergent beams, below.

A second run of simulation set was performed using a beam with $W_0 = 1.4$ cm, $W_x = 15$ cm, and $F_{0,x} = -54.63$ m. We believed that this step was necessary because weak fluctuation theory predictions for scintillation index have been present in the literature for quite some time [9], and off-axis scintillation index predictions have been compared to theoretical predictions. In light of that, we have included results for the 15 cm and 7.5 cm diffraction limited spot size cases in Figure 3-8 and Figure 3-9, respectively. As Figure 3-8 and Figure 3-9 demonstrate, for symmetric input beam parameters the theory appears to work quite well. Additionally, the attenuation of scintillation index via aperture averaging for this case is roughly the same as for asymmetric beam case with an identical turbulence profile.

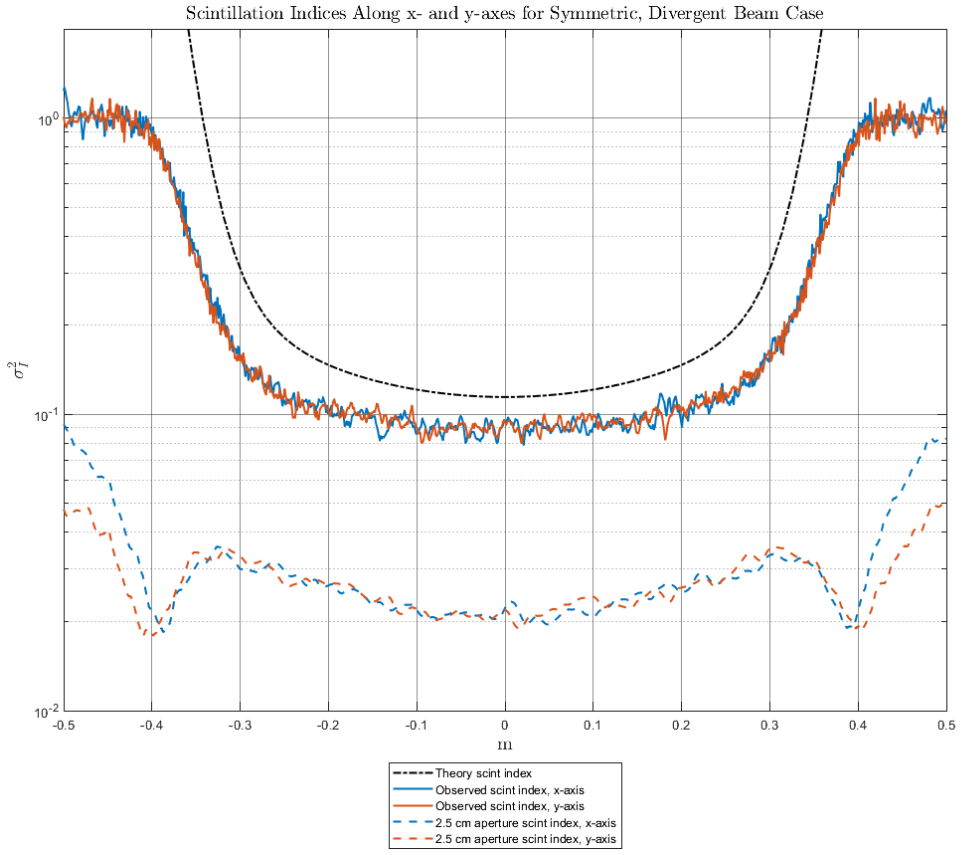


**Figure 3-8:** Comparison of observed and theoretically predicted scintillation indices in for $\mu_x = \mu_y = 1$, $W_0 = 1.4$ cm, $W = 15$ cm, $L$ = 530 m, spherical wave Rytov variance of .1 case.

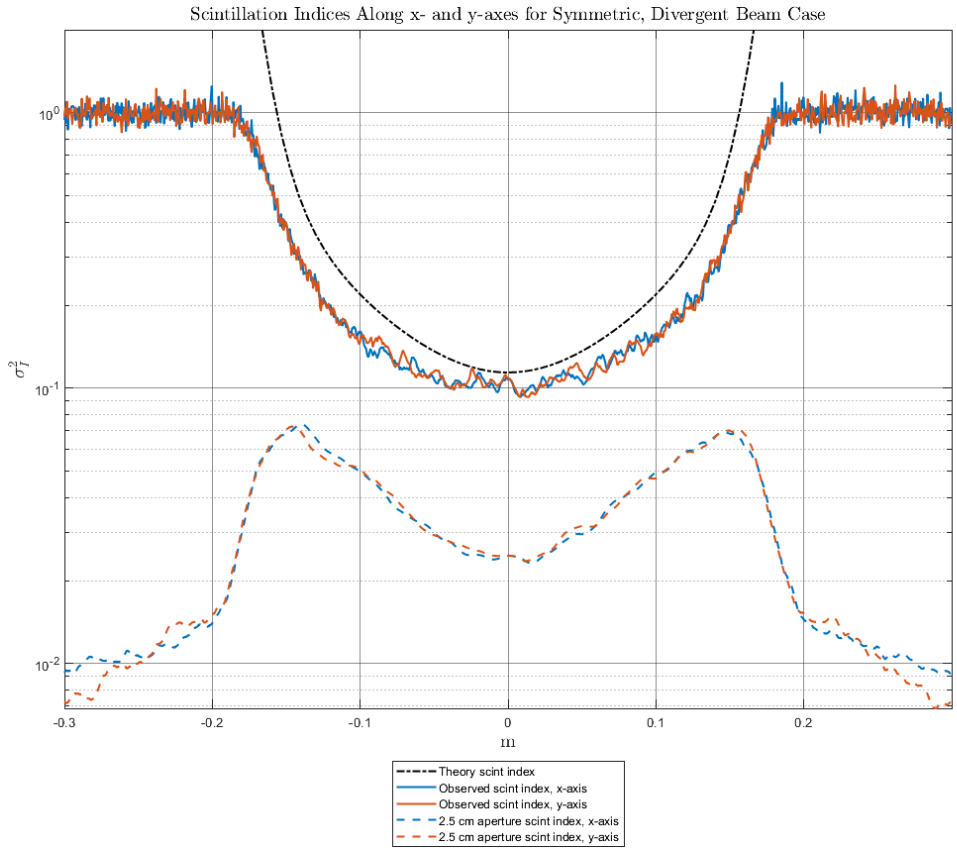


**Figure 3-9:** Comparison of observed and theoretically predicted scintillation indices in for $\mu_x = \mu_y = 1$, $W_0 = 1.4$ cm, $W = 7.5$ cm, $L$ = 530 m, spherical wave Rytov variance of .1 case.

Given the issues observed with the theoretical predictions we use an approximation aimed at better estimating the scintillation index within the spot ellipse, which will be of key importance in our experimental results presented in the next chapter. Noting that the radial component of scintillation index along the beam's semi-major axis is approximated quite well by Equation (3-24), we build a new approximation based on the following:

1. The radial component of the scintillation index is approximately parabolic within the diffraction limited spot ellipse [9, 24].

2. The on-axis component of scintillation index for divergent beams is better approximated by the spherical wave Rytov variance than Equation (3-23).
3. The scintillation index along the semi-minor axis is better approximated by scaling the semi-major axis prediction such that the scintillation index at the spot radius of the semi-minor axis equals the corresponding scintillation index at the spot radius of the semi-major axis.

In order to explicitly demonstrate observation number two we have included Figure 2-10 which shows that, for a divergent beam case, this observation is robust across a number of $\mu_y$ values. In Figure 2-10 we have provided some averaging of the scintillation index around the beam centroid using the following methods:

a) Using the point estimate as the beam center (0,0).
b) Averaging those factors collected within a 1 cm radius around the beam center.
c) Averaging the factors collected from points within half the spot radius for a given transverse angle across the receive plane (i.e. $\sqrt{x^2/W_x^2 + y^2/W_y^2} \leq .5$), which we dub the *half spot average* method.
d) Averaging the factors collected from points within the spot radius for a given transverse angle across the receive plane (i.e. $\sqrt{x^2/W_x^2 + y^2/W_y^2} \leq 1$), which we dub the *full spot average* method.

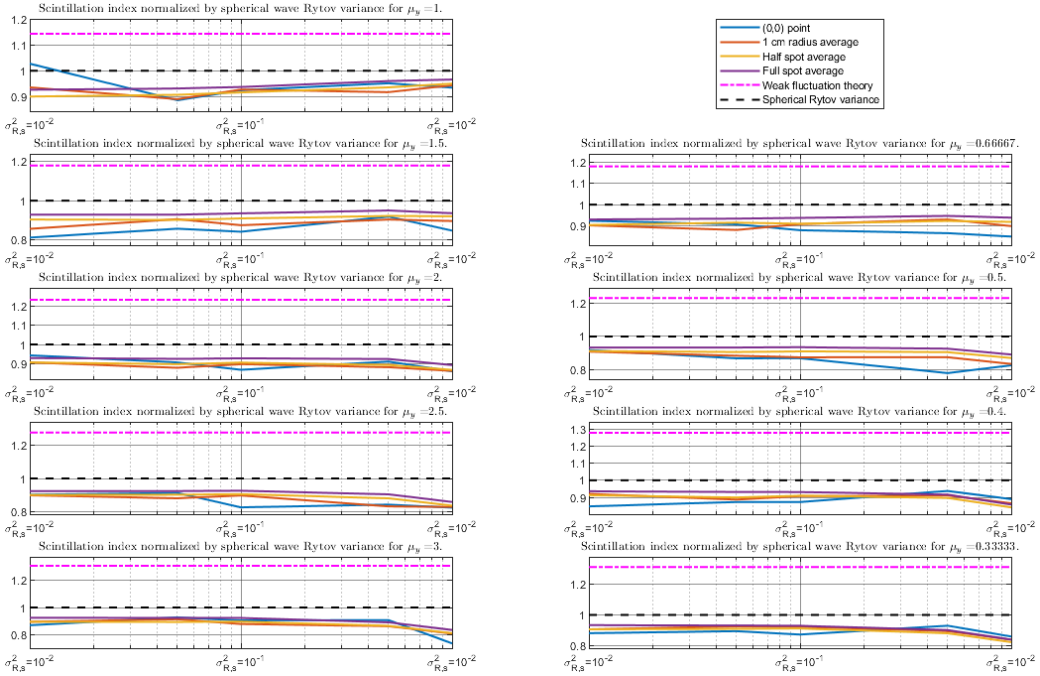


**Figure 3-10:** Comparison of observed and theoretically predicted scintillation indices plotted as functions of the spherical wave Rytov variance for an asymmetric beam in isotropic turbulence for a range of $\mu_y$'s with $\mu_x = 1$, $W_0 = 1.4$ cm, $W_x = 15$ cm, $W_y = 11.25$ cm, $L = 530$ m.

In order to deal with these observations as well as the issue of anisotropy (i.e. the faster rise of scintillation index along the axis of lower $\mu$), we investigate an approximation provided by Beason [87] for symmetric beams in the presence of anisotropic turbulence, assuming $\tilde{C}_n^2$ has been calibrated such that $\mu_x = 1$:

$$\sigma_{l,r}^2(x,y,L) \cong \frac{\pi\Gamma\left(2-\frac{\alpha}{2}\right)}{\alpha-1} A(\alpha)\tilde{C}_n^2 k_0^{4-\frac{\alpha}{2}} L^{\frac{\alpha}{2}-1} \Lambda^{\frac{\alpha}{2}} \times \int_0^{2\pi} \left(x\cos\varphi + \frac{y\sin\varphi}{\mu_y}\right)^2 \left(\cos^2\varphi + \frac{\sin^2\varphi}{\mu_y^2}\right)^{\frac{\alpha}{2}-2} d\varphi \tag{3-27}$$

For the isotropic turbulence case ($\mu_x = \mu_y = 1$), clearly the issue regarding equalizing the scintillation index at the spot radii can be achieved via the revised radial scintillation index approximation:

$$\tilde{\sigma}_{I,r}^2(x,y,L) \cong \frac{\pi\Gamma\left(2-\frac{\alpha}{2}\right)}{\alpha-1} A(\alpha)\tilde{C}_n^2 k_0^{4-\frac{\alpha}{2}} L^{\frac{\alpha}{2}-1} \cdot \left[Minumum(\Lambda_x,\Lambda_y)\right]^{\frac{\alpha}{2}}$$
$$\times \left(\cos^2[\angle(x+jy)] + \frac{\Lambda_y}{\Lambda_x}\sin^2[\angle(x+jy)]\right) \tag{3-28}$$
$$\times \int_0^{2\pi} \left(x\cos\varphi + \frac{y\sin\varphi}{\mu_y}\right)^2 \left(\cos^2\varphi + \frac{\sin^2\varphi}{\mu_y^2}\right)^{\frac{\alpha}{2}-2} d\varphi$$

We note that for Equation (3-28) yields, $\tilde{\sigma}_{I,r}^2(x,0,L) = \sigma_{I,r}^2(x,0,L)$, where $\sigma_{I,r}^2(x,0,L)$ is given by Equation (3-27). However for isotropic turbulence ($\mu_y = 1$), for $y = W_y$, Equation (3-28) yields $\tilde{\sigma}_{I,r}^2(0,W_y,L) = \sigma_{I,r}^2(W_x,0,L)$ by virtue of the factor $\left[Minumum(\Lambda_x,\Lambda_y)\right]^{\frac{\alpha}{2}} \times \cos^2[\angle(x+jy)] + \frac{\Lambda_y}{\Lambda_x}\sin^2[\angle(x+jy)]$. This is because of the following relationship:

$$\tilde{\sigma}_{I,r}^2(0,W_y,L) \cong \frac{4\pi^2\Gamma\left(2-\frac{\alpha}{2}\right)}{\alpha-1} A(\alpha)\tilde{C}_n^2 k_0^{4-\frac{\alpha}{2}} L^{\frac{\alpha}{2}-1} \cdot \Lambda_x^{\frac{\alpha}{2}} \cdot \frac{\Lambda_y}{\Lambda_x} \cdot W_y^2$$
$$= \frac{4\pi^2\Gamma\left(2-\frac{\alpha}{2}\right)}{\alpha-1} A(\alpha)\tilde{C}_n^2 k_0^{4-\frac{\alpha}{2}} L^{\frac{\alpha}{2}-1} \cdot \Lambda_x{}^{\frac{\alpha}{2}} \cdot \frac{W_x^2}{W_y^2} \cdot W_y^2 \tag{3-29}$$
$$= \tilde{\sigma}_{I,r}^2(W_x,0,L)$$

The results using this revise approximation are shown below. Although we acknowledge that the revision is not perfect, the results within the diffraction limited ellipse are much improved as compared to Figure 3-6.

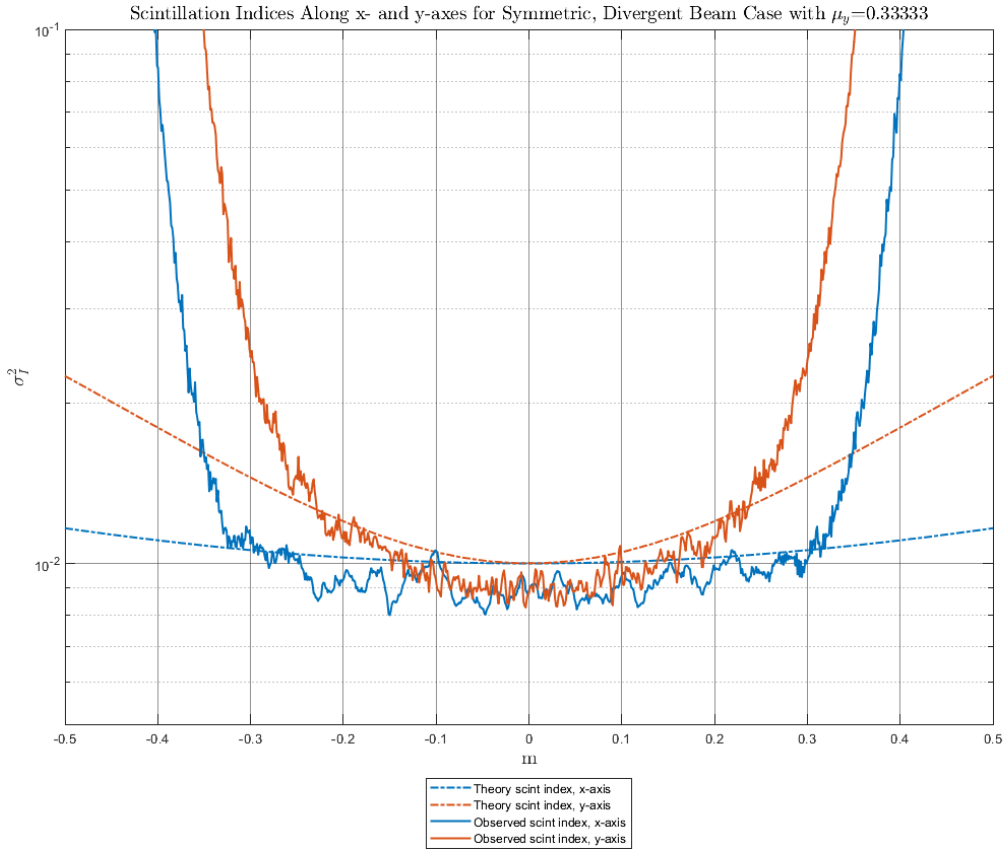


**Figure 3-11:** Comparison of observed and theoretically predicted scintillation indices for an asymmetric beam in anisotropic turbulence for $\mu_y = 1/3$, $W_0 = 1.4$ cm, $W = 15$ cm, $L = 530$ m, spherical wave Rytov variance of .01 case.

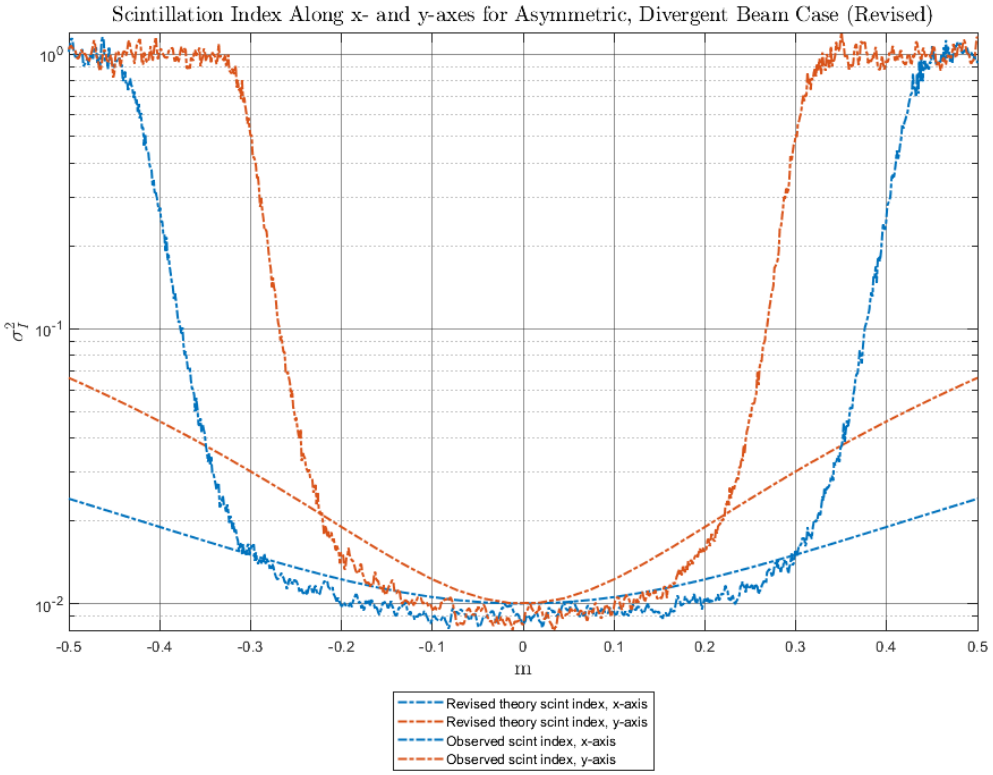


**Figure 3-12:** Comparison of observed and theoretically predicted scintillation indices for an asymmetric beam in isotropic turbulence for $\mu_x = \mu_y = 1$, $W_0 = 1.4$ cm, $W_x = 15$ cm, $W_y = 7.5$ cm, $L$ = 530 m, spherical wave Rytov variance of .01 case.

In order to use the approximations in experiments using apertured receiver systems, we seek to also assess the aperture averaging factor associated with divergent beams in anisotropic turbulence. Specifically, we are interested in the impact of a 2.5 cm circular aperture. Prior to reviewing the simulation data, we review the theory of aperture averaging of scintillation with regards to a parameter we have so far ignored in this chapter, which is the inner scale. The so called *Kolmogorov microscale* of turbulence is typically approximated by the expression [80]:

$$l_0 = \left(\frac{\nu^3}{\varepsilon}\right)^{1/4} \tag{3-30}$$

where $\nu$ is the kinematic viscosity, with units of $m^2/s$, and $\varepsilon$ is the rate of kinematic energy dissipation, with units of watts per kilogram or $m^2/s^3$. In Section 2.6 we discussed the modified atmospheric spectrum, which is dependent upon both inner and outer scale parameters. Prior to work done by Andrews [74] and Frehlich [53] to approximate the spectral energy density near the spectral cutoff studied by Hill [26], it was common to account for inner and outer scale effects by using the von Karman spectrum given by [9]:

$$\Phi_n(\kappa) = 0.0330 \cdot C_n^2 \cdot \frac{\exp(-\kappa^2/{\kappa_l}^2)}{(\kappa^2 + \kappa_0^2)^{11/6}} \tag{3-31}$$

$$\kappa_l = \frac{3.3}{l_0}, \qquad \kappa_0 = \frac{2\pi}{L_0} \tag{3-32}$$

This equation for the power spectrum is essentially identical to that of the modified spectrum, but without the *f* function factor given by Equation (2-30). The plot below displays the effect of inner scale on the scintillation index for vary beam conditions.

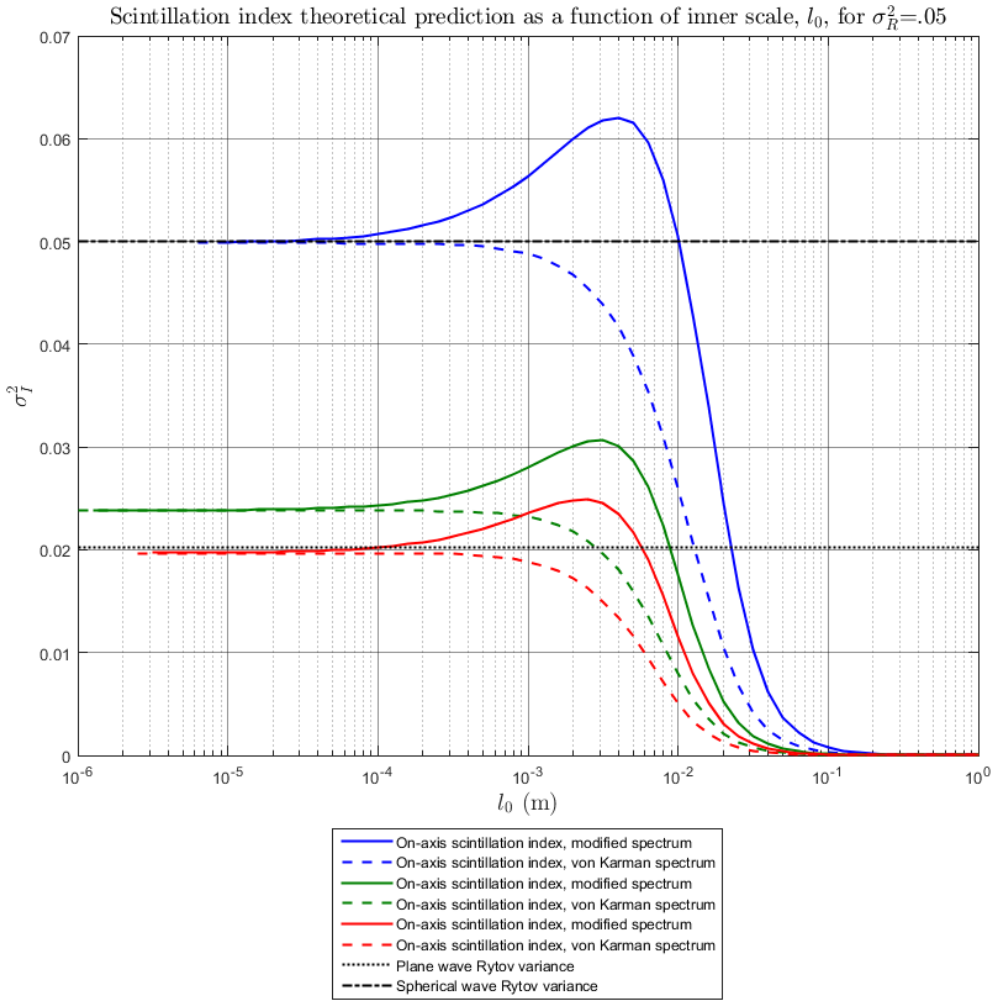


**Figure 3-13:** Theoretically predicted scintillation index as a function of inner scale, $l_0$, for a variety of beams in isotropic turbulence: 1) **Blue** curves represent prediction for a beam with $W_0 = 50$ cm; 2) **Green** curves represent prediction for an initially collimated beam with $W_0 = 1.4$ cm and $F_0 = 120$ m; 3) **Red** curves represent prediction for a beam with $W_0 = 50$ μm and $F_0 = 530$ m, which was the propagation distance for all curves. All results are for a wavelength of 632.8 μm and a plane wave Rytov variance of .05.

Before looking at inner scale affects, we note that Figure 3-13 shows that for an initially very wide, collimated beam the on-axis scintillation index approaches the plane was Rytov variance very closely for small inner scales. Additionally, the initially very small with a divergence equal to the propagation

distance behaves approximately the same as a spherical wave in Kolmogorov turbulence for small inner scales. These observations lend confidences that our numerical evaluations of the scintillation index integrals are correct.

However, the theoretical dependency of scintillation index on inner scale for on scintillation for both the modified spectrum and von Karman spectrum are both quiet drastic. Luckily, analysis of these effects when using an apertured receiver indicate the effects are tempered with large enough apertures, as we will demonstrate. Sasiala [88] has provided an aperture averaging filter function, *F*, for use in spectral domain scintillation index equations, in this case Equation (3-25), using a normalized Airy function given by:

$$F(\kappa, D) = \left[\frac{2J_1(\kappa D/2\,)}{\kappa D/2}\right]^2 \tag{3-33}$$

where $D$ is the diameter of the aperture, $\kappa = \sqrt{\kappa_x^2 + \kappa_y^2}$ is the radial wavenumber, and $J_1$ is the first order Bessel function of the first kind. Insertion of this filter function into Equation (3-25) yields the results below, demonstrating that aperturing tempers the results of the inner scale.

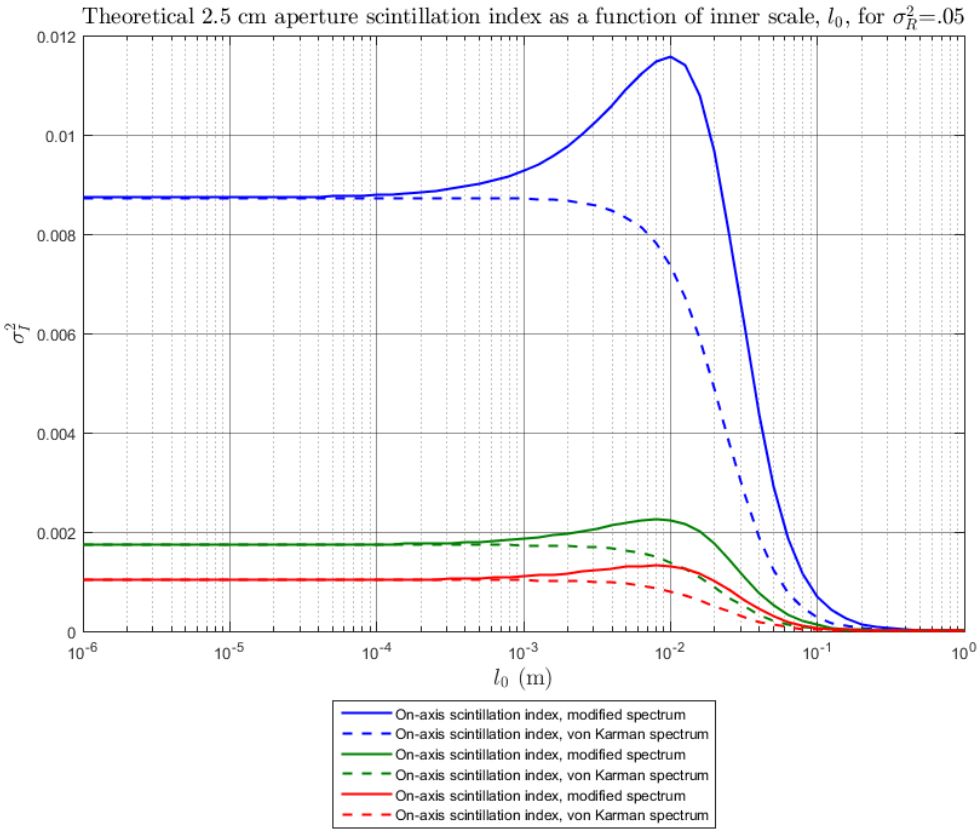


**Figure 3-14:** Theoretically predicted 2.5 cm diameter aperture averaged scintillation index as a function of inner scale, $l_0$, for a variety of beams in isotropic turbulence: 1) **Blue** curves represent prediction for a beam with $W_0 = 50$ cm; 2) **Green** curves represent prediction for an initially collimated beam with $W_0 = 1.4$ cm and $F_0 = 120$ m; 3) **Red** curves represent prediction for a beam with $W_0 = 50$ μm and $F_0 = 530$ m, which was the propagation distance for all curves. All results are for a wavelength of 632.8 μm and a plane wave Rytov variance of .05.

Although weak fluctuation theory approximations for the aperture averaging factor are available, we choose to investigate the aperture averaging factor using our wave propagation simulations directly. This is because all of the weak fluctuation theory filter functions for aperture averaging share the characteristic that they scale directly with the $C_n^2$ (and therefore the Rytov variances) along the propagation path whereas, as we will demonstrate, we note a

slight increase in the aperture averaging factor as the Rytov variance (and therefore $C_n^2$) is increased, as we will demonstrate. Before moving forward, we would like to discuss general trends of the aperture averaging function for asymmetric beams. The aperture averaging factor as a function of distance along the semi-major ($x$-) and semi-minor ($y$-) axes of the spot ellipse for a somewhat typical case is shown in Figure 3-15. Having examined many such plots we have observed that within the diffraction limited spot ellipse, if one ignores the noisiness of observation, the aperture averaging factor is approximately constant.

In order to mitigate the noisiness of the aperture averaging factor estimates, we compare several methods for estimating the on-axis aperture averaging factor in light of all of the phase screen simulation data we've collected:

1. Using the point estimate as the beam center (0,0).
2. Averaging those factors collected within a 1 cm radius around the beam center.
3. Averaging the factors collected from points within half the spot radius for a given transverse angle across the receive plane (i.e. $\sqrt{x^2/W_x^2 + y^2/W_y^2} \leq .5$), which we dub the *half spot average* method.
4. Averaging the factors collected from points within the spot radius for a given transverse angle across the receive plane (i.e. $\sqrt{x^2/W_x^2 + y^2/W_y^2} \leq 1$), which we dub the *full spot average* method.

Figure 3-16 and Figure 3-17 help visualize the impact of using the four cited methods. We note that generally, the *half spot ellipse method* significantly reduces the noisiness of the estimates without significantly appearing to attenuate the aperture averaging factor away from the 1 cm or point estimates, which cannot be said for the full spot average method.

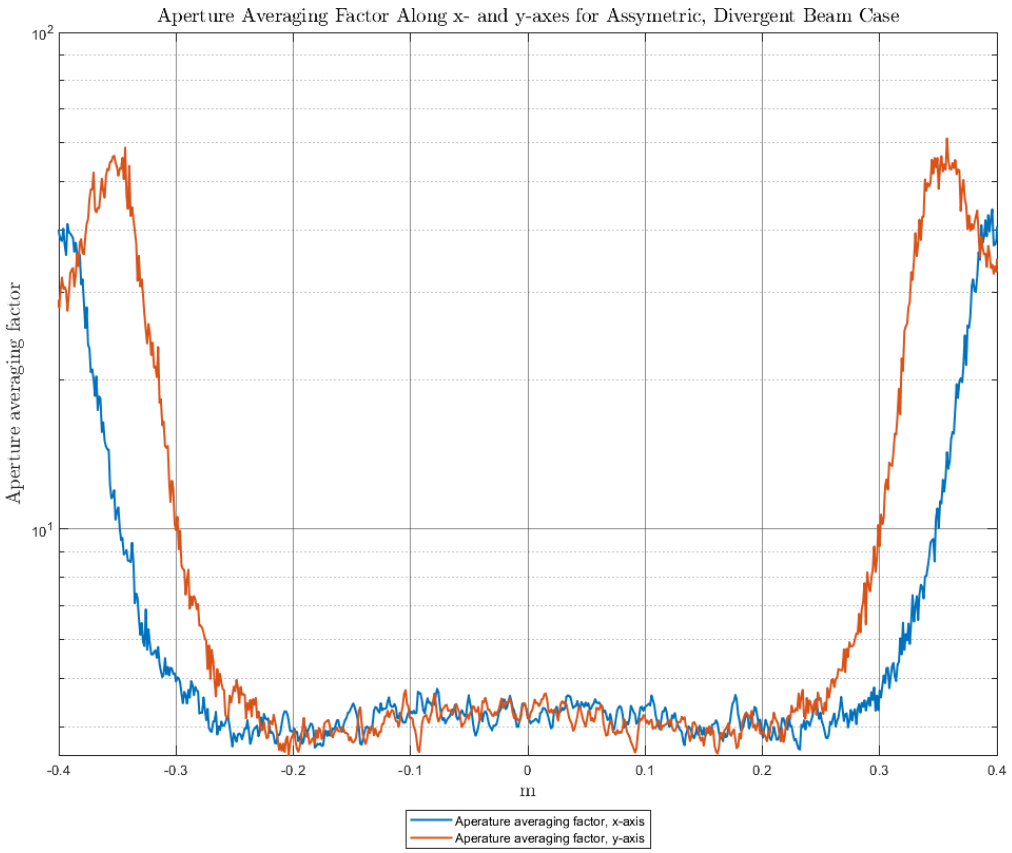


**Figure 3-15:** Aperture averaging factors along $x$- and $y$-axes for $\mu_x = \mu_y = 1$, $W_0 =$ 1.4 cm, $W_x = 15$ cm, $W_y = 11.25$ cm, $L$ = 530 m, spherical wave Rytov variance of .1 case.

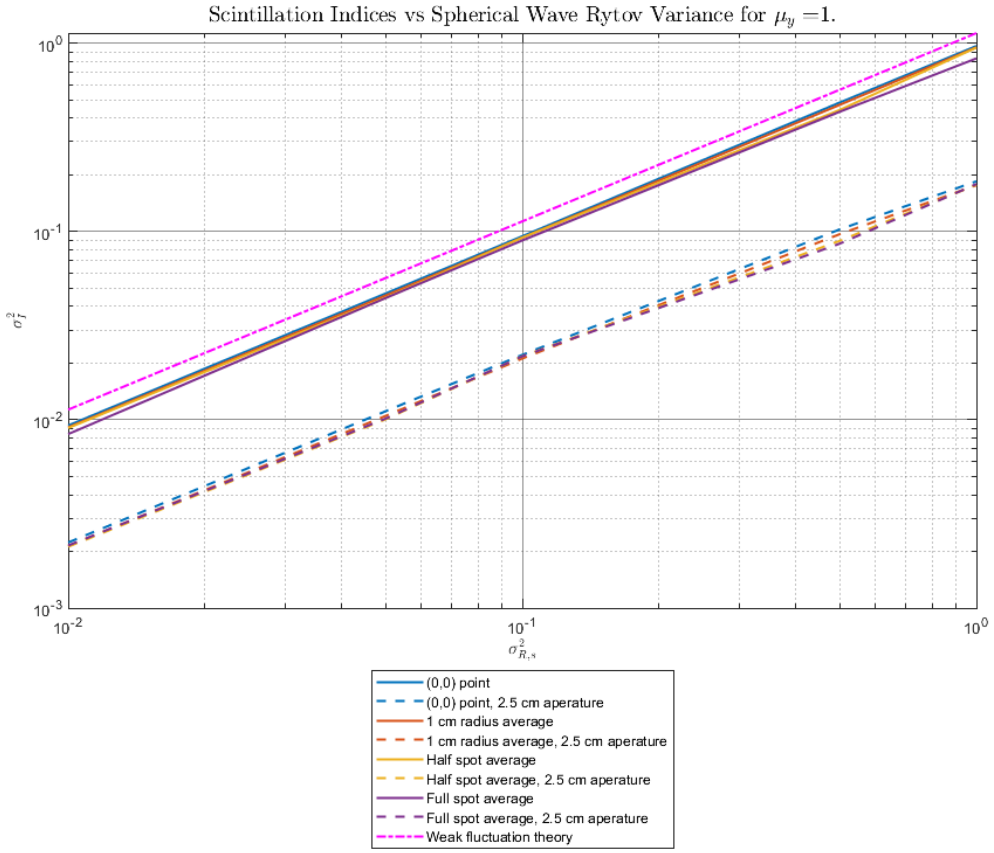


**Figure 3-16:** Comparison of point vs 2.5 diameter aperture averaged scintillation indices for a variety of spherical wave Rytov variances and an asymmetric beam in isotropic turbulence using $\mu_x = \mu_y = 1$, $W_0 = 1.4$ cm, $W_x = 15$ cm, $W_y = 7.5$ cm, $L$ = 530 m.

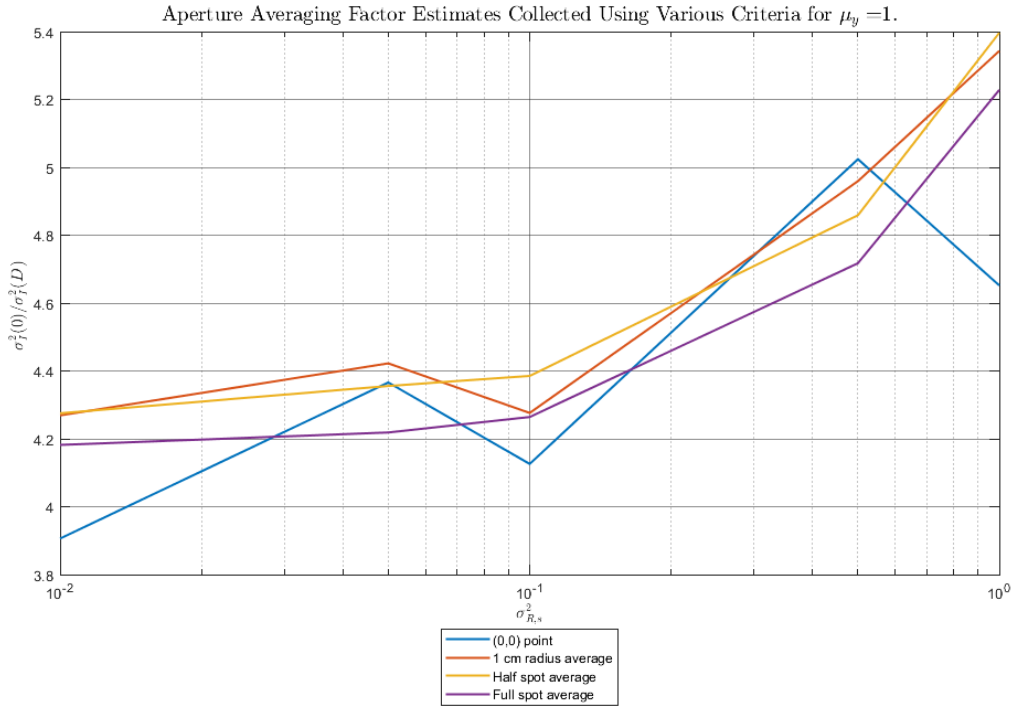


**Figure 3-17:** Comparison of 2.5 diameter aperture averaging factors for a variety of spherical wave Rytov variances for an asymmetric beam in isotropic turbulence using $\mu_x = \mu_y = 1$, $W_0 = 1.4$ cm, $W_x = 15$ cm, $W_y = 7.5$ cm, $L$ = 530 m. The results were further averaged using the following methods

Finally, in order to build confidence that the techniques discussed are correct for a range of anisotropy ratios, we have provided a plot of the half spot averaged aperture averaging factor across a number of $\mu_y$'s between 1/3rd and 3, while holding $\mu_x = 1$. Figure 3-18 demonstrates that for a wide range of anisotropy ratios, the aperture averaging factor as a function of the spherical wave Rytov variance is approximately constant over a wide range of $\mu_y$'s. Additionally, we have performed the same analysis for a variety of symmetric and asymmetric beams with differing spot sizes, and noted that the aperture averaging factors collected are approximately the same.

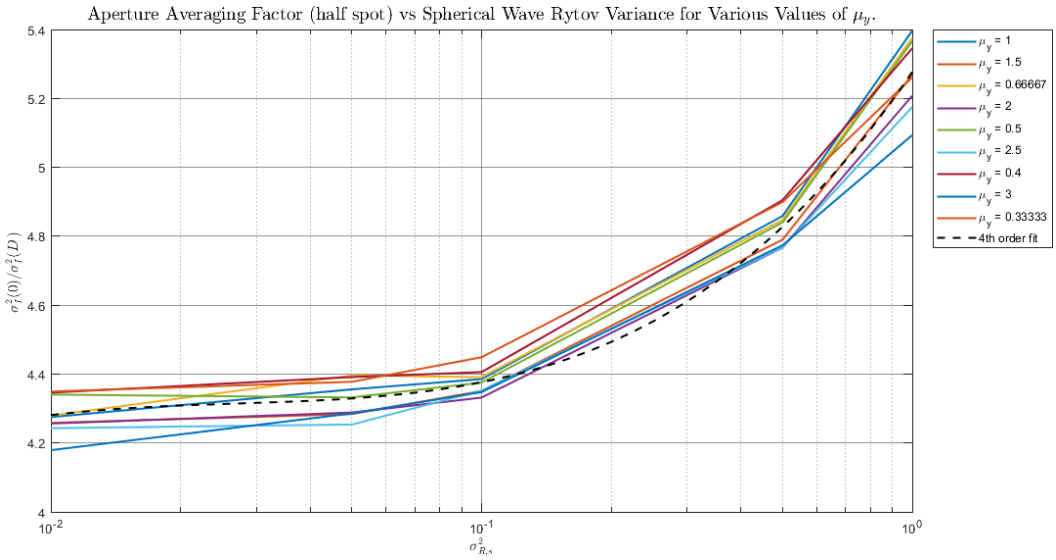


**Figure 3-18:** Aperture averaging factor for various values of $\mu_y$ plotted as a function of the spherical wave Rytov variances using an asymmetric beam in isotropic turbulence using $W_0 = 1.4$ cm, $W_x = 15$ cm, $W_y = 7.5$ cm, $L = 530$ m.

In the next chapter, we will use the aperture averaging factor collected for divergent beams in order to estimate $C_n^2$ over a long path in the weak fluctuation regime. In order to do so, we have performed a fourth order polynomial fit of the aperture averaging factor, averaged across all $\mu_y$'s, as a function of the natural logarithm of the spherical wave Rytov variance. Details regarding the fit plotted in Figure 3-18 are given in Equations (3-34) and (3-35). We note that there is only a small error of the fit across all $\mu_y$ (1.28% standard deviation, and 3.47% maximum error).

$$F_{ap}\left(\sigma_{R,s}^2, D\right) = \frac{\sigma_I^2(0)}{\sigma_I^2(D)} \cong \sum_{n=0}^{4} A_n \cdot \left[\ln\left(\sigma_{R,s}^2\right)\right]^n \tag{3-34}$$

$$\begin{bmatrix} A_0 \\ A_1 \\ A_2 \\ A_3 \\ A_4 \end{bmatrix} = \begin{bmatrix} 5.277 \\ 7.975 \cdot 10^{-1} \\ 2.342 \cdot 10^{-1} \\ 2.660 \cdot 10^{-2} \\ 6.847 \cdot 10^{-4} \end{bmatrix} \tag{3-35}$$

In conclusion, we have noted issues with the weak fluctuation theory predictions for the scintillation index of divergent and asymmetrical beams. However, the set of updated approximations developed in this section provide a good fit of the unexplained differences between the weak fluctuation theory results and the observed results from Monte-Carlo phase screen simulations of optical propagation through turbulence within the spot ellipse. We remind the reader, that both the weak fluctuation theory and the phase screen codes use the Markov Approximation (see Section 1.2) and the Paraxial Approximation, so these discrepancies are somewhat unexpected. Although it seems evident a thorough review of the mathematics and symmetry assumptions employed to develop the weak fluctuation theory predictions for beam waves needs to be performed, we leave these items as work to be performed in the future.

# Chapter 4 : Experimental Investigations Atmospheric Distortions Using a Multi-Aperture Transmissometer

## 4.1: Introduction

Lasers transmissometers are devices used to estimate the absorption of light traveling through the atmosphere [89]. These devices have applications in monitoring visibility conditions [90], measuring concentrations of aerosols in the atmosphere [91], estimating concentrations of dissolved particles in media [92], and estimating predictions of thermal blooming [93]. Accurate monitoring of atmospheric absorption of light is highly desirable in free-space optical (FSO), directed energy (DE), and remote sensing (RS) applications, as alteration of system performance due to aerosol effects can lead to system degradations and failures [94].

Transmissometers consist of transmitters and receivers, which are typically spaced at short distances so as to enable total collection of the transmitted laser beam at the receiving aperture in the presence of optical turbulence effects. Although other apparatus aimed at estimating extinction coefficients of the atmosphere over longer, multiple kilometer paths have been experimentally tested [95], devices typically produce useful extinction estimates below the strong turbulence regime. With these considerations as motivating factors, the Maryland Optics Group (MOG) has designed a multi-aperture transmissometer (MAT)

capable of long-path extinction coefficient estimates, which uses beam profiling techniques robust to optical turbulence distortions [71]. In this paper, we will demonstrate the successful operation of the MOG MAT at estimating absorption in the strong turbulence regime, as well as in estimating turbulence strength by virtue of estimates of the turbulent beam spreading along long paths along with scintillation index profiling.

## 4.2: MOG MAT Fundamentals

Laser transmissometers are devices traditionally used to measure the extinction coefficient of a medium by measuring the total intensity of light at a receiver larger in diameter than the diameter of the beam, and measuring the extinction coefficient as [83]:

$$\sigma = -\frac{1}{L} ln\left(\frac{\int I\, dA}{\int I_0 dA}\right) \tag{4-1}$$

$$\sigma_{dB} = -\frac{10}{L} log_{10}\left(\frac{\int I\, dA}{\int I_0 dA}\right) \tag{4-2}$$

Where $L$ is the propagation length, $I$ is the optical intensity at the receiver, $I_0$ is the optical intensity at the transmitter, and $\int dA$ is the area integral [94]. Due to beam spreading by optical turbulence effects, as well as diffractive effects, traditional transmissometer transmitters and receivers can only be spaced on the order of 10's of meters apart. In order to get an accurate measurement across, say, an airfield, transmissometers must be periodically spaced throughout the length of the field.

The multi-aperture, hexagonal transmissometer designed by the Maryland Optics Group utilizes an array of 13 point detectors, which sample incoming light at various positions. The device also uses three retroreflecting dielectric corner cubes to aid in aligning the transmitter at long range. Additionally, the device can be controlled using a touch screen or via a remote radio frequency link.

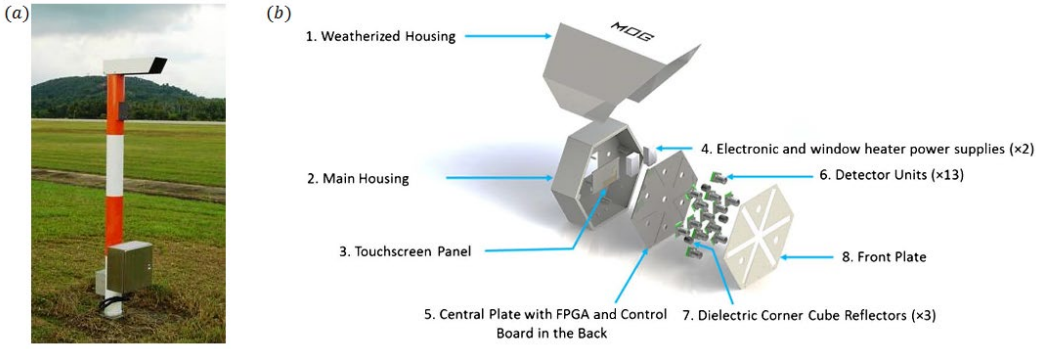


**Figure 4-1:** Juxtaposition of: a) Traditional single aperture transmissometer used for making a short range extinction estimate in an airfield; b) Maryland Optics Group multi-aperture transmissometer designed for estimating extinction coefficients over path lengths of the order of magnitude of a kilometer.

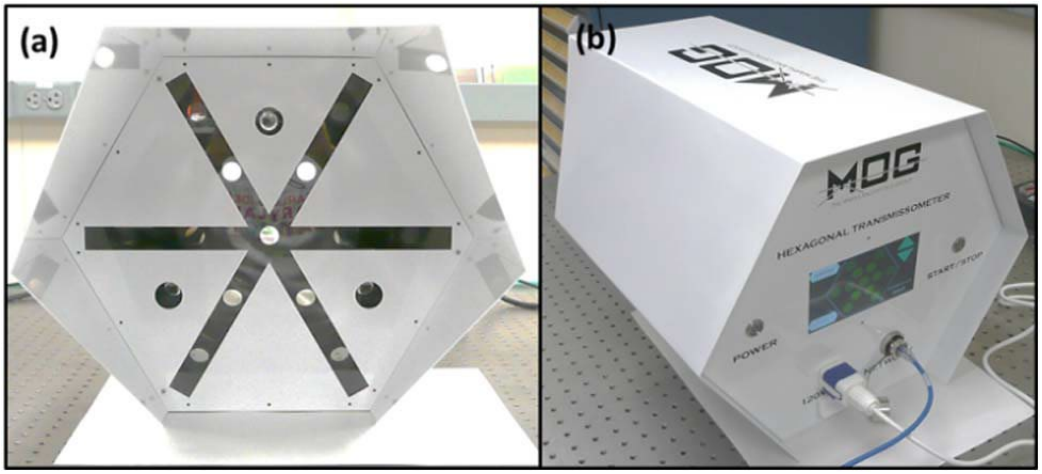


**Figure 4-2:** Pictures of the multi-aperture hexagonal transmissometer displacing: a) The thirteen detectors and corner cube reflectors; b) the local user interface.

The MOG MAT receiver utilizes an array of 13 point detectors that sample incoming light at various positions. The device also utilizes three retroreflecting dielectric corner cubes to aid visual alignment of the laser transmitter at long range. Figure 4-1 shows a breakout diagram of the MOG MAT and its various subcomponents. Typically, the transmitter is mounted on a stabilized tripod or optical table, and the receiver is mounted on a tripod. Table 4-1 summarizes the nominal specifications of the transmissometer system.

| **MOG Multi-Aperture Transmissometer Specifications** | |
|---|---|
| Transmitter | Receiver Detection |
| 632.8 nm HeNe Laser Source | 13 sub-aperture detectors |
| Greater than 95% $TEM_{00}$ Mode Purity | 60° angular spacing |
| Beam expanded to 2.8 cm diameter | 6.9 cm radial spacing |
| 10 Hz chopping frequency | 25 mm diameter aspherical lenses |
| | 16 mm lens focal length |
| Receiver Features | 632nm bandpass filters, ±5nm FWHM |
| Weatherized receiver housing | 550 Hz read-out rate |
| 3 retroreflecting cubes to aid alignment | |
| Transimpedance amplifiers | |

**Table 4-1:** Nominal MOG MAT specifications

Once the transmitter and receiver have been aligned, an optical chopping wheel is enabled at the transmitter, and the receiver is set to record. Binary files documenting timestamps and values of detector readings are created locally on the transmissometer, to be analyzed in post-processing. The optical intensity is

assumed to be directly proportional to the voltages recorded at each sub-aperture. Based upon sparse sampling techniques [96], the MOG MAT's thirteen sub-aperture detectors' recorded samples enable beam profiling of the average intensity profile of the received signal. The averaging time should be chosen to be long enough to minimize receiver noise and scintillation variations, but short enough that a significant global change in atmospheric conditions does not occur.

Previously, we presented several predictions of spot size as functions of $W_0$, $F_0$, $L$, $C_n^2$, $\mu_x$, $\mu_y$, and $\alpha$, e.g. as per Equations (3-6) through (3-17). We return to re-examine the spectral model as shown in (20) in order to make a point regarding degrees of freedom. We can give a structure constant specific to the *x*-direction:

$$\Phi_n\left(\vec{\kappa}_\rho, 0\right) = \frac{\tilde{C}_n^{\,2} A(\alpha)\mu_x\mu_y}{\left(\mu_x^{\,2}\kappa_x^{\,2} + \mu_y^{\,2}\kappa_y^{\,2}\right)^{\alpha/2}} = \frac{\tilde{C}_n^{\,2}\mu_x^{\,2-\alpha}A(\alpha)\frac{\mu_y}{\mu_x}}{\left(\kappa_x^{\,2} + \frac{\mu_y^{\,2}}{\mu_x^{\,2}}\kappa_y^{\,2}\right)^{\alpha/2}} \qquad (4\text{-}3)$$

We can write a similar form as (4-3) where $\kappa_y^{\,2}$ is not accompanied by any factors in the denominator. For the purposes of evaluating the two dimensional integrals of interest for wave propagation through turbulence, we can define a $\tilde{C}_{n,x}^{\;2}$ and a $\tilde{C}_{n,y}^{\;2}$as per:

$$\tilde{C}_{n,x}^{\;2} = \tilde{C}_n^{\,2}\mu_x^{\,2-\alpha}, \qquad \tilde{C}_{n,y}^{\;2} = \tilde{C}_n^{\,2}\mu_y^{\,2-\alpha} \qquad (4\text{-}4)$$

Therefore, the three variables $\tilde{C}_n^{\,2}$, $\mu_x$, and $\mu_y$ represent only two degrees of freedom. Note that power associated with $\mu_x$ and $\mu_y$ matches that given in Equation

(2-8). Also note that increasing the anisotropy parameters decreases the structure constant in either direction. Therefore, we may say that increasing the anisotropy parameters effectively decreases the level of turbulence.

There is an issue, however, using (4-4) for comparison with point detectors which do not use optical propagation to estimate turbulence or anisotropy. The three dimensional refractive index structure function is given by:

$$D_n(x,y,z) = \tilde{C}_n^2 \left( \sqrt{\frac{x^2}{\mu_x^2} + \frac{y^2}{\mu_y^2} + z} \right)^{\alpha-3} \tag{4-5}$$

This equation suggests that we should set $\tilde{C}_{n,x}^2$ and $\tilde{C}_{n,y}^2$ as per:

$$\tilde{C}_{n,x}^2 = \tilde{C}_n^2 \mu_x^{3-\alpha}, \qquad \tilde{C}_{n,y}^2 = \tilde{C}_n^2 \mu_y^{3-\alpha} \tag{4-6}$$

We elect to adjust results as per Equation (4-6) for consistency with other equipment under test.

## 4.2: Synchronization of Transmitter and Receiver for Elimination of Background Light

In order to measure light from a transmitting laser arriving at the transmissometer receiver, we estimate and remove background light by on / off modulating the beam with a chopping wheel, and subtracting the signal observed during the off period, from the on period [71]. In order to facilitate this, we must synchronize with the wheel, which we choose to run at 10 Hz, as the outer time scale is roughly .1 seconds [9], in order to generate approximately uncorrelated

samples, and the sampling frequency of recordings for each aperture is 250 Hz. In order to facilitate this, a new algorithm has been developed consisting of the following steps:

1. The transmissometer data is offloaded from the measurement device to a local computer.
2. The data is broken up into between 100 and 1000 samples, typically, within a program and stored in memory structures internal to the routine.
3. For each set of samples, a FFT is performed on the sum of the data from all detectors, and the peak frequency is assume to be the center frequency for synchronization, i.e. a rough frequency estimate.
4. For each set of samples, a phase-frequency correlation matrix is constructed (more info on this below) based off the rough frequency estimate, and the reference clock phase and frequency is derived from the reference clock parameters.
5. The sample sets are re-aligned in time, and the synchronization routine searches for sampling skips and repeats. Skips are handled by inserting a sample at the mean time between adjacent samples. Sample repeats are averaged into a common sample.
6. On- and off-samples are collected mid *on*-, *off*-cycle, and two adjacent off-samples values are averaged and subtracted from the straddled on-cycle in order

to generate the final approximately independent sample of the laser propagated through turbulence and absorbing atmosphere.

7. Samples are averaged, and the scintillation index estimated, as an input to later fitting.

To create the phase frequency correlation matrix, first a preliminary three dimensional data structure is created. As a pre-requisite, the number of elements in the *z*-direction must be the same length as the time series you are attempting to correlate with, namely sum of voltages signal. Along the *z*-direction of the data structure are a collection of reference clocks, with values +/- 1, which are running with difference frequencies, along the *x*-direction. Usually, we use values between 90% and 110% of the rough reference clock rate (from the FFT), and have on the order of 21 columns (for this example resolution is 1%). The *y*-direction of the data structure represents clocks started with different phases (resolution *1/N* cycles, with *N* the number of rows).

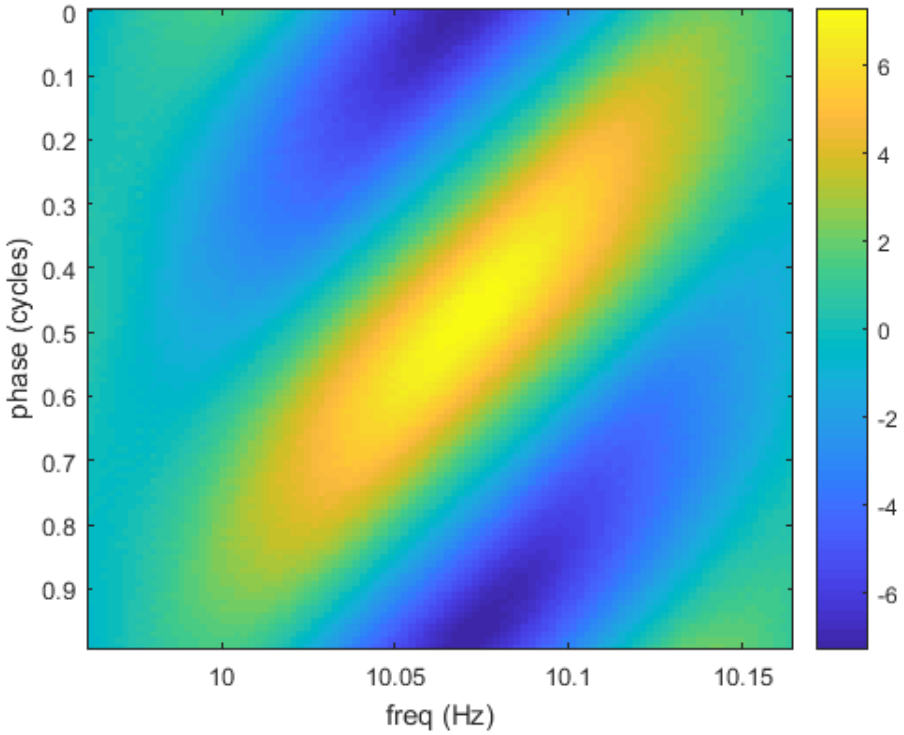


**Figure 4-3:** Example phase frequency correlation matrix generated by summing the final three dimensional data structure described in the text along the *z*-direction. Note, one cycle equals $2\pi$ radians.

Another, secondary three dimensional data structure is created by first level shifting, and gain controlling the sum of all the time domain signals, such that it is approximately zero mean and approximately constant envelope. This vector is then permuted such that it is *z*-directional, then replicated such that it has the same *x*- and *y*- dimensions as the primary three dimensional data structure. The final data structure is created by multiplying element-by-element the primary and secondary three dimension data structures along the *z*-direction, and normalizing for the number if *z*-directional samples summed across. These operations implement a

normalized cross-correlation of two signals, for each row / column pair. In analyzing the cross correlation values across multiple data sets (e.g. a 100 chop run is one data set) for a given attenuation level at the transmitter and beam divergence, a clear correlation coefficient threshold should become obvious to detect correct clock sync. Fig. 9 shows a representative example of a clock recovered from a data set.

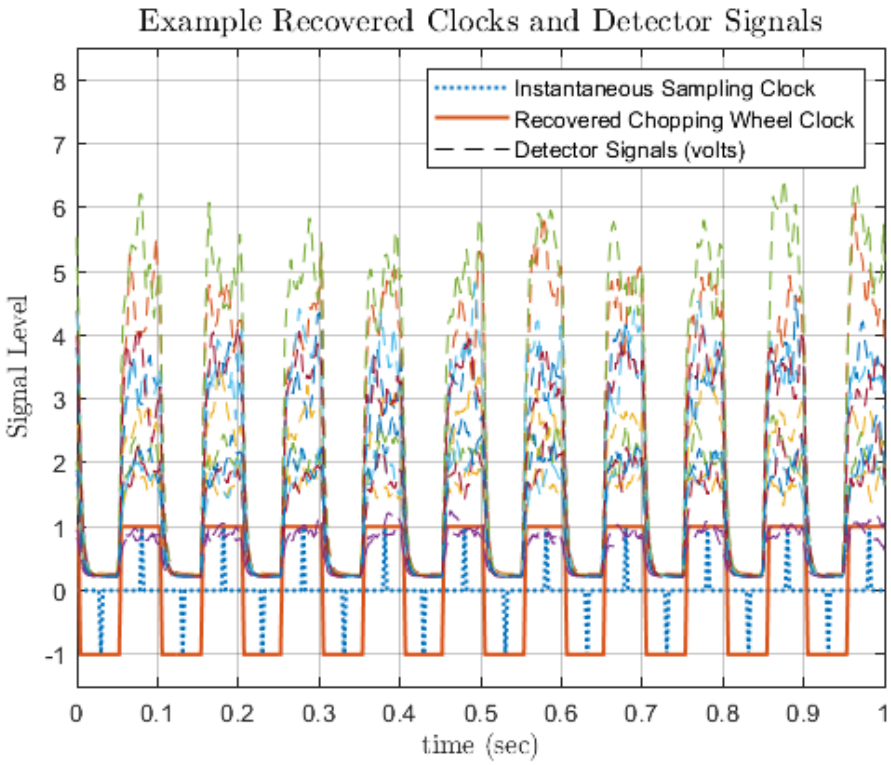


**Figure 4-4:** Example juxtaposition of the 13 signals from each aperture of a test (dashed lines) and the replica chopping wheel clock (**red** square wave) and the sampling clock (**blue** dotted line), which both appear at or below 1 on the *y*-axis of the plot. Sample clock values of 1 indicate that *on*-samples are taken and sample clock values of -1 indicate that *off*-samples are taken.

4.3: Estimates of Extinction Coefficient

As all theoretical models of beam propagation through turbulence predict a Gaussian beam at the receive plane, the mean value of all the on-samples for a given sample set can be summed, and together with the *x*-, *y*-locations of the optical detectors, provide all the information necessary to do a fit to an elliptic Gaussian profile. So far, we have generally assumed that the *x*-direction is the direction of the semi-major axis of the *spot size ellipse*, and the *y*-direction that of the semi-minor axis. However, relative to the transmissometer receiver alignment, we designate the relative angle between the transmissometer's *x*-axis (normally tangent to the earth's surface and perpendicular to the *z*-axis of propagation) as $\theta$. In general, a received elliptic Gaussian beam will have an intensity of the form [71]:

$$\langle I(x,y)\rangle = A \cdot \exp[-a(x-x_0)^2 + b(x-x_0)(y-y_0) - c(y-y_0)^2] \quad (4\text{-}7)$$

Where $x_0$, $y_0$ are the coordinates of the beam center at the receiver, and:

$$A \cong A_0 \frac{{W_0}^2}{W_{LT,x} W_{LT,y}} \cdot e^{-\sigma L} \quad (4\text{-}8)$$

$$a = \frac{2\cos^2\theta}{{W_{LT,x}}^2} + \frac{2\sin^2\theta}{W_{LT,y}}, \qquad b = \frac{\sin 2\theta}{W_{LT,y}} - \frac{\sin 2\theta}{W_{LT,x}},$$
$$c = \frac{2\sin^2\theta}{{W_{LT,x}}^2} + \frac{2\cos^2\theta}{{W_{LT,y}}^2} \quad (4\text{-}9)$$

Where $A_0$ in (4-8) is the peak intensity at the transmitter. For a known propagation distance, *L*, it is therefore possible to estimate $\sigma$, $W_{LT,x}$, $W_{LT,y}$, and $\theta$ simultaneously. We typically achieve this by performing a least squares best fit to

equation (4-7) using a numerical software such as MATLAB or Octave, and then we can also use the *goodness of fit* information returned by the software in order to provide thresholds for additional outlier removal. Nonlinear equation solvers, such as those previously described, can be used to then retrieve the parameters of interest, $\sigma$, $W_{LT,x}$, $W_{LT,y}$, and $\theta$.

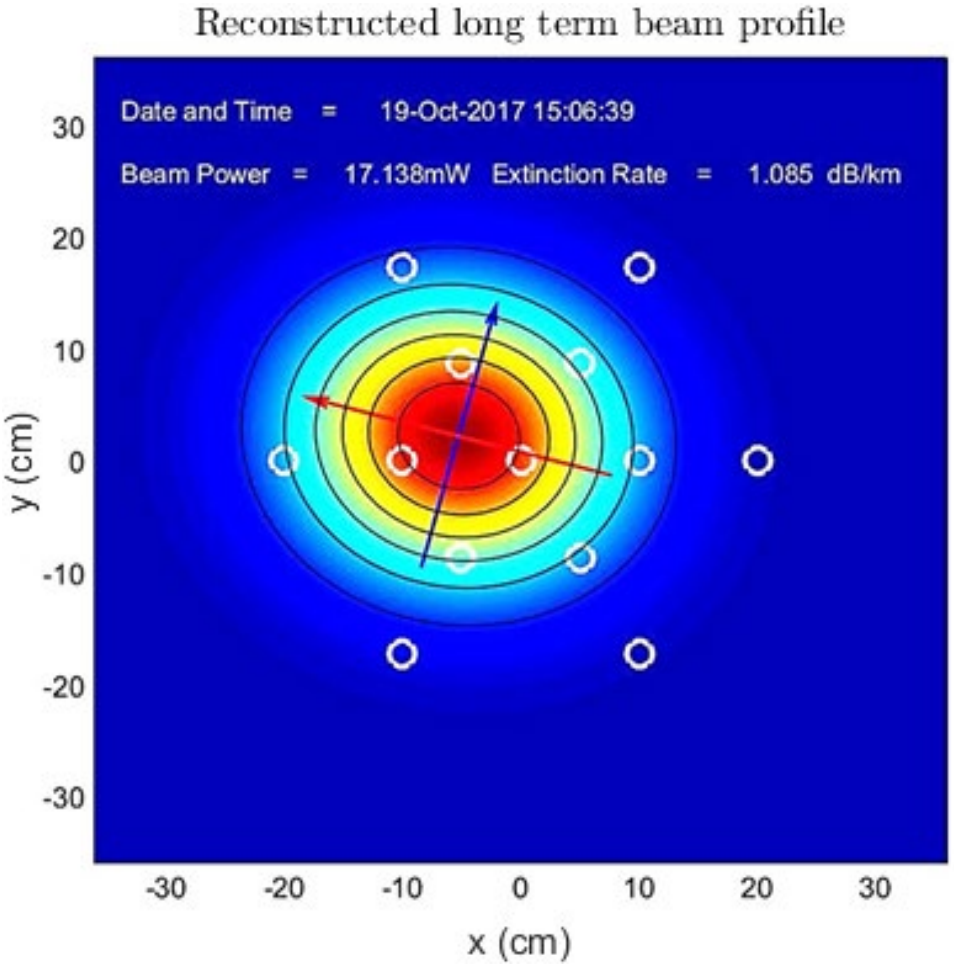


**Figure 4-5:** Example output of elliptic Gaussian fitting as displayed in MATLAB.

Once a fit has occurred, the estimated beam centroid at ($x_0$, $y_0$) is typically used for outlier removal. Beams with centroids determined to be significantly

outside the polygon defined by the outer detectors of the transmissometer aperture are removed from consideration. With the remaining fits, the total received integrated intensity can be estimated as:

$$P_{Tot,Rx} = \iint \langle I(x,y,L)\rangle dxdy = A\frac{\pi}{2}W_{LT,x}W_{LT,y} \tag{4-10}$$

The value of received power recovered using equation (4-10) is compared to previously determined calibrated value in order to estimate the extinction coefficient, in decibels per km, of the propagation path under test.

In order to validate the operation and measurements of our device, we arrange for remote testing at a large outdoor range in Central Florida. The Townes Institute Science and Technology Experimentation Facility (TISTEF) includes an approximately 1 km flat, outdoor range used for experiments regarding atmospheric optics, laser filamentation, and other wave propagation research. The facility has access to various commercial equipment for atmospheric research, and as such we made arrangements for side by side testing with a point visibility meter [97] owned by the institute.

To verify proof of concept, the MAT over a 980 m propagation path with a the commercial visibility meter from All Weather Inc (AWI) logging measurement simultaneously alongside the transmissometer in order to verify results. Although visibility meters typically output a visibility measurement in terms of a visible range, $R_v$, defined by a contrast ratio, $C_v$, which is typically standardized at either

.02 or .05. The extinction coefficient can be determined from visible range via the following relationships [97]:

$$\sigma = \frac{-ln(C_v)}{R_v}, \qquad \sigma_{dB} = \frac{-10\log_{10}(C_v)}{R_v} \tag{4-11}$$

Additionally, the visibility meter under test provided a precipitation rate estimate. Using the described algorithms, we are able to compare the MOG MAT results with the commercial visibility meter as shown in Figure 4-6. The overall test layout is shown in Figure 4-7.

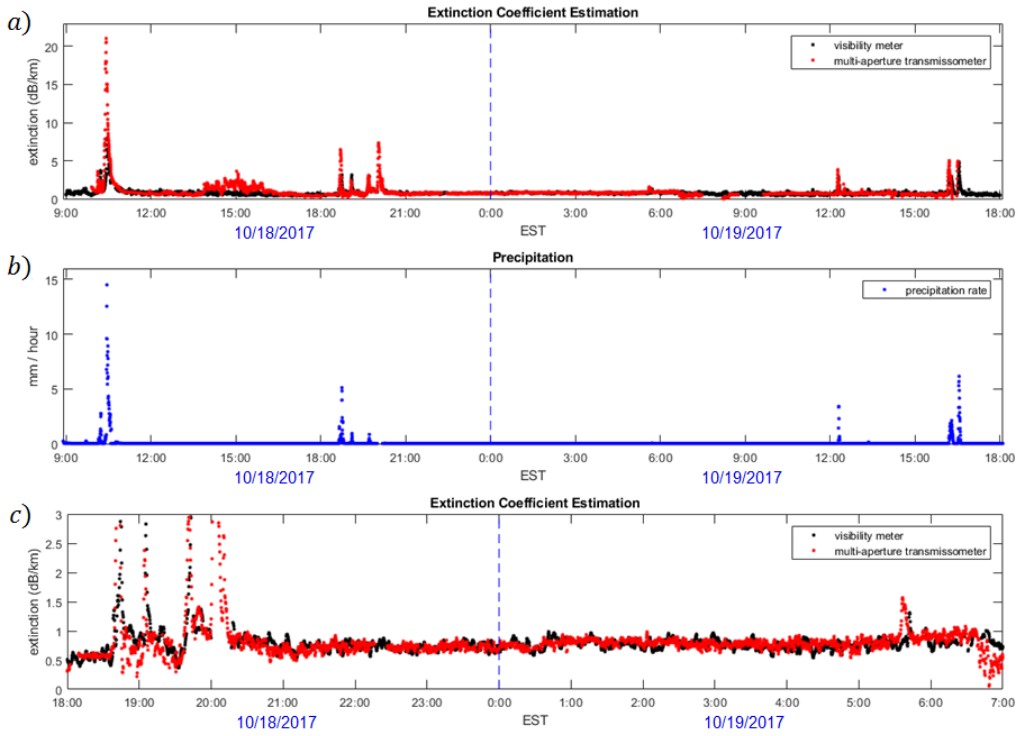


**Figure 4-6:** Comparison of visibility meter and MAT metrics over 2 days: a) Extinction coefficient estimates from the MAT (**red**) vs the visibility meter (**black**), b) Precipitation rate estimates from the visibility meter (**blue**), c) another rendition of the top figure, with the axis zoomed in to demonstrate that overall trends, and small features, of both devices' estimates of extinction correspond.

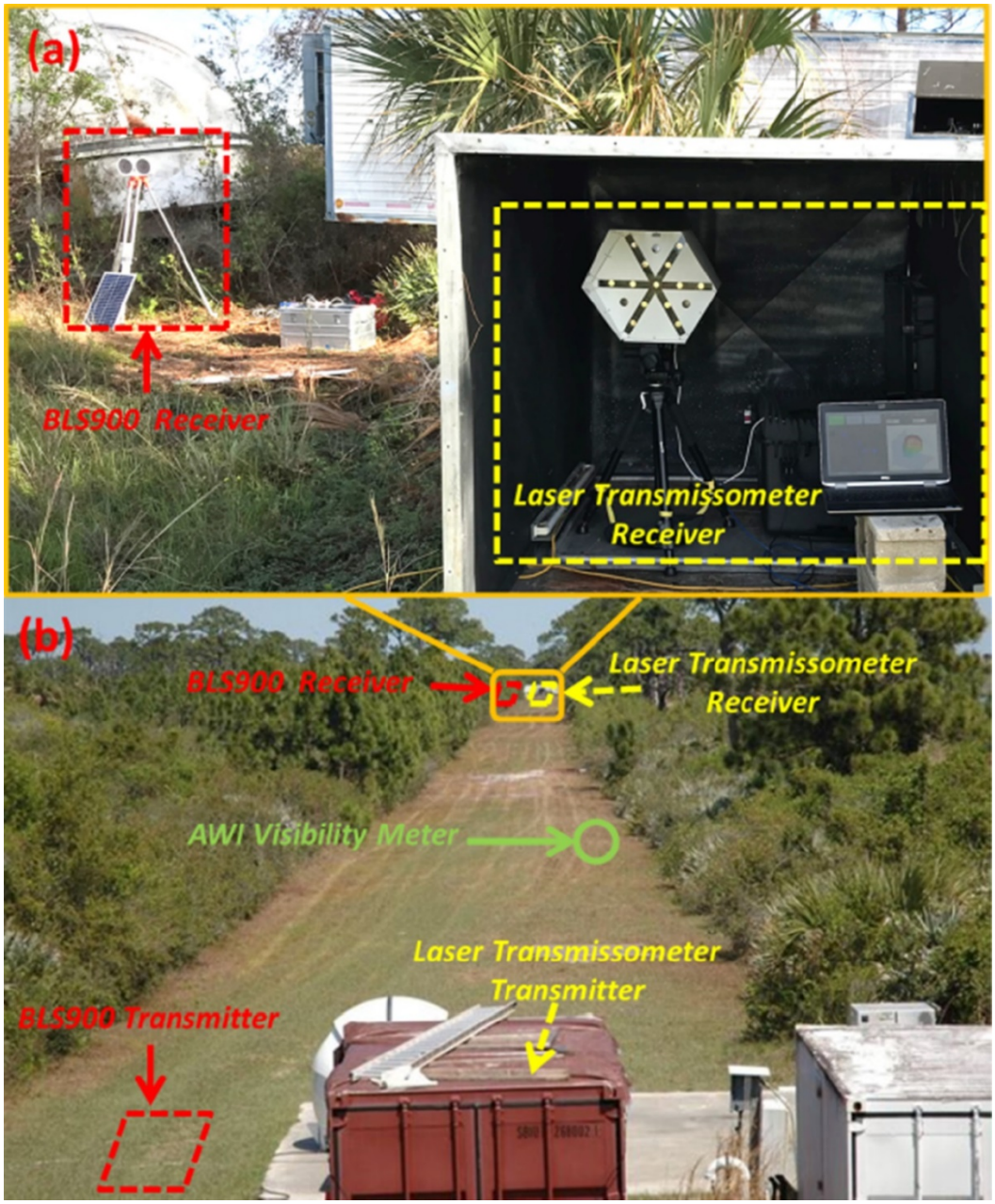


**Figure 4-7:** Equipment locations over TISTEF range: a) Layout picture on the receiver end; b) overall view of the TISTEF range from the transmitter end.

In general, the results of the transmissometer and visibility meter compare well during periods without significant precipitation. The MAT, however, seems

to have a higher sensitivity to precipitation, especially during heavy periods (above 8 mm/hour). This may have been due to the transmissometers lower elevation (approximately one meter off the ground) relative to the visibility meter (above 2 meters high), meaning the transmissometer may have observed both falling and "bouncing" rain drops during this period. We also note that during the test period, the transmitted beam was diverged via adjustments to a sliding lens in the beam expander in order to guarantee that multiple detectors on the transmissometer receiver were illuminated.

## 4.4: An Iterative Beam Fitting Approach to Capture Refractivity and Turbulence Effects

When the MOG experimental team first began performing beam profiling experiments using the MAT, based on the large volume of literature investigating and analyzing anisotropic optical turbulence effects [11, 18, 19, 23, 24, 25, 59, 76, 78, 79] we had been under the assumption that turbulence was the primary cause of observations of initially symmetric beam observed as elliptical after propagating through atmospheric distortions. During the course of our experimental campaign, through our own observation and more recent contributions to the literature [85, 86, 87] indicated that non-turbulence optical refractivity effects may dominate under some scenarios.

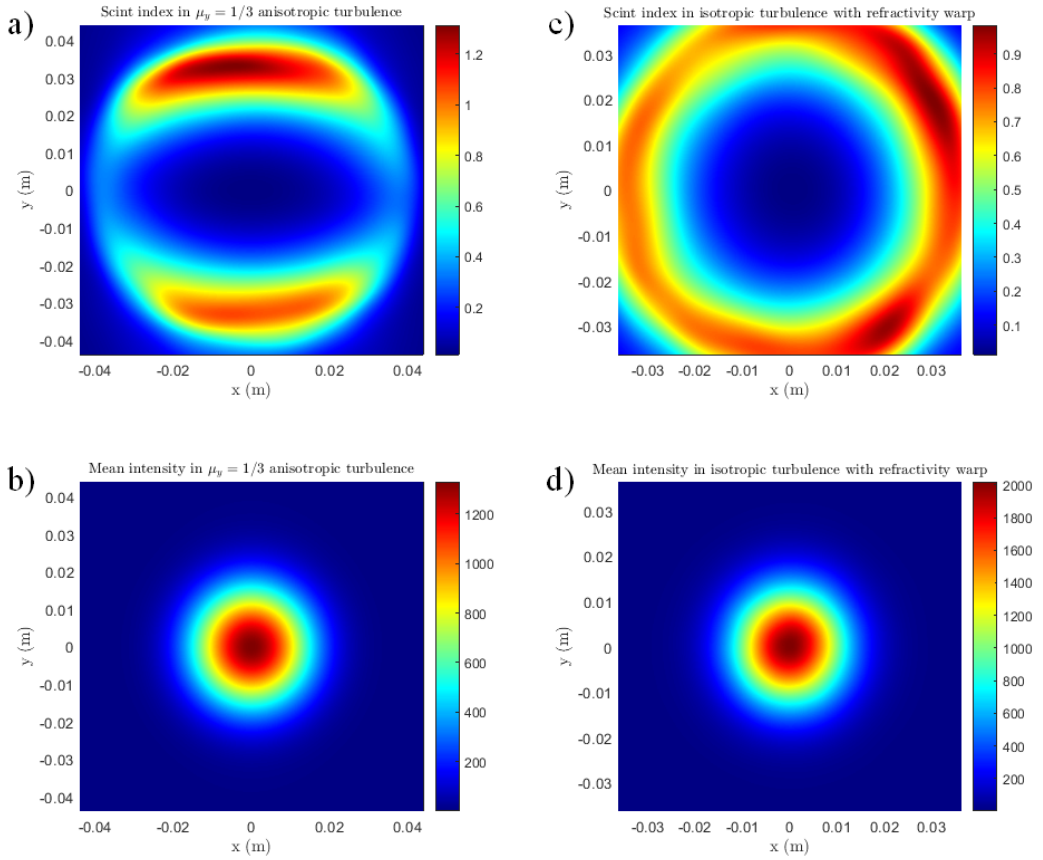


**Figure 4-8:** Simulation results illustrating differing scintillation index profiles despite comparable intensity profiles: a) Scintillation index profile for an initially collimated beam propagating 530 m through Kolmogorov, anisotropic turbulence with $\mu_x = 1$, $\mu_y = 1/3$, and spherical wave Rytov variance of 1; b) Mean intensity profile for an initially collimated beam propagating 530 m through Kolmogorov, anisotropic turbulence with $\mu_x = 1$, $\mu_y = 1/3$, and spherical wave Rytov variance of 1; c) Scintillation index profile approximating non-turbulent optical refractivity distortion using a beam which is initially collimated across the *x*-axis but with a radius of curvature of -4,142 m in the y-direction propagating through 530 m of Kolmogorov, isotropic turbulence with spherical wave Rytov variance of 1; d) Mean intensity profile approximating non-turbulent optical refractivity distortion using a beam which is initially collimated across the *x*-axis but with a radius of curvature of -4,142 m in the y-direction propagating through 530 m of Kolmogorov, isotropic turbulence with spherical wave Rytov variance of 1. A 2.5 cm diameter aperturing filter was used to collect all results for comparison with the collected transmissometer data.

More specifically, the type of non-turbulent optical refractivity distortion we are referring to occurs when the refractive index gradient is not constant (i.e. simply leading to tip and tilt), and has a significant parabolic component. As discussed in Section 3.5, and specifically displayed in Figure 3-6 and Figure 3-11, the hallmark feature distinguishing of non-turbulent optical refractivity distortion in contrast to anisotropic turbulence affects is that the scintillation index paraboloid's semi-major axis is in the same direction as the semi-major axis of the elliptical Gaussian intensity profile. For anisotropic turbulence alone, the inverse is the case. In order to show this, we have also included Figure 4-8, which demonstrates this fact for two cases: a) An initially collimated beam propagating 530 m through Kolmogorov, anisotropic turbulence with $\mu_x = 1$, $\mu_y = {}^1/_3$, and spherical wave Rytov variance of 1; b) Simulation approximating non-turbulent optical refractivity distortion using a beam which is initially collimated across the x-axis but with a radius of curvature of -4,142 m in the y-direction propagating through 530 m of Kolmogorov, isotropic turbulence with spherical wave Rytov variance of 1.

In field experiments, we have found the beam intensity and scintillation index profiles corresponding to non-turbulent optical refractivity distortion to be common. Figure 4-9 shows a somewhat typical case observed at the transmissometer receiver when doing near ground turbulence profiling. Note that, although there is a slight disagreement in the directionality of the intensity Gaussian

and scintillation index paraboloids, the fact that the semi-major axes are in approximately the same direction indicates that the non-turbulent refractivity distortion condition under discussion is clearly playing a role.

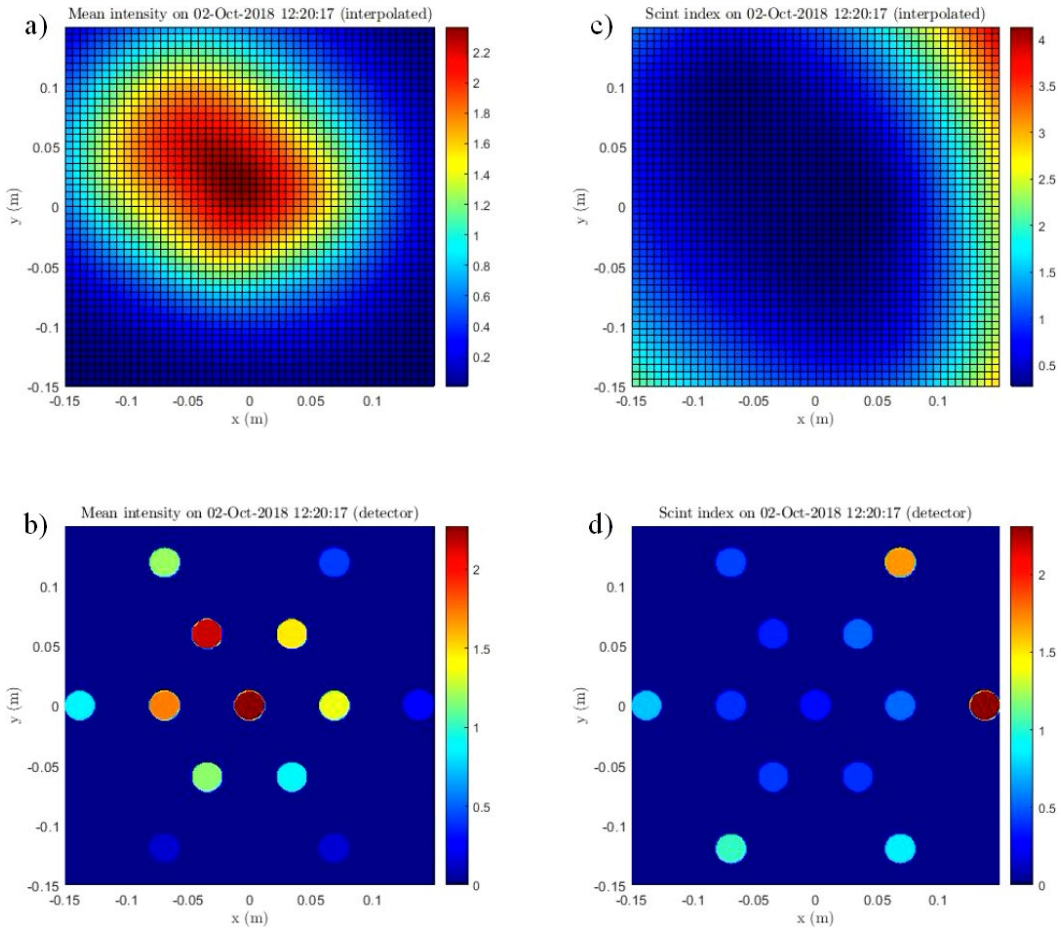


**Figure 4-9:** Example observed main intensity at the MAT receiver and from an outdoor field experiment. The observation that the intensity spot ellipse and the scintillation index are pointing in approximately the same directions indicate that refractivity effects are dominating optical propagation distortions. The subplots are: a) Interpolated mean optical intensity profile; b) Detector-by-detector mean optical intensity; c) Interpolated scintillation index profile; d) Detector-by-detector scintillation index.

Seeking to mitigate the effects of the somewhat unexpected non-turbulence optical refractivity distortion on the turbulence estimate, we have developed an

iterative fitting scheme aimed at addressing both sets of effects. In order to do so, we take advantage of the observations of Sections 3.2, 3.3, and 3.5. Specifically, we note that Equations (3-14) and (3-15) indicate that the size of the spot ellipse in a given direction is perturbed in a given direction as per:

$$W_{LT}\left(\theta_R, \theta_T, \Lambda_1, \Lambda_2, \rho_{s,x}, \rho_{s,y}\right) \cong \sqrt{\frac{2 \cdot L}{k_0 \Lambda_1}\cos^2(\theta_R) + \frac{2L}{k_0 \Lambda_2}\sin^2(\theta_R) + \frac{8L^2}{k_0 \rho_{s,x}^2}\cos^2(\theta_R - \theta_T) + \frac{8L^2}{k_0 \rho_{s,y}^2}\sin^2(\theta_R - \theta_T)} \tag{4-12}$$

Where $\Lambda_1$ and $\Lambda_2$ as the larger and smaller, respectively, Fresnel parameters [see Equations (3-19) and (3-22)] including diffractive and non-turbulent refractive effects, $\theta_R$ we dub the refractivity angle, $W(\theta_R)$ is the radius of the spot ellipse in the absence of turbulence in at a given angle, $\theta_T$ we dub the turbulence angle (the direction of higher turbulence), $\rho_{s,x}$ and $\rho_{s,y}$ are spherical wave coherence lengths along the major and minor axes of turbulence. The observed scintillation index at is given by:

$$\begin{aligned}\tilde{\sigma}_I^2\left(r, \theta_R, \theta_T, \tilde{C}_n^2, \mu_y\right) \cong & \\ \tilde{\sigma}_{I,l}^2 + \frac{\pi\Gamma\left(2 - \frac{\alpha}{2}\right)}{\alpha - 1} A(\alpha) \cdot \tilde{C}_n^2 \cdot k_0^{4-\frac{\alpha}{2}} L^{\frac{\alpha}{2}-1} \cdot {\Lambda_1}^{\frac{\alpha}{2}} \times \left[\cos^2(\theta_R) + \frac{\Lambda_2}{\Lambda_1}\sin^2(\theta_R)\right] & \\ \times r^2 \int_0^{2\pi} \left[\cos(\theta_R - \theta_T)\cos(\varphi - \theta_T) + \frac{\sin(\theta_R - \theta_T)\sin(\varphi - \theta_T)}{\mu_y}\right]^2 & \\ \times \left[\cos^2(\varphi - \theta_T) + \frac{\sin^2(\varphi - \theta_T)}{\mu_y^2}\right]^{\frac{\alpha}{2}-2} d\varphi & \end{aligned} \tag{4-13}$$

Equation (4-13) the leading term $\tilde{\sigma}_{I,l}^2$ is meant to allow for adjustments in the fit in order to capture both aperture averaging effects which may vary according to

distance across the receiver. Additionally, this allows for operation in the deep fluctuation regime, where the on-axis scintillation index is expected to saturate. During iterative fitting, we all this factor to be a free parameter estimated by the fitting routine.

Equation (4-13) is designed to generalize Equation (3-28) for the common case observed using the MAT system in which the direction of the refractivity distortion is not either in the same direction or at a right angle to the direction of higher turbulence. For a given set of input Fresnel parameters, performing a best fit for $\tilde{C}_n^2$, $\theta_R$, and $\mu_y$ using the detector-by-detector scintillation indices (after adjusting for offset of the beam centroid from center). Given that we follow the conventions of setting $\tilde{C}_n^2 = C_{n,x}^2$, $\mu_y = 1$, once a fit has occurred we have an estimate of the *x*- and *y*-direction spherical wave coherences lengths as per:

$$\rho_{0,x} = \left[ A(\alpha)\tilde{C}_n^2 k_0^2 L \frac{-\pi^2 \Gamma\left(1-\frac{\alpha}{2}\right)}{2^{\alpha-3}\Gamma\left(\frac{\alpha}{2}\right)} \right]^{\frac{1}{2-\alpha}} \tag{4-14}$$

$$\rho_{0,y} = \mu_y \left[ A(\alpha)\tilde{C}_n^2 k_0^2 L \frac{-\pi^2 \Gamma\left(1-\frac{\alpha}{2}\right)}{2^{\alpha-3}\Gamma\left(\frac{\alpha}{2}\right)} \right]^{\frac{1}{2-\alpha}} \tag{4-15}$$

The coherence length determined by the fit can then be fed back into the spot size estimate of Equation (4-12). In practice, in order to fit our spot size we make use of the equation:

$$\langle I(r, \theta_r, \theta_t, \Lambda_1, \Lambda_1, \rho_{s,x}, \rho_{s,y})\rangle = A \exp\left[\frac{-2r^2}{W_{LT}(\theta_r, \theta_t, \Lambda_1, \Lambda_1, \rho_{s,x}, \rho_{s,y})}\right] \quad (4\text{-}16)$$

where $A$ is the long term beam intensity at the centroid. Equations (4-12) through (4-16) provide a framework for iteratively fitting both turbulence-based and non-turbulent refractivity distortion based beam spreading. In order to limit the number of fit parameters, we will be holding the three dimensional power law, $\alpha$, to the $11/3^{\text{rds}}$ law of the Kolmogorov. We will later show additional justifications for this in the next section via frequency domain analysis using point detectors of turbulence (temperature probes).

Given the above analysis and observations, we have implemented an iterative fitting algorithm which can be summarized as follows. Using the observed detector-by-detector scintillation indices and detector positions, we fit the $\tilde{C}_n^2$, $\theta_t$, and $\mu_y$ using the best estimates of the beam centroid, $\theta_r$, $\Lambda_1$, and $\Lambda_2$. Using the estimates of the three turbulence parameters from the previous fit as well as the derived $\rho_{s,x}$ and $\rho_{s,y}$, we then fit the intensity profile using Equation (4-16) in order to obtain new estimates for $\theta_r$, $\Lambda_1$, and $\Lambda_2$. Figure 4-10 gives a high level visual summary of the iterative approach.

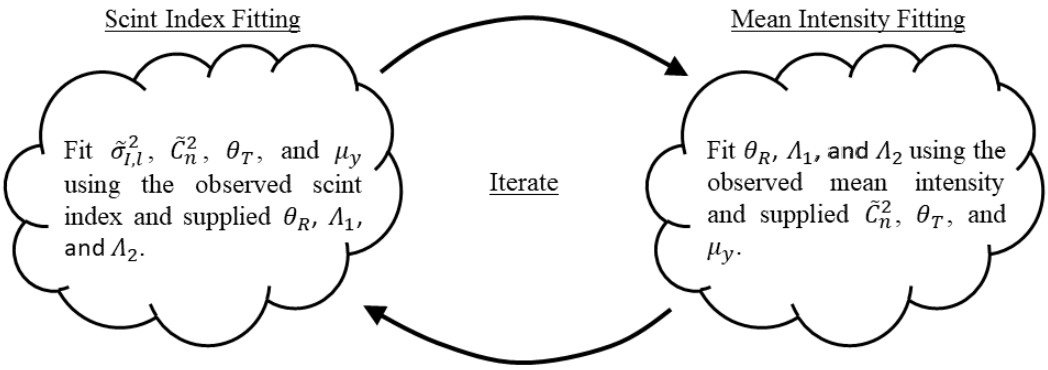


**Figure 4-10:** High level visual summary of the iterative fitting approach.

In order to provide more details regarding the technique we provide a list of specific steps. They are, as follows:

1. Using the long term mean intensity data collected at each detector perform a best fit, without differentiating between non-turbulence refractivity and turbulence effects, in order determine the beam centroid (i.e. $x_0$ and $y_0$) as well as initial estimates of $\theta_R$, $\Lambda_1$, and $\Lambda_2$. In order to achieve this, we perform a best fist for $x_0$, $y_0$, $\theta_R$, $\Lambda_1$, and $\Lambda_2$ while setting $\rho_{s,x}$ and $\rho_{s,y}$ to very long lengths (i.e. $10^6$ m) such that the contribution of turbulence is negligible.
2. Using the estimates of $x_0$, $y_0$, $\theta_R$, $\Lambda_1$, and $\Lambda_2$ from the previous step, fit the detector-by-detector scintillation indices using Equation (4-13) in order to provide updated estimates for $\tilde{\sigma}_{I,l}^2$, $\tilde{C}_n^2$, $\theta_T$, and $\mu_y$.
3. Calculate estimates for $\rho_{s,x}$ and $\rho_{s,y}$ using the $\tilde{C}_n^2$ estimate from the previous step and Equations (4-14) and (4-15).

4. Repeat the mean intensity best fit using updated values of $\rho_{s,x}$ and $\rho_{s,y}$ in order to produce updated estimates of $\theta_R$, $\Lambda_1$, and $\Lambda_2$.
5. Repeat steps 2 through 4 a pre-determined number of times.

We note that in step 5, an alternate approach would be to threshold the size of corrections wherein corrections below some predetermined value would signal to the iterative fitting loop to exit. We have found, however, that in the majority of cases the fitting routine predictively converges and, as such, will count on other outlier removing techniques to be discussed in order to remove bad fits which do not trend well with the data from nearby times. Results from a somewhat typical iterative fit are shown in Figure 4-11. We note that although 50 iterations of the fitting routine were performed, we've truncated the $x$-axes in the respective subplots due to the fit converging around 12 or 13 iterations. We chose 50 durations because after the algorithm initially converges, subsequent fits complete more quickly.

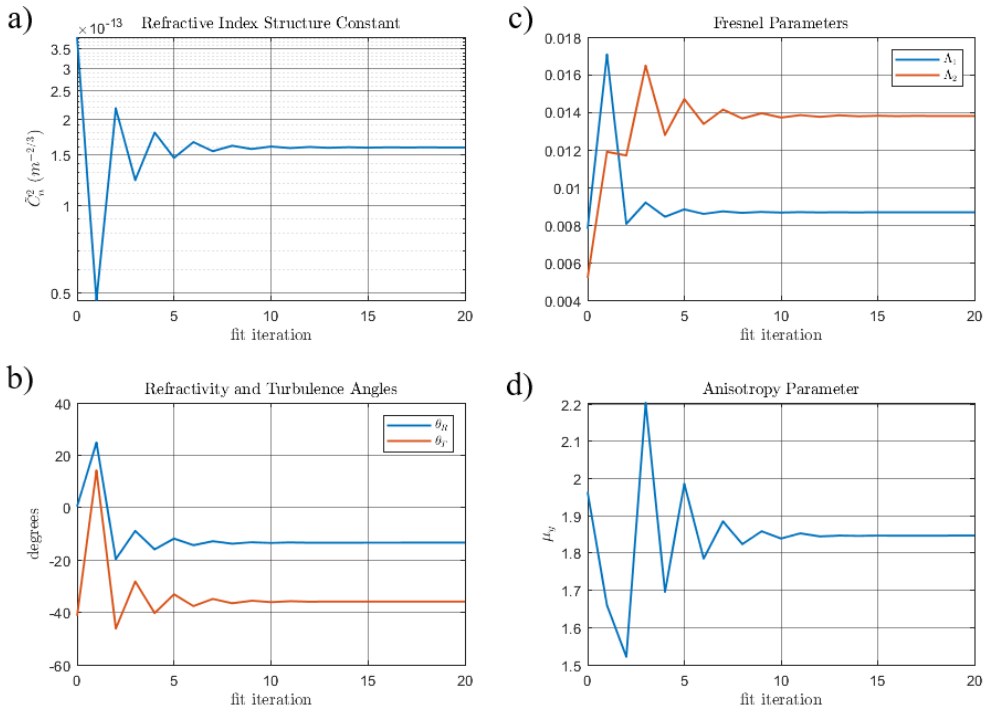


**Figure 4-11:** Behavior of turbulence and beam parameter estimates during iterative fitting. The subplots shown are as follows: a) The estimated refractive index structure constant, $C_n^2$; The turbulent and refractivity angles, $\theta_R$ and $\theta_T$, respectively; c) Fresnel parameters, $\Lambda_1$ and $\Lambda_2$, respectively; d) the anisotropy parameter, $\mu_y$.

While the iterative fitting routine reliably fits the data from the MAT receiver, we have noted that the turbulence estimates are typically above what is suggested by the observed on-axis scintillation index. This is most likely due to the fact that the aperture averaging factor for scintillation index is not constant across the beam profile, and in fact varies by position as illustrated in Section 3.5. In order to mitigate this feature, the final estimates of $\tilde{C}_n^2 = C_{n,x}^2$, $C_{n,y}^2$, and $\mu_y$ are determined by a combination of the scintillation indices observed at the transmissometer as well as the total change in the spot size estimates at the turbulent angles. In order to estimate $\tilde{C}_n^2$ using the observed on-axis scintillation index, we

first consider the approximation for the aperture averaging factor developed in Section 3.5. Specifically, Equations (3-34) and (3-35) are used in order to facilitate the adjustment for aperture averaging factor. Given the observation that the unapertured on-axis scintillation index for a divergent beam is well approximated by the spherical wave Rytov variance, we can also state that the spherical wave Rytov variance, $\sigma_{R,S}^2$, on-axis aperture averaged scintillation index, $\sigma_{I,l}^2(D)$, multiplied by the aperture averaging factor, $F_{ap}\left(\sigma_{R,S}^2, D\right)$. In order to estimate the actual $\sigma_{R,S}^2$, we create a vector of possible spherical wave Rytov variances from .001 to 10 and using our approximation, and given by $\boldsymbol{\sigma_{R,S}^2}$. A corresponding vector for the aperture averaging factor associated with the values in $\boldsymbol{\sigma_{R,S}^2}$ is created, dubbed $\boldsymbol{F_{ap}}$. Finally a vector of expected, observed on-axis scintillations indices for a given Rytov variance, dubbed $\boldsymbol{\sigma_{I,l}^2}$, is created using:

$$\boldsymbol{\sigma_{I,l}^2} = \boldsymbol{\sigma_{R,S}^2} \circ \boldsymbol{F_{ap}} \tag{4-17}$$

where $\circ$ denotes element-by-element multiplication (the Hadamard product). Given that both $\boldsymbol{\sigma_I^2}$ and $\boldsymbol{\sigma_{R,S}^2}$ are monotonically increasing, the true spherical wave Rytov variance may be estimated using the statement (in MATLAB):

$$\sigma_{R,S}^2 \cong \text{interp1}\left(\boldsymbol{\sigma_{I,l}^2}, \boldsymbol{\sigma_{R,S}^2}, \sigma_I^2(D)\right) \tag{4-18}$$

where the *interp1* operator denotes one dimensional linear interpolation. In practice, because the scintillation index is often observed varying log-normally we chose to perform the interpolation on the logarithmic scale, as per:

$$\sigma_{R,S}^2 \cong \exp\left[\text{interp1}\left(\ln\left[\boldsymbol{\sigma_{I,l}^2}\right], \ln\left[\boldsymbol{\sigma_{R,s}^2}\right], \ln[\sigma_I^2(D)]\right)\right] \tag{4-19}$$

In order to provide an updated estimate of the anisotropy parameter, $\mu_y$, we compare the change in the spot size prediction from the our initial beam fit, which has assumed negligible turbulent beam spreading, with the final output of the fit. The initial estimates for the Fresnel parameters we dub $\Lambda_{1,0}$ and $\Lambda_{2,0}$, with $\Lambda_{1,0}$ defined as the smaller of the two (corresponding to the larger spot size), and the initial angle for the fit is labeled $\theta_0$. Given the final fitting estimates for the diffraction and non-turbulent refractivity distortion Fresnel parameters along with the final estimated turbulence angle, $\theta_T$, we can calculate the estimated beam spreading due to optical turbulence effects along the major and minor axes of turbulence (*x*- and *y*-directions, respectively). First, we note that the spot sizes along the semi-major and semi-minor axes of the long-term beam profile, $W_{1,0}$ and $W_{2,0}$ respectively, are given by the initial fit are given by:

$$W_{1,0} = \sqrt{\frac{2L}{k_0 \Lambda_{1,0}}}, \qquad W_{2,0} = \sqrt{\frac{2L}{k_0 \Lambda_{2,0}}} \tag{4-20}$$

Similarly, the final beam sizes after removing the effects of optical turbulence induced beam spreading are given by:

$$W_x = \sqrt{\frac{2L}{k_0}\left[\frac{\cos^2(\theta_T - \theta_R)}{\Lambda_1} + \frac{\sin^2(\theta_T - \theta_R)}{\Lambda_2}\right]} \tag{4-21}$$

$$W_y = \sqrt{\frac{2L}{k_0}\left[\frac{\sin^2(\theta_T - \theta_R)}{\Lambda_1} + \frac{\cos^2(\theta_T - \theta_R)}{\Lambda_2}\right]} \tag{4-22}$$

For reasons which will later become clear, we are interested in the square of the total deviation in spot sizes along our *x*- and *y*-axes, i.e. the major and minor axes of turbulence. We calculate these deviations using the previously estimated parameters along with our formula for the long term spot given by Equation (4-12). We, therefore calculate these deviations, $\Delta W_x^2$ and $\Delta W_x^2$, via the equations:

$$\Delta W_x^2 = W_{1,0}^2 \cos^2(\theta_T - \theta_0) + W_{2,0}^2 \sin^2(\theta_T - \theta_0) - W_x^2 \tag{4-23}$$

$$\Delta W_y^2 = W_{1,0}^2 \sin^2(\theta_T - \theta_0) + W_{2,0}^2 \cos^2(\theta_T - \theta_0) - W_y^2 \tag{4-24}$$

Based upon investigation of Equations (3-10) and (3-11) when the beam is not affected by non-turbulence refractivity distortion, and therefore has a diffraction limited spot size *W*, we make the observation:

$$\frac{8L^2}{k_0 \rho_{s,x}^2} \cong W_{LT,x}^2 - W^2 \tag{4-25}$$

$$\frac{8L^2}{k_0 \rho_{s,y}^2} \cong W_{LT,y}^2 - W^2 \tag{4-26}$$

We assume that this relation still holds when turbulence is distorting an otherwise warped beam undergoing optical refractivity distortion. Coupling this with an investigation of Equations (4-14) and (4-15) yields the following simple relationship:

$$\mu_y = \frac{\rho_{s,x}}{\rho_{s,y}} = \sqrt{\frac{\Delta W_x^2}{\Delta W_y^2}} \tag{4-27}$$

Equation (4-27) provides the final estimate for the anisotropy parameter, $\mu_y$.

Using this estimate for $\mu_y$, we may now turn the estimate of the spherical wave Rytov variance into estimates for $C_{n,x}^2$ and $C_{n,y}^2$. An expression for the generalized spherical wave Rytov variance is given by Equation (1-59), and we will note that the quantity is directly proportional to $\tilde{C}_n^2$. Because we have chosen to fix our three dimensional power law, $\alpha$, to $11/3$ we may then rewrite Equation (1-59) as:

$$\begin{aligned}\sigma_{R,s}^2 \cong{}& \frac{-\Gamma\left(\frac{8}{3}\right)\Gamma\left(-\frac{5}{6}\right)\Gamma^2\left(\frac{11}{6}\right)}{2\pi\Gamma\left(\frac{11}{6}\right)}\cos\left(\frac{11\pi}{6}\right)\cos\left[\frac{5\pi}{12}\right]\tilde{C}_n^2 k_0^{\frac{7}{6}} L^{\frac{11}{6}} \\ &\times \int_0^{2\pi}\left(\cos^2\varphi + \frac{\sin^2\varphi}{{\mu_y}^2}\right)^{\frac{5}{6}} d\varphi \\ ={}& 0.4968 \cdot \tilde{C}_n^2 k_0^{\frac{7}{6}} L^{\frac{11}{6}} \times \frac{1}{2\pi}\int_0^{2\pi}\left(\cos^2\varphi + \frac{\sin^2\varphi}{{\mu_y}^2}\right)^{\frac{5}{6}} d\varphi\end{aligned} \tag{4-28}$$

We have written Equation (4-28) in this form in order to demonstrate that for the case of $\mu_y = 1$ this expression matches the Kolmogorov turbulence spherical wave Rytov variance given in [9]. Because we have set the convention that $\tilde{C}_n^2 = C_{n,x}^2$ by virtue of setting $\mu_x = 1$, we produce our final estimates of $C_{n,x}^2$ and $C_{n,y}^2$ using the equations:

$$C_{n,x}^2 = \frac{\sigma_{R,S}^2}{0.4968 \cdot k_0^{\frac{7}{6}} L^{\frac{11}{6}} \times \frac{1}{2\pi} \int_0^{2\pi} \left( \cos^2 \varphi + \frac{\sin^2 \varphi}{{\mu_y}^2} \right)^{\frac{5}{6}} d\varphi} \tag{4-29}$$

$$C_{n,y}^2 = \frac{C_{n,x}^2}{{\mu_y}^{2/3}} \tag{4-30}$$

Figure 4-12 shows an example of results collected using this approach. These results were collected along an approximately flat path on an airfield in Southern Maryland with the MAT transmitter and receiver both at a central elevation of 1.5 m. In order to stabilize the transmitter and receiver in order to mitigate the effects of vibrations, both pieces of equipment were placed in custom made racks of 80/20 T-slot structural framing with an approximately 1 m × 1 m square base. Both cinderblocks and sandbags were placed leaning upon the base of the structural framing at the corners to provide further stabilization. More details regarding the 80/20 racks will be provided in the next section. The results of Figure 4-12 show relatively stable fits for both the refractivity and turbulent angles, non-turbulent spot size estimates, and relatively stable estimates for $C_{n,x}^2$ and $C_{n,y}^2$. The anisotropy estimates are somewhat sporadic, however they trend relatively stably when the 5 minute median is plotted.

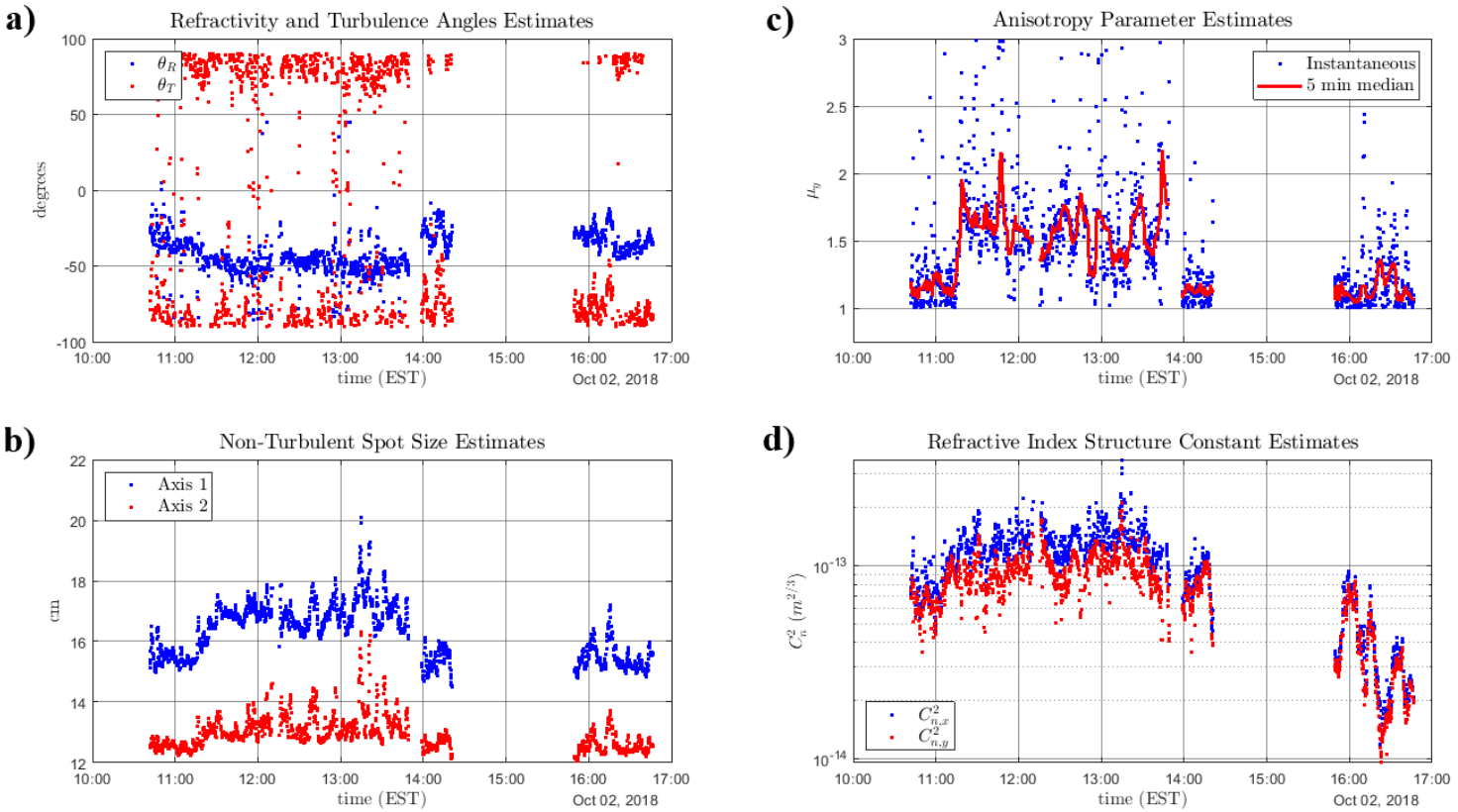


**Figure 4-12:** Output data from MAT experiment using the iterative fitting method: a) Refractive and turbulent angle estimates, $\theta_R$ and $\theta_T$, relative the an objective horizontal angle; b) Non-turbulence spot size estimate produced from best fits for $\Lambda_1$ and $\Lambda_2$; c) Estimates of the anisotropy parameter, $\mu_y$, given as both as an instantaneous estimate and the five minute median; d) Estimates of the refractive index structure constants, $C_{n,x}^2$ and $C_{n,y}^2$, with the $x$-axis being along the turbulent angle.

## 4.5: Turbulence Profiling Results in the Weak Fluctuation Regime

The MAT system was deployed in order to facilitate turbulence profiling alongside temperature probe based systems at a remote facility in Southern Maryland with access to a local airport which was able to provide a long, flat optical propagation path which is ideal for the study of approximately homogenous optical turbulence. The University of Maryland (UMD) Unmanned Aerial System (UAS) test site is located in California, St. Mary's County, Maryland, and has a relationship with the St. Mary's County Regional Airport which permits them to perform testing of drone systems and other scientific test campaigns. After a request was submitted to the UAS site and St. Mary's County Regional Airport, permission was granted in order to perform both MAT testing, as well as a vertical turbulence profiling test using a tethered weather balloon.


**Figure 4-13:** Approximate location of the Southern Maryland optical propagation path shown in within the St. Mary's County Airport complex **light orange** within the St. Mary's County Regional Airport complex. The MAT transmitter was in place on the east side, and the MAT receiver to the west.

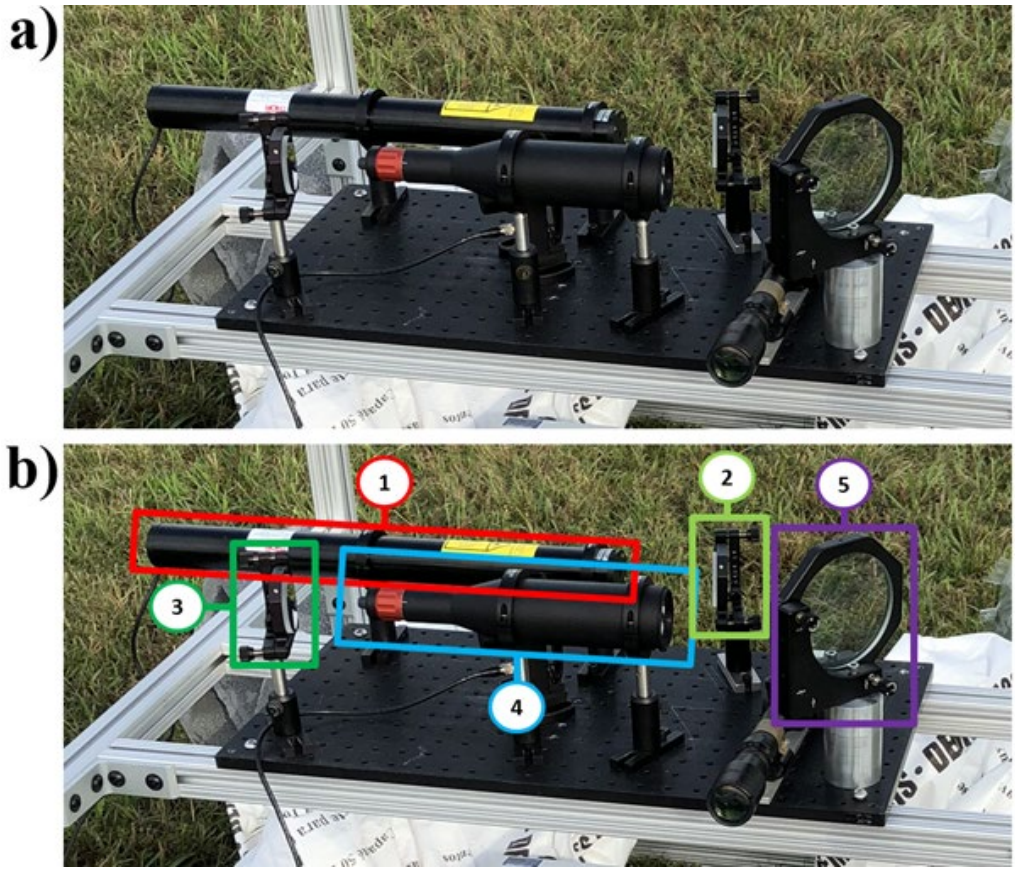


**Figure 4-14:** Images of the MAT transmitter breadboard: a) Without markup labeling; b) With markup labeling. In Image b) the labeled components are as follows: 1) Helium neon laser transmitter; 2) First redirection mirror; 3) Second redirection mirror; 4) Fixed magnification beam expander with adjustable sliding lens; 5) Steering mirror for downfield pointing. Additionally, although obscured by the beam expander, an optical chopping wheel is in place between the two redirection mirrors on the breadboard. A scope is placed on the breadboard adjacent to the steering mirror for alignment, however it is not a permanent component of the optical breadboard.

**Figure 4-15:** Alternative view of the MAT transmitter optical breadboard with the illuminated retroreflectors of the MAT receiver shown in the background. Note that the placement of the optical chopping wheel is shown more clearly in this figure.

**Figure 4-16:** Overall view of the MAT transmitter rack. Note that vibrational stabilization is applied using both sandbags and cinderblocks at the base. A weather station is attached at the top of the rack.

**Figure 4-17:** MAT receiver placed upon gimbal mount within structural framing rack and the operator shown during alignment. Note that the operator is standing upon a weatherized pelican case housing the logging computer for the MAT receiver.

For the test campaign, the receiver was housed in a similar rack of structural framing. Additionally, the MAT receiver was fastened to a gimbal mount which provide pitch, roll, and yaw adjustability enabling use to control for uneven ground conditions and keep the receiver oriented horizontally and in the direction of the target. Although the MAT receiver features optical detector systems with wide

acceptable angle, a sun shield is present on the MAT receiver in order to block both incident light from the sun, as well as reflected off of (primarily) the ground within the MAT receiver's view.

Once a coarse alignment is performed by searching for and illuminating the MAT receiver retroreflectors using the MAT transmitter breadboard's steering mirror, a fine alignment is performed with operators manning the transmitter and receiver while communicating over phone or radio. The MAT receiver features a touchscreen display featuring a readout of the detector-by-detector electrical intensity measurements, and the operators can coordinate to provide fine tuning increments at the transmitter steering mirror such that the beam is approximately centered with regards to the MAT receiver optics at the beginning of the data collection period. Additionally, in order to assure the detectors are not compressed, during this time neutral density (ND) filters are attached by the MAT transmitter operator such that the detected levels at the MAT receiver are below half of their maximum read-out level.

In addition to the MOG MAT, temperature based turbulence estimation devices were used for validation. We have deployed horizontally and vertically oriented commercial resistance temperature detector (RTD) probe systems to simultaneously estimate both $C_n^2$ and anisotropy [98]. The RTD systems are arrays of differential thermometer pairs used in order to infer parameters of the temperature structure function. This method follows that of Lawrence, et al. [99],

which has been demonstrated to very accurately predict $C_n^2$ relative to a large aperture scintillometer by Wang, et al. [100]. The RTD arrays each consist of eight non-uniformly placed probes, with probe pair separation distances between 2 and 50 cm such that measurements span within the inertial range of turbulence. Probes are polled by a data logging system once every 2 seconds, and a temperature structure function constant, $C_T^2$, is estimated in post-processing. As temperature fluctuations are the primary source of optical turbulence in the atmosphere [28], $C_T^2$ are $C_n^2$ are approximately related by a factor [99], given by Equation (1-14), and the structure functions of temperature and refractive index display the same anisotropy parameters and power law indices [9]. Due to uniformity of ground conditions in our experiments, we've assumed local results from the RTD systems approximately represent the path-averaged statistics, for comparison.

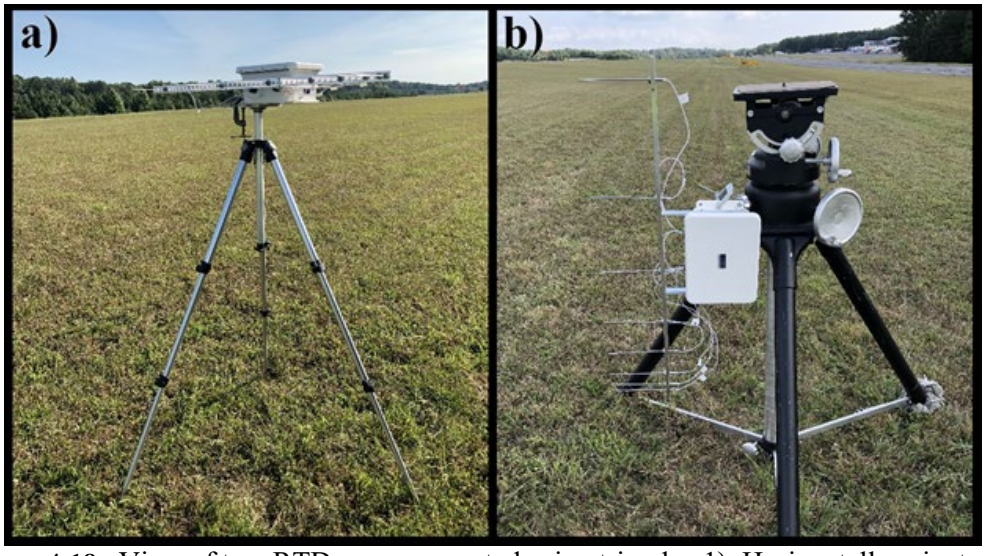


**Figure 4-18:** View of two RTD arrays mounted using tripods: 1) Horizontally oriented eight probe RTD array mounted to a tripod; 2) Vertically oriented eight probe RTD array mounted to the base of a heavy-duty tripod.

During the post-processing routine, $C_T^2$'s for individual sets of probe pairs are computed using the equation:

$$C_T^2(n,m,t) = \frac{\mathrm{var}\left[\Delta T_{n,m}\left(t-\frac{\Delta t}{2}\right), \Delta T_{n,m}\left(t-\frac{\Delta t}{2}+1\right), \ldots, \Delta T_{n,m}\left(t+\frac{\Delta t}{2}\right)\right]}{r_{n,m}^2} \quad (4\text{-}31)$$

where $C_T^2(n,m,t)$ is the single $C_T^2$ estimate for probes $n$ and $m$, var is the variance operator, $\Delta T_{n,m}$ is the Temperature difference between probes $n$ and $m$, $\Delta t$ is the scan time associated with the variance, and $r_{n,m}$ is the distance between probes $n$ and $m$. The final, average $C_T^2$ estimate is produced via:

$$\bar{C}_T^2(t) = \frac{\sum_{n=1}^{N-1}\sum_{m=n+1}^{N} C_T^2(n,m,t)}{N(N-1)/2} \quad (4\text{-}32)$$

The final RTD $C_n^2$ estimate is performed using [9]:

$$\begin{aligned} C_{n,RTD}^2(t) &= \left[77.6\times10^{-6}\left(1+\frac{7.52\times10^9}{\lambda^2}\right)\frac{\bar{P}(t)}{\bar{T}^2(t)}\right]^2 \bar{C}_T^2(t) \\ &\cong \left[79\times10^{-6}\frac{\bar{P}(t)}{\bar{T}^2(t)}\right]^2 \bar{C}_T^2(t) \end{aligned} \quad (4\text{-}33)$$

where $\bar{P}$ is the average pressure in millibar (mb), and $\bar{T}$ is the average temperature in Kelvin (K).

During the testing at the UMD UAS site, RTD array systems were placed at distances of 130 m, 223 m, and 310 meters from the MAT transmitter and adjacent to the optical propagation path in order to provide $C_{n,RTD}^2$ measurements

with comparison to the MAT turbulence estimates. Additionally, for a subset of tests the 8-probe RTD array was put in place vertically for comparison with the horizontal detectors in order to provide an estimate of anisotropy via the equation:

$$\mu_{y,RTD}(t) = \left[\frac{C_{n,x,RTD}^2(t)}{C_{n,y,RTD}^2(t)}\right]^{\frac{3}{2}} \tag{4-34}$$

where $C_{n,x,RTD}^2$ is an average $C_n^2$ estimate from the detectors oriented in the $x$-direction and $C_{n,y,RTD}^2$ is an average $C_n^2$ estimate from the detectors oriented in the $y$-direction. We note that in the figures to follow, because the MAT anisotropy ratio is determined along the direction determined to have more turbulence (i.e. $\theta_T$), we have elected to define the $x$-direction as vertical for comparison with the MAT data.

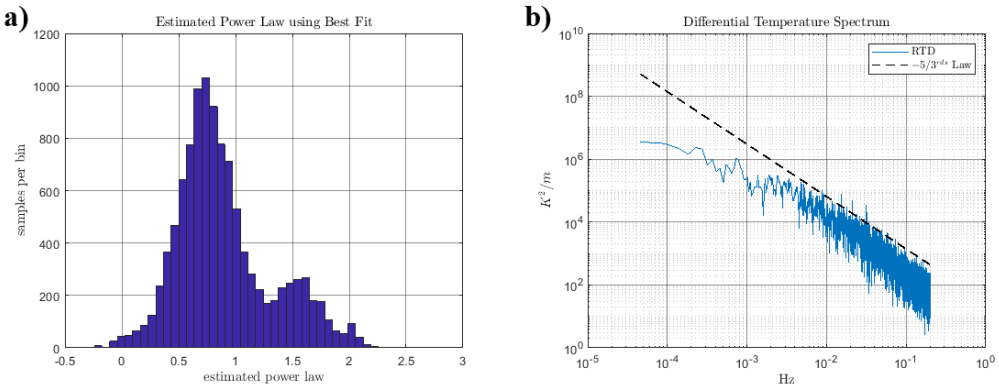


**Figure 4-19:** Power law estimates from the RTD array systems: a) Power law histogram in the spatial domain using a three minute variance scan time; b) Power law estimate in the time-frequency domain compared to the -5/3$^{rds}$ Law predicted by theory.

Although in previous sections we performed rigorous studies of theoretically proposed non-Kolmogorov turbulence we have elected to only consider the 2/3$^{rds}$ law of Kolmogorov in this section based upon data collected

using the RTD array systems. Histogram analysis of best fits for the RTD array data observed power law, shown in Figure 4-19a, shows a large amount of variation in the detected power law. However, we note that the largest two values in the histogram occur between .64 and .77. Additionally, we remind the reader that power law estimate above unity result in divergent wave structure functions, and so are considered unphysical. Time-frequency domain analysis of the differential temperature readings from the detectors, shown in Figure 4-19b, suggests that within the inertial range a $-5/3^{rds}$ law is indeed followed. Figure 4-19b plots the mean power spectrum from each probe pair's differential temperature, normalized by distance between probes, and averaged on the logarithmic scale. This matches the energy spectrum prediction of Kolmogorov [3] under the assumptions of Taylor's frozen flow hypothesis. In order to reduce the number of estimated parameters using fitting algorithms in this section, we have simply assumed a $2/3^{rds}$ spatial law and $-11/3^{rds}$ three dimensional spatial spectrum law in this section based on the RTD array data. We also note that separate analysis of temperature fluctuations from sonic anemometer data analyzed during testing at UCF as well as MAT optical detector power spectra collected without a chopping wheel at the MAT transmitter showed similar time-frequency characteristics to the RTD array data.

The results from testing with both the MAT transmitter and receiver at 150 cm average height was conducted at the UMD UAS site between 10 AM and 5 PM.

During the extent of the testing, the temperature measurements polled from a weather station attached at the top of the MAT transmitter structural framing rack began at 26 °C and steadily rose to a peak of 28 °C at 2 PM, and then varied between 27 °C and 28 °C for the rest of the testing. The atmospheric pressure at the start of testing was polled at 1019.9 mb and declined steadily to 1016.1 mb during the testing. Figure 4-20 and

Figure 4-21 summarize the results of the testing. Beginning with Figure 4-20, we note that the estimates of the refractivity angle and turbulence angle are at odds, however not orthogonal during the testing. The mean refractivity angle estimate was -41.5° and the mean turbulence angle estimate was -89.0° on this day. The median angles agreed with these metrics within 1.1°, and so were not significantly different. The mean and median $\mu_y$'s were both 1.40. The mean spot sizes (turbulent contribution removed) were 16.3 cm and 12.9 cm, with the medians agreeing to within 2 mm.

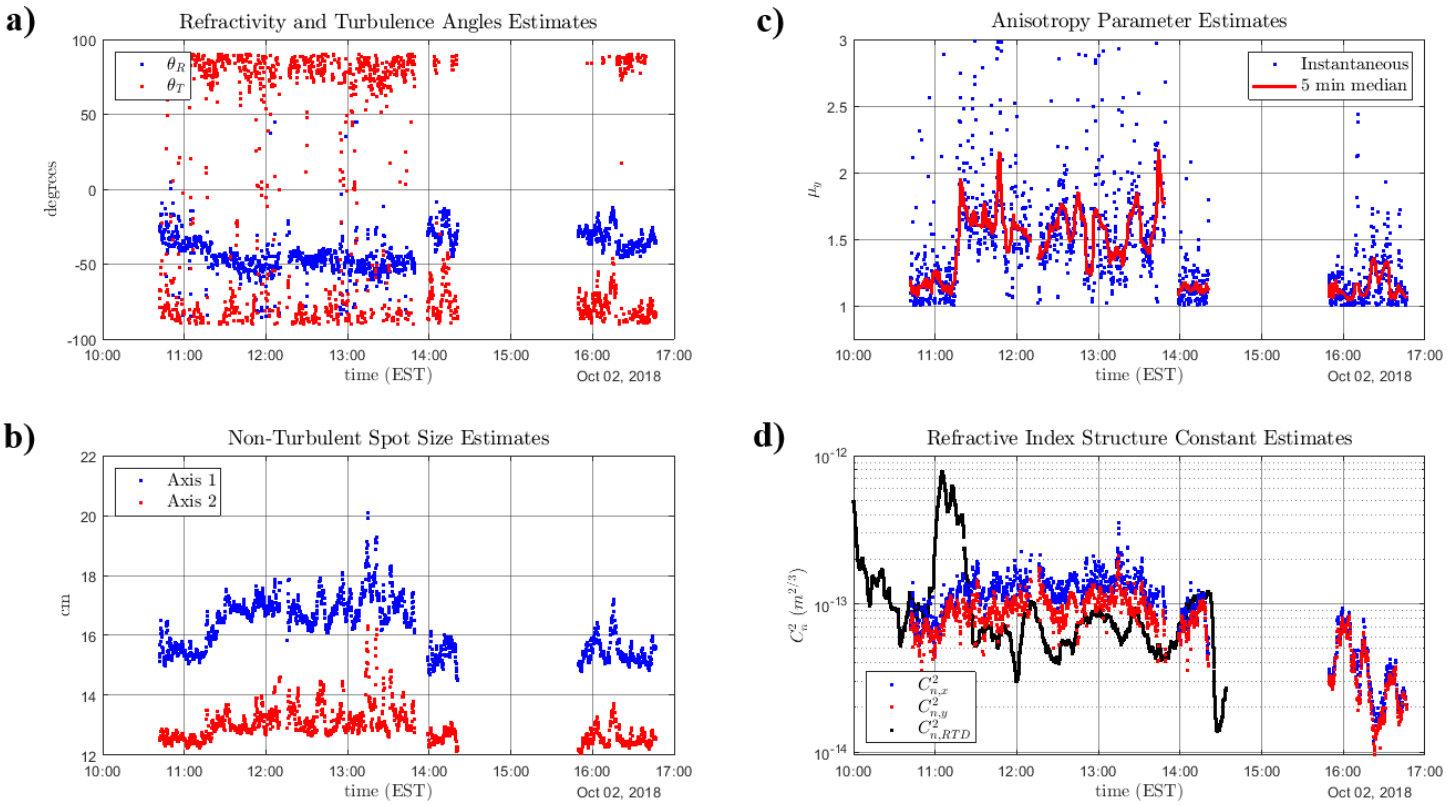


**Figure 4-20:** Output data from MAT experiment using the iterative fitting method, as well as a comparison with the RTD array averaged $C_n^2$ estimate with both sets of systems configured for 150 cm average elevation: a) Refractive and turbulent angle estimates, $\theta_R$ and $\theta_T$, relative the an objective horizontal angle; b) Non-turbulence spot size estimate produced from best fits for $\Lambda_1$ and $\Lambda_2$; c) Estimates of the anisotropy parameter, $\mu_y$, given as both as an instantaneous estimate and the five minute median; d) Estimates of the refractive index structure constants, $C_{n,x}^2$ and $C_{n,y}^2$, with the $x$-axis being along the turbulent angle, as well as the $C_n^2$ estimate from the RTD arrays averaged across all three systems.

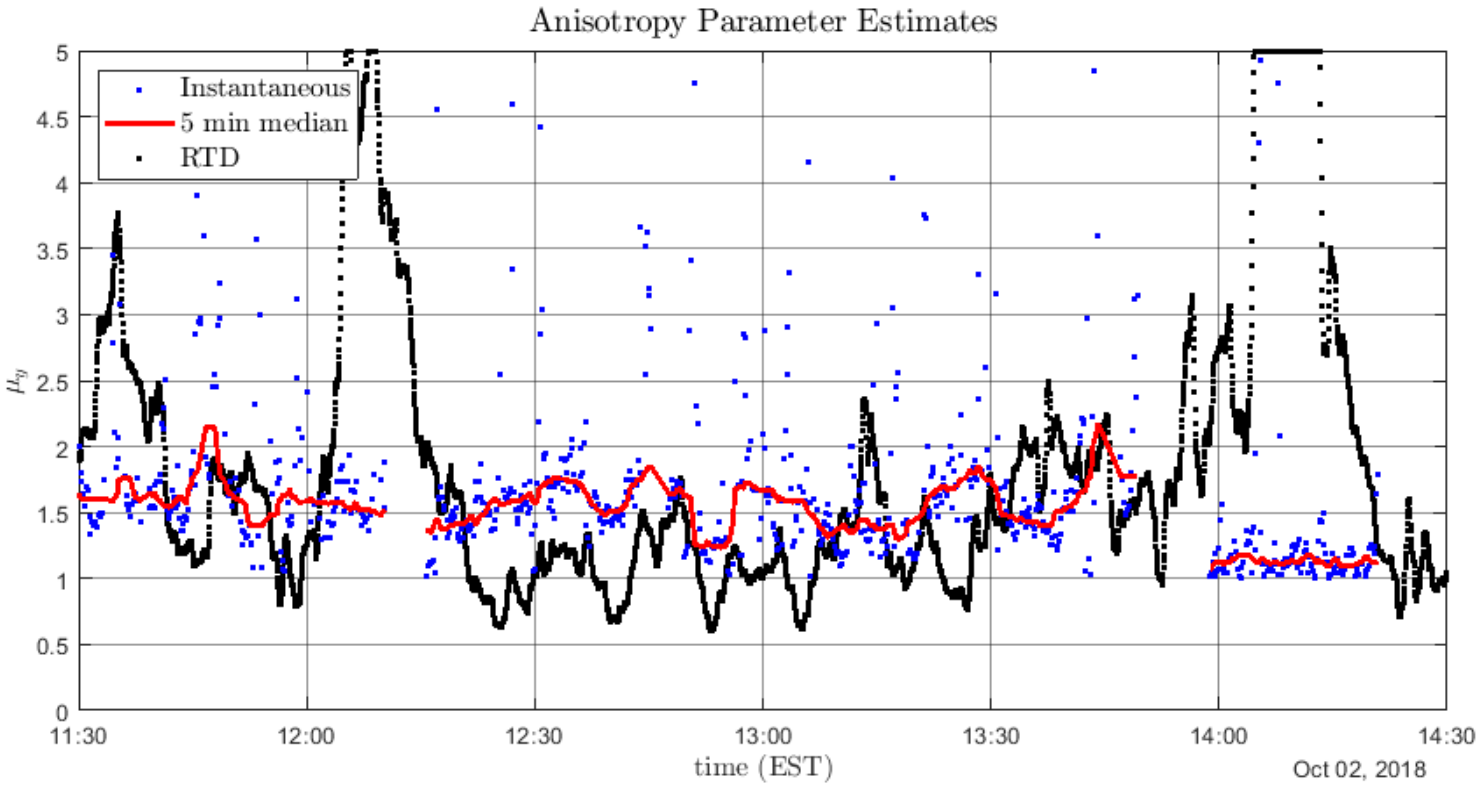


**Figure 4-21:** Anisotropy parameters using the MAT iterative fitting method compared with the estimate using the RTD array systems. The MAT system's instantaneous samples are computed using the normalized variance over one minute duration, with 10 seconds resolution. In addition to the instantaneous samples, a 5 minute median value is also shown. The RTD array systems' anisotropy parameter estimates are computed using temperature variances over three minutes duration, with 10 second resolution. Please note that the RTD array system's anisotropy estimate has be produced along the approximate turbulent angle estimated for this test, i.e. the *x*-direction is vertical and the *y*-direction is horizontal in this figure.

Figure 4-21 presents a comparison of the MAT iterative fitting algorithm's reported anisotropy parameter estimate versus the collected estimate from the RTD array systems. Additionally, a 5 minute median MAT anisotropy estimate is included. The RTD-based estimate was collected by averaging $C_n^2$ estimates from both horizontal systems and comparing with the estimates from the vertical system. While there is not complete agreement between MAT and RTD array system estimates, we note that rises in the anisotropy parameter appear to covary for the majority of occurrences. The RTD systems, however, produce much higher peak anisotropy parameter estimates and occasionally dip below unity (i.e. detects the turbulence direction is horizontal), whereas outside of 12:00 and 13:00 the MAT estimates are steadily vertical. Because the RTD probes were placed at different locations along the path and additionally are producing point estimates as opposed to path averages (the MAT system produces a weighted path average estimate) we assume the likely source of the discrepancy are inhomogeneities along the propagation path. Additionally, we note that the MAT comparisons seem to be more reasonable when compare to other estimates of anisotropy produced over long propagation paths at similar elevations. Beason, et al., [79] produced anisotropy parameter estimates at an elevation of 2 meters over a 1 km propagation path in January and February of 2017, and noted anisotropy estimates of $\mu_y/\mu_x$ between 1.05 and 1.67. The turbulence directions were reported as both horizontal and

vertical in this study. A similar study was performed in the summer by Wang, et al., [11] during which anisotropy estimates of $\mu_y/\mu_x$ between 1.11 and 3, however these measurements were taken at elevations varying between 39 and 139 cm during the summer. In Wang's study, the turbulence direction was always approximately vertical.

The MOG field experiment team's original plan for this test campaign was to test optical propagation path heights of 50, 100, and 150 cm sequentially in order to profiles turbulence and anisotropy at each height. Due to problems encountered during testing, such as issues keeping the MAT transmitter steadily pointed near the center of the MAT receiver, we were not able to accomplish these goals in sequence. Therefore, testing at 100 cm elevation was performed on October 1st, 2018. During this testing, the MAT system's estimate of the refractive and turbulent angles vary widely in a manor much different from the October 2nd 150 cm test. Additionally, we note that the anisotropy parameter also varies widely. Due to a concurrent test using the RTD arrays to profile inhomogeneous horizontal turbulence, no RTD arrays were placed vertically to provide an independent anisotropy estimate. Results from this testing are summarized in Figure 4-22. The mean and median refractivity angle estimates were -4.10° and 1.86° respectively. The mean turbulence angle estimates were -7.33° and -12.8° respectively. The mean and median $\mu_y$'s were 2.05 and 1.80. The mean spot sizes (turbulent contribution removed) were 19.2 cm and 17.9 cm, with the medians being 19.0 cm

and 17.9. Additionally, we note that the $C_{n,x}^2$ and $C_{n,y}^2$ estimates are relatively accurate relative to the average produced by the RTD array systems. We note the temperature on this day was noted as 25° C and the pressure noted at 1024.7 mb at 11:55 AM.

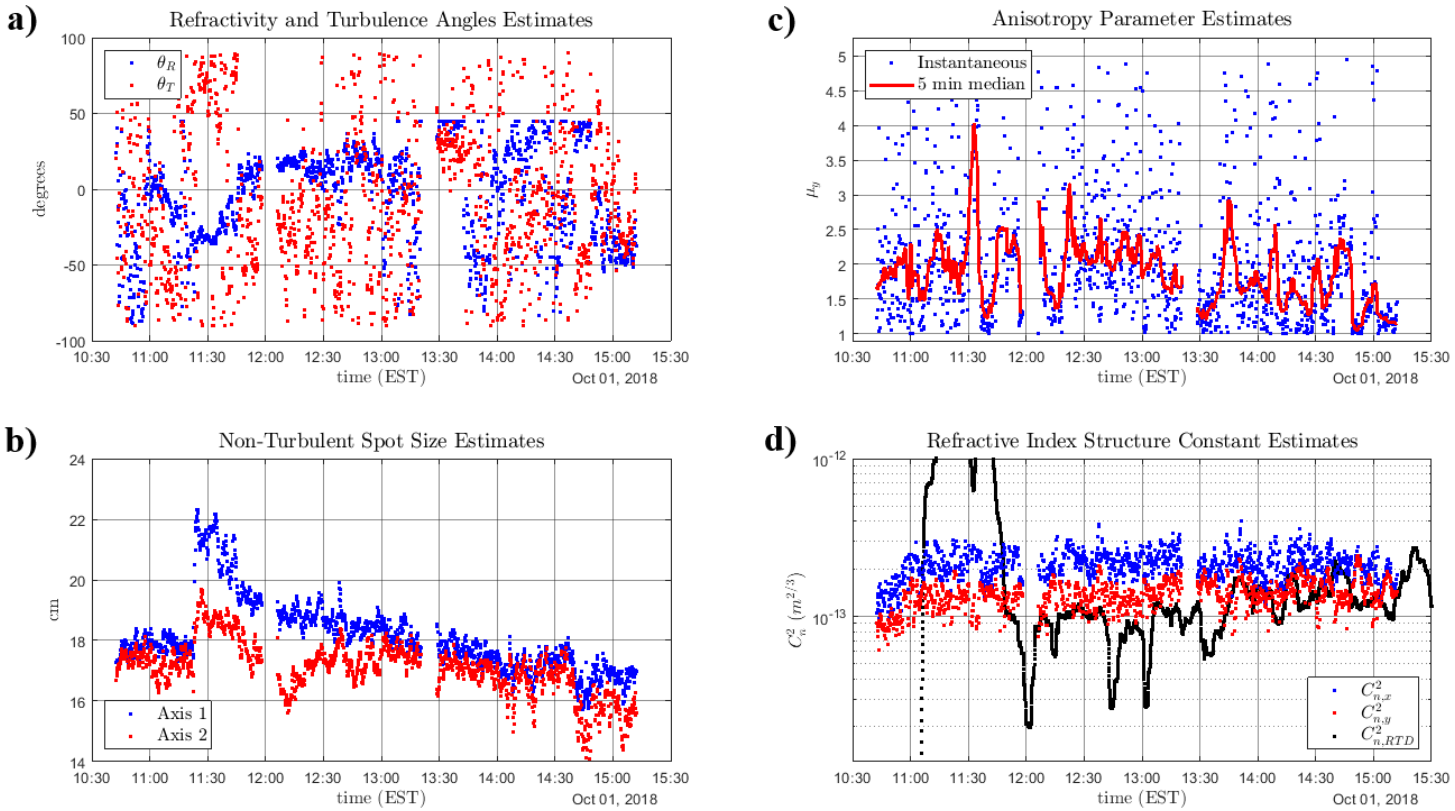


**Figure 4-22:** Output data from MAT experiment using the iterative fitting method, as well as a comparison with the RTD array averaged $C_n^2$ estimate with both sets of systems configured for 100 cm average elevation: a) Refractive and turbulent angle estimates, $\theta_R$ and $\theta_T$, relative the an objective horizontal angle; b) Non-turbulence spot size estimate produced from best fits for $\Lambda_1$ and $\Lambda_2$; c) Estimates of the anisotropy parameter, $\mu_y$, given as both as an instantaneous estimate and the five minute median; d) Estimates of the refractive index structure constants, $C_{n,x}^2$ and $C_{n,y}^2$, with the $x$-axis being along the turbulent angle.

Because the MAT anisotropy estimate seems to be performing poorly on October 1st, we sought to investigate possible reasons to explain our problems. Review of the individual intensity and scintillation index profiles from the testing indicated that atypical scintillation index profiles were at times accompanying the otherwise nominal intensity fits. An example plot is shown in Figure 4-23. Because this type of a scintillation index profile has not been observed in phase screen simulations, we assume this type of a profile indicates an extreme refractive index profile is present, causing the laser to interact with itself in an atypical manor. In our testing with other research groups, we have been told that large aperture optical scintillometers will often report strange results relative to other equipment on particularly hot days when the scintillometers are placed at ground elevation. The UCF group, as an example, typically places there commercial large aperture scintillometer atop a trailer when testing at the Kennedy Space Center (KSC) Shuttle Landing Facility (SLF) runway. Within our atmospheric testing community, this is sometimes referred to as a *micro-mirage effect*, because a mirage may not be visible when viewing incoherent light, however analysis of coherent light (which may interfere with itself) shows odd characteristics. For this data set, another source of error may be that given the observed scintillation indices and computed aperture averaging factors given in Section 3.5, the true Rytov variance for the shown data sample is likely above 1, and therefore we are not approximately within the weak fluctuation regime. However, phase screen simulations in the deep

fluctuation regime still show parabolic scintillation index profiles, and so we believe this is unlikely the major source of error.

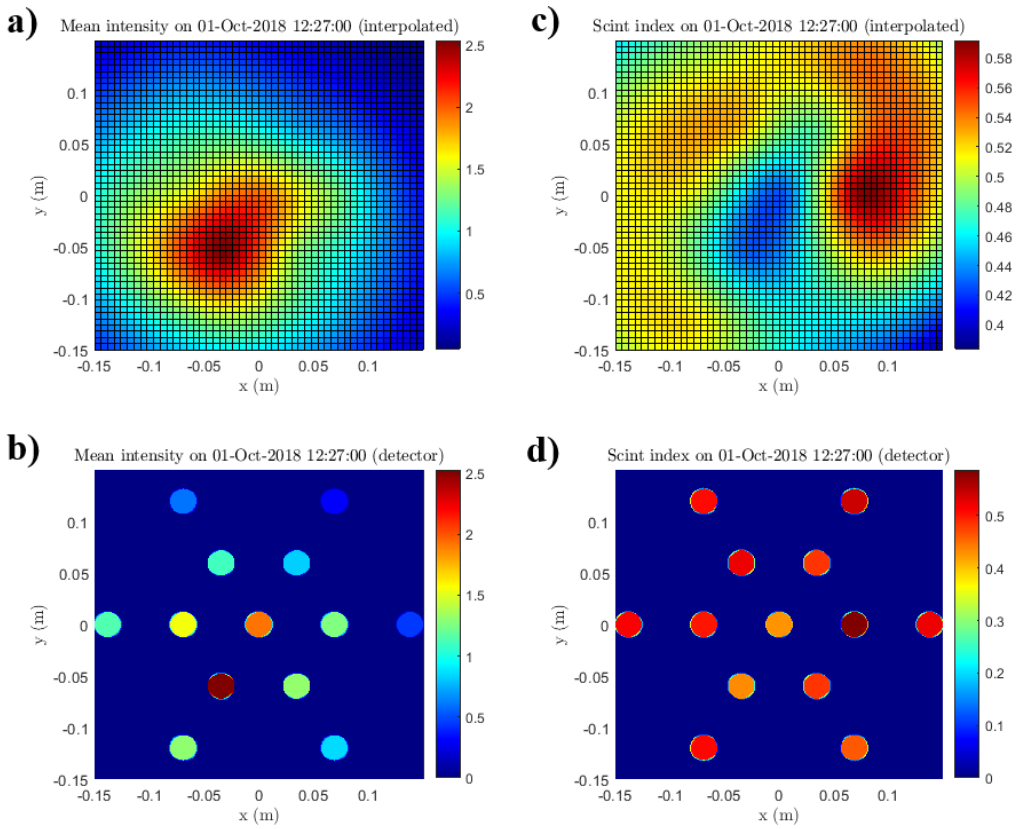


**Figure 4-23:** Example observed main intensity at the MAT receiver and from an outdoor field experiment on October 1st, 2018 at 100 cm elevation. The subplots are: a) Interpolated mean optical intensity profile; b) Detector-by-detector mean optical intensity; c) Interpolated scintillation index profile; d) Detector-by-detector scintillation index.

Testing at 50 cm elevation was performed on September 27th and October 3rd with mixed results. On September 27th although the angle estimates appeared to be relatively stable, the anisotropy parameter varied widely. The mean and median refractivity angle estimates were 70.0° and 67.7°, while the mean and median turbulence angles were -35.0° and -44.2°. The mean and median anisotropy

estimates were 1.92 and 1.53. The mean non-turbulent spot sizes were 21.3 cm and 18.6, with the medians within 1 mm of the mean. $C_{n,x}^2$ and $C_{n,y}^2$ estimates are relatively accurate relative to the average produced by the RTD array systems. The temperature and pressure for September 27th, 2018 were noted at 20° C and 1018.1 mb at 10:08 AM.

Two datasets were collected using the MAT on October 3rd, 2018 with improved results. Because the direction of greater turbulence seems to have switched between the collected data sets, we will present the relevant statistics separately beginning with the data set collected between 10:00 AM and 11:00 AM. Mean and median refractivity angle estimates were -17.7° and -18.6°, while the mean and median turbulence angles were 87.4° and 86.7°. The mean and median anisotropy estimates were 1.69 and 1.49. The mean non-turbulent spot sizes were 14.9 cm and 12.7, with the medians within 1 mm of the mean. $C_{n,x}^2$ and $C_{n,y}^2$ estimates are relatively accurate relative to the average produced by the RTD array systems.

For the second data set of October 3rd, 2018 which was collected between 11:10 AM and 12:15 PM we note that the direction of turbulence notably changed to being approximately horizontal. Mean and median refractivity angle estimates were -8.9° and -7.3°, while the mean and median turbulence angles were -15.7° and -22.5°. The mean and median anisotropy estimates were 1.28 and 1.19. The mean non-turbulent spot sizes were 14.5 cm and 12.5, with the medians within 1 mm of

the mean. $C_{n,x}^2$ and $C_{n,y}^2$ estimates are relatively accurate relative to the average produced by the RTD array systems.

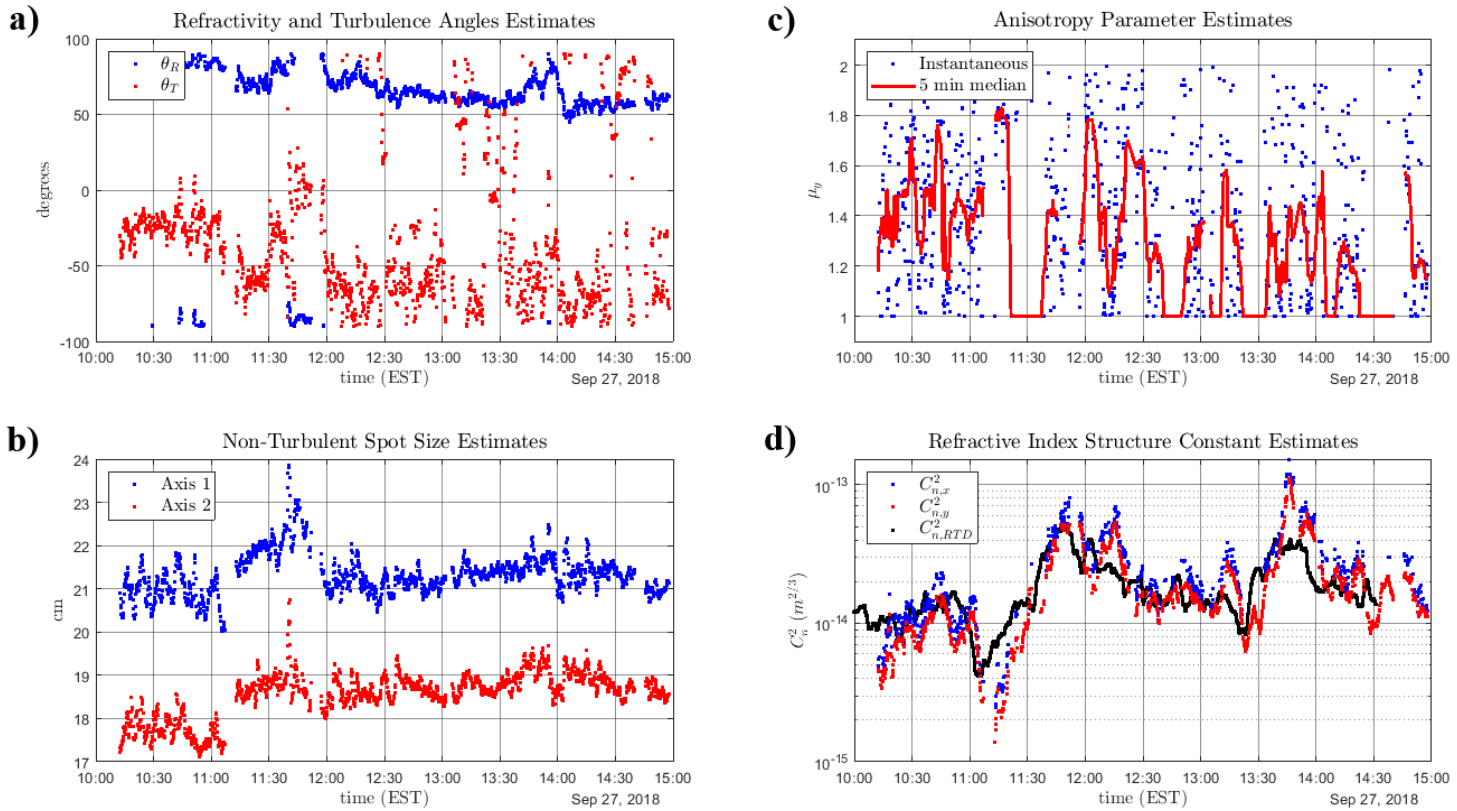


**Figure 4-24:** Output data from MAT experiment using the iterative fitting method, as well as a comparison with the RTD array averaged $C_n^2$ estimate with both sets of systems configured for 50 cm average elevation on September 27th, 2018: a) Refractive and turbulent angle estimates, $\theta_R$ and $\theta_T$, relative the an objective horizontal angle; b) Non-turbulence spot size estimate produced from best fits for $\Lambda_1$ and $\Lambda_2$; c) Estimates of the anisotropy parameter, $\mu_y$, given as both as an instantaneous estimate and the five minute median; d) Estimates of the refractive index structure constants, $C_{n,x}^2$ and $C_{n,y}^2$, with the $x$-axis being along the turbulent angle.

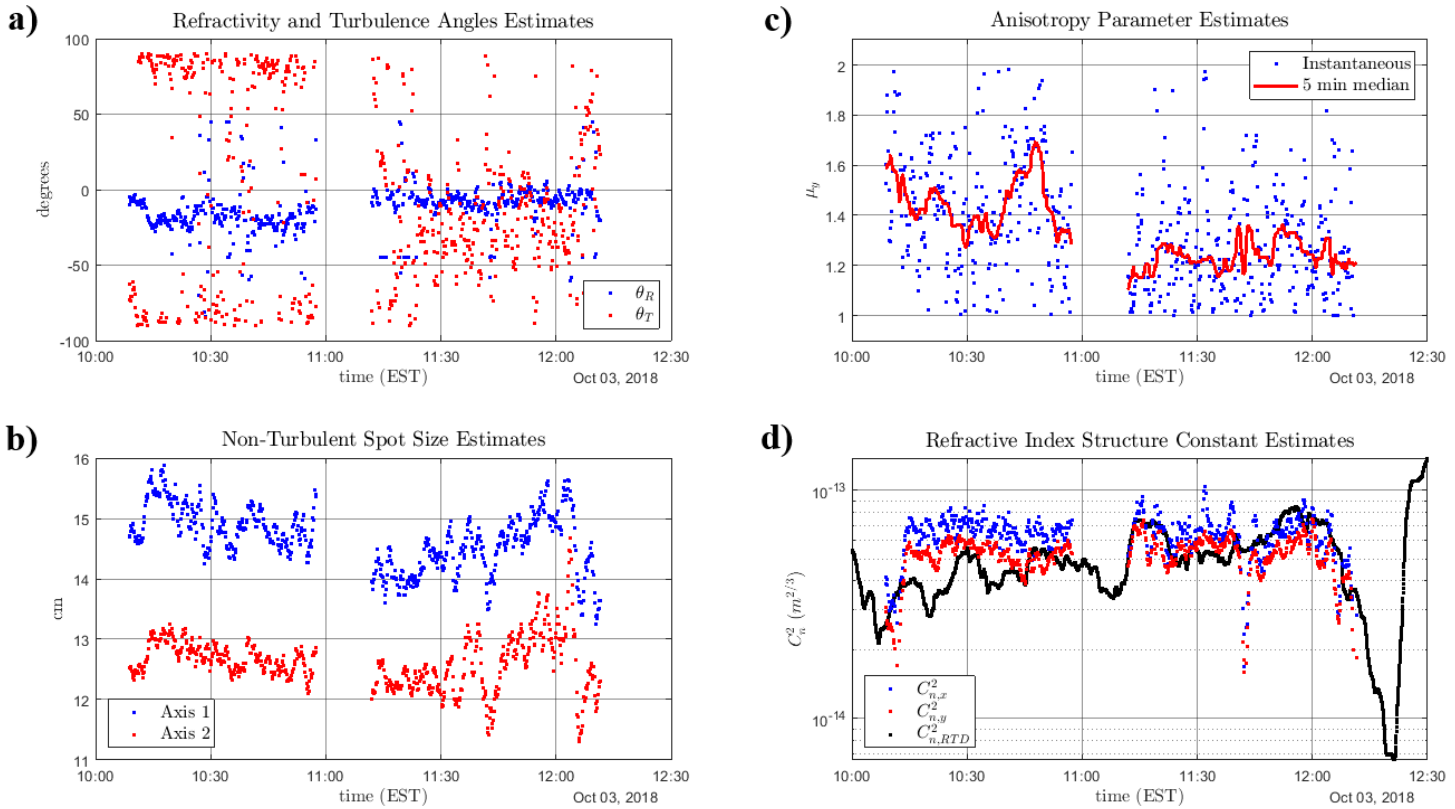


**Figure 4-25:** Output data from MAT experiment using the iterative fitting method, as well as a comparison with the RTD array averaged $C_n^2$ estimate with both sets of systems configured for 50 cm average elevation on October 3rd, 2018: a) Refractive and turbulent angle estimates, $\theta_R$ and $\theta_T$, relative the an objective horizontal angle; b) Non-turbulence spot size estimate produced from best fits for $\Lambda_1$ and $\Lambda_2$; c) Estimates of the anisotropy parameter, $\mu_y$, given as both as an instantaneous estimate and the five minute median; d) Estimates of the refractive index structure constants, $C_{n,x}^2$ and $C_{n,y}^2$, with the $x$-axis being along the turbulent angle.

Again, a possible explanation for the disconnect in results between the September 27th and October 3rd data is the prevalence of odd scintillation index profiles seen in the September 27th data which is not prevalent in the October 3rd data set. Figure 4-26 shows a capture of the September 27th data and Figure 4-27 displays a capture of the October 3rd data. We note that the low scintillation indices observed on September 27th indicate that we are indeed within the weak fluctuation regime, supporting the *micro-mirage effect* hypothesis.

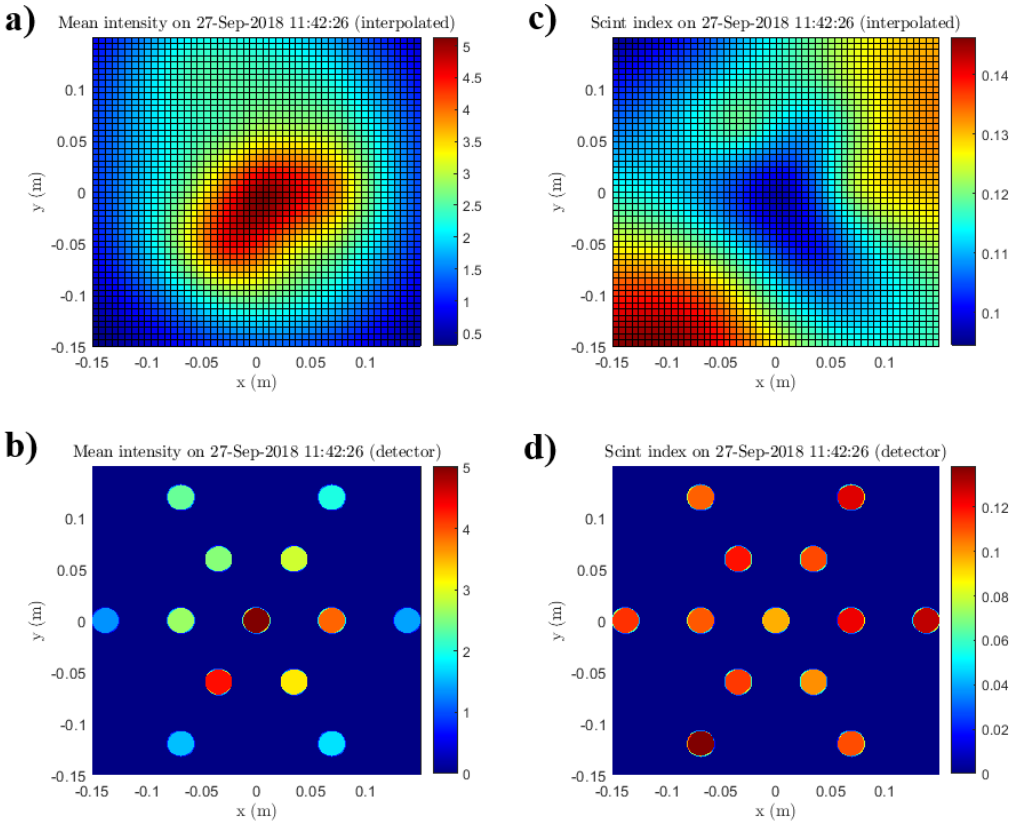


**Figure 4-26:** Example observed main intensity at the MAT receiver and from an outdoor field experiment on September 27th, 2018 at 50 cm elevation. The subplots are: a) Interpolated mean optical intensity profile; b) Detector-by-detector mean optical intensity; c) Interpolated scintillation index profile; d) Detector-by-detector scintillation index.

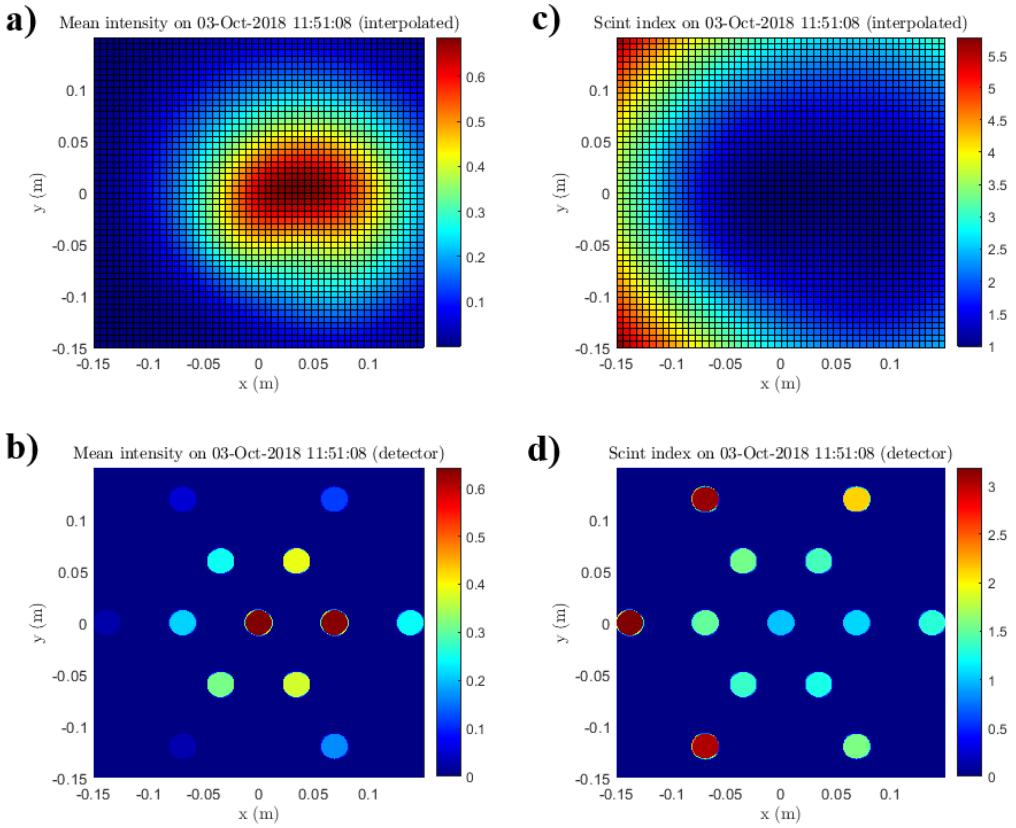


**Figure 4-27:** Example observed main intensity at the MAT receiver and from an outdoor field experiment on October 3rd, 2018 at 50 cm elevation. The subplots are: a) Interpolated mean optical intensity profile; b) Detector-by-detector mean optical intensity; c) Interpolated scintillation index profile; d) Detector-by-detector scintillation index.

In conclusion, the MAT turbulence profiling experiment seems to be a partial success. We see that at some times we produce anisotropy and turbulent angle estimates which seem to correlate with observations made using the RTD arrays. However, during the one experiment where we had placed an RTD array in a vertical configuration for anisotropy profiling validation, only slightly more than half of the data seemed correlated well between systems. We note also, that inhomogeneity of the turbulence profile in the propagation direction was most

likely playing a roll. On the other hand we see good agreement between the $C_n^2$ estimates produced by the MAT and the RTD array systems in place along the path. Therefore, in the weak fluctuation regime the MAT seems to be operating as a reliable scintillometer. Additionally, we have produced experimental observations of atypical scintillation index profiles which may spur additional study of refractive index affects affecting near surface coherent light propagation.

## 4.6: Simultaneous Extinction Rate and Turbulence Profiling in the Deep Fluctuation Regime

Prior to the testing at the UMD UAS site, a conceptually simpler test was performed at the KSC SLF runway in Merritt Island, Florida in early May, 2018. The testing concept was to use an initially collimated beam, such that the initial beam parameters were well understood, over a long path such that significant beam expansion due to turbulence was observed. In that manner, given the diffraction limited spot size, *W*, is well known $C_{n,x}^2$ and $C_{n,y}^2$ can be estimated using the below set of equations, assuming a -11/3$^{rds}$ spectral power law:

$$\rho_{s,x} \cong \sqrt{\frac{8L^2}{k_0}\left(W_{LT,x}^2 - W^2\right)} \tag{4-35}$$

$$\rho_{s,y} \cong \sqrt{\frac{8L^2}{k_0}\left(W_{LT,y}^2 - W^2\right)} \tag{4-36}$$

$$C_{n,x}^2 = \frac{1.8300}{k_0^2 \cdot L \cdot \rho_{s,x}^{5/3}} \tag{4-37}$$

$$\mu_y = \sqrt{\frac{W_{LT,x}^2 - W^2}{W_{LT,y}^2 - W^2}} \tag{4-38}$$

$$C_{n,y}^2 = \frac{C_{n,x}^2}{\mu_y^{2/3}} \tag{4-39}$$

In order to test this method, we performed testing over a 2 km propagation path at the KSC SLF. The SLF features a roughly 5 km long runway with has been specially engineered to run tangent to the curvature of the earth, and as such is ideal for deep fluctuation regime experiments. An aerial view of the KSC SLF is given in Figure 4-28a.

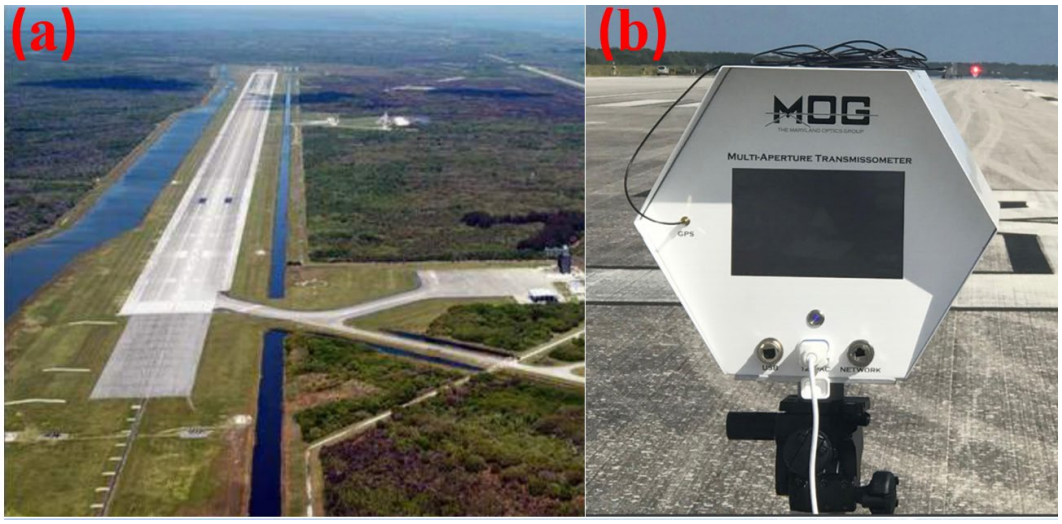


**Figure 4-28:** (a) Aerial view of the SLF site; (b) MAT receiver with a GPS receiver resting on the sun-shield.

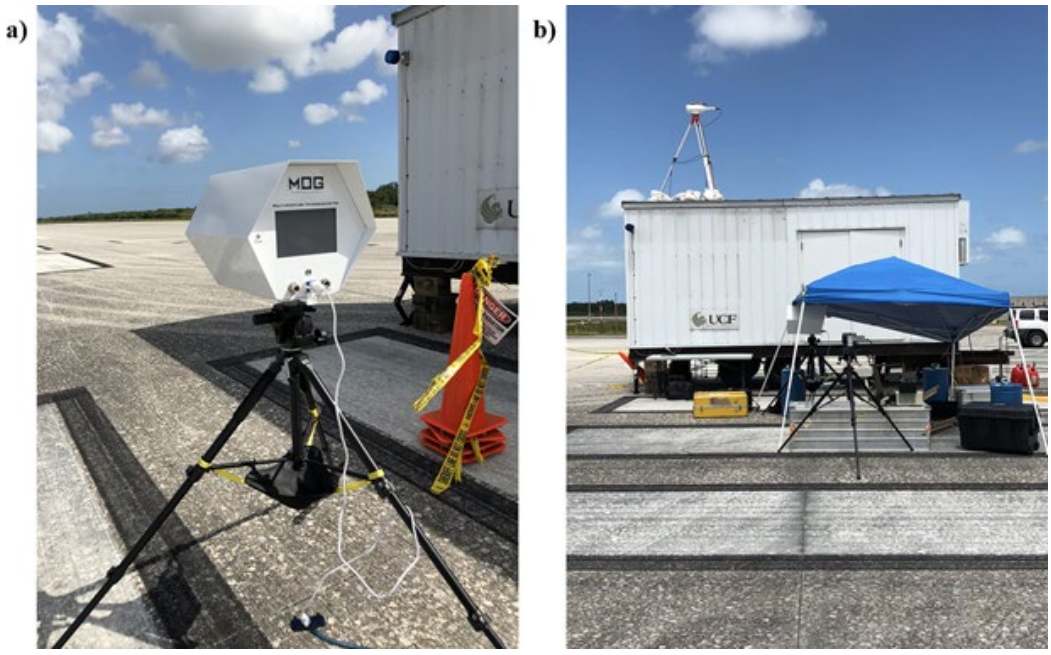


**Figure 4-29:** a) MAT receiver initial setup; (b) MAT receiver in operation partially under a canopy adjacent to a USC trailer with a scintillometer transmitter on the roof.

In order to avoid vibrations and disturbances, the MAT transmitter was placed in a UCF trailer and all optics of the operational MAT system were mounted to an optics table. A shearing interferometer was used in tandem with beam expander lens position adjustments in order to collimate the transmit beam. Once again, an optical chopping wheel was in place to aid the removal of background light, and a large steering mirror was used for pointed at the target. Additionally, the transmit spot size was measured at 1.4 cm and the transmitter wavelength was once again 632.8 nm.

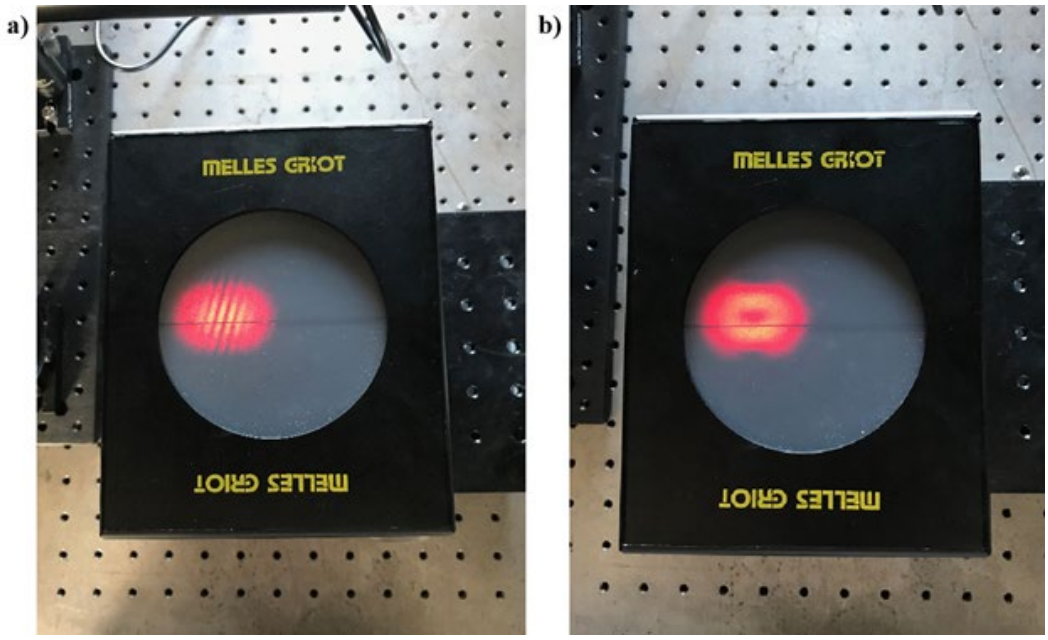


**Figure 4-30:** Images of the shearing interferometer hologram during collimation procedure, with the beam propagating from left to right: a) Shearing interferometer readout for weakly divergent beam; b) Shearing interferometer readout for a collimated beam.

The biggest issue for the May 2018 testing was maintaining accurate pointing on the MAT receiver. For that reason, there are large dropouts in the data. However, we believe the data collected is quite consistent during periods when the MAT is operating successfully. Figure 4-31 displays comparisons between the MAT $C_n^2$ estimates and those of RTD probes placed near the MAT transmitter at approximately 1 m (4-probe RTD array) and 1.5 m (8-probe RTD array) elevation. The MAT transmitter was at roughly 2 m elevation, and the receiver at roughly 1.5 m elevation at the end of the 2 km propagation path.

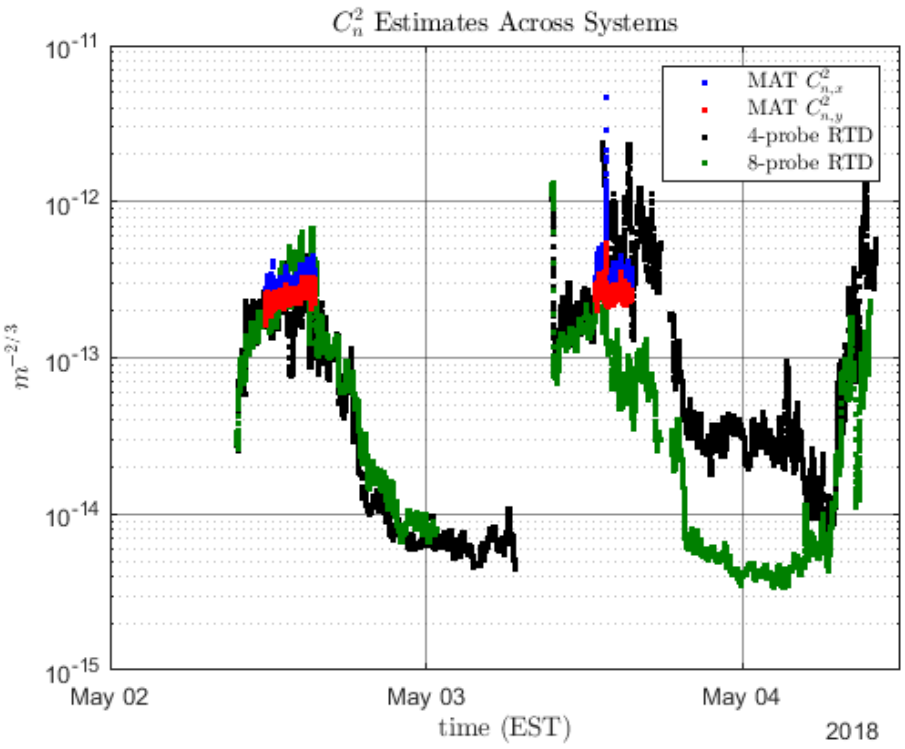


**Figure 4-31:** $C_n^2$ estimates from the MAT system as well as two RTD array systems from May, 2018 testing.

Figure 4-31 summarizes the MAT and RTD turbulence estimates over both days. Individual plots are given below. Along with the turbulence estimates, in order to demonstrate that the MAT system is able to estimate extinction coefficient accurately we have also included plots of comparisons between the MAT extinction rate estimate alongside those from UCF's commercial visibility meter placed midway along the propagation path. We believe the results match very well, given that the MAT produces a path averaged estimate and the visibility meter provides a point estimate.

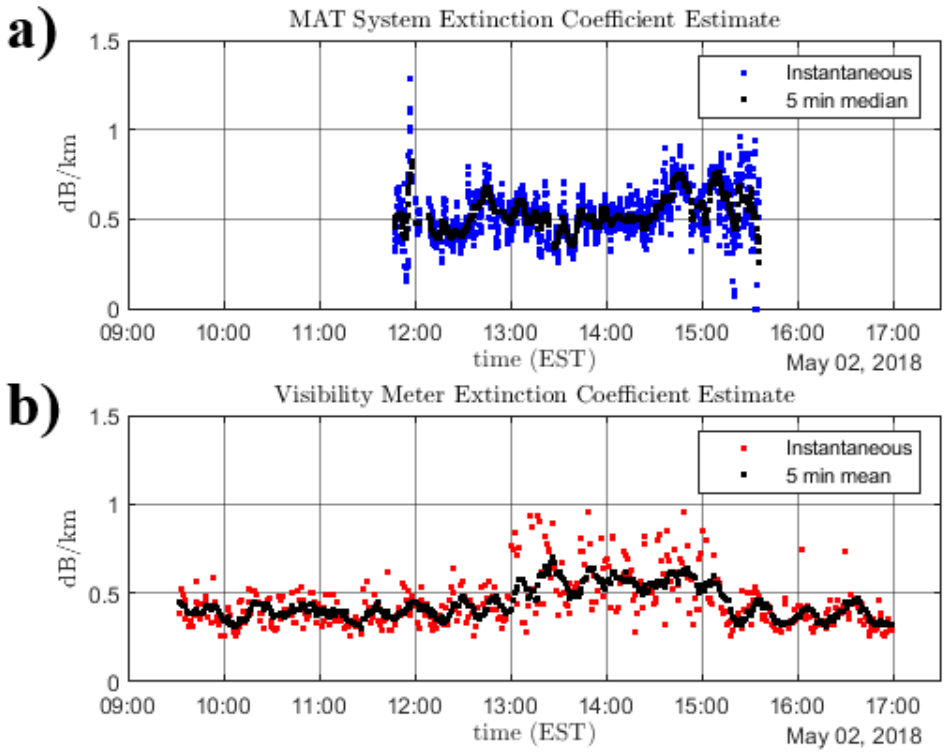


**Figure 4-32:** a) Extinction rate estimate from the MAT system on May 2nd, 2018; b) Extinction rate estimate from UCF's commercial visibility meter on May 2nd, 2018.

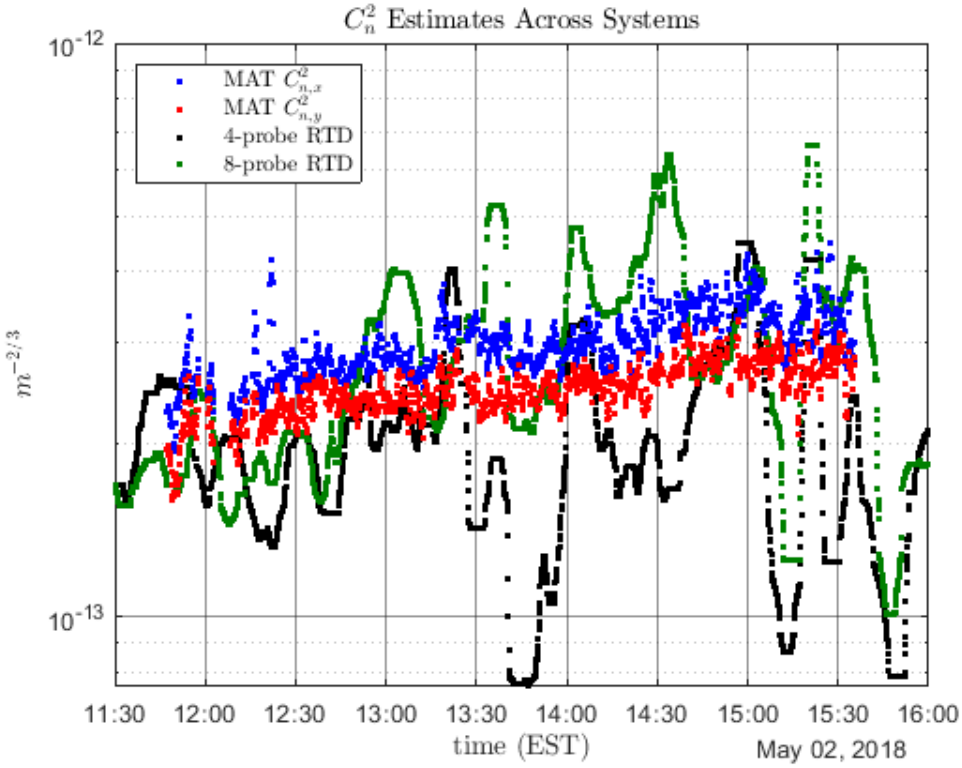


**Figure 4-33:** $C_n^2$ estimates from the MAT system as well as two RTD array systems from May 2nd, 2018 testing. Please note that the *x*-direction for the MAT estimate is given by the beam angle in the next figure.

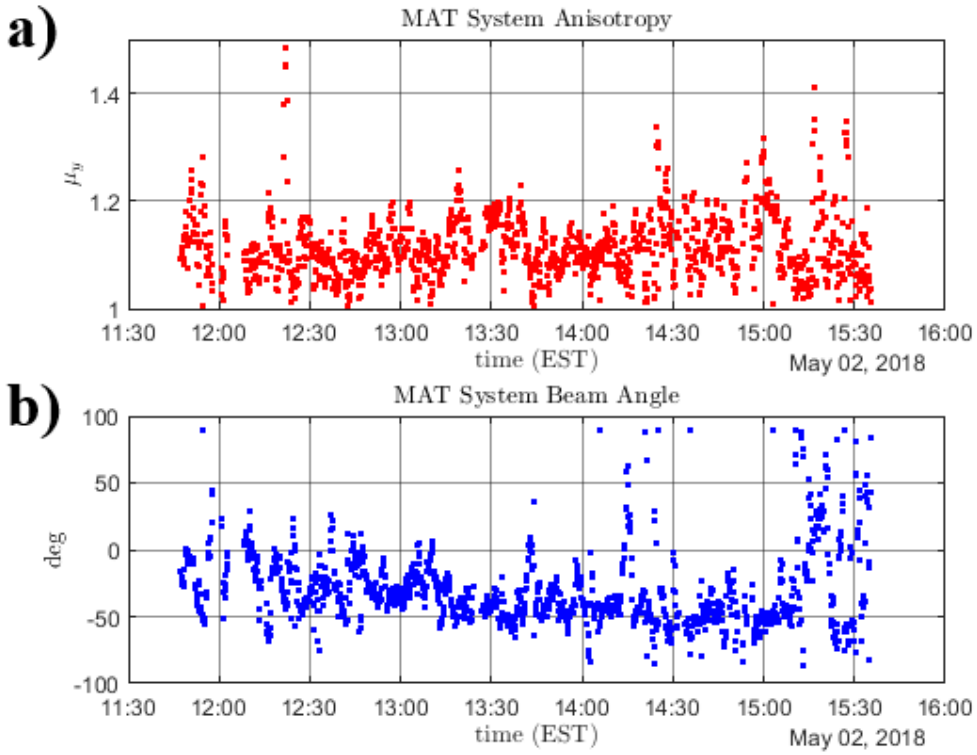


**Figure 4-34:** a) Anisotropy parameter estimate from the MAT system from May 2nd, 2018 testing; b) Beam angle estimate from the MAT system from May 2nd, 2018 testing, i.e. the major axis of turbulence under our assumptions.

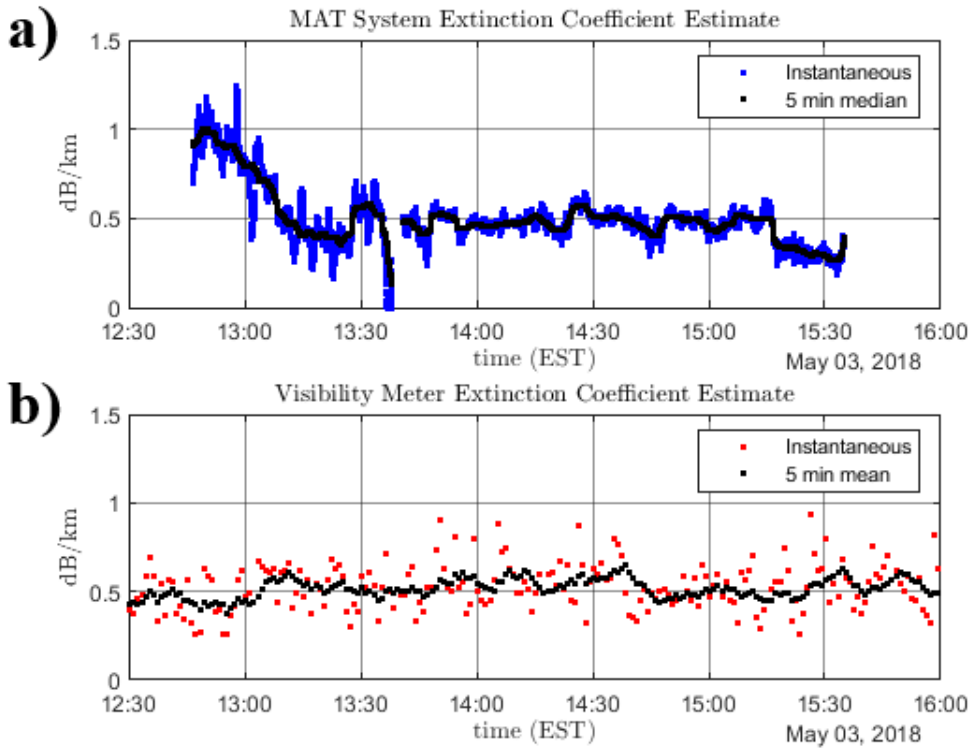


**Figure 4-35:** a) Extinction rate estimate from the MAT system on May 3rd, 2018; b) Extinction rate estimate from UCF's commercial visibility meter on May 3rd, 2018.

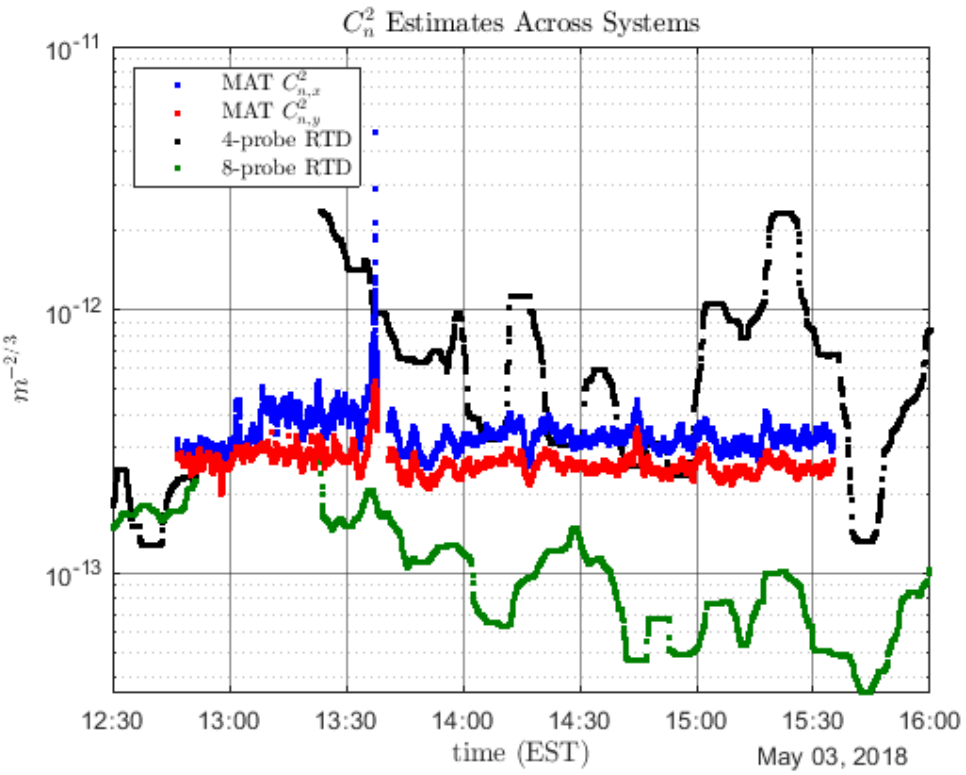


**Figure 4-36:** $C_n^2$ estimates from the MAT system as well as two RTD array systems from May 3rd, 2018 testing. Please note that the *x*-direction for the MAT estimate is given by the beam angle in the next figure.

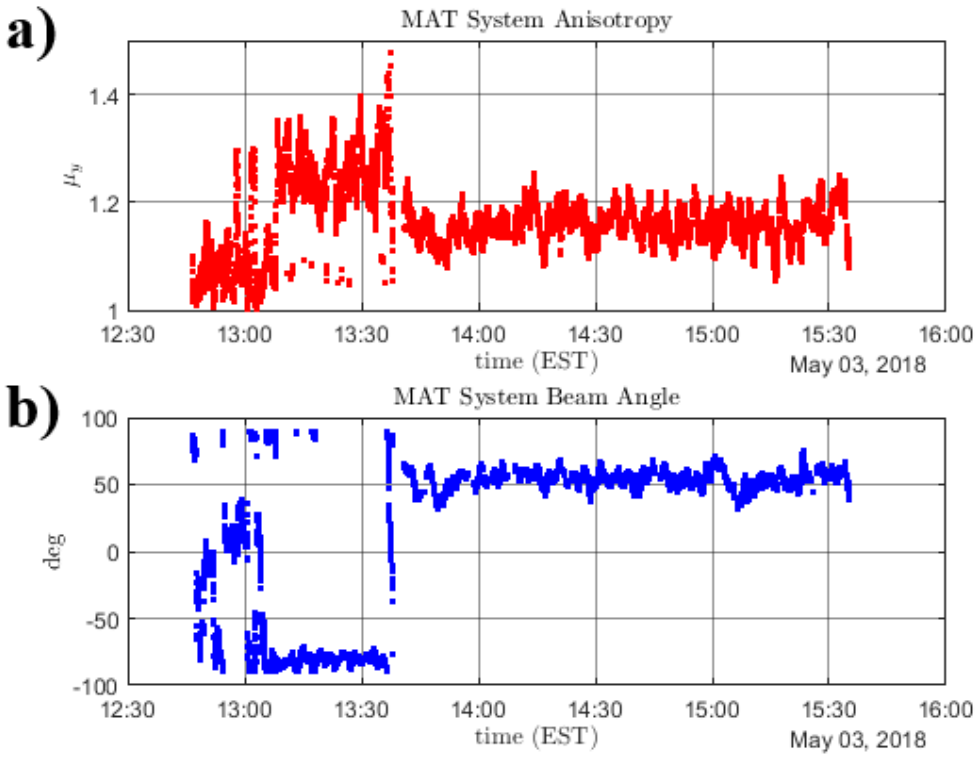


**Figure 4-37:** a) Anisotropy parameter estimate from the MAT system from May 3rd, 2018 testing; b) Beam angle estimate from the MAT system from May 3rd, 2018 testing, i.e. the major axis of turbulence under our assumptions.

The data collected during the early May 2018 testing is limited, but very interesting as compared to the data collected in the weak fluctuation regime at the UMD UAS test site. Noting that some of the MAT turbulence estimates approach $C_n^2$'s of $5 \times 10^{-13}\ m^{-2/3}$, we first discuss the extinction coefficient estimates. At the noted $C_n^2$, along with the propagation lengths and wavenumbers under test, the Rytov variance is 100.78, putting our testing squarely within the strong fluctuation regime [9], or deep turbulence. The transmissometer extinction rate estimates still compare very closely to the point visibility meter in spite of the optical turbulence

effects, although there are some clear spikes in extinction at low readings. Given the complications of the testing, and the fact that others may have been working along the propagation path, the spikes in extinction estimates from the MAT system may have been due to exhaust fumes from portable generators or vehicles along the path blowing into the propagation path, or due to short duration pointing inaccuracies due to sudden changes in steady-state refraction along the path. A cloud passing overhead can, for instance, cause a sudden dip of the beam centroid at the detector. We also note low extinction reading, which may have been due to light pollution. The transmissometer synchronization and background light remove routines work well for slow changes in background light, however if a blinking instrument light was captured by the transmissometer this type of light pollution would most likely not be successfully removed by our algorithms.

The turbulence estimates from the MAT system seem quite steady as compared to readings from the RTD array systems. Given that our diffraction limited spot size for this test was 3.2 cm, and long term spot sizes upwards of 30 cm were commonly observed, this indicates that the change in coherence length is the main driver of the long term spot size. Given that the spherical wave coherence length in homogenous turbulence is dependent upon the propagation distance according to a -3/5 law [see Equations (3-16) and (3-17)], and the beam expansion used to estimate $C_n^2$ is given by approximately $\sqrt{8L^2/(k_0\rho_s^2)}$, we assume the estimates weight inhomogeneities by a 2/3$^{rds}$ law of distance to the from the receiver

(integration of a 2/3rds law weighting over $L$ yields a 5/3rds law). Despite the $C_n^2$ estimates weighting turbulence near the transmitter higher, we still appear to get a very good average estimate with a low incidence of extreme fluctuations.

Given the work in the previous section, the estimates of anisotropy are somewhat surprising. The spot size ratios in the deep turbulence regime appear to be closer than what was noted in the weak turbulence regime (see Figure 4-38), with a fit routine attempting to mitigate the effects of turbulence. Additionally, we note that typical anisotropy estimates in the deep fluctuation regime seem to hover between 1 and 1.2. Much of the weak fluctuation regime anisotropy readings were more extreme than this, with exceptions being parts of the days' testing on Oct 2nd and Oct 3rd, 2018. This may point to issues in the weak fluctuation regime iterative fitting method, the approximations used, or (perhaps) a problem with the optics in the weak fluctuation regime testing. Alternatively, it may be the case that strong turbulence is simply more isotropic than weak turbulence. Certainly, we can infer that any refractivity distortions observed in the weak fluctuation regime testing appear to be approximately negligible in our strong fluctuation regime testing. This may, again, be a natural element of deep turbulence or point to the collimation of the laser in deep turbulence testing mitigated problems with transmitter optics, such as differing radii of curvature along different axes of the transmit beam. Regardless, we believe that in this section we have demonstrated a reliable approach for simultaneous estimating atmospheric turbulence and extinction rate in

a regime where the scintillation index is expected to saturate. In the future, it is possible that this method could be made more reliable using automated transmitter pointing along with a control loop with a low enough bandwidth as to allow all the low temporal frequency contributions of turbulence to manifest, but still allow for accurate point over the long term. The temporal frequency analysis in the previous section suggests that 1 mHz would likely be sufficient.

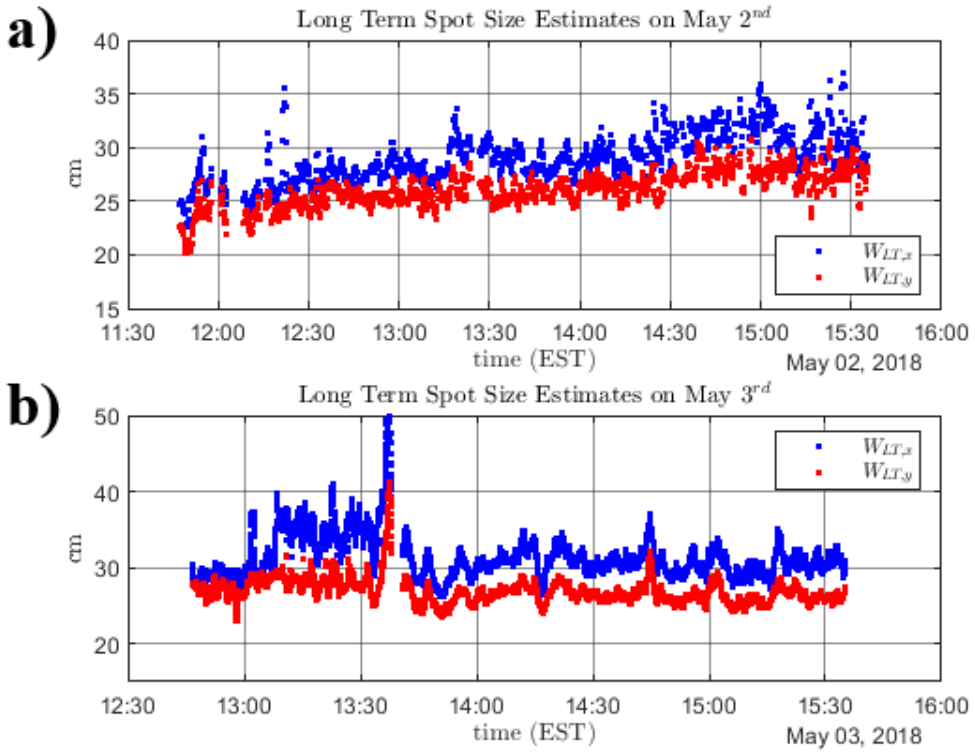


**Figure 4-38:** MAT long term spot size estimates on: a) May 2nd, 2018; b) May 3rd, 2018.

# Chapter 5 : Summary and Future Work

## 5.1: Summary

The work contained in this dissertation has demonstrated novel methods for both simulation and experimental characterization of atmospheric optical turbulence. We have developed new method for performing computational optics simulations of wave propagation through novel forms of atmospheric turbulence, presented a thorough survey of performance of various theoretical predictions' performance when tested using Monte-Carlo simulation methods. These investigations of theoretical predictions using simulations have informed our experimental methods, and based on this we have developed new methods for the characterization of anisotropic turbulence in the weak and deep fluctuation regimes.

In Chapter 2, recent theoretical investigations of non-Kolmogorov and anisotropic turbulence spawned an investigation regarding the convergence of statistical metrics of interest in the simulation of atmospheric optical turbulence under new symmetry and power law assumption. This led us to augment standard algorithms to include randomized spectral sampling as well as new guidelines regarding the number of subharmonic frequency elements which should be added to the FFT-based phase screens in order to assure accurate statistics. While the focus was initially on anisotropic, non-Kolmogorov spectral models, being aware of other widespread spectral models (i.e. the modified atmospheric spectrum) in

common use in the atmospheric optics community we began to investigate the impact of using the revised method on other spectral models, with positive results both with and without considering the effects of randomized subharmonic distortions. Additionally, we have provided an abundance of data regarding the relationship between both power law (in the case of non-Kolmogorov turbulence) and outer scale (in the case of the modified atmospheric spectrum) and statistical accuracy parameterized by number of subharmonics added to the phase screens, which should be of great utility to researchers attempting to choose an ideal set of model parameters.

Using the newly refined phase screen algorithm, in Chapter 3 we use the revised method to investigate the accuracy of theoretical predictions regarding both long term spot size and scintillation index statistics. In Section 3.2, we have investigated several predictions regarding long term spot size of collimated Gaussian beams propagating through deep atmospheric turbulence. We have demonstrated that extensions of the weak fluctuation regime predictions into the strong fluctuation regime are not accurate, and additionally that expressions depending upon an inverse relationship between the coherence length of a spherical wave and the spot size growth are more accurate than expressions based upon the coherence length of plane waves when the spot size results are parameterized according to the three dimensional spectral power law of turbulence, $\alpha$, across reasonable values of 3 to 4. We then continued with a similar analysis applied to

beams focused upon the receive plane propagating through anisotropic, non-Kolmogorov turbulence. We find that while the expressions which were determine to be very accurate for initially collimated beam were the most accurate predictors of long term spot size for focused beams, there was a non-negligible disagreement between predictions and results for low values of $\alpha$. The observation echoes sentiments in the literature that the behavior of focused beams propagation through turbulence are not completely understood. Additionally, analysis of the scintillation index behavior of focused beams in Section 3.3 showed a stark disagreement with theoretical predictions. Finally, in Section 3.5 we have demonstrated problems applying the weak fluctuation approximations to beams with initially circular Gaussian intensity but in which the initial radius of curvature varies with angle. Having reviewed the Rytov method's application in predicting weak fluctuation regime results [9], it is my feeling that this is mostly because extensions of the age-old analysis to more recent developments (such as the consideration of refractivity distortions) the statistical moments of the field need to be re-derived from first principles without the symmetry assumptions present in the original analysis. Despite these issues, we have derived some useful approximations based upon the wave optics simulation results, and applied them to our experimental analysis.

Chapter 4 describes a variety of experiments using the MAT system to profile both extinction rate and turbulence in outdoor field tests, as well as the

fundamental method of operation of MAT system. As noted in Sections 4.3 and 4.6, the system appears to very accurately estimate extinction coefficient in the weak and deep fluctuation regimes, provided the transmitter is accurately aligned with the receiver. Additionally, we consider it quite impressive that the transmissometer extinction rate estimate appears to be accurate when tested in experiments featuring Rytov variances nearing 100. In Section 4.4 we have outlined a method for iterative fitting refractivity and turbulence parameters in scenarios were the initial beam radius of curvature and steady-state atmospheric refractive affects are not understood, which is based partly upon observations from phase screen simulations in the previous chapter. We consider this work to be partially successful. Although we have not been able to observe high accuracy in comparison with point detectors extrapolating $C_n^2$ estimates from observations of temperature fluctuations, we do find that in the weak fluctuation regime the transmissometer is working quite accurately as a scintillometer. The turbulence results of Section 4.6 in the deep fluctuation regime are very encouraging, and quite stable when compared to point detectors. However, the low anisotropy parameters measured in this test cause us to question some of the higher values (i.e. above 1.3) noted in Section 4.5. While the results were encouraging, the major downside to testing in the deep fluctuation regime and over long propagation paths is the temperamental pointing accuracy associated with ranges nearing 2 km.

In final summary, in this thesis we have reviewed and augment simulation techniques for the study of optical propagation through atmospheric turbulence, and successfully demonstrated a revised simulation method. These methods have been used to both confirm and draw skepticism upon various predictions regarding long term spot size and scintillation index of waves propagating through atmospheric turbulence. Additionally, these methods were applied in order to inform atmospheric distortion testing in outdoor field experiments, and while not all the efforts have been completely successful, we have produced novel methods for estimating turbulence in the weak and strong fluctuation regimes. Possible improvements to the methods given in this dissertation will be discussed in the next section.

## 5.2: Future Work

During the course of performing research in support of this dissertation, we have gained a familiarity with the mathematics underlying theoretical investigations of optical wave propagation through atmospheric turbulence as well as methods for simulating these effects. The stark difference between predicted and simulated scintillations index of beams with differing radii of curvature dependent upon the polar angle across the transmit beam profile highlights a major problem with the theoretical predictions appearing in the literature [87]. Therefore, a promising area of future work is to revisit the fundamental equations of weak

fluctuation theory, and attempt to repair problems in current derivations. Additionally, we believe that these so-called *warped beams* may have applications, such as in communications with low earth orbit satellites where a vehicle is moving quickly along a well-known orbital path. In this field, *along-track* or *time-bias* prediction errors [101] are the major source of error, as opposed to predictions of the orbital path. For that scenario, purposefully diverging the transmit beam along one axis in order to produce an elliptical diffraction pattern would seem to be beneficial in lowering the required output power of the transmitter. *Warped beams* is one method of achieving this, as are anisotropic partially coherent beams. We intend to study this topic further using phase screen simulations.

Finally, given the issues observed when testing using a divergent beam in the weak fluctuation regime along with the newfound concerns regarding non-turbulent refractivity distortions, we believe many of the problems observed in the UMD UAS site testing could be resolved by coordinating the testing of the MAT system in tandem with a wavefront sensor. The MOG group has developed a configurable wavefront sensor capable of operating in both plenoptic sensor and light field (LCF) camera configurations. In outdoor experiments, we have demonstrated direct detection of the wave structure function (WSF) of a received beam as well as the transverse mutual coherence function (MCF), and therefore also the anisotropy ratio. A view of the experimental setup is shown in Figure 5-1,

and recovered WSF's along the major and minor axes of turbulence are shown in Figure 5-2 (both taken from [102]).

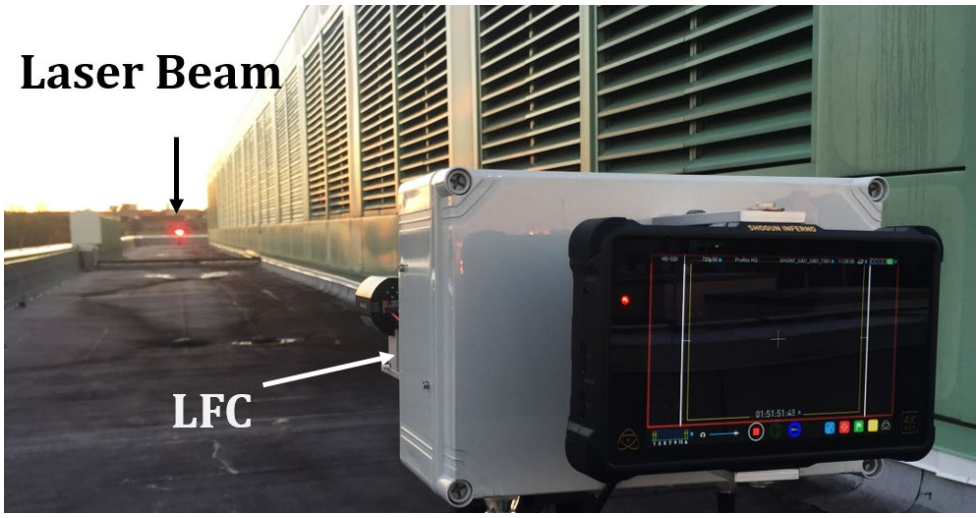


**Figure 5-1:** View of test laser transmitter and LCF in October 2019 experiment.

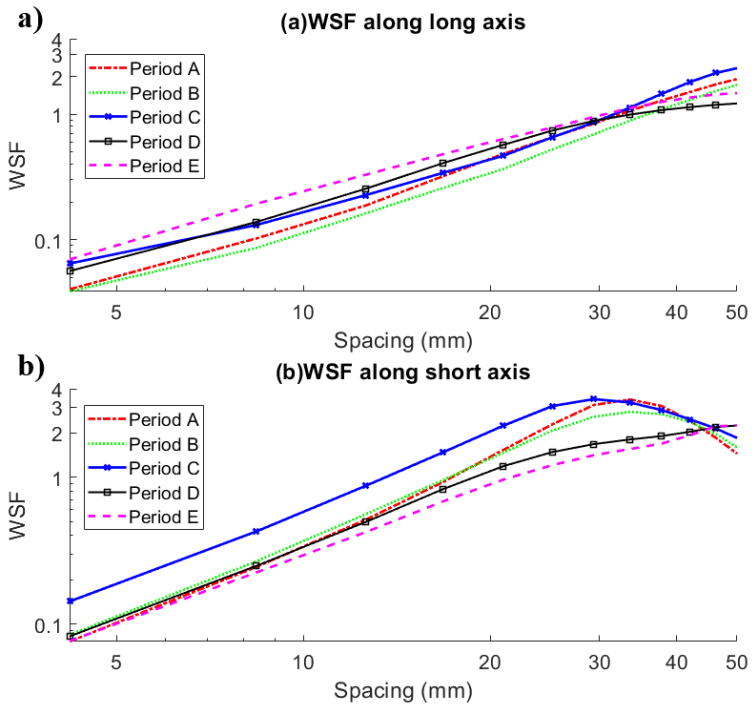


**Figure 5-2:** Recovered WSF's from the LFC October 2019 experiment: a) Along the minor axis of turbulence; b) Along the major axis of turbulence.

Fielding the light field camera in tandem with the MAT system would facilitate simultaneous estimates of optical turbulence, anisotropy ratios, and allow for any non-turbulent refractive effects (or problems with transmitter optics) to be estimated, as well. The LFC system has the added feature that the WSF estimates are true path averages, and are not weighted towards the transmitter. This would allow for the turbulence estimates derived from LFC observations to be equally valid if the propagation path was in the opposite direction of that of the MAT system. Therefore, receivers and transmitters could be mounted on the same structural housing and beams propagated in opposing directions in order to avoid light pollution, although the MAT receiver's retroreflecting corner cubes may need to be covered after alignment. We believe a very fruitful experimental campaign would result from this joint testing approach.

# Appendices

## Appendix A: Tables of RMS Error Statistics over Region of Interest

| | $\alpha$ | | | | | | | | | |
|---|---|---|---|---|---|---|---|---|---|---|
| $N_p$ | **3.1** | **3.2** | **3.3** | **3.4** | **3.5** | **3.6** | **11/3** | **3.7** | **3.8** | **3.9** |
| **0** | 0.69 | 1.21 | 1.48 | 1.05 | 6.35 | 4.17 | 8.23 | 12.59 | 9.31 | 55.33 |
| **1** | 0.63 | 0.56 | 1.26 | 1.65 | 2.75 | 13.87 | 5.25 | 6.88 | 16.10 | 42.68 |
| **2** | 0.60 | 0.55 | 0.87 | 1.19 | 1.93 | 1.92 | 3.33 | 3.62 | 99.54 | 33.01 |
| **3** | 0.62 | 0.56 | 0.88 | 0.95 | 0.76 | 1.98 | 5.00 | 3.77 | 12.57 | 33.91 |
| **4** | 0.65 | 0.55 | 0.93 | 0.96 | 0.86 | 1.89 | 3.06 | 2.46 | 12.78 | 24.91 |
| **5** | 0.63 | 0.59 | 0.82 | 0.73 | 0.63 | 0.49 | 1.84 | 1.27 | 4.87 | 32.69 |
| **6** | 0.61 | 0.55 | 0.81 | 0.76 | 0.60 | 0.71 | 1.84 | 0.91 | 5.82 | 28.33 |
| **7** | 0.62 | 0.54 | 0.86 | 0.87 | 0.61 | 0.53 | 1.04 | 0.97 | 6.26 | 20.29 |
| **8** | 0.62 | 0.53 | 0.84 | 0.84 | 0.50 | 1.01 | 0.76 | 0.94 | 4.83 | 21.54 |
| **9** | 0.62 | 0.54 | 0.86 | 0.84 | 0.51 | 0.60 | 0.55 | 0.72 | 4.15 | 33.83 |
| **10** | 0.62 | 0.54 | 0.86 | 0.86 | 0.46 | 0.59 | 0.91 | 0.56 | 2.43 | 16.74 |
| **11** | 0.62 | 0.54 | 0.87 | 0.86 | 0.49 | 0.64 | 0.77 | 0.31 | 1.91 | 13.53 |
| **12** | 0.62 | 0.54 | 0.88 | 0.87 | 0.50 | 0.67 | 0.83 | 0.30 | 2.02 | 7.79 |
| **13** | 0.62 | 0.54 | 0.87 | 0.87 | 0.49 | 0.71 | 0.62 | 0.28 | 1.00 | 13.15 |
| **14** | 0.62 | 0.54 | 0.87 | 0.87 | 0.49 | 0.70 | 0.64 | 0.28 | 1.51 | 6.99 |
| **15** | 0.62 | 0.54 | 0.87 | 0.87 | 0.48 | 0.72 | 0.67 | 0.43 | 1.22 | 9.55 |
| **16** | 0.62 | 0.54 | 0.87 | 0.87 | 0.48 | 0.74 | 0.67 | 0.26 | 0.83 | 6.09 |
| **17** | 0.62 | 0.54 | 0.87 | 0.86 | 0.48 | 0.73 | 0.68 | 0.27 | 1.08 | 6.92 |
| **18** | 0.62 | 0.54 | 0.87 | 0.86 | 0.48 | 0.73 | 0.68 | 0.29 | 0.69 | 5.54 |
| **19** | 0.62 | 0.54 | 0.87 | 0.86 | 0.48 | 0.72 | 0.67 | 0.29 | 0.70 | 5.73 |
| **20** | 0.62 | 0.54 | 0.87 | 0.86 | 0.47 | 0.72 | 0.68 | 0.29 | 0.57 | 5.35 |
| **21** | 0.62 | 0.54 | 0.87 | 0.86 | 0.48 | 0.73 | 0.68 | 0.29 | 0.47 | 4.12 |
| **22** | 0.62 | 0.54 | 0.87 | 0.86 | 0.48 | 0.73 | 0.68 | 0.30 | 0.54 | 3.57 |
| **23** | 0.62 | 0.54 | 0.87 | 0.86 | 0.48 | 0.72 | 0.69 | 0.30 | 0.48 | 3.53 |
| **24** | 0.62 | 0.54 | 0.87 | 0.86 | 0.48 | 0.72 | 0.68 | 0.30 | 0.50 | 3.60 |
| **25** | 0.62 | 0.54 | 0.87 | 0.86 | 0.48 | 0.73 | 0.69 | 0.30 | 0.41 | 2.61 |

**Table A-1:** RMS error over region of interest computed using the randomized hybrid subharmonic method along *x*- and *y*-directions of 5,000 phase screens for 512 × 512 grid using various spectral power laws ($\alpha$'s) and number of subharmonic constellations, $N_p$. $\mu_x = \mu_y = 1$ for all entries.

| | α | | | | | | | | | |
|---|---|---|---|---|---|---|---|---|---|---|
| $N_p$ | 3.1 | 3.2 | 3.3 | 3.4 | 3.5 | 3.6 | 11/3 | 3.7 | 3.8 | 3.9 |
| 0 | 32.82 | 37.16 | 42.53 | 47.70 | 54.16 | 60.81 | 65.75 | 68.32 | 77.16 | 87.54 |
| 1 | 9.51 | 11.93 | 15.29 | 18.96 | 25.17 | 32.44 | 38.71 | 42.20 | 55.71 | 74.51 |
| 2 | 2.06 | 1.95 | 2.65 | 3.70 | 7.67 | 13.52 | 19.28 | 22.64 | 38.06 | 62.28 |
| 3 | 3.65 | 4.31 | 4.03 | 4.67 | 2.96 | 1.60 | 5.80 | 8.56 | 24.02 | 51.25 |
| 4 | 4.79 | 6.02 | 6.68 | 8.71 | 8.71 | 6.57 | 3.76 | 1.92 | 12.37 | 41.27 |
| 5 | 5.25 | 6.72 | 8.03 | 11.05 | 12.00 | 11.77 | 10.08 | 8.99 | 3.24 | 32.59 |
| 6 | 5.41 | 7.06 | 8.62 | 12.16 | 13.91 | 15.05 | 14.70 | 14.15 | 3.99 | 24.86 |
| 7 | 5.46 | 7.16 | 8.92 | 12.77 | 15.03 | 17.21 | 17.98 | 17.87 | 9.87 | 17.84 |
| 8 | 5.49 | 7.20 | 9.08 | 13.04 | 15.68 | 18.53 | 20.13 | 20.63 | 14.45 | 11.17 |
| 9 | 5.50 | 7.21 | 9.13 | 13.17 | 16.06 | 19.36 | 21.58 | 22.59 | 18.47 | 5.73 |
| 10 | 5.51 | 7.22 | 9.16 | 13.25 | 16.31 | 19.94 | 22.61 | 23.97 | 21.49 | 0.73 |
| 11 | 5.51 | 7.23 | 9.15 | 13.31 | 16.41 | 20.37 | 23.36 | 24.95 | 23.94 | 3.63 |
| 12 | 5.51 | 7.23 | 9.15 | 13.33 | 16.46 | 20.59 | 23.92 | 25.75 | 25.93 | 7.59 |
| 13 | 5.51 | 7.23 | 9.16 | 13.35 | 16.49 | 20.78 | 24.28 | 26.34 | 27.40 | 11.27 |
| 14 | 5.51 | 7.23 | 9.16 | 13.36 | 16.52 | 20.88 | 24.51 | 26.68 | 28.74 | 14.50 |
| 15 | 5.51 | 7.23 | 9.16 | 13.36 | 16.53 | 20.93 | 24.68 | 26.93 | 29.72 | 17.21 |
| 16 | 5.51 | 7.23 | 9.16 | 13.36 | 16.54 | 20.98 | 24.79 | 27.13 | 30.68 | 19.89 |
| 17 | 5.51 | 7.23 | 9.16 | 13.36 | 16.55 | 20.99 | 24.86 | 27.30 | 31.41 | 22.38 |
| 18 | 5.51 | 7.23 | 9.16 | 13.36 | 16.55 | 21.02 | 24.92 | 27.39 | 31.85 | 24.44 |
| 19 | 5.51 | 7.23 | 9.16 | 13.36 | 16.55 | 21.03 | 24.95 | 27.44 | 32.24 | 26.32 |
| 20 | 5.51 | 7.23 | 9.16 | 13.36 | 16.55 | 21.04 | 24.97 | 27.51 | 32.58 | 28.02 |
| 21 | 5.51 | 7.23 | 9.16 | 13.36 | 16.55 | 21.04 | 24.98 | 27.55 | 32.79 | 29.49 |
| 22 | 5.51 | 7.23 | 9.16 | 13.36 | 16.55 | 21.05 | 25.00 | 27.59 | 33.01 | 30.74 |
| 23 | 5.51 | 7.23 | 9.16 | 13.36 | 16.55 | 21.05 | 25.02 | 27.63 | 33.13 | 32.04 |
| 24 | 5.51 | 7.23 | 9.16 | 13.36 | 16.55 | 21.05 | 25.03 | 27.63 | 33.28 | 33.06 |
| 25 | 5.51 | 7.23 | 9.16 | 13.36 | 16.55 | 21.05 | 25.03 | 27.64 | 33.39 | 34.02 |

**Table A-2:** RMS error over region of interest computed using the Frehlich subharmonic method along *x*- and *y*-directions of 5,000 phase screens for 512 × 512 grid using various spectral power laws ($\alpha$'s) and number of subharmonic constellations, $N_p$. $\mu_x = \mu_y = 1$ for all entries.

| | α | | | | | | | | | |
|---|---|---|---|---|---|---|---|---|---|---|
| $N_p$ | 3.1 | 3.2 | 3.3 | 3.4 | 3.5 | 3.6 | 11/3 | 3.7 | 3.8 | 3.9 |
| 0 | 32.82 | 37.16 | 42.53 | 47.70 | 54.16 | 60.81 | 65.75 | 68.32 | 77.16 | 87.54 |
| 1 | 16.19 | 19.37 | 23.61 | 28.83 | 35.59 | 42.97 | 49.04 | 52.62 | 64.37 | 79.83 |
| 2 | 9.77 | 11.74 | 14.50 | 18.55 | 24.20 | 30.92 | 36.92 | 40.49 | 53.87 | 72.95 |
| 3 | 7.47 | 8.60 | 10.24 | 13.25 | 17.68 | 23.15 | 28.62 | 31.99 | 45.48 | 66.55 |
| 4 | 6.61 | 7.31 | 8.29 | 10.46 | 13.97 | 17.91 | 22.93 | 25.93 | 38.41 | 60.82 |
| 5 | 6.28 | 6.81 | 7.41 | 9.08 | 11.82 | 14.67 | 18.75 | 21.58 | 33.05 | 55.71 |
| 6 | 6.16 | 6.52 | 6.99 | 8.38 | 10.59 | 12.63 | 15.98 | 18.28 | 28.74 | 50.99 |
| 7 | 6.13 | 6.44 | 6.80 | 7.98 | 9.90 | 11.30 | 14.04 | 15.93 | 25.23 | 47.02 |
| 8 | 6.11 | 6.40 | 6.71 | 7.77 | 9.47 | 10.47 | 12.63 | 14.32 | 22.27 | 43.42 |
| 9 | 6.11 | 6.39 | 6.66 | 7.66 | 9.22 | 9.93 | 11.62 | 13.21 | 20.04 | 40.22 |
| 10 | 6.11 | 6.38 | 6.63 | 7.64 | 9.10 | 9.61 | 11.01 | 12.29 | 18.17 | 37.21 |
| 11 | 6.11 | 6.38 | 6.63 | 7.61 | 9.03 | 9.36 | 10.52 | 11.72 | 16.71 | 34.59 |
| 12 | 6.11 | 6.39 | 6.63 | 7.59 | 8.98 | 9.19 | 10.21 | 11.25 | 15.60 | 32.20 |
| 13 | 6.10 | 6.39 | 6.63 | 7.58 | 8.96 | 9.10 | 10.03 | 10.96 | 14.68 | 30.15 |
| 14 | 6.10 | 6.39 | 6.63 | 7.58 | 8.94 | 9.08 | 9.88 | 10.69 | 13.95 | 28.25 |
| 15 | 6.11 | 6.39 | 6.63 | 7.58 | 8.94 | 9.05 | 9.78 | 10.53 | 13.32 | 26.44 |
| 16 | 6.10 | 6.39 | 6.63 | 7.58 | 8.94 | 9.03 | 9.69 | 10.41 | 12.87 | 24.84 |
| 17 | 6.10 | 6.39 | 6.63 | 7.58 | 8.93 | 9.01 | 9.64 | 10.32 | 12.49 | 23.41 |
| 18 | 6.10 | 6.39 | 6.63 | 7.58 | 8.93 | 9.00 | 9.60 | 10.24 | 12.16 | 22.19 |
| 19 | 6.10 | 6.39 | 6.63 | 7.58 | 8.93 | 9.00 | 9.59 | 10.22 | 11.97 | 21.17 |
| 20 | 6.10 | 6.39 | 6.63 | 7.58 | 8.93 | 8.99 | 9.55 | 10.19 | 11.71 | 20.14 |
| 21 | 6.10 | 6.39 | 6.63 | 7.58 | 8.93 | 8.98 | 9.54 | 10.16 | 11.55 | 19.27 |
| 22 | 6.10 | 6.39 | 6.63 | 7.58 | 8.93 | 8.99 | 9.55 | 10.15 | 11.43 | 18.50 |
| 23 | 6.10 | 6.39 | 6.63 | 7.58 | 8.93 | 8.98 | 9.54 | 10.14 | 11.33 | 17.76 |
| 24 | 6.10 | 6.39 | 6.63 | 7.58 | 8.93 | 8.98 | 9.54 | 10.13 | 11.26 | 17.07 |
| 25 | 6.10 | 6.39 | 6.63 | 7.58 | 8.93 | 8.98 | 9.54 | 10.12 | 11.17 | 16.50 |

**Table A-3:** RMS error over region of interest computed using the Lane subharmonic method along *x*- and *y*-directions of 50,000 phase screens for 512 × 512 grid using various spectral power laws ($\alpha$'s) and number of subharmonic constellations, $N_p$. $\mu_x = \mu_y = 1$ for all entries.

| | α | | | | | | | | | |
|---|---|---|---|---|---|---|---|---|---|---|
| $N_p$ | 3.1 | 3.2 | 3.3 | 3.4 | 3.5 | 3.6 | 11/3 | 3.7 | 3.8 | 3.9 |
| 0 | 0.88 | 1.58 | 0.98 | 3.04 | 10.59 | 10.92 | 8.59 | 11.76 | 4.30 | 51.95 |
| 1 | 0.94 | 0.81 | 0.97 | 2.44 | 1.51 | 8.00 | 6.93 | 8.01 | 25.56 | 29.46 |
| 2 | 0.65 | 0.41 | 1.03 | 0.93 | 4.97 | 4.06 | 5.44 | 2.35 | 2089.99 | 45.20 |
| 3 | 0.79 | 0.33 | 1.01 | 0.86 | 0.89 | 0.99 | 2.85 | 6.27 | 7.21 | 34.02 |
| 4 | 0.73 | 0.36 | 0.82 | 0.98 | 1.01 | 1.20 | 2.87 | 3.74 | 6.63 | 36.21 |
| 5 | 0.72 | 0.39 | 0.98 | 0.93 | 0.39 | 0.69 | 0.72 | 2.89 | 10.05 | 31.62 |
| 6 | 0.75 | 0.43 | 0.97 | 0.96 | 0.27 | 0.54 | 0.58 | 2.76 | 8.97 | 23.55 |
| 7 | 0.75 | 0.38 | 0.92 | 1.00 | 0.26 | 0.47 | 1.58 | 1.24 | 6.17 | 23.03 |
| 8 | 0.76 | 0.39 | 0.91 | 1.00 | 0.32 | 0.50 | 5.27 | 0.56 | 70.46 | 21.88 |
| 9 | 0.76 | 0.40 | 0.91 | 0.99 | 0.32 | 0.52 | 0.48 | 1.15 | 4.51 | 16.12 |
| 10 | 0.75 | 0.41 | 0.91 | 0.99 | 0.35 | 0.46 | 0.54 | 0.68 | 3.47 | 17.30 |
| 11 | - | - | - | - | - | - | 0.51 | 0.48 | 4.92 | 16.14 |
| 12 | - | - | - | - | - | - | 0.47 | 0.52 | 1.07 | 14.04 |
| 13 | - | - | - | - | - | - | 0.48 | 0.43 | 1.23 | 9.73 |
| 14 | - | - | - | - | - | - | 0.49 | 3.86 | 1.56 | 9.63 |
| 15 | - | - | - | - | - | - | 0.49 | 0.34 | 0.62 | 8.38 |
| 16 | - | - | - | - | - | - | 0.52 | 0.33 | 0.93 | 8.11 |
| 17 | - | - | - | - | - | - | 0.46 | 0.32 | 0.96 | 5.01 |
| 18 | - | - | - | - | - | - | 0.48 | 0.33 | 0.87 | 6.07 |
| 19 | - | - | - | - | - | - | 0.52 | 0.32 | 0.62 | 5.35 |
| 20 | - | - | - | - | - | - | 0.51 | 0.32 | 1.14 | 3.94 |

**Table A-4:** RMS error over region of interest computed using the randomized hybrid subharmonic method along *x*- and *y*-directions of 5,000 phase screens for 1024 × 1024 grid using various spectral power laws ($\alpha$'s) and number of subharmonic constellations, $N_p$. $\mu_x = 1$, $\mu_y = 2$ for all entries. Hyphen ( - ) entries indicate no RMS error was computed for this entry.

| | $\alpha$ | | | | | | | | | |
|---|---|---|---|---|---|---|---|---|---|---|
| $N_p$ | **3.1** | **3.2** | **3.3** | **3.4** | **3.5** | **3.6** | **11/3** | **3.7** | **3.8** | **3.9** |
| **0** | 29.13 | 33.66 | 38.75 | 44.12 | 50.49 | 57.65 | 62.98 | 65.60 | 75.01 | 86.31 |
| **1** | 8.45 | 10.35 | 13.09 | 17.71 | 23.29 | 30.72 | 37.27 | 40.86 | 54.78 | 73.88 |
| **2** | 8.88 | 9.69 | 9.57 | 9.47 | 10.06 | 13.16 | 19.03 | 22.38 | 38.00 | 62.32 |
| **3** | 9.44 | 10.50 | 10.23 | 10.57 | 10.64 | 9.95 | 9.88 | 10.38 | 24.47 | 51.83 |
| **4** | 9.67 | 10.84 | 10.62 | 11.07 | 11.44 | 10.78 | 10.50 | 10.76 | 13.76 | 42.46 |
| **5** | 9.76 | 11.00 | 10.98 | 11.63 | 12.31 | 11.50 | 11.14 | 11.48 | 10.19 | 34.27 |
| **6** | 9.78 | 11.01 | 11.19 | 12.25 | 13.70 | 13.95 | 13.00 | 12.21 | 10.84 | 26.83 |
| **7** | 9.78 | 11.04 | 11.30 | 12.73 | 14.71 | 15.88 | 15.74 | 15.30 | 11.17 | 19.97 |
| **8** | 9.79 | 11.05 | 11.33 | 13.03 | 15.26 | 17.23 | 17.80 | 17.77 | 12.01 | 13.96 |
| **9** | 9.79 | 11.06 | 11.34 | 13.16 | 15.55 | 18.07 | 19.30 | 19.56 | 15.31 | 9.50 |
| **10** | 9.78 | 11.06 | 11.36 | 13.22 | 15.76 | 18.62 | 20.19 | 20.89 | 18.25 | 9.67 |
| **11** | - | - | - | - | - | - | 20.85 | 21.77 | 20.57 | 10.02 |
| **12** | - | - | - | - | - | - | 21.34 | 22.53 | 22.53 | 10.38 |
| **13** | - | - | - | - | - | - | 21.63 | 23.00 | 23.91 | 10.87 |
| **14** | - | - | - | - | - | - | 21.85 | 23.38 | 25.08 | 11.34 |
| **15** | - | - | - | - | - | - | 22.03 | 23.62 | 26.06 | 14.05 |
| **16** | - | - | - | - | - | - | 22.14 | 23.83 | 26.80 | 16.80 |
| **17** | - | - | - | - | - | - | 22.23 | 23.95 | 27.48 | 19.10 |
| **18** | - | - | - | - | - | - | 22.27 | 24.05 | 27.96 | 21.08 |
| **19** | - | - | - | - | - | - | 22.28 | 24.13 | 28.36 | 22.74 |
| **20** | - | - | - | - | - | - | 22.33 | 24.19 | 28.72 | 24.16 |

**Table A-5:** RMS error over region of interest computed using the Frehlich subharmonic method along *x*- and *y*-directions of 5,000 phase screens for 1024 × 1024 grid using various spectral power laws ($\alpha$'s) and number of subharmonic constellations, $N_p$. $\mu_x = 1$, $\mu_y = 2$ for all entries. Hyphen ( - ) entries indicate no RMS error was computed for this entry.

| | $\alpha$ | | | | | | | | | |
|---|---|---|---|---|---|---|---|---|---|---|
| $N_p$ | **3.1** | **3.2** | **3.3** | **3.4** | **3.5** | **3.6** | **11/3** | **3.7** | **3.8** | **3.9** |
| **0** | 4.06 | 2.17 | 1.11 | 14.06 | 5.60 | 4.69 | 9.75 | 17.79 | 46.46 | 48.45 |
| **1** | 1.47 | 3.00 | 2.81 | 2.64 | 4.92 | 3.46 | 24.36 | 17.49 | 24.18 | 56.47 |
| **2** | 1.68 | 2.94 | 1.40 | 2.63 | 4.49 | 4.48 | 10.50 | 10.48 | 26.66 | 48.96 |
| **3** | 1.61 | 1.34 | 1.13 | 2.44 | 3.21 | 7.16 | 1.97 | 3.47 | 15.62 | 25.81 |
| **4** | 1.39 | 1.61 | 1.08 | 1.47 | 1.38 | 1.33 | 2.01 | 6.58 | 15.45 | 36.92 |
| **5** | 1.61 | 1.82 | 1.22 | 1.87 | 1.30 | 5.20 | 2.49 | 3.95 | 27.76 | 16.82 |
| **6** | 1.73 | 1.51 | 1.19 | 1.92 | 1.63 | 0.96 | 1.98 | 1.48 | 6.37 | 31.25 |
| **7** | 1.75 | 1.64 | 1.24 | 2.03 | 1.65 | 0.95 | 1.52 | 2.79 | 4.86 | 26.08 |
| **8** | 1.72 | 1.61 | 1.23 | 1.77 | 1.51 | 1.21 | 1.48 | 1.20 | 5.57 | 23.56 |
| **9** | 1.73 | 1.66 | 1.25 | 1.88 | 1.61 | 1.45 | 1.77 | 1.48 | 3.81 | 18.55 |
| **10** | 1.73 | 1.65 | 1.24 | 1.98 | 1.58 | 1.26 | 1.65 | 2.64 | 3.00 | 20.05 |
| **11** | - | - | - | - | - | - | 1.58 | 1.47 | 2.12 | 11.43 |
| **12** | - | - | - | - | - | - | 1.47 | 1.51 | 3.55 | 14.99 |
| **13** | - | - | - | - | - | - | 1.83 | 1.42 | 1.65 | 13.16 |
| **14** | - | - | - | - | - | - | 1.78 | 1.85 | 1.45 | 11.92 |
| **15** | - | - | - | - | - | - | 1.66 | 1.67 | 2.27 | 6.82 |
| **16** | - | - | - | - | - | - | 1.65 | 1.66 | 1.40 | 10.23 |
| **17** | - | - | - | - | - | - | 1.58 | 1.62 | 1.31 | 4.01 |
| **18** | - | - | - | - | - | - | 1.68 | 1.65 | 1.63 | 10.09 |
| **19** | - | - | - | - | - | - | 1.72 | 1.67 | 1.68 | 7.16 |
| **20** | - | - | - | - | - | - | 1.71 | 1.77 | 1.68 | 9.09 |

**Table A-6:** RMS error over region of interest computed using the randomized hybrid subharmonic method along *x*- and *y*-directions of 5,000 phase screens for 2048 × 2048 grid using various spectral power laws ($\alpha$'s) and number of subharmonic constellations, $N_p$. $\mu_x = 1$, $\mu_y = 2$ for all entries. Hyphen ( - ) entries indicate no RMS error was computed for this entry.

| | $\alpha$ | | | | | | | | | |
|---|---|---|---|---|---|---|---|---|---|---|
| $N_p$ | **3.1** | **3.2** | **3.3** | **3.4** | **3.5** | **3.6** | **11/3** | **3.7** | **3.8** | **3.9** |
| **0** | 29.42 | 33.40 | 39.23 | 43.60 | 50.96 | 57.19 | 62.52 | 65.32 | 74.43 | 86.02 |
| **1** | 10.54 | 11.74 | 13.03 | 16.50 | 25.08 | 30.29 | 36.80 | 41.16 | 54.30 | 73.44 |
| **2** | 11.62 | 11.40 | 11.45 | 8.24 | 9.49 | 13.85 | 17.76 | 24.07 | 37.29 | 61.71 |
| **3** | 11.93 | 11.98 | 11.63 | 9.67 | 10.13 | 13.16 | 11.82 | 11.33 | 23.73 | 51.42 |
| **4** | 12.26 | 12.42 | 12.59 | 11.48 | 10.05 | 13.46 | 12.59 | 10.74 | 13.90 | 42.08 |
| **5** | 12.44 | 12.49 | 12.31 | 13.27 | 10.55 | 14.18 | 12.92 | 11.51 | 12.77 | 33.85 |
| **6** | 12.51 | 12.57 | 12.33 | 14.09 | 12.11 | 14.90 | 14.99 | 12.03 | 12.95 | 27.03 |
| **7** | 12.58 | 12.63 | 12.28 | 14.49 | 12.95 | 16.12 | 17.84 | 13.45 | 13.10 | 20.53 |
| **8** | 12.55 | 12.63 | 12.19 | 14.73 | 13.56 | 17.53 | 20.25 | 15.89 | 13.48 | 15.14 |
| **9** | 12.55 | 12.68 | 12.24 | 14.83 | 13.97 | 18.48 | 22.20 | 17.38 | 14.85 | 10.59 |
| **10** | 12.56 | 12.69 | 12.26 | 14.85 | 14.21 | 19.05 | 23.39 | 18.49 | 17.70 | 9.08 |
| **11** | - | - | - | - | - | - | 24.42 | 19.31 | 20.20 | 10.22 |
| **12** | - | - | - | - | - | - | 24.86 | 20.02 | 22.14 | 10.75 |
| **13** | - | - | - | - | - | - | 25.18 | 20.71 | 23.92 | 10.54 |
| **14** | - | - | - | - | - | - | 25.39 | 21.15 | 25.32 | 10.19 |
| **15** | - | - | - | - | - | - | 25.48 | 21.20 | 26.53 | 11.73 |
| **16** | - | - | - | - | - | - | 25.48 | 21.51 | 27.40 | 14.22 |
| **17** | - | - | - | - | - | - | 25.51 | 21.62 | 27.98 | 16.22 |
| **18** | - | - | - | - | - | - | 25.55 | 21.69 | 28.33 | 17.93 |
| **19** | - | - | - | - | - | - | 25.60 | 21.83 | 28.81 | 19.49 |
| **20** | - | - | - | - | - | - | 25.59 | 21.92 | 29.05 | 21.16 |

**Table A-7:** RMS error over region of interest computed using the Frehlich subharmonic method along *x*- and *y*-directions of 5,000 phase screens for 2048 × 2048 grid using various spectral power laws ($\alpha$'s) and number of subharmonic constellations, $N_p$. $\mu_x$ = 1, $\mu_y$ = 2 for all entries. Hyphen ( - ) entries indicate no RMS error was computed for this entry.

| | $L_0$ | | | | | | | | | | |
|---|---|---|---|---|---|---|---|---|---|---|---|
| $N_p$ | $10^0$ | $10^{0.5}$ | $10^1$ | $10^{1.5}$ | $10^2$ | $10^{1.5}$ | $10^3$ | $10^{3.5}$ | $10^4$ | $10^{4.5}$ | $10^5$ |
| **0** | 1.16 | 1.40 | 1.53 | 1.71 | 2.88 | 31.31 | 12.94 | 12.91 | 6.16 | 17.46 | 12.26 |
| **1** | 1.39 | 1.33 | 2.18 | 2.10 | 1.49 | 2.81 | 20.22 | 18.76 | 9.81 | 6.23 | 10.45 |
| **2** | 1.42 | 1.25 | 2.20 | 1.82 | 1.36 | 1.80 | 2.25 | 5.34 | 2.68 | 3.76 | 3.15 |
| **3** | 1.42 | 1.26 | 2.22 | 1.37 | 1.97 | 2.73 | 2.96 | 7.14 | 3.28 | 2.95 | 4.24 |
| **4** | 1.42 | 1.26 | 2.23 | 1.38 | 1.44 | 2.08 | 1.13 | 2.04 | 2.07 | 1.84 | 1.59 |
| **5** | 1.42 | 1.26 | 2.23 | 1.36 | 1.37 | 1.86 | 0.85 | 2.42 | 1.39 | 2.47 | 2.67 |
| **6** | 1.42 | 1.26 | 2.23 | 1.36 | 1.36 | 1.80 | 0.96 | 2.31 | 1.73 | 1.90 | 3.33 |
| **7** | 1.42 | 1.26 | 2.23 | 1.36 | 1.35 | 1.80 | 0.95 | 2.46 | 1.80 | 2.09 | 2.67 |
| **8** | 1.42 | 1.26 | 2.23 | 1.36 | 1.36 | 1.80 | 0.95 | 2.50 | 1.93 | 2.21 | 2.79 |
| **9** | 1.42 | 1.26 | 2.23 | 1.36 | 1.36 | 1.80 | 0.95 | 2.50 | 1.91 | 2.19 | 2.98 |
| **10** | 1.42 | 1.26 | 2.23 | 1.36 | 1.36 | 1.80 | 0.95 | 2.50 | 1.91 | 2.27 | 2.95 |
| **11** | 1.42 | 1.26 | 2.23 | 1.36 | 1.36 | 1.80 | 0.95 | 2.50 | 1.91 | 2.27 | 2.96 |
| **12** | 1.42 | 1.26 | 2.23 | 1.36 | 1.36 | 1.80 | 0.95 | 2.50 | 1.91 | 2.27 | 2.96 |
| **13** | 1.42 | 1.26 | 2.23 | 1.36 | 1.36 | 1.80 | 0.95 | 2.50 | 1.91 | 2.27 | 2.96 |
| **14** | 1.42 | 1.26 | 2.23 | 1.36 | 1.36 | 1.80 | 0.95 | 2.50 | 1.91 | 2.27 | 2.96 |
| **15** | 1.42 | 1.26 | 2.23 | 1.36 | 1.36 | 1.80 | 0.95 | 2.50 | 1.91 | 2.27 | 2.96 |
| **16** | 1.42 | 1.26 | 2.23 | 1.36 | 1.36 | 1.80 | 0.95 | 2.50 | 1.91 | 2.27 | 2.96 |
| **17** | 1.42 | 1.26 | 2.23 | 1.36 | 1.36 | 1.80 | 0.95 | 2.50 | 1.91 | 2.27 | 2.96 |
| **18** | 1.42 | 1.26 | 2.23 | 1.36 | 1.36 | 1.80 | 0.95 | 2.50 | 1.91 | 2.27 | 2.96 |
| **19** | 1.42 | 1.26 | 2.23 | 1.36 | 1.36 | 1.80 | 0.95 | 2.50 | 1.91 | 2.27 | 2.96 |
| **20** | 1.42 | 1.26 | 2.23 | 1.36 | 1.36 | 1.80 | 0.95 | 2.50 | 1.91 | 2.27 | 2.96 |

**Table A-8:** RMS error over region of interest computed along *x*- and *y*-directions for 5000 phase screens using the hybrid method and the modified spectrum, with $l_0 = M\Delta x/100$ and $M = 512$ (i.e. grid size 512 × 512).

| | $L_0$ | | | | | | | | | | |
|---|---|---|---|---|---|---|---|---|---|---|---|
| $N_p$ | $10^0$ | $10^{0.5}$ | $10^1$ | $10^{1.5}$ | $10^2$ | $10^{1.5}$ | $10^3$ | $10^{3.5}$ | $10^4$ | $10^{4.5}$ | $10^5$ |
| **0** | 2.70 | 24.92 | 44.52 | 53.06 | 57.41 | 59.17 | 61.49 | 62.42 | 64.16 | 62.92 | 63.61 |
| **1** | 1.90 | 4.96 | 6.39 | 14.30 | 24.19 | 27.55 | 30.90 | 33.88 | 36.28 | 35.67 | 35.91 |
| **2** | 1.94 | 4.23 | 3.43 | 7.73 | 1.55 | 5.19 | 8.60 | 12.25 | 16.95 | 16.32 | 16.04 |
| **3** | 1.95 | 4.23 | 3.93 | 13.86 | 12.56 | 8.81 | 5.24 | 2.67 | 3.20 | 3.21 | 2.75 |
| **4** | 1.95 | 4.23 | 3.92 | 14.08 | 16.27 | 17.84 | 14.83 | 11.39 | 7.51 | 7.39 | 7.27 |
| **5** | 1.95 | 4.23 | 3.92 | 14.07 | 16.47 | 20.05 | 21.15 | 17.46 | 14.37 | 14.77 | 14.49 |
| **6** | 1.95 | 4.23 | 3.92 | 14.07 | 16.48 | 20.26 | 23.01 | 21.55 | 19.41 | 19.60 | 18.90 |
| **7** | 1.95 | 4.23 | 3.92 | 14.07 | 16.48 | 20.26 | 23.25 | 22.58 | 21.81 | 22.44 | 21.53 |
| **8** | 1.95 | 4.23 | 3.92 | 14.07 | 16.48 | 20.26 | 23.25 | 22.58 | 22.61 | 24.20 | 23.46 |
| **9** | 1.95 | 4.23 | 3.92 | 14.07 | 16.48 | 20.26 | 23.25 | 22.59 | 22.67 | 24.80 | 24.77 |
| **10** | 1.95 | 4.23 | 3.92 | 14.07 | 16.48 | 20.26 | 23.25 | 22.59 | 22.65 | 24.85 | 25.21 |
| **11** | 1.95 | 4.23 | 3.92 | 14.07 | 16.48 | 20.26 | 23.25 | 22.59 | 22.65 | 24.83 | 25.25 |
| **12** | 1.95 | 4.23 | 3.92 | 14.07 | 16.48 | 20.26 | 23.25 | 22.59 | 22.65 | 24.83 | 25.26 |
| **13** | 1.95 | 4.23 | 3.92 | 14.07 | 16.48 | 20.26 | 23.25 | 22.59 | 22.65 | 24.83 | 25.26 |
| **14** | 1.95 | 4.23 | 3.92 | 14.07 | 16.48 | 20.26 | 23.25 | 22.59 | 22.65 | 24.83 | 25.26 |
| **15** | 1.95 | 4.23 | 3.92 | 14.07 | 16.48 | 20.26 | 23.25 | 22.59 | 22.65 | 24.83 | 25.26 |
| **16** | 1.95 | 4.23 | 3.92 | 14.07 | 16.48 | 20.26 | 23.25 | 22.59 | 22.65 | 24.83 | 25.26 |
| **17** | 1.95 | 4.23 | 3.92 | 14.07 | 16.48 | 20.26 | 23.25 | 22.59 | 22.65 | 24.83 | 25.26 |
| **18** | 1.95 | 4.23 | 3.92 | 14.07 | 16.48 | 20.26 | 23.25 | 22.59 | 22.65 | 24.83 | 25.26 |
| **19** | 1.95 | 4.23 | 3.92 | 14.07 | 16.48 | 20.26 | 23.25 | 22.59 | 22.65 | 24.83 | 25.26 |
| **20** | 1.95 | 4.23 | 3.92 | 14.07 | 16.48 | 20.26 | 23.25 | 22.59 | 22.65 | 24.83 | 25.26 |

**Table A-9:** RMS error over region of interest computed along *x*- and *y*-directions for 5000 phase screens using the Frehlich subharmonic method and the modified spectrum, with $l_0 = M\Delta x/100$ and $M = 512$ (i.e. grid size 512 × 512).

| | $L_0$ | | | | | | | | | | |
|---|---|---|---|---|---|---|---|---|---|---|---|
| $N_p$ | $10^0$ | $10^{0.5}$ | $10^1$ | $10^{1.5}$ | $10^2$ | $10^{1.5}$ | $10^3$ | $10^{3.5}$ | $10^4$ | $10^{4.5}$ | $10^5$ |
| **0** | 2.70 | 24.92 | 44.52 | 53.06 | 57.41 | 59.17 | 61.49 | 62.42 | 64.16 | 62.92 | 63.61 |
| **1** | 2.28 | 6.72 | 17.35 | 29.58 | 35.49 | 39.85 | 44.10 | 44.58 | 46.91 | 45.35 | 46.65 |
| **2** | 2.29 | 5.64 | 9.02 | 13.55 | 20.67 | 26.74 | 30.43 | 32.64 | 34.52 | 33.07 | 35.55 |
| **3** | 2.30 | 5.61 | 8.54 | 8.63 | 11.13 | 17.82 | 21.65 | 23.84 | 25.84 | 24.91 | 27.72 |
| **4** | 2.30 | 5.61 | 8.55 | 8.28 | 7.91 | 11.75 | 15.54 | 17.62 | 20.27 | 18.79 | 22.37 |
| **5** | 2.30 | 5.61 | 8.55 | 8.29 | 7.64 | 9.58 | 11.85 | 13.54 | 15.97 | 14.57 | 18.50 |
| **6** | 2.30 | 5.61 | 8.55 | 8.29 | 7.64 | 9.43 | 9.89 | 11.02 | 12.61 | 12.02 | 15.78 |
| **7** | 2.30 | 5.61 | 8.55 | 8.29 | 7.64 | 9.44 | 9.82 | 9.86 | 10.60 | 10.23 | 13.81 |
| **8** | 2.30 | 5.61 | 8.55 | 8.29 | 7.64 | 9.44 | 9.82 | 9.86 | 9.85 | 8.95 | 12.79 |
| **9** | 2.30 | 5.61 | 8.55 | 8.29 | 7.64 | 9.44 | 9.82 | 9.86 | 9.78 | 8.17 | 12.08 |
| **10** | 2.30 | 5.61 | 8.55 | 8.29 | 7.64 | 9.44 | 9.82 | 9.85 | 9.77 | 8.19 | 11.57 |
| **11** | 2.30 | 5.61 | 8.55 | 8.29 | 7.64 | 9.44 | 9.82 | 9.85 | 9.77 | 8.19 | 11.57 |
| **12** | 2.30 | 5.61 | 8.55 | 8.29 | 7.64 | 9.44 | 9.82 | 9.85 | 9.77 | 8.19 | 11.57 |
| **13** | 2.30 | 5.61 | 8.55 | 8.29 | 7.64 | 9.44 | 9.82 | 9.85 | 9.77 | 8.19 | 11.57 |
| **14** | 2.30 | 5.61 | 8.55 | 8.29 | 7.64 | 9.44 | 9.82 | 9.85 | 9.77 | 8.19 | 11.57 |
| **15** | 2.30 | 5.61 | 8.55 | 8.29 | 7.64 | 9.44 | 9.82 | 9.85 | 9.77 | 8.19 | 11.57 |
| **16** | 2.30 | 5.61 | 8.55 | 8.29 | 7.64 | 9.44 | 9.82 | 9.85 | 9.77 | 8.19 | 11.57 |
| **17** | 2.30 | 5.61 | 8.55 | 8.29 | 7.64 | 9.44 | 9.82 | 9.85 | 9.77 | 8.19 | 11.57 |
| **18** | 2.30 | 5.61 | 8.55 | 8.29 | 7.64 | 9.44 | 9.82 | 9.85 | 9.77 | 8.19 | 11.57 |
| **19** | 2.30 | 5.61 | 8.55 | 8.29 | 7.64 | 9.44 | 9.82 | 9.85 | 9.77 | 8.19 | 11.57 |
| **20** | 2.30 | 5.61 | 8.55 | 8.29 | 7.64 | 9.44 | 9.82 | 9.85 | 9.77 | 8.19 | 11.57 |

**Table A-10:** RMS error over region of interest computed along *x*- and *y*-directions for 5000 phase screens using the Lane subharmonic method and the modified spectrum, with $l_0 = M\Delta x/100$ and $M = 512$ (i.e. grid size 512 × 512).

| | $L_0$ | | | | | | | | | | |
|---|---|---|---|---|---|---|---|---|---|---|---|
| $N_p$ | $10^0$ | $10^{0.5}$ | $10^1$ | $10^{1.5}$ | $10^2$ | $10^{1.5}$ | $10^3$ | $10^{3.5}$ | $10^4$ | $10^{4.5}$ | $10^5$ |
| **0** | 1.21 | 1.44 | 1.89 | 3.36 | 9.18 | 11.03 | 6.15 | 6.22 | 14.61 | 19.50 | 29.15 |
| **1** | 1.03 | 0.92 | 3.14 | 2.78 | 4.85 | 1.25 | 7.06 | 7.37 | 7.15 | 10.51 | 16.78 |
| **2** | 1.04 | 0.91 | 1.71 | 2.59 | 1.36 | 2.77 | 3.96 | 3.60 | 6.09 | 3.86 | 5.74 |
| **3** | 1.04 | 0.90 | 2.08 | 2.61 | 2.70 | 1.44 | 1.31 | 2.68 | 2.60 | 4.20 | 5.91 |
| **4** | 1.04 | 0.90 | 2.07 | 2.73 | 2.43 | 1.31 | 1.25 | 2.06 | 3.03 | 6.84 | 2.23 |
| **5** | 1.04 | 0.90 | 2.07 | 2.73 | 2.57 | 1.36 | 1.83 | 1.17 | 1.64 | 1.27 | 4.02 |
| **6** | 1.04 | 0.90 | 2.07 | 2.74 | 2.57 | 1.46 | 1.50 | 1.37 | 1.59 | 0.92 | 1.13 |
| **7** | 1.04 | 0.90 | 2.07 | 2.74 | 2.57 | 1.47 | 1.55 | 1.24 | 1.33 | 1.50 | 1.26 |
| **8** | 1.04 | 0.90 | 2.07 | 2.74 | 2.57 | 1.47 | 1.55 | 1.28 | 1.37 | 1.33 | 1.20 |
| **9** | 1.04 | 0.90 | 2.07 | 2.74 | 2.57 | 1.47 | 1.55 | 1.28 | 1.37 | 1.39 | 1.38 |
| **10** | 1.04 | 0.90 | 2.07 | 2.74 | 2.57 | 1.47 | 1.55 | 1.28 | 1.36 | 1.34 | 1.12 |

**Table A-11:** RMS error over region of interest computed along *x*- and *y*-directions for 5000 phase screens using the hybrid method and the modified spectrum, with $l_0 = M\Delta x/100$ and $M = 1024$ (i.e. grid size 1024 × 1024).

| | $L_0$ | | | | | | | | | | |
|---|---|---|---|---|---|---|---|---|---|---|---|
| $N_p$ | $10^0$ | $10^{0.5}$ | $10^1$ | $10^{1.5}$ | $10^2$ | $10^{1.5}$ | $10^3$ | $10^{3.5}$ | $10^4$ | $10^{4.5}$ | $10^5$ |
| **0** | 3.20 | 24.54 | 43.89 | 51.83 | 57.69 | 60.35 | 61.92 | 62.51 | 63.15 | 63.31 | 63.88 |
| **1** | 1.27 | 4.86 | 5.18 | 13.93 | 24.33 | 29.36 | 34.35 | 35.32 | 35.42 | 35.93 | 36.80 |
| **2** | 1.25 | 4.08 | 4.15 | 9.66 | 1.36 | 7.56 | 13.18 | 16.00 | 15.03 | 15.07 | 16.39 |
| **3** | 1.25 | 4.07 | 4.60 | 15.45 | 13.30 | 7.28 | 1.55 | 3.41 | 1.09 | 3.38 | 3.22 |
| **4** | 1.25 | 4.06 | 4.62 | 16.02 | 17.01 | 16.93 | 10.75 | 7.04 | 9.75 | 7.33 | 6.01 |
| **5** | 1.25 | 4.06 | 4.62 | 16.03 | 17.14 | 18.96 | 17.14 | 14.09 | 16.32 | 14.13 | 11.18 |
| **6** | 1.25 | 4.06 | 4.62 | 16.03 | 17.16 | 18.98 | 18.95 | 18.05 | 20.62 | 19.02 | 15.00 |
| **7** | 1.25 | 4.06 | 4.62 | 16.03 | 17.16 | 18.97 | 18.97 | 19.59 | 23.89 | 22.71 | 17.83 |
| **8** | 1.25 | 4.06 | 4.62 | 16.03 | 17.16 | 18.97 | 18.99 | 19.78 | 24.89 | 24.70 | 19.74 |
| **9** | 1.25 | 4.06 | 4.62 | 16.03 | 17.16 | 18.97 | 18.99 | 19.77 | 25.07 | 25.21 | 21.44 |
| **10** | 1.25 | 4.06 | 4.62 | 16.03 | 17.16 | 18.97 | 18.99 | 19.77 | 25.08 | 25.26 | 21.81 |

**Table A-12:** RMS error over region of interest computed along $x$- and $y$-directions for 5000 phase screens using the Frehlich subharmonic method and the modified spectrum, with $l_0 = M\Delta x/100$ and $M = 1024$ (i.e. grid size $1024 \times 1024$).

| | $L_0$ | | | | | | | | | | |
|---|---|---|---|---|---|---|---|---|---|---|---|
| $N_p$ | $10^0$ | $10^{0.5}$ | $10^1$ | $10^{1.5}$ | $10^2$ | $10^{1.5}$ | $10^3$ | $10^{3.5}$ | $10^4$ | $10^{4.5}$ | $10^5$ |
| **0** | 2.00 | 1.45 | 2.85 | 1.73 | 2.71 | 4.88 | 14.90 | 40.83 | 13.39 | 7.63 | 20.21 |
| **1** | 1.67 | 2.79 | 2.42 | 2.81 | 2.48 | 2.55 | 7.48 | 10.41 | 13.92 | 7.38 | 13.85 |
| **2** | 1.70 | 3.01 | 2.67 | 3.41 | 1.08 | 1.05 | 5.29 | 1.59 | 1.83 | 6.98 | 6.35 |
| **3** | 1.70 | 2.99 | 2.66 | 2.89 | 1.37 | 1.34 | 1.45 | 1.51 | 1.80 | 1.85 | 2.96 |
| **4** | 1.70 | 2.99 | 2.64 | 2.71 | 1.25 | 1.11 | 1.64 | 1.50 | 0.81 | 1.63 | 1.44 |
| **5** | 1.70 | 2.99 | 2.65 | 2.66 | 1.25 | 1.26 | 1.51 | 1.08 | 0.88 | 1.89 | 1.41 |
| **6** | 1.70 | 2.99 | 2.65 | 2.66 | 1.26 | 1.28 | 1.55 | 1.32 | 0.94 | 1.89 | 2.01 |
| **7** | 1.70 | 2.99 | 2.65 | 2.66 | 1.26 | 1.27 | 1.51 | 1.36 | 1.02 | 1.47 | 2.36 |
| **8** | 1.70 | 2.99 | 2.65 | 2.66 | 1.26 | 1.28 | 1.52 | 1.34 | 1.25 | 1.54 | 2.52 |
| **9** | 1.70 | 2.99 | 2.65 | 2.66 | 1.26 | 1.28 | 1.52 | 1.34 | 1.15 | 1.58 | 2.43 |
| **10** | 1.70 | 2.99 | 2.65 | 2.66 | 1.26 | 1.28 | 1.52 | 1.34 | 1.14 | 1.56 | 2.63 |

**Table A-13:** RMS error over region of interest computed along *x*- and *y*-directions for 5000 phase screens using the hybrid subharmonic method and the modified spectrum, with $l_0 = M\Delta x/100$ and $M = 2048$ (i.e. grid size 2048 × 2048).

| | $L_0$ | | | | | | | | | | |
|---|---|---|---|---|---|---|---|---|---|---|---|
| $N_p$ | $10^0$ | $10^{0.5}$ | $10^1$ | $10^{1.5}$ | $10^2$ | $10^{1.5}$ | $10^3$ | $10^{3.5}$ | $10^4$ | $10^{4.5}$ | $10^5$ |
| **0** | 2.40 | 25.64 | 44.36 | 52.02 | 57.11 | 60.46 | 61.43 | 62.33 | 62.87 | 63.10 | 63.74 |
| **1** | 2.12 | 5.86 | 5.35 | 14.39 | 24.44 | 29.58 | 31.35 | 34.58 | 35.67 | 35.66 | 37.39 |
| **2** | 2.16 | 4.84 | 4.50 | 7.57 | 3.31 | 7.92 | 9.68 | 14.75 | 15.45 | 15.90 | 17.69 |
| **3** | 2.16 | 4.83 | 4.86 | 13.43 | 11.28 | 8.46 | 6.07 | 2.56 | 2.25 | 2.73 | 5.01 |
| **4** | 2.16 | 4.83 | 4.85 | 13.75 | 15.36 | 17.15 | 15.87 | 8.84 | 8.16 | 7.61 | 5.28 |
| **5** | 2.16 | 4.83 | 4.85 | 13.74 | 15.83 | 19.90 | 22.01 | 16.95 | 15.14 | 13.90 | 11.99 |
| **6** | 2.16 | 4.83 | 4.85 | 13.74 | 15.85 | 19.97 | 23.72 | 21.79 | 20.02 | 18.91 | 16.28 |
| **7** | 2.16 | 4.83 | 4.85 | 13.74 | 15.85 | 19.98 | 23.77 | 23.17 | 23.04 | 22.48 | 19.40 |
| **8** | 2.16 | 4.83 | 4.85 | 13.74 | 15.85 | 19.98 | 23.79 | 23.33 | 24.13 | 23.89 | 21.75 |
| **9** | 2.16 | 4.83 | 4.85 | 13.74 | 15.85 | 19.98 | 23.79 | 23.34 | 24.12 | 24.56 | 23.40 |
| **10** | 2.16 | 4.83 | 4.85 | 13.74 | 15.85 | 19.98 | 23.79 | 23.34 | 24.12 | 24.64 | 24.06 |

**Table A-14:** RMS error over region of interest computed along *x*- and *y*-directions for 5000 phase screens using the Frehlich subharmonic method and the modified spectrum, with $l_0 = M\Delta x/100$ and $M = 2048$ (i.e. grid size 2048 × 2048).

## Appendix B: Charts of RMS Error Statistics over Entire Domain

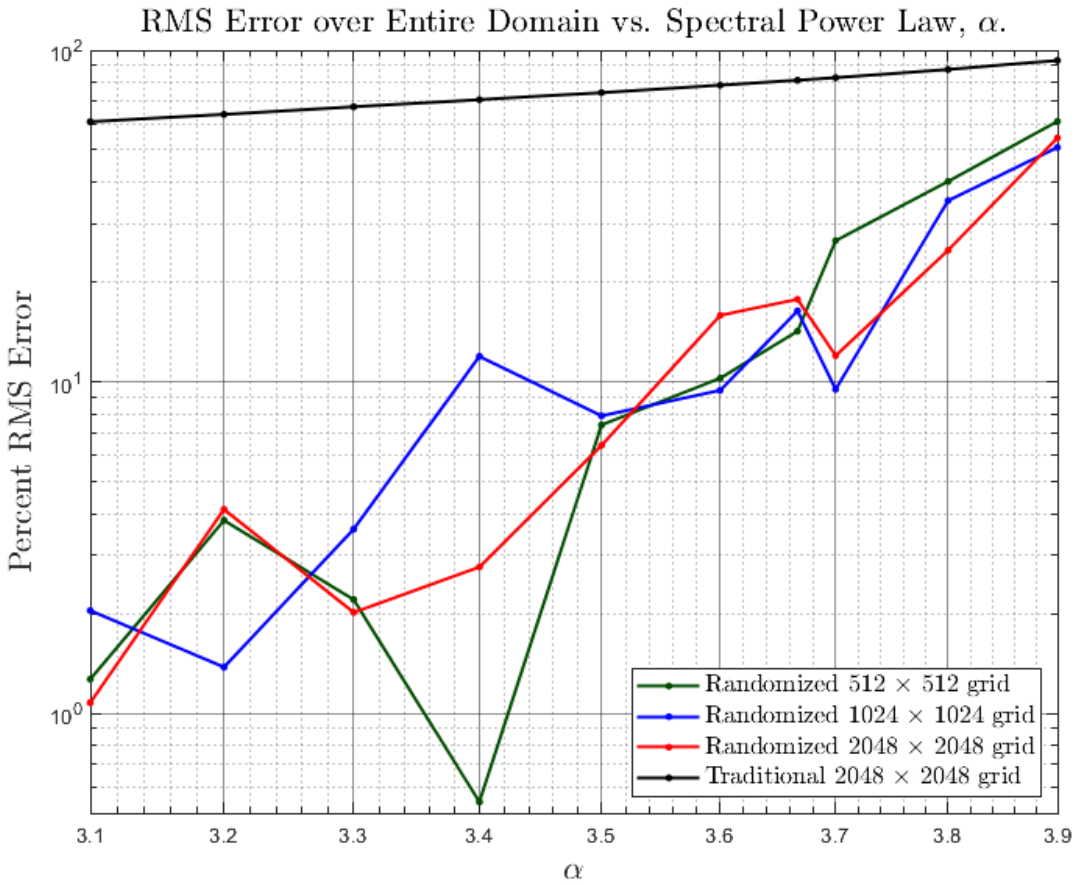


**Figure B-1:** RMS error as a percent relative to theory over 50,000 phase screen trials over the entire simulated domain as parameterized by the three dimensional spectral power law, $\boldsymbol{\alpha}$. 512 × 512, 1024 × 1024, 2048 × 2048 grid results are shown for randomized method. For the traditional method, the 2048 × 2048 grid is shown. Other grid sizes are not shown for the traditional method because the results appear to completely overlap at this scale. No subharmonics were used in the phase screens used to generate statistics in this chart.

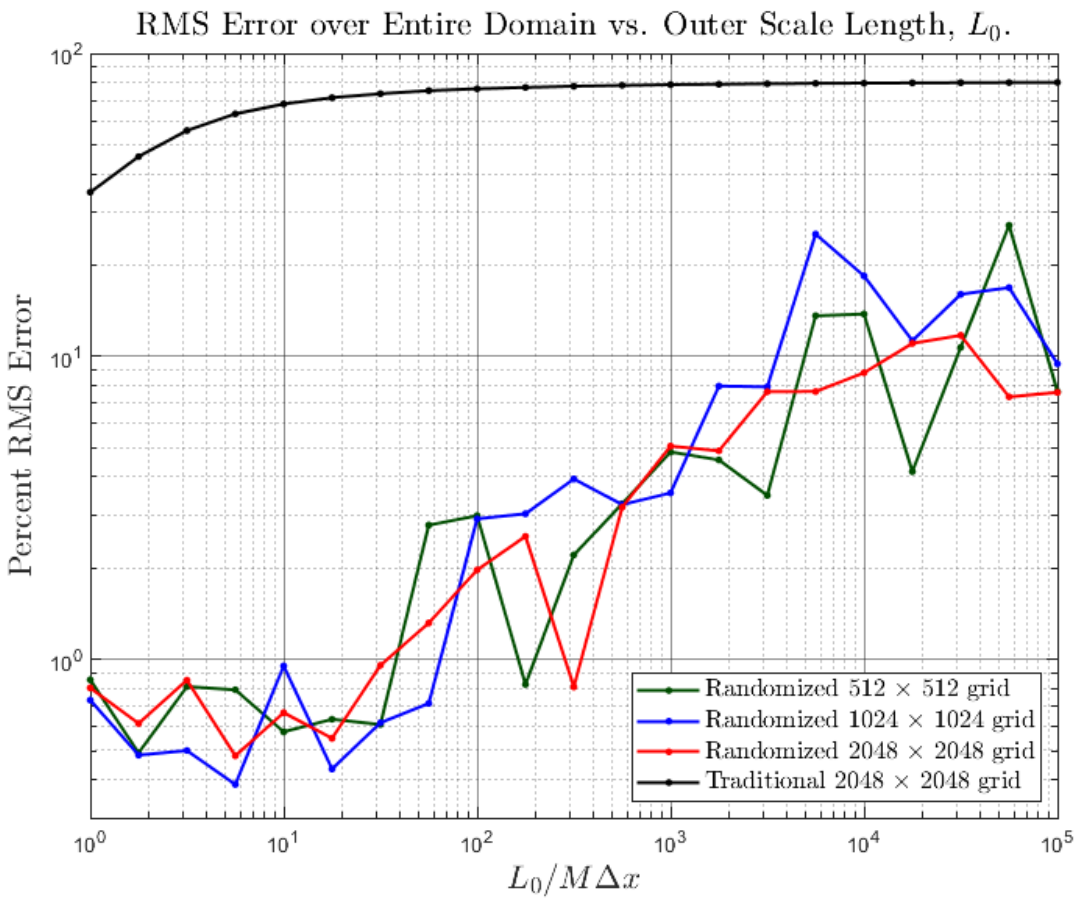


**Figure B-2:** RMS error as a percent relative to theory for the modified spectrum over 50,000 phase screen trials for the entire domain region of interest as parameterized by the three dimensional spectral power law, $\alpha$. 512 × 512, 1024 × 1024, 2048 × 2048 grid results are shown for randomized method. The outer scale has been normalized by the domain width, $M\Delta x$ (m), to make the results applicable for any domain size. For the traditional method only the 2048 × 2048 grid is shown due to significant overlap of the RMS error metric.

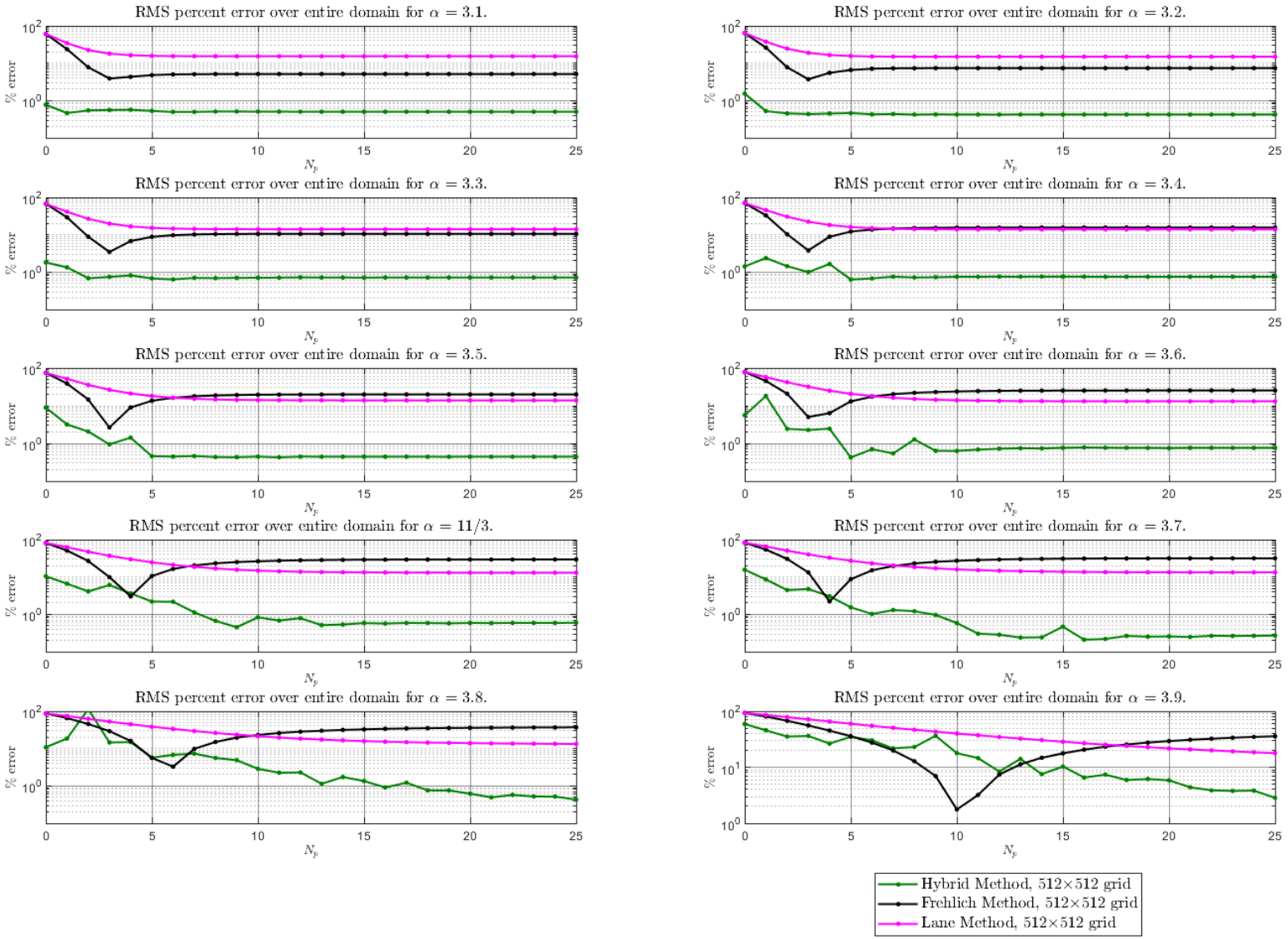


**Figure B-3:** RMS error over entire domain computed along *x*- and *y*-directions of 50,000 phase screens for 512 × 512 grid using various spectral power laws ($\alpha$'s) and number of subharmonic constellations, $N_p$. $\mu_x = \mu_y = 1$ for all data points. The randomized hybrid method (**green**), Frehlich subharmonic method (**black**), and Lane subharmonic method (**magenta**) are shown.

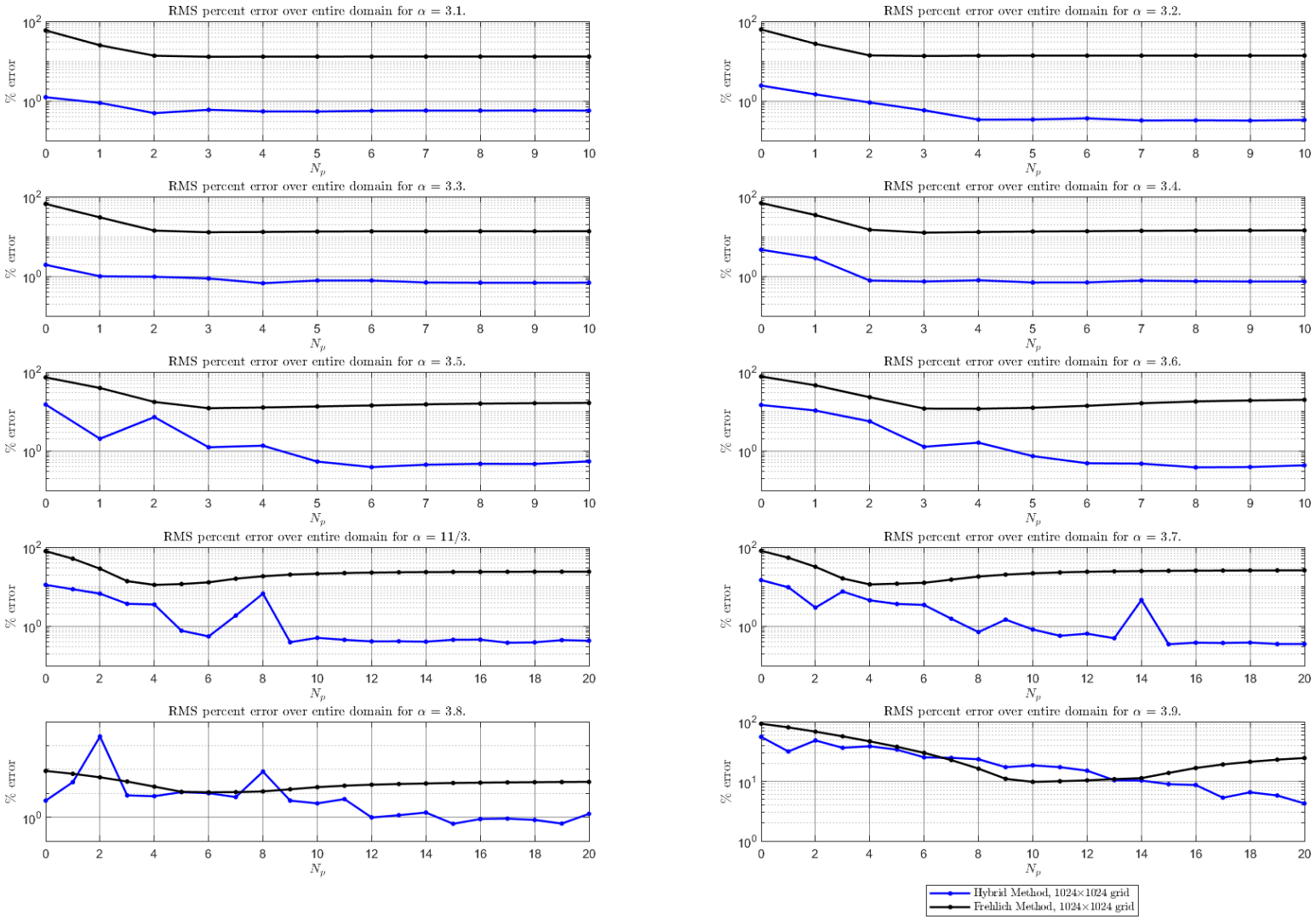


**Figure B-4:** RMS error over entire domain computed along $x$- and $y$-directions of 50,000 phase screens for 1024 × 1024 grid using various spectral power laws ($\alpha$'s) and number of subharmonic constellations, $N_p$. $\mu_x = 1$, $\mu_y = 2$ for all data points. The randomized hybrid method (**blue**) and Frehlich subharmonic method (**black**) are shown.

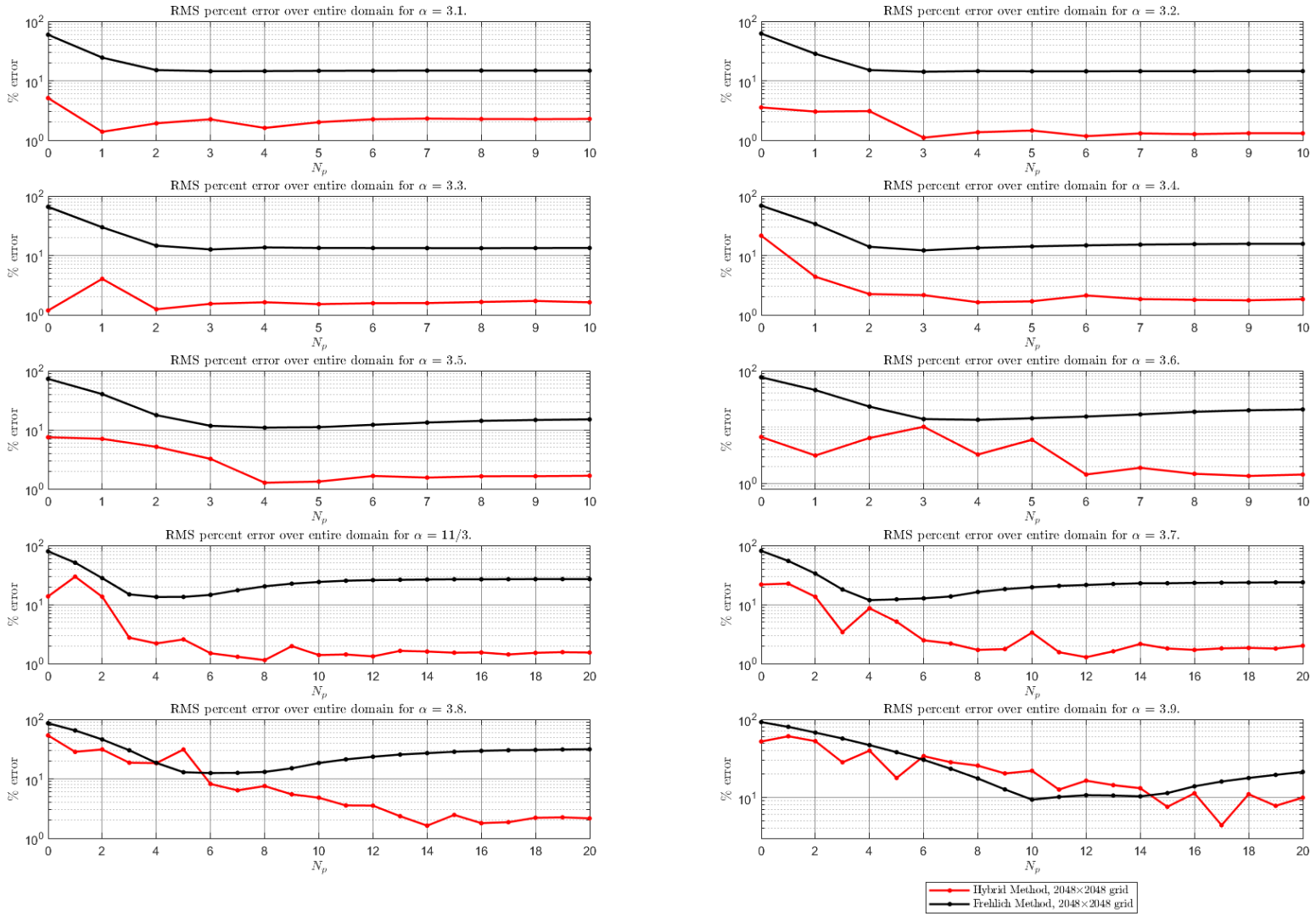


**Figure B-5:** RMS error over entire domain computed along *x*- and *y*-directions of 5,000 phase screens for 2048 × 2048 grid using various spectral power laws ($\alpha$'s) and number of subharmonic constellations, $N_p$. $\mu_x = 1$, $\mu_y = 2$ for all data points. The randomized hybrid method (**red**) and Frehlich subharmonic method (**black**) are shown.

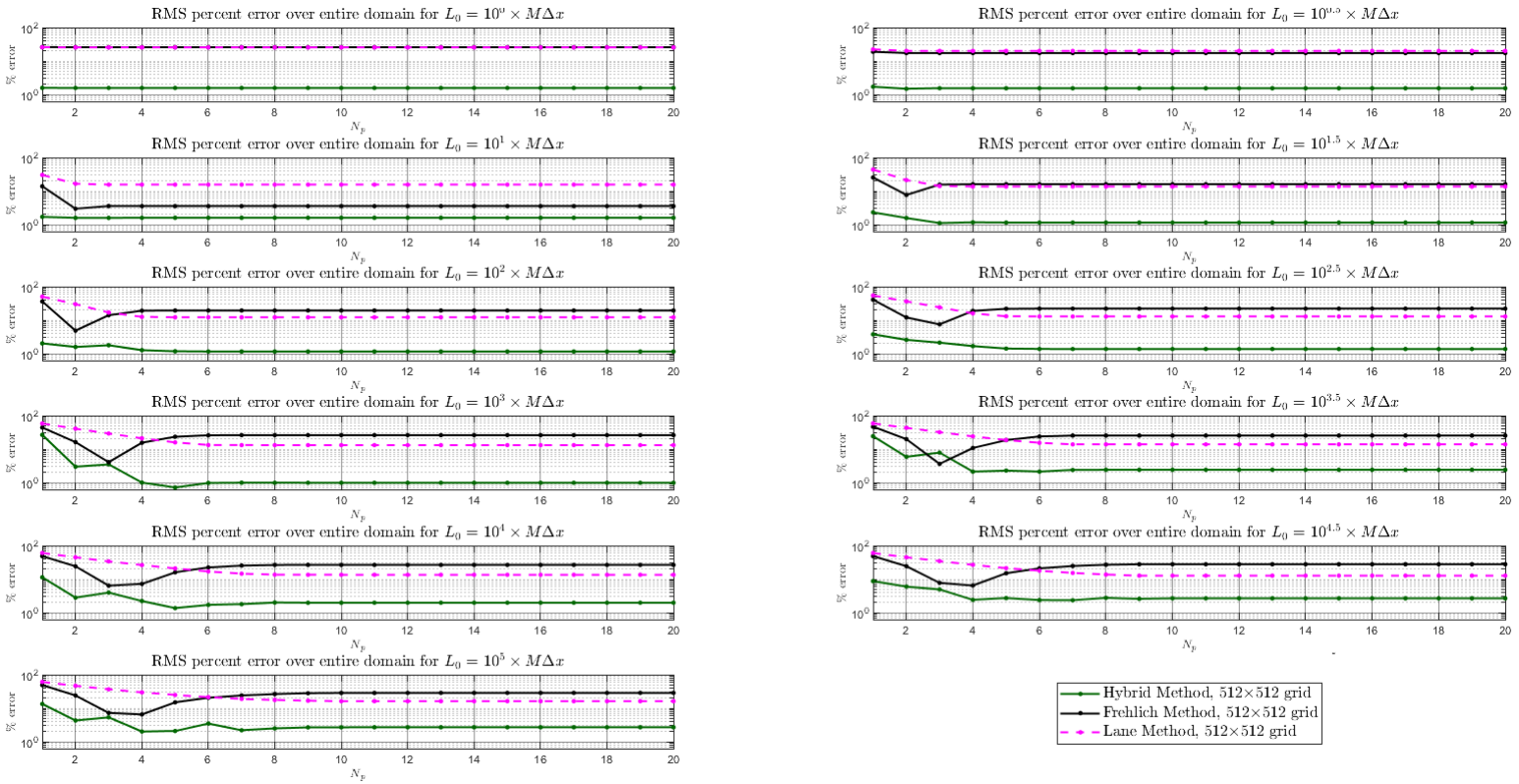


**Figure B-6:** RMS error over entire domain for the modified spectrum computed along *x*- and *y*-directions for 5,000 phase screens using modified spectrum, with $l_0 = M\Delta x/100$ and $M = 512$ (i.e. grid size 512 × 512).

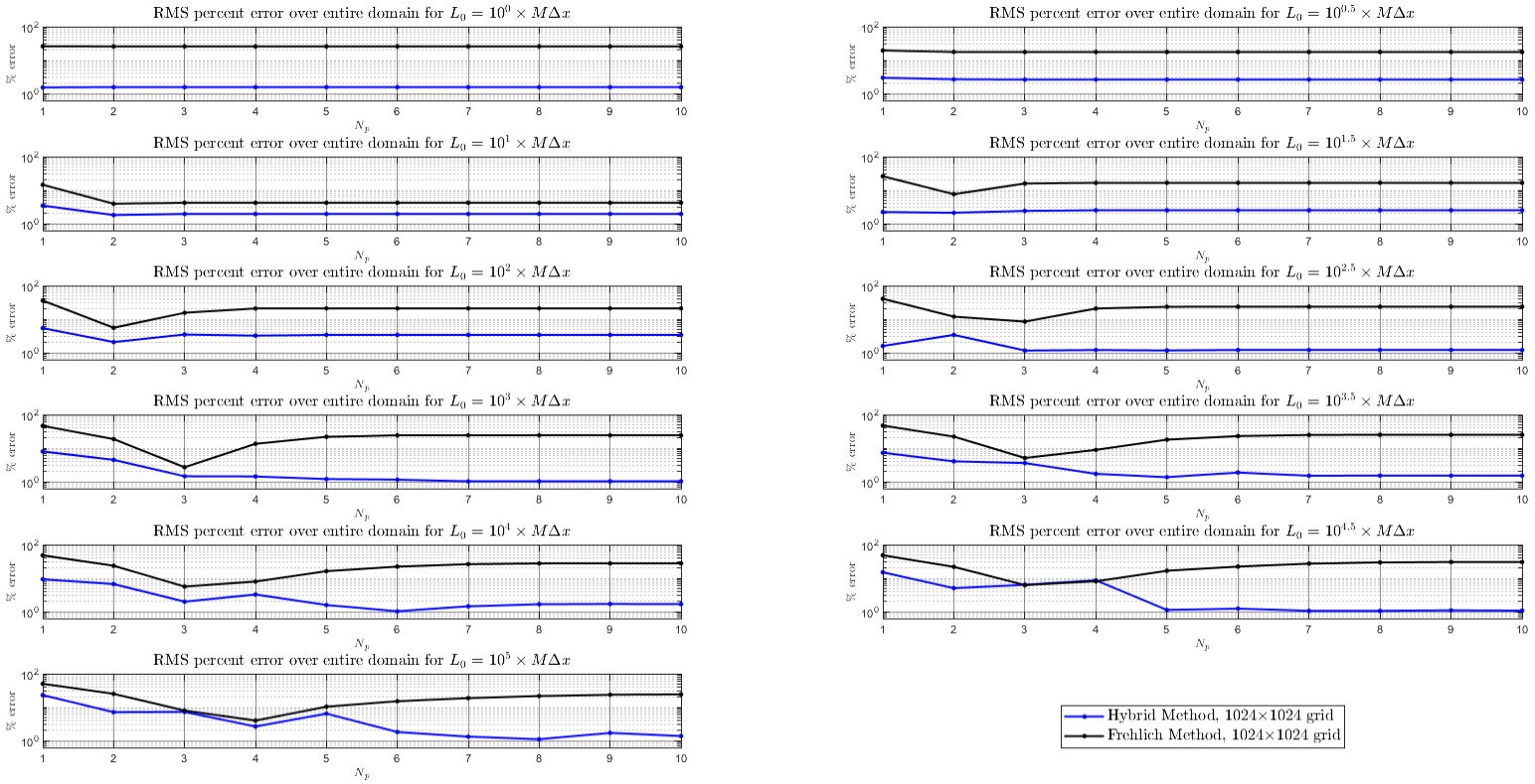


**Figure B-7:** RMS error over entire domain computed along *x*- and *y*-directions for 5000 phase screens using modified spectrum, with $l_0 = M\Delta x/100$ and $M = 1024$ (i.e. grid size 1024 × 1024).

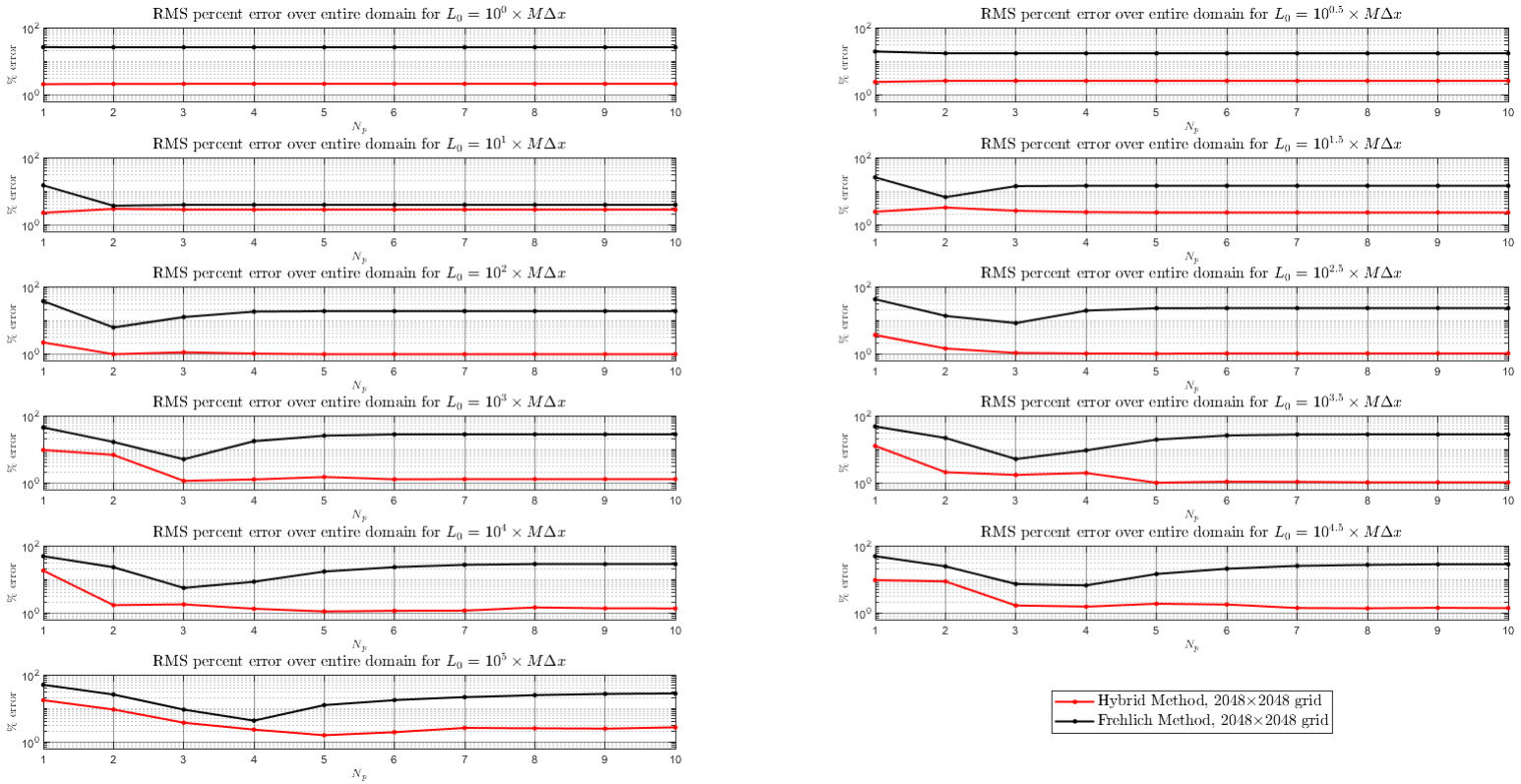


**Figure B-8:** RMS error over entire domain computed along *x*- and *y*-directions for 5000 phase screens using modified spectrum, with $l_0 = M\Delta x/100$ and $M = 2048$ (i.e. grid size 2048 × 2048).

## Appendix C: Tables of Non-Kolmogorov RMS Error Statistics over Entire Domain

| | $\alpha$ | | | | | | | | | |
|---|---|---|---|---|---|---|---|---|---|---|
| $N_p$ | **3.1** | **3.2** | **3.3** | **3.4** | **3.5** | **3.6** | **11/3** | **3.7** | **3.8** | **3.9** |
| **0** | 2.24 | 2.33 | 6.37 | 2.40 | 5.31 | 15.08 | 24.92 | 29.87 | 36.12 | 60.02 |
| **1** | 2.09 | 2.69 | 4.46 | 3.61 | 9.77 | 6.51 | 14.32 | 4.11 | 34.06 | 54.30 |
| **2** | 2.05 | 2.52 | 3.47 | 1.77 | 54.07 | 9.01 | 4.71 | 16.80 | 29.89 | 40.97 |
| **3** | 2.72 | 2.35 | 1.76 | 2.92 | 2.72 | 5.96 | 4.10 | 7.76 | 14.78 | 45.58 |
| **4** | 2.64 | 2.22 | 1.69 | 2.56 | 3.65 | 2.89 | 2.47 | 10.06 | 18.26 | 39.54 |
| **5** | 2.87 | 2.23 | 1.68 | 2.16 | 1.89 | 1.96 | 4.47 | 2.40 | 10.77 | 39.29 |
| **6** | 2.84 | 2.27 | 1.63 | 2.18 | 2.10 | 1.36 | 1.52 | 6.45 | 10.17 | 28.35 |
| **7** | 2.93 | 2.24 | 1.75 | 2.23 | 1.92 | 1.13 | 7.74 | 4.15 | 8.42 | 13.49 |
| **8** | 2.99 | 2.21 | 1.72 | 2.35 | 1.74 | 1.06 | 1.58 | 3.69 | 7.21 | 20.94 |
| **9** | 3.00 | 2.25 | 1.73 | 2.09 | 1.75 | 1.09 | 1.18 | 3.11 | 5.24 | 19.09 |
| **10** | 2.99 | 2.24 | 1.69 | 2.23 | 1.64 | 1.14 | 1.44 | 3.97 | 3.64 | 23.16 |
| **11** | 3.00 | 2.24 | 1.65 | 2.22 | 1.63 | 1.00 | 1.33 | 2.96 | 3.80 | 17.92 |
| **12** | 2.99 | 2.25 | 1.67 | 2.27 | 1.69 | 0.98 | 1.71 | 2.44 | 2.24 | 17.93 |
| **13** | 2.99 | 2.24 | 1.69 | 2.26 | 1.75 | 1.04 | 1.64 | 2.92 | 2.55 | 15.50 |
| **14** | 3.00 | 2.25 | 1.68 | 2.29 | 1.71 | 1.12 | 1.63 | 3.16 | 2.98 | 11.43 |
| **15** | 2.99 | 2.25 | 1.67 | 2.27 | 1.74 | 1.04 | 1.79 | 3.00 | 3.16 | 10.07 |
| **16** | 3.00 | 2.25 | 1.67 | 2.25 | 1.72 | 1.07 | 1.68 | 2.84 | 2.26 | 10.76 |
| **17** | 2.99 | 2.25 | 1.67 | 2.27 | 1.71 | 1.05 | 1.71 | 3.08 | 2.23 | 10.81 |
| **18** | 2.99 | 2.25 | 1.67 | 2.27 | 1.72 | 1.08 | 1.67 | 2.92 | 3.35 | 9.80 |
| **19** | 2.99 | 2.25 | 1.67 | 2.27 | 1.72 | 1.07 | 1.67 | 2.88 | 2.63 | 13.37 |
| **20** | 2.99 | 2.25 | 1.67 | 2.27 | 1.73 | 1.06 | 1.63 | 2.73 | 2.62 | 7.46 |

**Table C-1:** RMS error over entire domain computed using the randomized hybrid subharmonic method along $x$- and $y$-directions of 50,000 phase screens for 512 × 512 grid using various spectral power laws ($\alpha$'s) and number of subharmonic constellations, $N_p$. $\mu_x = \mu_y = 1$ for all entries.

| | $\alpha$ | | | | | | | | | |
|---|---|---|---|---|---|---|---|---|---|---|
| $N_p$ | **3.1** | **3.2** | **3.3** | **3.4** | **3.5** | **3.6** | **11/3** | **3.7** | **3.8** | **3.9** |
| **0** | 61.06 | 63.93 | 67.56 | 70.85 | 74.26 | 78.44 | 81.17 | 82.83 | 87.55 | 93.00 |
| **1** | 23.65 | 24.96 | 29.84 | 33.54 | 38.31 | 45.63 | 51.29 | 54.34 | 65.85 | 80.21 |
| **2** | 7.72 | 7.38 | 8.30 | 10.61 | 14.20 | 21.59 | 26.79 | 30.38 | 45.64 | 67.56 |
| **3** | 3.04 | 6.35 | 4.44 | 3.39 | 2.71 | 5.28 | 9.87 | 13.43 | 28.98 | 55.81 |
| **4** | 3.46 | 8.66 | 8.01 | 7.62 | 9.16 | 5.93 | 2.85 | 2.33 | 16.74 | 45.86 |
| **5** | 3.83 | 9.92 | 10.04 | 11.29 | 13.62 | 12.54 | 10.55 | 8.74 | 7.56 | 37.50 |
| **6** | 4.00 | 10.20 | 10.99 | 12.88 | 16.03 | 17.33 | 15.56 | 15.81 | 2.63 | 29.16 |
| **7** | 4.11 | 10.30 | 11.25 | 13.76 | 17.44 | 20.26 | 19.36 | 20.54 | 8.59 | 22.11 |
| **8** | 4.14 | 10.39 | 11.50 | 14.16 | 18.71 | 21.72 | 22.65 | 25.21 | 14.22 | 15.51 |
| **9** | 4.13 | 10.46 | 11.65 | 14.33 | 19.40 | 22.71 | 24.73 | 27.72 | 19.21 | 9.54 |
| **10** | 4.13 | 10.49 | 11.69 | 14.47 | 19.56 | 23.38 | 26.20 | 29.40 | 23.19 | 2.97 |
| **11** | 4.13 | 10.50 | 11.71 | 14.58 | 19.71 | 23.96 | 27.32 | 30.92 | 26.20 | 2.25 |
| **12** | 4.12 | 10.50 | 11.69 | 14.59 | 19.79 | 24.48 | 27.85 | 31.79 | 28.26 | 6.45 |
| **13** | 4.12 | 10.50 | 11.70 | 14.56 | 19.89 | 24.84 | 28.24 | 32.37 | 30.10 | 10.65 |
| **14** | 4.13 | 10.50 | 11.70 | 14.58 | 19.89 | 25.09 | 28.69 | 33.01 | 31.76 | 14.24 |
| **15** | 4.13 | 10.50 | 11.69 | 14.57 | 19.88 | 25.19 | 28.94 | 33.05 | 32.98 | 17.56 |
| **16** | 4.13 | 10.50 | 11.69 | 14.57 | 19.89 | 25.28 | 29.02 | 33.23 | 33.95 | 20.65 |
| **17** | 4.13 | 10.50 | 11.70 | 14.57 | 19.91 | 25.35 | 29.11 | 33.18 | 34.83 | 23.50 |
| **18** | 4.13 | 10.50 | 11.69 | 14.58 | 19.93 | 25.41 | 29.20 | 33.16 | 35.41 | 26.07 |
| **19** | 4.13 | 10.50 | 11.69 | 14.58 | 19.94 | 25.42 | 29.27 | 33.21 | 35.79 | 28.45 |
| **20** | 4.13 | 10.50 | 11.69 | 14.58 | 19.94 | 25.43 | 29.31 | 33.30 | 36.05 | 30.77 |

**Table C-2:** RMS error over entire domain computed using the Frehlich subharmonic method along *x*- and *y*-directions of 50,000 phase screens for 512 × 512 grid using various spectral power laws ($\alpha$'s) and number of subharmonic constellations, $N_p$. $\mu_x = \mu_y = 1$ for all entries.

| | $\alpha$ | | | | | | | | | |
|---|---|---|---|---|---|---|---|---|---|---|
| $N_p$ | **3.1** | **3.2** | **3.3** | **3.4** | **3.5** | **3.6** | **11/3** | **3.7** | **3.8** | **3.9** |
| **0** | 61.06 | 63.93 | 67.56 | 70.85 | 74.26 | 78.44 | 81.17 | 82.83 | 87.55 | 93.00 |
| **1** | 32.70 | 33.33 | 38.75 | 41.82 | 47.70 | 54.22 | 59.85 | 62.00 | 72.08 | 84.23 |
| **2** | 19.37 | 18.95 | 22.88 | 24.29 | 29.63 | 37.54 | 42.76 | 44.17 | 58.29 | 75.22 |
| **3** | 14.74 | 12.51 | 15.07 | 16.20 | 20.02 | 27.10 | 30.83 | 31.45 | 47.39 | 67.53 |
| **4** | 12.94 | 10.51 | 11.16 | 11.98 | 13.35 | 19.79 | 22.47 | 22.77 | 38.38 | 60.62 |
| **5** | 12.58 | 9.92 | 9.81 | 9.93 | 10.25 | 15.15 | 16.87 | 17.19 | 31.05 | 54.84 |
| **6** | 12.21 | 9.77 | 9.38 | 8.87 | 9.17 | 12.57 | 13.04 | 12.16 | 24.66 | 49.26 |
| **7** | 12.14 | 9.73 | 9.15 | 8.47 | 8.82 | 11.42 | 10.20 | 10.87 | 19.69 | 43.92 |
| **8** | 12.11 | 9.70 | 9.06 | 8.24 | 8.82 | 11.23 | 10.05 | 11.37 | 15.68 | 39.49 |
| **9** | 12.12 | 9.72 | 9.04 | 8.16 | 8.94 | 11.03 | 10.47 | 11.58 | 12.37 | 34.96 |
| **10** | 12.12 | 9.73 | 9.02 | 8.15 | 9.07 | 11.03 | 10.69 | 11.60 | 12.52 | 30.74 |
| **11** | 12.13 | 9.74 | 9.02 | 8.13 | 9.04 | 11.24 | 11.01 | 12.24 | 12.92 | 28.04 |
| **12** | 12.14 | 9.75 | 9.01 | 8.10 | 9.07 | 11.19 | 11.21 | 12.34 | 13.06 | 24.83 |
| **13** | 12.14 | 9.75 | 9.02 | 8.11 | 9.05 | 11.31 | 11.27 | 12.47 | 13.33 | 22.07 |
| **14** | 12.14 | 9.75 | 9.01 | 8.10 | 9.09 | 11.36 | 11.32 | 12.39 | 13.21 | 19.64 |
| **15** | 12.14 | 9.75 | 9.01 | 8.10 | 9.04 | 11.36 | 11.36 | 12.36 | 13.63 | 17.34 |
| **16** | 12.14 | 9.75 | 9.01 | 8.10 | 9.03 | 11.38 | 11.38 | 12.48 | 13.77 | 15.09 |
| **17** | 12.14 | 9.75 | 9.00 | 8.09 | 9.04 | 11.37 | 11.33 | 12.48 | 13.72 | 13.57 |
| **18** | 12.14 | 9.75 | 9.00 | 8.09 | 9.04 | 11.36 | 11.36 | 12.43 | 13.76 | 13.15 |
| **19** | 12.14 | 9.75 | 9.00 | 8.09 | 9.04 | 11.37 | 11.31 | 12.47 | 13.87 | 13.00 |
| **20** | 12.14 | 9.75 | 9.00 | 8.09 | 9.04 | 11.39 | 11.32 | 12.52 | 13.97 | 13.05 |

**Table C-3:** RMS error over entire domain computed using the Lane subharmonic method along *x*- and *y*-directions of 50,000 phase screens for 512 × 512 grid using various spectral power laws ($\alpha$'s) and number of subharmonic constellations, $N_p$. $\mu_x = \mu_y = 1$ for all entries.

| | $\alpha$ | | | | | | | | | |
|---|---|---|---|---|---|---|---|---|---|---|
| $N_p$ | **3.1** | **3.2** | **3.3** | **3.4** | **3.5** | **3.6** | **11/3** | **3.7** | **3.8** | **3.9** |
| **0** | 1.24 | 2.42 | 1.93 | 4.63 | 14.96 | 14.56 | 11.18 | 14.72 | 4.92 | 55.72 |
| **1** | 0.89 | 1.45 | 1.00 | 2.83 | 2.04 | 10.53 | 8.65 | 9.71 | 29.37 | 31.70 |
| **2** | 0.49 | 0.91 | 0.97 | 0.78 | 7.19 | 5.60 | 6.68 | 2.96 | 2401.99 | 48.54 |
| **3** | 0.60 | 0.58 | 0.88 | 0.73 | 1.24 | 1.27 | 3.70 | 7.57 | 8.17 | 36.55 |
| **4** | 0.54 | 0.34 | 0.67 | 0.79 | 1.36 | 1.62 | 3.54 | 4.53 | 7.56 | 38.82 |
| **5** | 0.54 | 0.34 | 0.78 | 0.69 | 0.54 | 0.74 | 0.77 | 3.66 | 11.20 | 34.04 |
| **6** | 0.56 | 0.36 | 0.78 | 0.69 | 0.39 | 0.49 | 0.55 | 3.46 | 10.10 | 25.29 |
| **7** | 0.57 | 0.32 | 0.69 | 0.77 | 0.45 | 0.48 | 1.86 | 1.54 | 6.93 | 24.77 |
| **8** | 0.57 | 0.32 | 0.68 | 0.75 | 0.47 | 0.38 | 6.70 | 0.71 | 81.45 | 23.48 |
| **9** | 0.57 | 0.32 | 0.68 | 0.73 | 0.47 | 0.39 | 0.39 | 1.47 | 4.94 | 17.32 |
| **10** | 0.57 | 0.33 | 0.69 | 0.73 | 0.54 | 0.43 | 0.51 | 0.83 | 3.78 | 18.58 |
| **11** | - | - | - | - | - | - | 0.45 | 0.57 | 5.70 | 17.30 |
| **12** | - | - | - | - | - | - | 0.41 | 0.65 | 0.97 | 15.12 |
| **13** | - | - | - | - | - | - | 0.42 | 0.50 | 1.21 | 10.46 |
| **14** | - | - | - | - | - | - | 0.41 | 4.62 | 1.56 | 10.33 |
| **15** | - | - | - | - | - | - | 0.45 | 0.35 | 0.53 | 8.98 |
| **16** | - | - | - | - | - | - | 0.46 | 0.38 | 0.83 | 8.70 |
| **17** | - | - | - | - | - | - | 0.38 | 0.38 | 0.87 | 5.32 |
| **18** | - | - | - | - | - | - | 0.39 | 0.38 | 0.76 | 6.56 |
| **19** | - | - | - | - | - | - | 0.44 | 0.35 | 0.54 | 5.80 |
| **20** | - | - | - | - | - | - | 0.43 | 0.35 | 1.38 | 4.27 |

**Table C-4:** RMS error over entire domain computed using the randomized hybrid subharmonic method along x- and *y*-directions of 50,000 phase screens for 1024 × 1024 grid using various spectral power laws ($\alpha$'s) and number of subharmonic constellations, $N_p$. $\mu_x = 1$, $\mu_y = 2$ for all entries. Hyphen ( - ) entries indicate no RMS error was computed for this entry.

| | $\alpha$ | | | | | | | | | |
|---|---|---|---|---|---|---|---|---|---|---|
| $N_p$ | 3.1 | 3.2 | 3.3 | 3.4 | 3.5 | 3.6 | 11/3 | 3.7 | 3.8 | 3.9 |
| 0 | 59.08 | 62.33 | 65.64 | 69.03 | 72.73 | 76.73 | 79.70 | 81.17 | 86.30 | 92.46 |
| 1 | 25.01 | 27.26 | 30.04 | 34.45 | 39.19 | 45.76 | 51.23 | 54.21 | 65.60 | 80.38 |
| 2 | 13.67 | 13.89 | 13.98 | 14.67 | 17.38 | 22.90 | 28.59 | 31.90 | 46.69 | 68.11 |
| 3 | 12.85 | 13.46 | 12.74 | 12.45 | 12.06 | 11.82 | 13.85 | 16.21 | 31.19 | 56.90 |
| 4 | 12.94 | 13.65 | 12.95 | 12.89 | 12.59 | 11.71 | 11.15 | 11.44 | 19.05 | 46.87 |
| 5 | 12.98 | 13.77 | 13.22 | 13.28 | 13.33 | 12.37 | 11.72 | 11.92 | 11.54 | 38.05 |
| 6 | 13.00 | 13.72 | 13.39 | 13.51 | 14.15 | 13.87 | 12.91 | 12.58 | 11.00 | 30.04 |
| 7 | 13.00 | 13.74 | 13.45 | 13.79 | 15.11 | 16.10 | 15.95 | 15.13 | 11.23 | 22.74 |
| 8 | 13.00 | 13.76 | 13.46 | 14.00 | 15.77 | 17.85 | 18.45 | 18.09 | 11.97 | 16.33 |
| 9 | 13.00 | 13.76 | 13.45 | 14.09 | 16.16 | 18.92 | 20.26 | 20.28 | 14.76 | 11.04 |
| 10 | 12.99 | 13.76 | 13.46 | 14.14 | 16.42 | 19.65 | 21.39 | 21.91 | 18.08 | 9.80 |
| 11 | - | - | - | - | - | - | 22.20 | 23.00 | 20.72 | 10.06 |
| 12 | - | - | - | - | - | - | 22.81 | 23.95 | 22.95 | 10.41 |
| 13 | - | - | - | - | - | - | 23.17 | 24.51 | 24.50 | 10.90 |
| 14 | - | - | - | - | - | - | 23.46 | 24.98 | 25.84 | 11.34 |
| 15 | - | - | - | - | - | - | 23.67 | 25.28 | 27.01 | 13.84 |
| 16 | - | - | - | - | - | - | 23.82 | 25.52 | 27.87 | 16.74 |
| 17 | - | - | - | - | - | - | 23.92 | 25.68 | 28.65 | 19.20 |
| 18 | - | - | - | - | - | - | 23.99 | 25.80 | 29.22 | 21.33 |
| 19 | - | - | - | - | - | - | 24.00 | 25.88 | 29.68 | 23.12 |
| 20 | - | - | - | - | - | - | 24.06 | 25.95 | 30.10 | 24.63 |

**Table C-5:** RMS error over entire domain computed using the Frehlich subharmonic method along x and y directions of 50,000 phase screens for 1024 × 1024 grid using various spectral power laws ($\alpha$'s) and number of subharmonic constellations, $N_p$. $\mu_x = 1$, $\mu_y = 2$ for all entries. Hyphen ( - ) entries indicate no RMS error was computed for this entry.

| | α | | | | | | | | | |
|---|---|---|---|---|---|---|---|---|---|---|
| $N_p$ | 3.1 | 3.2 | 3.3 | 3.4 | 3.5 | 3.6 | 11/3 | 3.7 | 3.8 | 3.9 |
| 0 | 5.11 | 3.56 | 1.19 | 21.50 | 7.47 | 6.66 | 13.72 | 21.82 | 53.72 | 52.02 |
| 1 | 1.38 | 3.02 | 4.04 | 4.38 | 7.02 | 3.12 | 29.55 | 22.56 | 28.40 | 60.73 |
| 2 | 1.92 | 3.08 | 1.24 | 2.24 | 5.14 | 6.39 | 13.54 | 13.51 | 31.17 | 52.60 |
| 3 | 2.24 | 1.10 | 1.54 | 2.15 | 3.21 | 10.12 | 2.74 | 3.40 | 18.67 | 28.16 |
| 4 | 1.61 | 1.36 | 1.63 | 1.63 | 1.27 | 3.25 | 2.19 | 8.63 | 18.37 | 39.70 |
| 5 | 2.01 | 1.45 | 1.52 | 1.69 | 1.33 | 5.94 | 2.57 | 5.12 | 31.11 | 17.73 |
| 6 | 2.25 | 1.17 | 1.57 | 2.12 | 1.65 | 1.44 | 1.50 | 2.47 | 8.19 | 33.84 |
| 7 | 2.31 | 1.30 | 1.58 | 1.84 | 1.55 | 1.89 | 1.30 | 2.18 | 6.40 | 28.22 |
| 8 | 2.27 | 1.26 | 1.65 | 1.79 | 1.63 | 1.48 | 1.14 | 1.70 | 7.56 | 25.55 |
| 9 | 2.26 | 1.31 | 1.71 | 1.76 | 1.64 | 1.35 | 1.97 | 1.76 | 5.48 | 20.31 |
| 10 | 2.28 | 1.31 | 1.63 | 1.83 | 1.67 | 1.43 | 1.39 | 3.34 | 4.82 | 21.94 |
| 11 | - | - | - | - | - | - | 1.42 | 1.56 | 3.56 | 12.61 |
| 12 | - | - | - | - | - | - | 1.32 | 1.28 | 3.54 | 16.41 |
| 13 | - | - | - | - | - | - | 1.64 | 1.61 | 2.35 | 14.38 |
| 14 | - | - | - | - | - | - | 1.60 | 2.15 | 1.63 | 13.13 |
| 15 | - | - | - | - | - | - | 1.53 | 1.80 | 2.47 | 7.59 |
| 16 | - | - | - | - | - | - | 1.54 | 1.70 | 1.80 | 11.30 |
| 17 | - | - | - | - | - | - | 1.43 | 1.81 | 1.86 | 4.41 |
| 18 | - | - | - | - | - | - | 1.52 | 1.84 | 2.21 | 11.00 |
| 19 | - | - | - | - | - | - | 1.56 | 1.79 | 2.25 | 7.81 |
| 20 | - | - | - | - | - | - | 1.54 | 2.00 | 2.16 | 9.95 |

**Table C-6:** RMS error over entire domain computed using the randomized hybrid subharmonic method along *x*- and *y*-directions of 5,000 phase screens for 2048 × 2048 grid using various spectral power laws ($\alpha$'s) and number of subharmonic constellations, $N_p$. $\mu_x = 1$, $\mu_y = 2$ for all entries. Hyphen ( - ) entries indicate no RMS error was computed for this entry.

| | $\alpha$ | | | | | | | | | |
|---|---|---|---|---|---|---|---|---|---|---|
| $N_p$ | 3.1 | 3.2 | 3.3 | 3.4 | 3.5 | 3.6 | 11/3 | 3.7 | 3.8 | 3.9 |
| 0 | 59.36 | 62.17 | 65.71 | 68.72 | 72.81 | 76.57 | 79.48 | 80.96 | 86.00 | 92.30 |
| 1 | 24.48 | 28.38 | 29.79 | 33.75 | 40.16 | 45.30 | 51.10 | 54.63 | 65.08 | 80.17 |
| 2 | 15.07 | 15.08 | 14.60 | 13.98 | 17.67 | 23.08 | 27.99 | 33.37 | 45.88 | 67.70 |
| 3 | 14.45 | 14.15 | 12.62 | 12.17 | 11.67 | 13.85 | 14.84 | 17.95 | 30.20 | 56.85 |
| 4 | 14.50 | 14.50 | 13.62 | 13.43 | 10.87 | 13.44 | 13.41 | 11.83 | 18.56 | 46.82 |
| 5 | 14.68 | 14.40 | 13.38 | 14.16 | 11.06 | 14.31 | 13.43 | 12.22 | 12.91 | 37.93 |
| 6 | 14.73 | 14.41 | 13.33 | 14.78 | 12.14 | 15.38 | 14.57 | 12.72 | 12.51 | 30.32 |
| 7 | 14.81 | 14.45 | 13.29 | 15.21 | 13.26 | 16.77 | 17.44 | 13.69 | 12.61 | 23.27 |
| 8 | 14.79 | 14.45 | 13.26 | 15.51 | 14.15 | 18.64 | 20.30 | 16.30 | 13.06 | 17.49 |
| 9 | 14.79 | 14.51 | 13.32 | 15.67 | 14.65 | 19.83 | 22.51 | 18.24 | 15.07 | 12.67 |
| 10 | 14.79 | 14.51 | 13.36 | 15.68 | 14.98 | 20.54 | 24.05 | 19.60 | 18.43 | 9.37 |
| 11 | - | - | - | - | - | - | 25.27 | 20.66 | 21.23 | 10.17 |
| 12 | - | - | - | - | - | - | 25.84 | 21.44 | 23.53 | 10.69 |
| 13 | - | - | - | - | - | - | 26.20 | 22.27 | 25.56 | 10.58 |
| 14 | - | - | - | - | - | - | 26.50 | 22.85 | 27.06 | 10.33 |
| 15 | - | - | - | - | - | - | 26.68 | 22.92 | 28.51 | 11.38 |
| 16 | - | - | - | - | - | - | 26.72 | 23.26 | 29.50 | 13.90 |
| 17 | - | - | - | - | - | - | 26.78 | 23.40 | 30.23 | 15.99 |
| 18 | - | - | - | - | - | - | 26.85 | 23.52 | 30.59 | 17.74 |
| 19 | - | - | - | - | - | - | 26.92 | 23.67 | 31.12 | 19.46 |
| 20 | - | - | - | - | - | - | 26.90 | 23.75 | 31.40 | 21.24 |

**Table C-7:** RMS error over entire domain computed using the Frehlich subharmonic method along x and y directions of 5,000 phase screens for 2048 × 2048 grid using various spectral power laws ($\alpha$'s) and number of subharmonic constellations, $N_p$. $\mu_x = 1$, $\mu_y = 2$ for all entries. Hyphen ( - ) entries indicate no RMS error was computed for this entry.

# Bibliography


[1] G. I. Taylor, "Statistical Theory of Turbulence," *Proceedings of the Royal Society of London. Series A - Mathematical and Physical Sciences,* vol. 151, pp. 421-444, 1935.

[2] A. N. Kolmogorov, "The Local Structure of Turbulence in Incompressible Viscous Fluid for Very Large Reynolds Numbers," *Proceedings: Mathematical and Physical Sciences,* vol. 434, pp. 9-13, 1991.

[3] A. N. Kolmogorov, "Dissipation of Energy in the Locally Isotropic Turbulence," *Proceedings: Mathematical and Physical Sciences,* vol. 434, pp. 15-17, 1991.

[4] A. M. Obukov, "On the distribution of energy in the spectrum of turbulent flow," *Bull. Acad. Sci. USSR, Geog. Geophys.,* vol. 5, pp. 453-466, 1941.

[5] L. A. Chernov, Wave propagation in a random medium., New York: McGraw-Hill, 1960.

[6] V. I. Tatarskiĭ, Wave propagation in a turbulent medium., New York: McGraw-Hill, 1961.

[7] D. L. Fried, "Statistics of a Geometric Representation of Wavefront Distortion," *J. Opt. Soc. Am.,* vol. 55, pp. 1427-1435, 11 1965.

[8] A. Ishimaru, *Wave propagation and scattering in random media,* Oxford ;: Oxford University Press, 1997.

[9] L. C. Andrews and R. L. Phillips, *Laser beam propagation through random media,* 2nd ed. ed., Bellingham, Wash.: SPIE, 2005, pp. 35-438.

[10] M. Bester, W. C. Danchi, C. G. Degiacomi, L. J. Greenhill and C. H. Townes, "Atmospheric fluctuations - Empirical structure functions and projected performance of future instruments," *The Astrophysical Journal,* vol. 392, p. 357, 1992.

[11] F. Wang, I. Toselli, J. Li and O. Korotkova, "Measuring anisotropy ellipse of atmospheric turbulence by intensity correlations of laser light," *Opt. Lett.,* vol. 42, pp. 1129-1132, 3 2017.

[12] S. Gladysz, K. Stein, E. Sucher, D. Sprung, R. S. Clouds, Atmosphere XVIII, O. Atmospheric Propagation and D. E. U. 2. 0. 2. 2. 0. 2. Adaptive Systems XVI Dresden, "Measuring non-Kolmogorov turbulence," *Proceedings of SPIE - The International Society for Optical Engineering,* vol. 8890, 2013.

[13] D. Dayton, B. Pierson, B. Spielbusch and J. Gonglewski, "Atmospheric structure function measurements with a Shack--Hartmann wave-front sensor," *Opt. Lett.,* vol. 17, pp. 1737-1739, 12 1992.

[14] A. Berdja, "On the DIMM interpretation of non-Kolmogorov turbulence in the atmospheric surface layer," *Monthly Notices of the Royal Astronomical Society,* vol. 409, pp. 722-726, 11 2010.

[15] J. T. Beyer, M. C. Roggemann, L. J. Otten, T. J. Schulz, T. C. Havens and W. W. Brown, "Experimental estimation of the spatial statistics of turbulence-induced index of refraction fluctuations in the upper atmosphere," *Appl. Opt.,* vol. 42, pp. 908-921, 2 2003.

[16] A. Smirnov, S. Shi and I. Celik, "Random Flow Generation Technique for Large Eddy Simulations and Particle-Dynamics Modeling," *Journal of Fluids Engineering,* vol. 123, pp. 359-371, 2 2001.

[17] C. Cambon, "Strongly Anisotropic Turbulence, Statistical Theory and DNS," in *Turbulence and Interactions*, Berlin, 2009.

[18] G. E. Elsinga and I. Marusic, "The anisotropic structure of turbulence and its energy spectrum," *Physics of Fluids,* vol. 28, p. 011701, 2016.

[19] A. Kon, "Qualitative theory of amplitude and phase fluctuations in a medium with anisotropic turbulent irregularities," *Waves in Random and Complex Media,* vol. 4, pp. 297-306, 1994.

[20] B. E. Stribling, B. M. Welsh and M. C. Roggemann, "Optical propagation in non-Kolmogorov atmospheric turbulence," *Proceedings of SPIE - The International Society for Optical Engineering,* p. 181, 1995.

[21] R. R. Beland, "Some aspects of propagation through weak isotropic non-Kolmogorov turbulence," *Proceedings of SPIE - The International Society for Optical Engineering,* p. 6, 1995.

[22] I. Toselli, L. C. Andrews, R. L. Phillips and V. Ferrero, "Free-space optical system performance for laser beam propagation through non-Kolmogorov turbulence," *Optical engineering : the journal of the Society of Photo-optical Instrumentation Engineers.,* vol. 47, p. 26003, 2008.

[23] L. C. Andrews, R. L. Phillips, R. Crabbs, L. Communication, P. T. Atmosphere and 1. Oceans III 3 2014 08 17 2014 08, "Propagation of a Gaussian-beam wave in general anisotropic turbulence," *Proceedings of SPIE - The International Society for Optical Engineering,* vol. 9224, 2014.

[24] L. C. Andrews, R. L. Phillips and R. Crabbs, "Laser Beam Propagation through the Low Atmosphere, Year 3 Final Report," 2015.

[25] M. Beason, L. Andrews, R. Phillips, L. Communication, P. Atmosphere and 0. Oceans VI 2017 6 2017 08 08 2017 08, "Study on the effect of

anisotropy on a propagating beam," *Proceedings of SPIE - The International Society for Optical Engineering,* vol. 10408, 2017.

[26] R. J. Hill, "Models of the scalar spectrum for turbulent advection," *Journal of Fluid Mechanics,* vol. 88, p. 541–562, 1978.

[27] E. W. Weisstein, "Wiener-Khinchin Theorem," [Online]. Available: http://mathworld.wolfram.com/Wiener-KhinchinTheorem.html.

[28] J. C. Owens, "Optical Refractive Index of Air: Dependence on Pressure, Temperature and Composition," *Appl. Opt.,* vol. 6, pp. 51-59, 1 1967.

[29] R. M. Williams and C. A. Paulson, "Microscale temperature and velocity spectra in the atmospheric boundary layer," *Journal of Fluid Mechanics,* vol. 83, p. 547–567, 1977.

[30] A. Zangwill, "Retardation and Radiation," in *Modern Electrodynamics*, New York, Cambridge University Press, 2012, pp. 714-774.

[31] D. G. Voelz, *Computational fourier optics : a MATLAB tutorial,* Bellingham, Wash.: SPIE Press, 2011, pp. 63-87, 113-140.

[32] G. B. Arfken, F. E. Harris and H.-J. Weber, "Integral Equations," in *Mathematical methods for physicists : a comprehensive guide*, Seventh edition. ed., Waltham, MA: Academic Press, 2013, pp. 1047-1079.

[33] J. D. Schmidt, *Numerical Simulation of Optical Wave Propagation with Examples in MATLAB,* Bellingham, Wash.: SPIE, 2010, pp. 15-37, 87-113, 133-147.

[34] C. C. Davis, *The optics of Gaussian beams,* Cambridge, UK: Cambridge University Press, 2014, p. 438–444.

[35] M. G. Kendall, A. Stuart, J. K. Ord, S. F. Arnold and A. O'Hagan, Kendall's advanced theory of statistics., 6th ed. ed., New York: Halsted Press, 1994.

[36] E. W. Weisstein, "Hypergeometric Function," [Online]. Available: http://mathworld.wolfram.com/HypergeometricFunction.html.

[37] V. I. Tatarskii, The effects of the turbulent atmosphere on wave propagation, Jerusalem: Israel program for scientific translations, 1971.

[38] X. Xiao and D. Voelz, "Beam wander analysis for focused partially coherent beams propagating in turbulence," *Optical Engineering,* vol. 51, p. 026001, 2012.

[39] J. W. Goodman, Introduction to Fourier Optics, 4 ed., New York: W.H. Freedman and Company, 2017, pp. 10, 64-66.

[40] J. A. Fleck, J. R. Morris and M. D. Feit, "Time-dependent propagation of high energy laser beams through the atmosphere," *Applied Physics,* vol. 10, pp. 129-160, 01 6 1976.

[41] J. A. Fleck, J. R. Morris and M. D. Feit, "Time-dependent propagation of high-energy laser beams through the atmosphere: II," *Applied Physics,* vol. 14, pp. 99-115, 01 9 1977.

[42] P. Sprangle, J. R. Peñano, A. Ting and B. Hafizi, "Incoherent Combining of High-Power Fiber Lasers for Long-Range Directed Energy Applications," Washington, 2006.

[43] P. Sprangle, J. R. Peñano and B. Hafizi, "Beam Combining and Atmospheric Propagation of High Power Lasers," Washington, 2011.

[44] J. P. Palastro, J. Peñano, W. Nelson, G. DiComo, M. Helle, L. A. Johnson and B. Hafizi, "Reciprocity breaking during nonlinear propagation of adapted beams through random media," *Opt. Express,* vol. 24, pp. 18817-18827, 8 2016.

[45] J. Gustafsson, B. F. Akers, J. A. Reeger and S. S. Sritharan, "Atmospheric Propagation of High Energy Lasers," *Engineering Mathematics Letters,* vol. 2019, p. Article ID 7, 2019.

[46] V. P. Kandidov, O. G. Kosareva, M. P. Tamarov, A. Brodeur and S. L. Chin, "Nucleation and random movement of filaments in the propagation of high-power laser radiation in a turbulent atmosphere," *Quantum Electronics,* vol. 29, pp. 911-915, 10 1999.

[47] S. L. Chin, A. Talebpour, J. Yang, S. Petit, V. P. Kandidov, O. G. Kosareva and M. P. Tamarov, "Filamentation of femtosecond laser pulses in turbulent air," *Applied Physics B,* vol. 74, pp. 67-76, 01 1 2002.

[48] J. R. Peñano, P. Sprangle, B. Hafizi, A. Ting, D. F. Gordon and C. A. Kapetanakos, "Propagation of ultra-short, intense laser pulses in air," *Physics of Plasmas,* vol. 11, pp. 2865-2874, 2004.

[49] A. Couairon and A. Mysyrowicz, "Femtosecond filamentation in transparent media," *Physics Reports,* vol. 441, pp. 47-189, 2007.

[50] A. Houard, M. Franco, B. Prade, A. Durécu, L. Lombard, P. Bourdon, O. Vasseur, B. Fleury, C. Robert, V. Michau, A. Couairon and A. Mysyrowicz, "Femtosecond filamentation in turbulent air," *Phys. Rev. A,* vol. 78, no. 3, p. 033804, 9 2008.

[51] J. Peñano, B. Hafizi, A. Ting and M. Helle, "Theoretical and numerical investigation of filament onset distance in atmospheric turbulence," *J. Opt. Soc. Am. B,* vol. 31, pp. 963-971, 5 2014.

[52] R. G. Lane, A. Glindemann and J. C. Dainty, "Simulation of a Kolmogorov phase screen," *Waves in Random Media,* vol. 2, pp. 209-224, 1992.

[53] R. Frehlich, "Simulation of laser propagation in a turbulent atmosphere," *Appl. Opt.,* vol. 39, pp. 393-397, 1 2000.

[54] N. A. Roddier, "Atmospheric wavefront simulation using Zernike polynomials," *Optical Engineering,* vol. 29, pp. 1174-1180, 1990.

[55] W. P. Burckel and R. N. Gray, "Turbulence phase screens based on polar-logarithmic spectral sampling," *Appl. Opt.,* vol. 52, pp. 4672-4680, 7 2013.

[56] M. Charnotskii, "Sparse spectrum model for a turbulent phase," *J. Opt. Soc. Am. A,* vol. 30, pp. 479-488, 3 2013.

[57] W. Nelson, J. P. Palastro, C. C. Davis and P. Sprangle, "Propagation of Bessel and Airy beams through atmospheric turbulence," *J. Opt. Soc. Am. A,* vol. 31, pp. 603-609, 3 2014.

[58] W. Nelson, J. P. Palastro, C. Wu and C. C. Davis, "Enhanced backscatter of optical beams reflected in turbulent air," *J. Opt. Soc. Am. A,* vol. 32, pp. 1371-1378, 7 2015.

[59] X. Xiao, D. G. Voelz, I. Toselli and O. Korotkova, "Gaussian beam propagation in anisotropic turbulence along horizontal links: theory, simulation, and laboratory implementation," *Appl. Opt.,* vol. 55, pp. 4079-4084, 5 2016.

[60] D. G. Voelz, E. Wijerathna, A. Muschinski and X. Xiao, "Computer simulations of optical turbulence in the weak- and strong-scattering regime: angle-of-arrival fluctuations obtained from ray optics and wave optics," *Optical Engineering,* vol. 57, pp. 1 - 9 - 9, 2018.

[61] S. K. Mitra, "Digital signal processing: a computer-based approach," 2 ed., Boston, McGraw-Hill/Irwin, 2001, pp. 140-143, 584-593.

[62] M. Charnotskii, "Statistics of the sparse spectrum turbulent phase," *J. Opt. Soc. Am. A,* vol. 30, pp. 2455-2465, 12 2013.

[63] D. A. Paulson, C. Wu and C. C. Davis, "A detailed comparison of non-Kolmogorov and anisotropic optical turbulence theories using wave optics simulations," in *Laser Communication and Propagation through the Atmosphere and Oceans VII*, 2018.

[64] S. A. Orszag, "Comparison of Pseudospectral and Spectral Approximation," *Studies in Applied Mathematics,* vol. 51, pp. 253-259, 1972.

[65] "NIST Digital Library of Mathematical Functions," [Online]. Available: http://dlmf.nist.gov/10.22.E45.

[66] D. A. Paulson, C. Wu and C. C. Davis, "Randomized spectral sampling for efficient simulation of laser propagation through optical turbulence," *J. Opt. Soc. Am. B,* vol. 36, pp. 3249-3262, 11 2019.

[67] J. D. Mansell, R. Praus and S. Coy, "Determining wave-optics mesh parameters for complex optical systems," *Proc. SPIE 6675, Optical Modeling and Performance Predictions,* vol. III, p. 66750H, 14 9 2007.

[68] S. Coy, "Choosing mesh spacings and mesh dimensions for wave optics simulation," *Proc. SPIE 5894, Advanced Wavefront Control: Methods, Devices, and Applications,* vol. III, p. 589405, 18 8 2005.

[69] S. M. Flatté, G.-Y. Wang and J. Martin, "Irradiance variance of optical waves through atmospheric turbulence by numerical simulation and comparison with experiment," *J. Opt. Soc. Am. A,* vol. 10, pp. 2363-2370, 11 1993.

[70] K. D. Ridley and E. Jakeman, "Incomplete phase conjugation through a random phase screen. II. Numerical simulations," *J. Opt. Soc. Am. A,* vol. 13, pp. 2393-2402, 12 1996.

[71] C. Wu, J. R. Rzasa, J. Ko, D. A. Paulson, J. Coffaro, J. Spychalsky, R. F. Crabbs and C. C. Davis, "Multi-aperture laser transmissometer system for long-path aerosol extinction rate measurement," *Appl. Opt.,* vol. 57, pp. 551-559, 1 2018.

[72] Y. Cheon and A. Muschinski, "Closed-form approximations for the angle-of-arrival variance of plane and spherical waves propagating through homogeneous and isotropic turbulence," *J. Opt. Soc. Am. A,* vol. 24, pp. 415-422, 2 2007.

[73] F. H. Champagne, C. A. Friehe, J. C. LaRue and J. C. Wynagaard, "Flux Measurements, Flux Estimation Techniques, and Fine-Scale Turbulence Measurements in the Unstable Surface Layer Over Land," *Journal of the Atmospheric Sciences,* vol. 34, pp. 515-530, 1977.

[74] L. C. Andrews, "An Analytical Model for the Refractive Index Power Spectrum and Its Application to Optical Scintillations in the Atmosphere," *Journal of Modern Optics,* vol. 39, pp. 1849-1853, 1992.

[75] L. C. Andrews, S. Vester and C. E. Richardson, "Analytic Expressions for the Wave Structure Function Based on a Bump Spectral Model for Refractive Index Fluctuations," *Journal of Modern Optics,* vol. 40, pp. 931-938, 1993.

[76] I. Toselli, B. Agrawal and S. Restaino, "Light propagation through anisotropic turbulence," *J. Opt. Soc. Am. A,* vol. 28, pp. 483-488, 3 2011.

[77] L. C. Andrews, R. L. Phillips, R. Crabbs and T. Leclerc, "Deep turbulence propagation of a Gaussian-beam wave in anisotropic non-Kolmogorov turbulence," *Proc. SPIE 8874, Laser Communication and Propagation through the Atmosphere and Oceans,* vol. II, p. 887402, 2013.

[78] F. Wang and O. Korotkova, "Random optical beam propagation in anisotropic turbulence along horizontal links," *Opt. Express,* vol. 24, pp. 24422-24434, 10 2016.

[79] M. Beason, C. Smith, J. Coffaro, S. Belichki, J. Spychalsky, F. Titus, R. Crabbs, L. Andrews and R. Phillips, "Near ground measure and theoretical model of plane wave covariance of intensity in anisotropic turbulence," *Opt. Lett.,* vol. 43, pp. 2607-2610, 6 2018.

[80] S. M. Ghiaasiaan, "Fundamental of Turbulence and External Turbulent Flow," in *Convective Heat and Mass Transfer*, New York, Cambridge University Press, 2011, pp. 177-207.

[81] R. L. Fante, "Electromagnetic beam propagation in turbulent media," *Proceedings of the IEEE,* vol. 63, pp. 1669-1692, 12 1975.

[82] E. M. Johansson and D. T. Gavel, "Simulation of stellar speckle imaging," *Proceedings SPIE 2200, Amplitude and Intensity Spatial Interferometry,* vol. II, p. 372–383, 1994.

[83] D. A. Paulson, C. Wu, J. R. Rzasa, J. Ko, M. V. Iersel, J. Coffaro, C. Smith, R. Crabbs and C. C. Davis, "A multi-aperture laser transmissometer for detailed characterization of laser propagation over long paths through the turbulent atmosphere," in *Laser Communication and Propagation through the Atmosphere and Oceans VII*, 2018.

[84] J. C. Ricklin, W. B. Miller and L. C. Andrews, "Effective beam parameters and the turbulent beam waist for convergent Gaussian beams," *Appl. Opt.,* vol. 34, pp. 7059-7065, 10 1995.

[85] V. A. Kulikov and M. A. Vorontsov, "Analysis of the joint impact of atmospheric turbulence and refractivity on laser beam propagation," *Opt. Express,* vol. 25, pp. 28524-28535, 11 2017.

[86] M. A. Vorontsov, V. A. Kulikov and Z. Yang, "Accounting for optical refractivity and turbulence effects in optical wave propagation over long distances," in *Long-Range Imaging III*, 2018.

[87] M. Beason, F. Sanzone, B. Berry, J. Coffaro, J. Spychalski, F. Titus, R. Crabbs, L. Andrews and R. Phillips, "Considering Power Law, Optical Refractivity, and Anisotropy Using Gaussian Beam Statistics," in *Imaging and Applied Optics 2019 (COSI, IS, MATH, pcAOP)*, 2019.

[88] R. J. Sasiela, Electromagnetic wave propagation in turbulence : evaluation and application of Mellin transforms, Berlin ;: Springer-Verlag, 1994, pp. 47-58.

[89] B. S. Pritchard and W. G. Elliott, "Two Instruments for Atmospheric Optics Measurements∗," *J. Opt. Soc. Am.,* vol. 50, pp. 191-202, 3 1960.

[90] J. L. Gaumet and A. Petitpa, "Lidar-Transmissometer Visibility Comparisons Over Slant and Horizontal Paths," *Journal of Applied Meteorology (1962-1982),* vol. 21, pp. 683-694, 1982.

[91] P. C. Ariessohn, S. A. Self and R. H. Eustis, "Two-wavelength laser transmissometer for measurements of the mean size and concentration of coal ash droplets in combustion flows," *Appl. Opt.,* vol. 19, pp. 3775-3781, 11 1980.

[92] H. Barth, K. Grisard, K. Holtsch, R. Reuter and U. Stute, "Polychromatic transmissometer for in situ measurements of suspended particles and gelbstoff in water," *Appl. Opt.,* vol. 36, pp. 7919-7928, 10 1997.

[93] G. P. Perram, S. J. Cusumano, R. L. Hengehold, S. T. Fiorino and A. F. I. Technology (U.S.), An introduction to laser weapon systems, 1st ed. ed., Albuquerque, NM: Directed Energy Professional Society, 2010, pp. 209-217.

[94] R. F. Lutomirski, "Atmospheric degradation of electrooptical system performance," *Appl. Opt.,* vol. 17, pp. 3915-3921, 12 1978.

[95] W. T. Kreiss, J. M. Lansinger, W. G. Tank and M. L. Pitchford, "Field Testing Of A Long-Path Laser Transmissometer Designed For Atmospheric Visibility Measurements," in *Advances in Laser Technology for the Atmospheric Sciences*, 1977.

[96] S. G. Mallat and G. Peyré, *A wavelet tour of signal processing : the sparse way,* 3rd ed. ed., Amsterdam ;: Elsevier/Academic Press, 2009.

[97] J. V. Winstanley and M. J. Adams, "Point Visibility Meter: a forward scatter instrument for the measurement of aerosol extinction coefficient," *Appl. Opt.,* vol. 14, pp. 2151-2157, 9 1975.

[98] C. Wu, D. A. Paulson, M. V. Iersel, J. Coffaro, M. Beason, C. Smith, R. F. Crabbs, R. Phillips, L. Andrews and C. C. Davis, "Near ground surface turbulence measurements and validation: a comparison between different systems," in *Laser Communication and Propagation through the Atmosphere and Oceans VII*, 2018.

[99] R. S. Lawrence, G. R. Ochs and S. F. Clifford, "Measurements of Atmospheric Turbulence Relevant to Optical Propagation," *J. Opt. Soc. Am.,* vol. 60, p. 826–830, 6 1970.

[100] T.-i. Wang, G. R. Ochs and S. F. Clifford, "A saturation-resistant optical scintillometer to measure Cn2†," *J. Opt. Soc. Am.,* vol. 68, p. 334–338, 3 1978.

[101] S. Bauer and J. Steinborn, "Time bias service: analysis and monitoring of satellite orbit prediction quality," *Journal of Geodesy,* vol. 93, pp. 1-11, 10 2019.

[102] C. Wu, D. A. Paulson, J. R. Rzasa and C. C. Davis, "Light field camera study of near-ground turbulence anisotropy and observation of small outer-scales," *Opt. Lett.,* vol. 45, p. 1156–1159, 3 2020.

[103] "Solvers," [Online]. Available: https://octave.org/doc/v4.0.1/Solvers.html.

[104] "fsolve," [Online]. Available: https://www.mathworks.com/help/optim/ug/fsolve.html.

[105] G. A. Tyler and D. L. Fried, "A wave optics propagation algorithm," 1982.

[106] "NIST Digital Library of Mathematical Functions," [Online]. Available: https://dlmf.nist.gov/7.7.E3.

[107] *File:Transmissometer.jpg. (2015, May 6).,* Wikimedia Commons, the free media repository., 2008.

[108] "Visibility Sensors - All Weather Inc," [Online]. Available: https://www.allweatherinc.com/meteorological-sensors/visibility-sensors/. [Accessed 13 March 2020].